

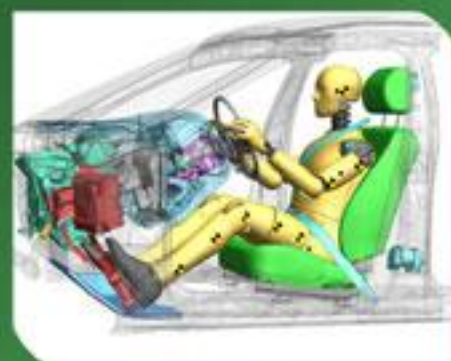
**MMSE** *Vol.4*

ISSN 2412-5954

#4  
2016

SCIENTIFIC PERIODICALS

# MECHANICS, MATERIALS SCIENCE & ENGINEERING

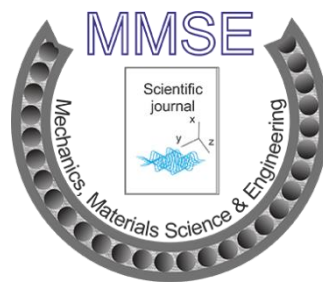


WWW.MMSE.XYZ

OPEN  ACCESS

Sankt Lorenzen 36, 8715, Sankt Lorenzen, Austria

*Mechanics, Materials Science & Engineering Journal*



*May 2016*

Mechanics, Materials Science & Engineering Journal (MMSE Journal) is journal that deals in peer-reviewed, open access publishing, focusing on wide range of subject areas, including economics, business, social sciences, engineering etc.

MMSE Journal is dedicated to knowledge-based products and services for the academic, scientific, professional, research and student communities worldwide.

Open Access model of the publications promotes research by allowing unrestricted availability of high quality articles.

All authors bear the personal responsibility for the material they published in the Journal.

The Journal Policy declares the acceptance of the scientific papers worldwide, if they passed the peer-review procedure.

Editor-in-Chief Mr. Peter Zisser

Dr. Zheng Li, University of Bridgeport, USA

Prof. Kravets Victor, Ukraine

Ph.D., Shuming Chen, College of Automotive Engineering, China

Dr. Yang Yu, University of Technology Sydney, Australia

Prof. Amelia Carolina Sparavigna, Politecnico di Torino, Italy

ISSN 2412-5954

e-ISSN 2414-6935

Design and layout: Mechanics, Materials  
Science & Engineering Journal, [www.mmse.xyz](http://www.mmse.xyz)

Technical support: [hotmail@mmse.xyz](mailto:hotmail@mmse.xyz)

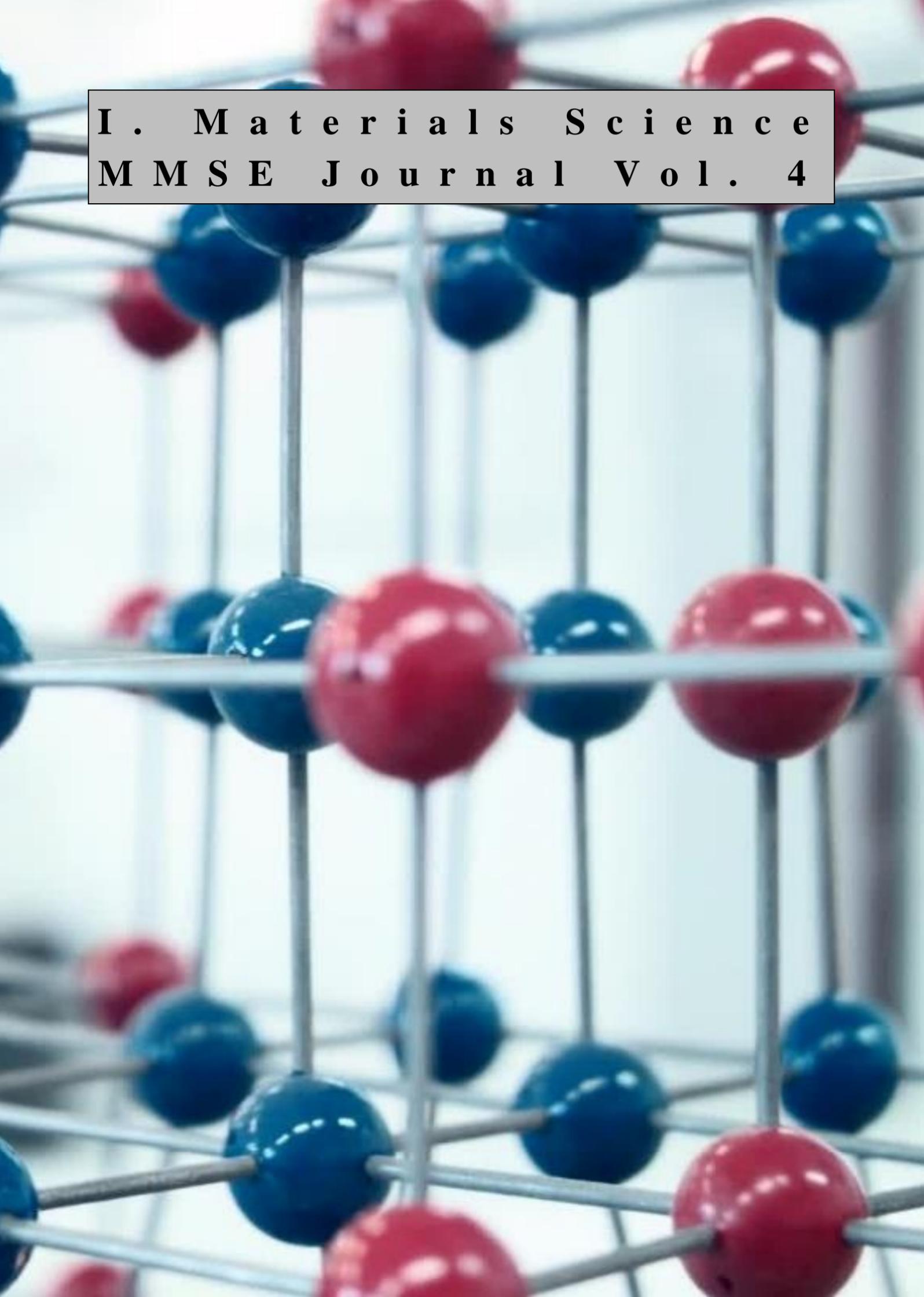
©2016, Magnolithe GmbH

© Copyright, by the authors

## CONTENT

<b>I. Materials Science MMSE Journal Vol. 4 .....</b>	<b>6</b>
<b>Experimental Characterization of Innovative Viscoelastic Foams.</b> <i>Massimo Viscardi, Maurizio Arena .....</i>	<b>7</b>
<b>Optimization Of Tribological Properties Of Aluminium Honeycomb Reinforced Polymeric Composites Using Grey Based Fuzzy Algorithm.</b> <i>K.Panneerselvam, K.Lokesh, Chandresh D., T.N.S.Ramakrishna .....</i>	<b>15</b>
<b>Formation And Distribution of Brittle Structures in Friction Stir Welding of AA 6061 To Copper. Influence of Preheat.</b> <i>Seyed Vahid Safi, Hossein Amirabadi, Mohammad Kazem Besharati Givi .....</i>	<b>25</b>
<b>Isothermal Pneumo-Forming of Hemispherical Parts Made Out of Anisotropic Materials In Short-Term Creep Mode.</b> <i>S.N. Larin, V.I. Platonov, Nuzhdin G.A. ....</i>	<b>34</b>
<b>MHD Stagnation Point Flow in a Boundary Layer Of a Nano Fluid Over a Stretching Sheet in the Presence of Viscous Dissipation and Chemical Reaction.</b> <i>Ch. Achi Reddy, B. Shankar ....</i>	<b>45</b>
<b>Quality Characteristics of Cutting Surfaces in the Milling of the Titanium Alloy Ti10V2Fe3Al.</b> <i>Michael Storchak, Lucas Saxarra, Like Jiang, Yiping Xu, Xun Li .....</i>	<b>57</b>
<b>A Comparison between Dual Phase Steel and Interstitial Free Steel Due To the Springback Effect.</b> <i>E.A. Silva, L.F.V.M. Fernandes, N.A.S. Sampaio, R.B. Ribeiro, J.W.J. Silva, M.S. Pereira. ....</i>	<b>71</b>
<b>II. MECHANICAL ENGINEERING &amp; PHYSICS MMSE JOURNAL VOL. 4 .....</b>	<b>81</b>
<b>On Application of the Ground Effect For Highspeed Surface Vehicles.</b> <i>Kravets Viktor V., Kravets Vl.V. &amp; Fedoriachenko S.A. ....</i>	<b>82</b>
<b>On the Comparison Between the Approximate And Precise Methods of Piled Raft Foundation Analysis.</b> <i>Abbasali Taghavi Ghalesari .....</i>	<b>88</b>
<b>Dynamic Stress and Strain Analysis for 8x4 Truck Frame.</b> <i>Nagwa Ahmed Abdel-halim .....</i>	<b>96</b>
<b>Identification of Standing Pressure Waves Sources in Primary Loops of NPP with WWER and PWR.</b> <i>K.N. Proskuriakov, A.I. Fedorov, M.V. Zaporozhets and G.Y. Volkov .....</i>	<b>109</b>
<b>Methods for Solving a Stress Behaviour of Welded Joints under Repeated Loads.</b> <i>Semrád K., Čerňan J. ....</i>	<b>128</b>
<b>Numerical Modelling of Basin Type Solar Stills.</b> <i>Nguyen The Bao .....</i>	<b>133</b>
<b>VII. ENVIRONMENTAL SAFETY MMSE JOURNAL VOL. 4.....</b>	<b>148</b>
<b>HAVS and HAV-nots: Investigating Resonance in the Human Arm Caused by Contact with Machinery.</b> <i>Irina Viktorova, Matthew Fleck and Muhammed Kose .....</i>	<b>149</b>

<b>Monitoring the Natural Factors Influence on Vegetation Development by Using Moderate-Resolution Imaging Spectroradiometer (Modis) Images with OBIA Method in Uzbekistan.</b> <i>Sh. B. Akmalov, J. V. Gerts, D. B. Omonov</i> .....	156
<b>An Empirically Derived Arc Flash Discharge Energy Model and Comparison to Established Safety Codes.</b> <i>Irina Viktorova &amp; Michael Bates</i> .....	160
<b>On Development of a New Filtering Half-Mask.</b> <i>S.I. Cheberyachko, D.I. Radchuk, Y.I. Cheberyachko, M.O. Ziborova</i> .....	164
<b>Fluid Injection Induced Seismicity in the Oil and Gas Field Areas: Monitoring and Modelling.</b> <i>A. Zabolotin, A.V. Konovalov, A.A. Stepnov, A.S. Sychov, D.E. Tomilev</i> .....	170
<b>The Effect of Microwave Radiation on the Properties of Canola Seeds.</b> <i>Roudane M., Hemis M.</i> .....	179
<b><u>IX. ECONOMICS &amp; MANAGEMENT MMSE JOURNAL VOL. 4.....</u></b>	<b>187</b>
<b>Human Capital and Growth of E-postal Services: A cross-country Analysis in Developing Countries.</b> <i>Dalibor Gottwald, Libor Švadlenka, Hana Pavlisová</i> .....	188
<b><u>X. PHILOSOPHY OF RESEARCH AND EDUCATION MMSE JOURNAL VOL. 4.....</u></b>	<b>210</b>
<b>Systematic Analysis and Synthesis of Integral Estimations of Bachelors' Training in the Field of Financial Monitoring.</b> <i>Alena Gaibatova, Grigory Krylov1, Ilya Seryy, Anastasiia Vorobeva, Konstantin Vorobev</i> .....	211



**I . M a t e r i a l s S c i e n c e**  
**M M S E J o u r n a l V o l . 4**

# Experimental Characterization of Innovative Viscoelastic Foams

Massimo Viscardi<sup>1</sup>, Maurizio Arena<sup>1</sup>

1 – University of Naples “Federico II”, Department of Industrial Engineering, Via Claudio, 21 – 80125 Napoli, Italy



DOI 10.13140/RG.2.1.5150.6325

**Keywords:** noise control, automotive, damping, foam, viscoelasticity.

**ABSTRACT.** The evolutionary trend in the automotive industry has produced over time numerous performance and aesthetic innovations, however, the exponential development related to transportation technologies also introduced new requirements concerning the environmental impact [1]. The awareness of ecological issues has led to a reorganization of the evaluations and the vehicle design, currently aimed at reducing the problems that have emerged in empirical investigations and the parallel increase in environmental solutions. The vehicle renewal process involves targeted technical mutations both to observance of ecology as to the safety and comfort of the driver. New recyclable materials and more resistant have been developed in order to minimize the environmental impact of the vehicle even at the end of the operating life of its components, as well as solutions relating to the reduction of noise pollution generated as a response to the requirements of comfort. Modern research programs on a global scale have set themselves the objective of exploiting the potentiality of innovative technologies in the optimization of vehicles efficiency, the noise reduction and in the consequent reduction of fuel burn. One of the crucial topics in the greening of the new generation automotive sector is therefore the use and development of high vibro-acoustic performance materials. The goal of this research is properly focused on the analysis of viscoelastic materials appointed to increase the damping of the vibrations generated in a vehicle. The use of a viscoelastic material in this context is due to its high property to convert vibrational energy into heat, providing a significant dissipation of the vibrations. Trade-off analyses are performed in order define the stiffness and damping capacity of several viscoelastic foams with different thickness and density.

**Introduction.** The purpose of the present work is the experimental investigation of new materials and technologies to reduce the noise and vibrations produced inside motor vehicles. It is known, that there are several noise causes of the vehicles, both in the cockpit and in the environment: those of great impact are related to the engine and to the tyre/road interaction processes, that induce noise into the cockpit both through a structure-borne path contribution (mainly the vibration of the car floor induced by the mechanical forcing of the car body floor) and an air-borne path contribution. In Figure 1 these noise sources are evident for a moving car.

Nomenclature	
$\delta$	Logarithmic decrement
$FE$	Finite Element
$F$	Force
$F$	Frequency
$FRF$	Frequency Response Function
$g$	g-force
$k$	Static stiffness
$t$	Time
$w$	Static deflection
$\zeta$	Damping ratio

The new low-consumption engines also provide a design, which causes a higher specific noise than the previous ones: new soundproofing solutions are therefore necessary. In this research contest, innovative materials, targeted at the reduction of the car-body floor, will be analysed and compared to “standard one”; in the specific, viscoelastic foams will be investigated as a valid alternative to conventional add-on damping element as generally used in these applications [2]. The investigation of this class of viscoelastic material in this context is due to the high ability to convert vibration energy into thermal energy, providing a significant increase of vibration damping, hence this aspect will be study in terms of both static and dynamic stiffness and damping factor [3-6].

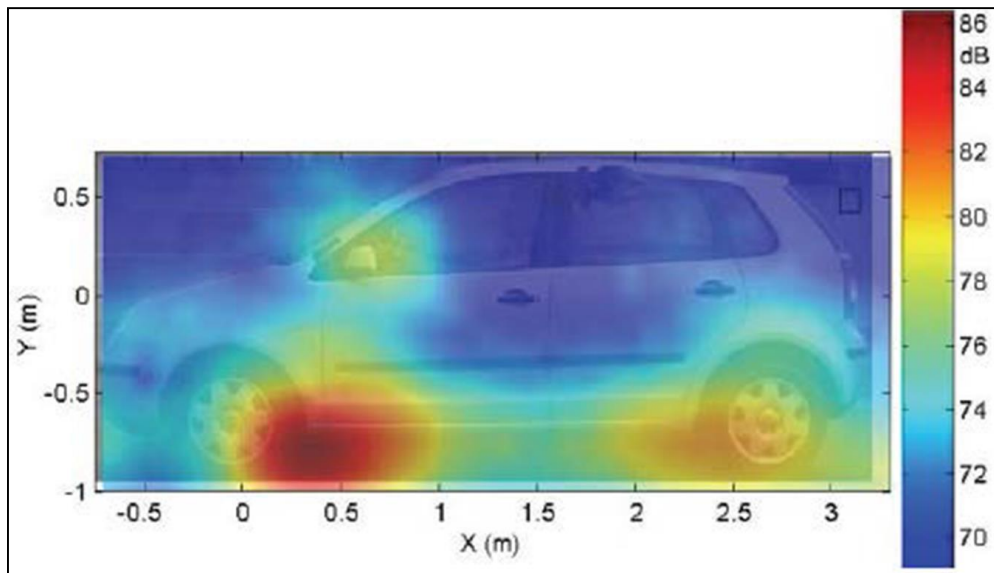


*Fig. 1. Vibration distribution color map*



*Fig. 2. Technological application*

Standard foams are already used as a part of the car-body carpet element, but their role is mainly the decoupling of the carpet from the floor; basic idea of the research is to force this element to strongly contribute to the vibrational energy dissipation.

Within the paper, viscoelastic foams with different physical properties (density, thickness, structure) will be compared. The first experimental step concerns static stiffness measurements of the several viscoelastic foams.

In the second phase, damping characteristics of each foam have been carried out by the use of modal testing. Furthermore, in some cases, the dynamic stiffness has been measured for comparison with the static one.

**Experimental measures.** The experimental measurements performed in this research have allowed estimating the properties of stiffness and damping of innovative viscoelastic foams with different densities and thicknesses.

**Static stiffness.** In this section, the results of laboratory tests in order to measure the stiffness coefficient (1) will be explained.

$$k = \frac{F}{w} = \frac{[N]}{[mm]} \quad (1)$$

The experimental investigation concerns the comparison of original foam (intended as the standard foam already used in most of the automotive applications) 65-30 and two other viscoelastic foams 65-30, 75-30 where these two digit represent respectively density ( $\text{Kg}/\text{m}^3$ ) and thickness (mm).

The static stiffness of each viscoelastic foam was evaluated in correspondence of different compression load settings by means of a test facility, shown in Fig. 3.



*Fig. 3. Static test facility*

In Figure 4 the trends of load versus static displacement have been plotted with reference to each case of investigation.

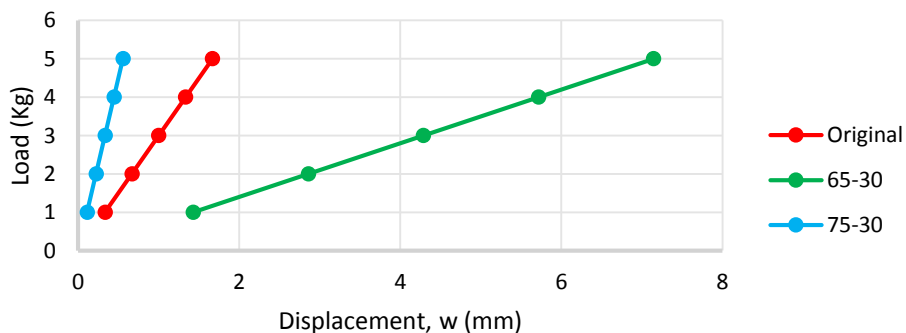


*Fig. 4. Load-Displacement Curve*

Table 1. Static stiffness measure

ID Foam	Slope (Kg/mm)	Static stiffness, k (N/mm)
Original 65-30	3	29.43
Visco 65-30	0.7	6.867
Visco 75-30	9	88.29

**Dynamic stiffness.** The dynamic stiffness is defined as the ratio between the dynamic force and the dynamic displacement: it is the quantity that expresses the elastic capacity of a material subjected to a harmonic stress. An excitation source, an accelerometric transducer, a test material (viscoelastic foam), and a rigid support plate are necessary to perform a dynamic test. The dynamic stiffness is comparable with the static value as a result of spectral analysis, as can be seen in Figure 5 for the Visco 75-30 foam.

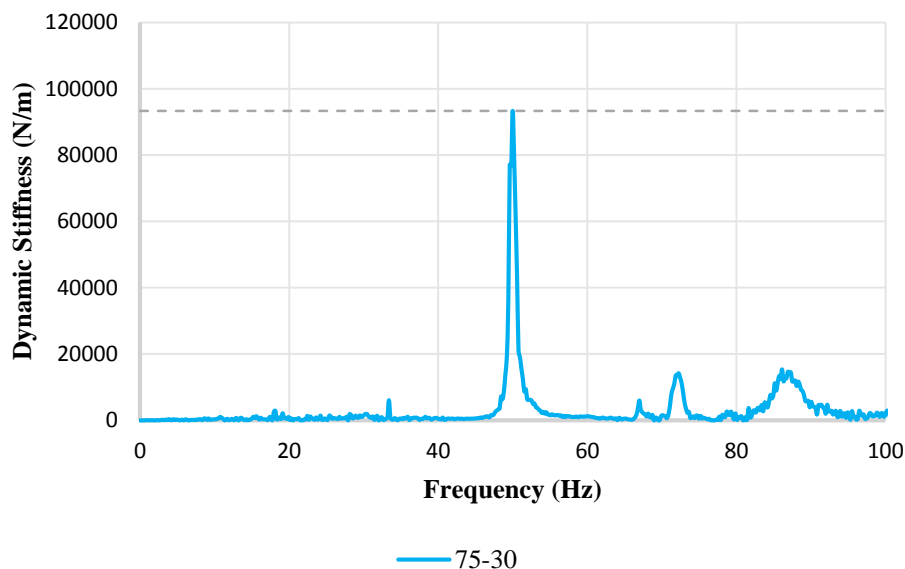
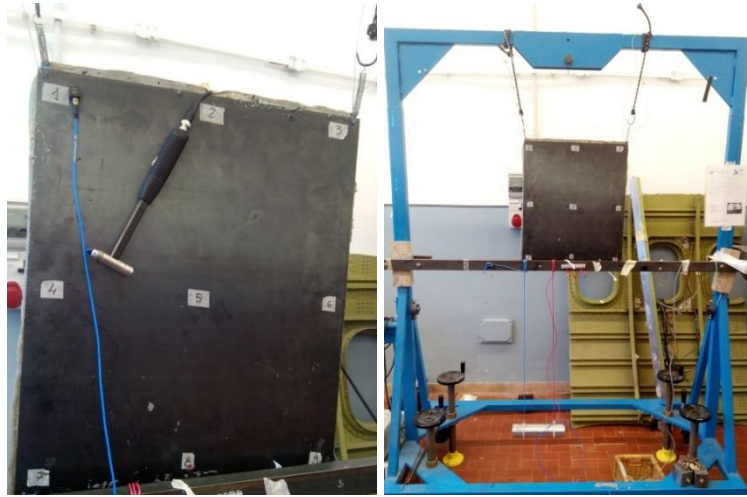


Fig. 5. Dynamic stiffness, Viscoelastic Foams 75-30

For the characteristic curve, 1024 points were chosen in a 0-100 Hz frequency range. It is clear that the stiffness of the foam 75-30 in correspondence of 50 Hz (first mode of vibration of the structure), is about 93500 N/m, next to the respective static stiffness value.

**Modal Analysis.** For the purposes of the frequency response measurement an LMS TestLab system has been used; 9 acquisition points have been defined for the mode shape reconstruction by the use of the rowing hammer technique. The goal of the spectral test is to compare the structure without material (Baseline) with the coated structure (viscoelastic foam) so as to discriminate the dynamic response of each foam. In Figure 6 the setup made for the dynamic test, is shown.



*Fig. 6. Riding plate in free-free conditions*

In Figure 7 the first elastic mode shape of the metal plate, which the resonance frequency is, about 48 Hz is represented.

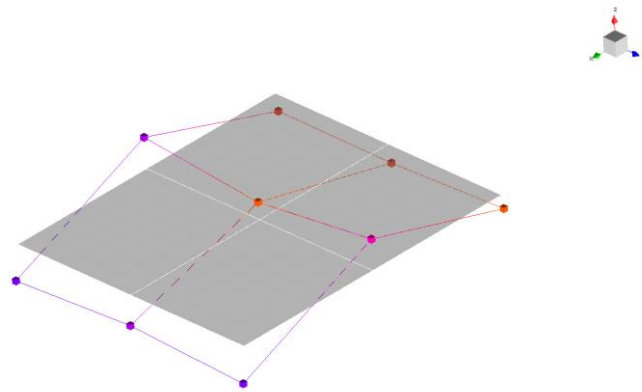


*Fig. 7. Baseline configuration first mode shape,  $f = 47.8$  Hz*

The following figures show the most significant frequency responses (FRF) of the tested materials.

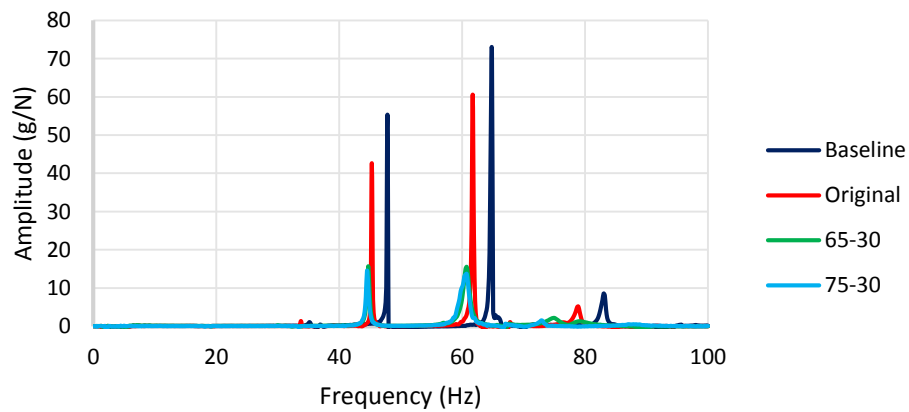


*Fig. 8. Frequency Response Function (FRF)*

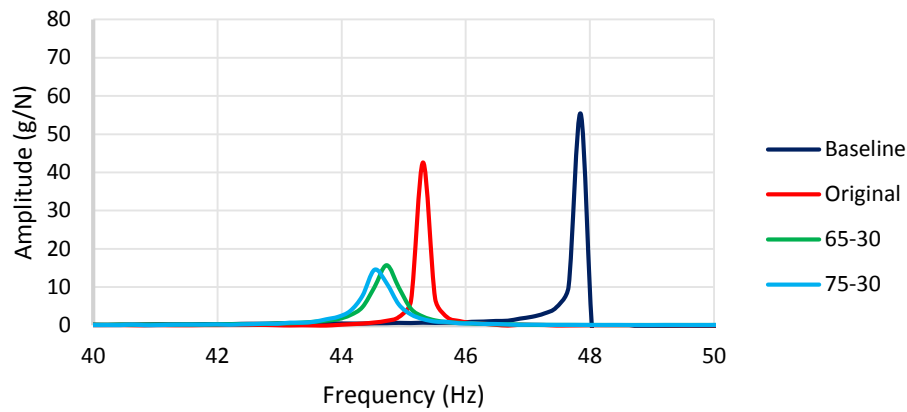


Fig. 9. Zoom about the first resonance frequency bandwidth

The results processing leads to observe a significant reduction of the resonance peak mainly due to the 65-30 and 75-30 viscoelastic foams. The added mass is perceived as a shift of the transfer function curve in virtue of (2):

$$f = \frac{1}{2\pi} \sqrt{\frac{k}{m}} \quad (2)$$

**Half-Power bandwidth method.** The system response close to the resonance region is strictly dependent on the damping. To estimate damping factor from frequency domain, the half-power bandwidth method is usable. In this method, two point corresponding to 3 dB down from the resonance peak are considered.

The damping factor  $\zeta$ , is so defined as:

$$\zeta = \frac{f_2 - f_1}{f_n} \quad (3)$$

Where  $f_1$  and  $f_2$  represent the cut-off frequencies at the two points with an amplitude of 3 dB under the resonance value,  $f_n$  is the value of the natural frequency. In Table 2 the damping coefficients obtained by that method for some of the foams are reported.

Table 2. Trade-Off damping coefficients, Half-Power Bandwidth

	Baseline	Original Foam	Visco Foam 65-30	Visco Foam 75-30
Frequency (Hz)	47.8	47.3	44.7	44.5
Max Amplitude (g/N)	55.4	43.1	15.7	14.5
Damping Ratio, $\zeta$	0.11	0.19	0.56	0.60

**Logarithmic decrement method.** To estimate the value of damping factor in time domain through logarithmic decrement method it is necessary to know peak amplitude in two consecutive points,  $Y_1$  and  $Y_2$ .

$$\delta = \ln \left| \frac{Y_1}{Y_2} \right|. \quad (4)$$

$$\zeta \approx \frac{\delta}{2\pi}. \quad (5)$$

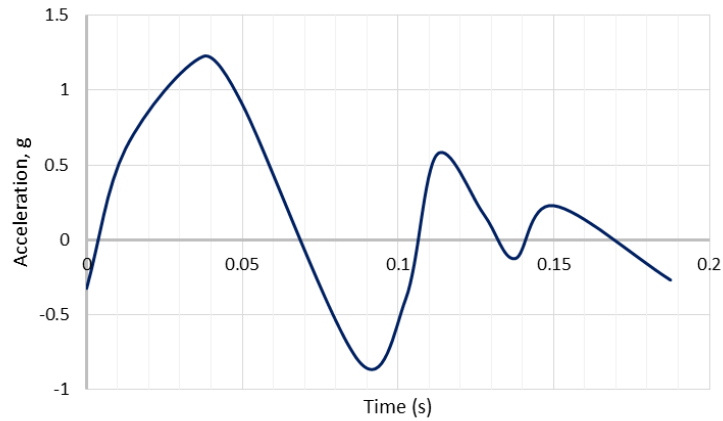


Fig. 10. Time History, Baseline

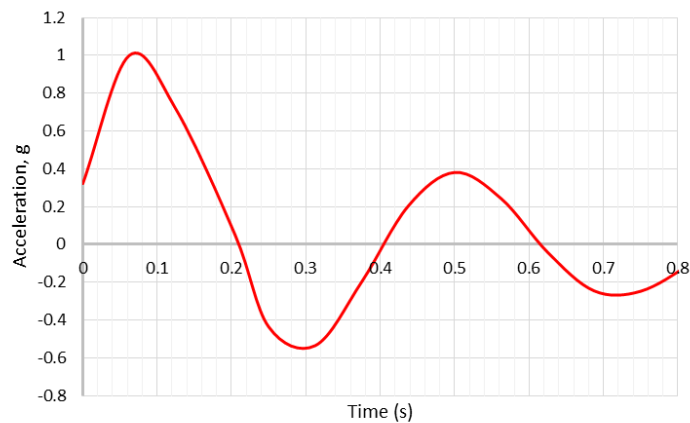


Fig. 11. Time History, Original Foam

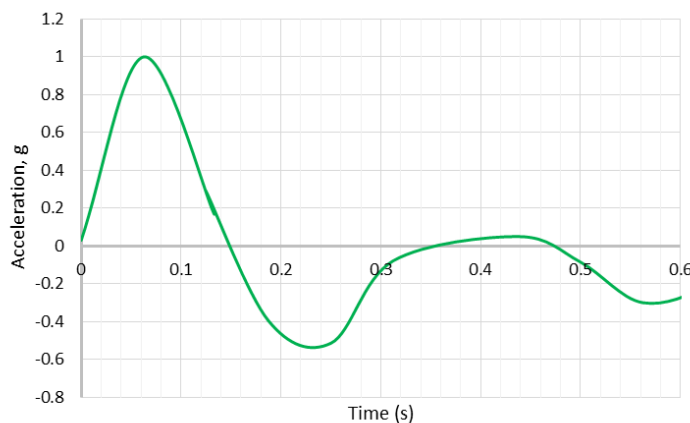


Fig. 12. Time History, 65-30

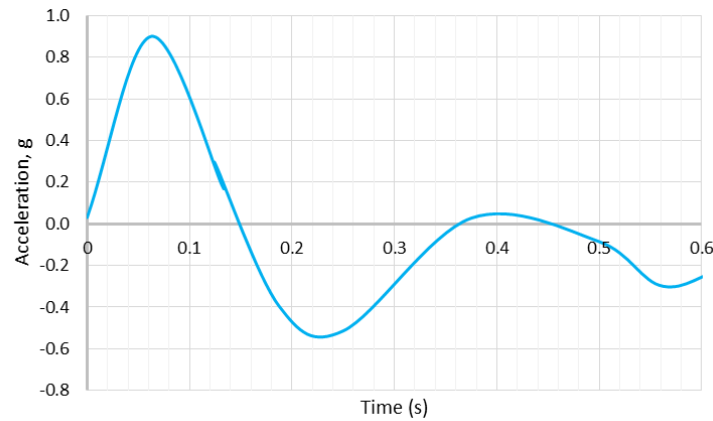


Fig. 13. Time History, 75-30

Table 3. Trade-Off damping coefficients, Logarithmic Decrement

	Baseline	Original Foam	Foam 65-30	Foam 75-30
Logarithmic decrement, $\delta$	0.77	0.96	3.01	3.52
Damping Ratio, $\zeta$	0.12	0.15	0.48	0.56

**Summary.** Acoustic and vibrational aspects are becoming central in many engineering field as those including automotive application and many transportation systems where the research of light-weighting construction solutions is a demanding aspect. Along the presented research, some viscoelastic foams have been studied as a possible mean to reduce the vibration induced noise inside a vehicle; the use of these foams could lead to the overall weight reduction because of the elimination of extra treatment nowadays used for this specific target.

It has been assessed that the use of viscoelastic materials brought significant benefits in terms of vibration's damping that has been approximately measured four times than the standard commercial solution. As regard the weight aspects, these viscoelastic foams are porous by nature, they have low density, and therefore they are particularly suitable for light-weighting application.

For the next developments, a numerical FE model will be developed to be correlated with the experimental one. Also direct acoustic measurements (to directly evaluate the radiated power from the panel) will be performed through a piezo-electric as an input source and a microphone as a transducer for the acquisition.

## References

- [1] D. Roylance, *Mechanical properties of materials*, pp. 37-40, 2008.
- [2] D. Roylance, *Engineering viscoelasticity*, pp. 8-14, October 24, 2001.
- [3] M. Carfagni, E. Lenzi, M. Pierini, *The loss factor as a measure of mechanical damping*.
- [4] M. Akay, *Introduction to polymer science and technology*, 2012.
- [5] Ricci, F., Viscardi, M., *Dynamic behaviour of metallic and composite plates under in-plane loads* (2000) Proceedings of the International Modal Analysis Conference - IMAC, 1, pp. 99-103.
- [6] Siano D., Viscardi M., Napolitano P., Panza, M.A., *Numerical and experimental acoustic performance investigations of a high-speed train composite sandwich panel*, WSEAS Transactions on Applied and Theoretical Mechanics, Volume 9, Issue 1, 2014, Pages 290-300.

# Optimization Of Tribological Properties Of Aluminium Honeycomb Reinforced Polymeric Composites Using Grey Based Fuzzy Algorithm

K.Panneerselvam<sup>1</sup>, K.Lokesh<sup>1</sup>, Chandresh D.<sup>1</sup>, T.N.S.Ramakrishna<sup>1</sup>

1 – Department of Production Engineering, National Institute of Technology, Tiruchirappalli-620015, India



DOI 10.13140/RG.2.1.4683.1762

**Keywords:** fuzzy logic, grey relational analysis (GRA), nylon 6, optimization, polypropylene (PP), tribology.

**ABSTRACT.** In this research two composite materials were fabricated by using two matrix materials and one common reinforcement material. The two matrix materials were Polypropylene and Nylon 6. Reinforcement material was Aluminium honeycomb core. Compression moulding machine was used for the fabrication of these composite materials. Two body abrasive wear experiments were conducted by using a pin-on-disc Tribotester under dry sliding condition and at room temperature. The design process parameters for two-body abrasive wear test were normal load, sliding velocity, sliding distance and abrasive paper grit size. The output responses were Coefficient Of Friction (COF) and Specific Wear Rate (SWR). The design of experiments is based on L<sub>9</sub> Taguchi orthogonal array. Grey fuzzy logic algorithm was used for the optimization of input process parameters. For polypropylene composite material the highest Grey Fuzzy Reasoning Grade (GFRG) is obtained at 30 N normal load, 0.523 m/s sliding velocity, 450 m sliding distance, 320 grit size of abrasive paper and these are the optimum level of process parameters. For nylon composite material highest GFRG is obtained at 30 N normal load, 1.046 m/s sliding velocity, 150 m sliding distance, 400 grit size of abrasive paper and these are the optimum level of process parameters. The optimum level of process parameters were also validated with conformation experiments.

**Introduction.** Literatures reveals that there are different approaches to handle prediction and multi-objective optimization problems. The common approaches includes Response Surface Methodology (RSM), [1,2], Artificial Neural Network (ANN), Genetic Algorithm (GA), [3], Fuzzy regression, [4] and Desirability Function (DF) approach, [5,6]. From last few years, polymeric composite materials have been widely used in many industries. Some of polymer materials, mainly thermoplastics are polypropylene (PP), Nylon etc., have shown grater improvement in their tribological and mechanical properties. The major advantage of polymer composite from a tribological point of view is their low wear rate [7]. Incorporation of inorganic particles into the polymers is best and an effective way to fabricate polymer composite materials with improved tribological properties. The degree of the reinforcement of the filler is depends up on the many factors like composition of the filler material, size of the filler, shape of the filler, matrix and filler bonding etc. [8]. The incorporation of the fillers can improve the tribological application depends on the type of application i.e., friction coefficient and wear resistance were not the properties of the base material. In particular brake pads and clutches require high coefficient of friction and low wear resistance whereas gears and bearings require low coefficient of friction and wear rate [9]. The major advantage of the polymer composites are of their self-lubricating property in tribological point of view.

The present research work analysis based on fuzzy-logic finds applications in uncertain environment conditions. From last few years, fuzzy-logic-based multi-criteria optimizatin methods were mostly using in optimization of tribological parameters. It is also shoewξ that application of fuzzy logic technique improves the multi objective responses. Grey Relational Analysis (GRA) has strong potential to improve the capability of fuzzy-logic in multi-objective optimization problems. In grey fuzzy logic technique the optimization of multiple responses can be effectively changed into single Grey Fuzzy Reasoning Grade (GFRG).

**Experimental Details. Material preparation.** Polypropylene and Nylon 6 were used as matrix materials and aluminium honeycomb was used as a reinforcing material. Aluminium honeycomb core made of alloy 3003 H18 of thickness 4.9 mm and cell size of 6 mm were used. Compression Moulding was carried out to produce plates of dimension 150 x 150 x 9 mm<sup>3</sup>. Initially the empty die was placed between the top and bottom heaters and it was pre heated up to 200°C for polypropylene and 250°C for Nylon 6 material. When the required temperature was reached the Aluminium honeycomb core and Polypropylene sheet materials were kept inside the die and heated for 10 mins. The compression moulding pressure was set to 150 bars. Then pressure was applied in such a way that Aluminium honeycomb core can be reinforced between Polypropylene sheets. When the required temperature was reached the AHC and Nylon 6 GF composite granules materials were kept inside the die and heated for 10 mins. The compression moulding pressure was set to 150 bars. Then pressure was applied in such a way that Aluminium honeycomb core can be reinforced with Nylon 6 GF composite granules. After heating for the pre-set time it was air cooled for 24 hours for both materials.

**Experimental design.** The process parameters considered for friction and wear test were normal load (N), sliding velocity (m/s), sliding distance (m), abrasive paper grit size (µm) and the output responses were coefficient of friction (µ) and specific wear rate (mm<sup>3</sup>/N-m). Total of 9 experimental runs were conducted to take an interaction of the process parameters. The process parameters and their different levels for L<sub>9</sub> orthogonal design is given in the Table 1.

Table1. Factors and different levels for L<sub>9</sub> orthogonal design.

Process Parameters		Levels		
		1	2	3
A	Applied Load (N)	10	20	30
B	Sliding Velocity (m/s)	0.523	1.046	1.569
C	Sliding Distance (m)	150	300	450
D	Abrasive Paper Grit Size	180	320	400

**Experimental setup.** Friction and wear test for Aluminium honeycomb reinforced PPG composite material was conducted by using DUCOM Pin-On-Disc Tribotester as shown in the Fig. 1 according to G99-05 standard in dry sliding conditions at room temperature. The samples were cut in the dimensions of 9×9×4 mm. The material specimens were glued to the metal pin. By using loading lever load can be applied on the specimen. Force sensor can measure the frictional force. The samples were weighted before and after the experiments by using electronic balance with an accuracy of 0.0001 g. The formula used for calculation of specific wear rate was,

$$K_0 = (w_1 - w_2) / (\rho \times S_d \times L) \quad (1)$$

Where,  $w_1$  and  $w_2$  are the weight of the sample before and after the abrasion test in gm,  $\rho$  is the density of the composite material,  $K_0$  is the specific wear rate in mm<sup>3</sup>/N-m,  $S_d$  is the sliding distance in meters, and  $L$  is the load in N. The Experimental results were shown in the Table 2 and Table 3 for polypropylene and Nylon 6 composite materials respectively.

**Grey based fuzzy logic. Grey relational analysis (GRA).** The Grey relational analysis is a sub part of grey system which was proposed by Deng in 1982 [10,11]. Taguchi method is used to optimize single response characteristics while Grey relational analysis was used to multi objective optimization. Therefore Grey relational analysis is somewhat complicated [12,13]. In grey relational

analysis the output responses obtained from the conducted experiments were normalized in between 0-1 using lower the better characteristics by using following equation.



Fig. 1. Schematic diagram of Pin-on-Disc Tribotester.

Table2. Experimental results of polypropylene composite material.

Expt. No.	Applied Load (N)	Sliding Velocity(m/s)	Sliding Distance(m)	Abrasive paper size( $\mu\text{m}$ )	Coefficient of friction( $\mu$ )	Specific wear rate ( $\text{mm}^3/\text{N}\cdot\text{m}$ )
1	10	0.523	150	180	0.73	0.0629
2	10	1.046	300	320	0.64	0.0257
3	10	1.569	450	400	0.58	0.0140
4	20	0.523	300	400	0.66	0.0147
5	20	1.046	450	180	0.59	0.0090
6	20	1.569	150	320	0.54	0.0247
7	30	0.523	450	320	0.49	0.0068
8	30	1.046	150	400	0.45	0.0193
9	30	1.569	300	180	0.56	0.0086

$$x_{ij} = \frac{\eta_{ij} - \min_j \eta_{ij}}{\max_j \eta_{ij} - \min_j \eta_{ij}}, \quad (2)$$

where  $x_{ij}$  – the sequence after data processing;

$\eta_{ij}$  – the original sequence of  $S/N$  ratio (where  $i=1,2,3\dots m, j=1,2,3\dots n$ );

$\max \eta_{ij}$  – largest value of  $\eta_{ij}$ ;

$\min \eta_{ij}$  – smallest value of  $\eta_{ij}$ .

Table3. Experimental results of Nylon 6 composite material.

Expt. No.	Applied Load (N)	Sliding Velocity(m/s)	Sliding Distance(m)	Abrasive paper size( $\mu\text{m}$ )	Coefficient of friction( $\mu$ )	Specific wear rate ( $\text{mm}^3/\text{N-m}$ )
1	10	0.523	150	180	0.62	0.0707
2	10	1.046	300	320	0.55	0.0287
3	10	1.569	450	400	0.51	0.0145
4	20	0.523	300	400	0.59	0.0151
5	20	1.046	450	180	0.54	0.0095
6	20	1.569	150	320	0.49	0.0267
7	30	0.523	450	320	0.45	0.0078
8	30	1.046	150	400	0.38	0.0204
9	30	1.569	300	180	0.51	0.0092

In the second step grey relational coefficient is calculated using Eq. (3)

$$\xi_{ij} = \frac{\min_i \min_j |x_i^0 - x_{ij}| - \zeta \max_i \max_j |x_i^0 - x_{ij}|}{|x_i^0 - x_{ij}| + \zeta \max_i \max_j |x_i^0 - x_{ij}|} \quad (3)$$

where  $x_i^0$  – ideal normalized S/N ratio for the  $i$ th performance characteristic;

$\zeta$  – distinguishing coefficient which is in the range  $0 \leq \zeta \leq 1$ .

The value of the grey relational coefficient is higher it implies that the corresponding process parameter is closer to the optimum value.

Finally the grey relational grade can be calculated by using the Eq. (4)

$$\gamma_i = \frac{1}{n} \sum_{k=1}^n \xi_i(k), \quad (4)$$

where  $\gamma_i$  – grey relational grade;

$n$  – number of process responses.

**Rule based Fuzzy modelling.** In GRA, each and every response is characterized as either ‘nominal-the-better’ or ‘lower-the-better’ or ‘higher-the-better’ quality characteristics and this results indicates some level of uncertainty. This level of uncertainty can be efficiently investigated with help of fuzzy-logic technique [14,15]. Thus complex multi-objective optimization problem can be solved by combining fuzzy-logic and GRA techniques. Fuzzy-logic technique consists of a fuzzifier, membership functions, fuzzy rule base, inference engine and defuzzifier [16]. Out of these elements, the fuzzifier uses membership functions to fuzzify the GRC of input parameters, ( $X1$  = grey relation coefficient for coefficient of friction,  $X2$  = grey relation coefficient for specific wear rate). Membership function was used to map the values of inputs ( $X1$  and  $X2$ ) and output ( $Y1$ =GFRG) parameters in the range of 0 to 1. The structure of two inputs and one output Fuzzy logic unit as shown in the Fig. 2 Fuzzy reasoning can be performed by the inference engine to generate a fuzzy value of the fuzzy rules. The rules writing procedure can be described as follows. In this experimental work nine fuzzy rules can be written for two inputs and one output are developed for inference.

Rule 1 : if x1 is A1;and x2 is B1; then y is C1;else

Rule 2 : if x1 is A2;and x2 is B2; then y is C2; else.. .

Rule n : if x1 is An;and x2 is Bn; then y is Cn

Ai, Bi, and Ci are fuzzy subsets as per the corresponding membership functions.

Finally the fuzzy value can be converted into the crisp output with the help of defuzzifier by using centroid defuzzification method (Eq. 5).

$$Y_o = \frac{\sum Y \mu_{C0}(Y)}{\sum \mu_{C0}(Y)}, \quad (5)$$

where  $Y_o$  – Grey Fuzzy Reasoning Grade (GFRG).

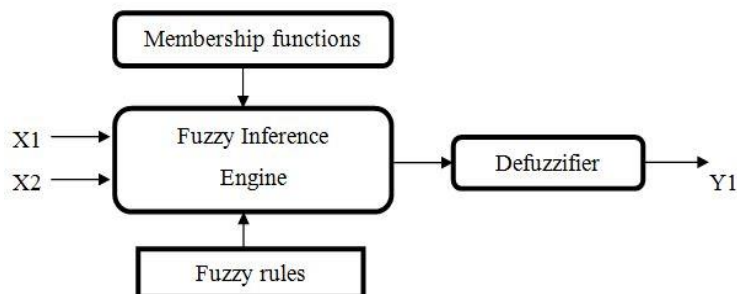


Fig. 2. Structure of two input and one output Fuzzy logic unit.

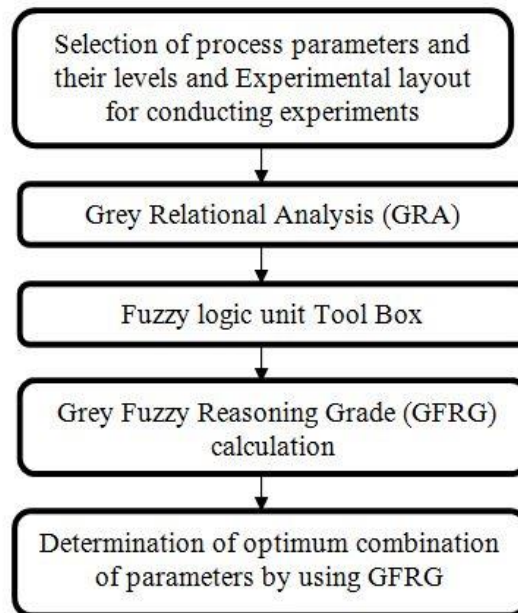


Fig. 3. Grey fuzzy logic method.

The steps of grey-fuzzy-logic method are illustrated in Fig. 3 and described as follows:

1. The experimental values of coefficient of friction and specific wear rate are normalized in between 0 and 1.
2. Grey relational coefficient (GRC) is calculated for each and every response.

3. Then fuzzy-logic technique is applied. In this technique the fuzzifier uses the membership functions to fuzzify the Grey relational coefficient (GRC) of each response.

4. Fuzzy rules (if-then control rules) can be generated and finally fuzzy predicted value converted into Grey Fuzzy Reasoning Grade (GFRG) by using defuzzifier.

**Results and Discussion.** For each and every combination of parameters overall grey relational grade and grey relational coefficients were calculated. By using MATLAB (R2015a) grey-fuzzy reasoning grade is obtained with help of fuzzy logic tool box. Grey relational coefficients of coefficient of friction and specific wear rate were the inputs to the fuzzy logic tool box. For fuzzy modelling, triangular shaped membership function was used. The names of membership functions are LOWEST, LOWER, LOW, LOW MEDIUM (LM), MEDIUM, HIGH MEDIUM (HM), HIGH, HIGHER, and HIGHEST are used to indicate the grey relational coefficients (GRC) of input variables and output variable grey relational grade (GRG). The membership functions used in this fuzzy logic tool box can be shown in Fig. 4 and Fig. 5. The fuzzy logic rule viewer can be shown in Fig. 6. In fuzzy rule viewer nine rows indicates the nine fuzzy rules and the first two columns indicates two input variables i.e. grey relational coefficients of coefficient of friction and specific wear rate respectively. The final column of fuzzy rule viewer gives the grey-fuzzy reasoning grade (GFRG) with defuzzification.

#### Aluminium honeycomb reinforced with Polypropylene Composite.

Table 4. Grey relational coefficients and grey relational grade.

Expt. No	Grey relational coefficient		Grey relational grade	Rank
	COF	SWR		
1	0.3333	0.3333	0.3333	9
2	0.4242	0.5974	0.5108	8
3	0.5185	0.7957	0.6571	5
4	0.4000	0.7802	0.5901	7
5	0.5000	0.9272	0.7136	4
6	0.6089	0.6104	0.6095	6
7	0.7777	1.0000	0.8888	1
8	1.0000	0.6917	0.8458	2
9	0.5600	0.9396	0.7498	3

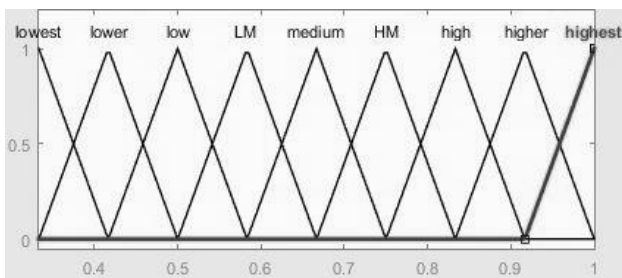


Fig. 4. Membership function for coefficient of friction and specific wear rate.

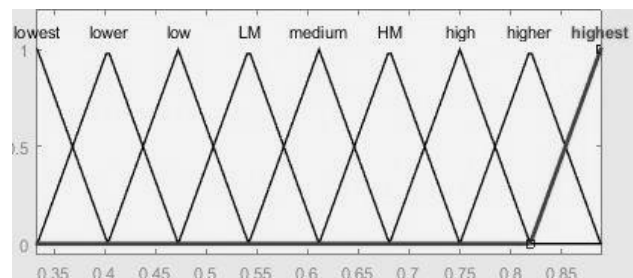


Fig. 5. Membership function for Grey relational grade.

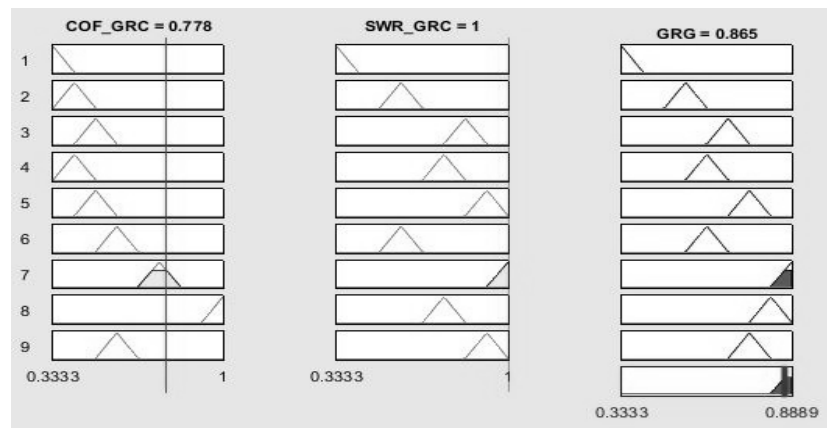


Fig. 6. Fuzzy logic rules viewer.

Table 5. Grey Fuzzy reasoning grades and their Rank.

Expt. No	Grey Fuzzy Reasoning Grade (GFRG)	Rank
1	0.355	9
2	0.542	8
3	0.681	5
4	0.611	7
5	0.749	4
6	0.620	6
7	0.865	1
8	0.819	2
9	0.750	3

The GFRG values of all the experiments were shown in Table .5 From Table. 5 , it shows that the seventh experiment combination of parameters will be the optimum combination of parameters having highest grey-fuzzy reasoning grade. So, the optimum combination of parameters were 30 N normal load, 0.523 m/s sliding velocity, 450 m sliding distance, 320 grit size of abrasive paper.

Confirmation test was conducted to validate the experimental results. The predicted GFRG for the optimal combination of the parameters is calculated by using following equation:

$$Y_0 = Y_{0m} + \sum_{i=1}^n Y_{0i} - Y_{0m} \quad (6)$$

where  $Y_0$  – estimated GFRG;

$Y_{0m}$  – total mean GFRG;

$Y_{0i}$  – mean value of GFRG at the optimal level;

$n$  – number of parameters affecting the multiple performance characteristics.

Table 6. Conformation test results.

	Optimum process Parameters	
	Prediction	Experiment
Parameter Levels	A3B1C3D2	A3B1C3D2
GFRG	0.865	0.888

Conformation test results are shown in the Table. 6. At optimum combination of parameters (A3B1C3D2) the estimated GFRG is 0.865 and experimental GFRG is 0.888. Therefore gain can be observed in GFRG which shows that we acn use grey fuzzy logic algorithm for the multi objective optimization.

### Aluminium honeycomb reinforced with Nylon 6 Composite

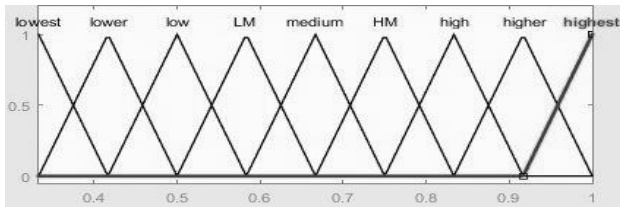


Fig. 7. Membership function for coefficient of friction and specific wear rate.

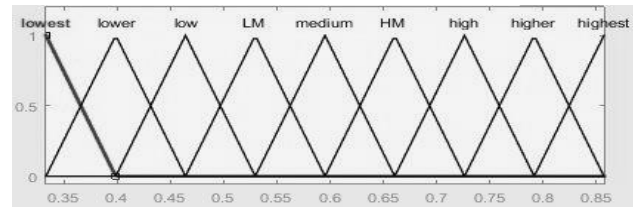


Fig. 8. Membership function for Grey relational grade.

Table 7. Grey relational coefficients and grey relational grade.

Expt. No	Grey relational coefficient		Grey relational grade	Rank
	COF	SWR		
1	0.3333	0.3333	0.3333	9
2	0.4137	0.6007	0.5072	8
3	0.4800	0.8243	0.6521	5
4	0.3636	0.8116	0.5876	6
5	0.4285	0.9487	0.6886	4
6	0.5217	0.6246	0.5731	7
7	0.6315	1.0000	0.8157	2
8	1.0000	0.7139	0.8569	1
9	0.4800	0.9573	0.7186	3

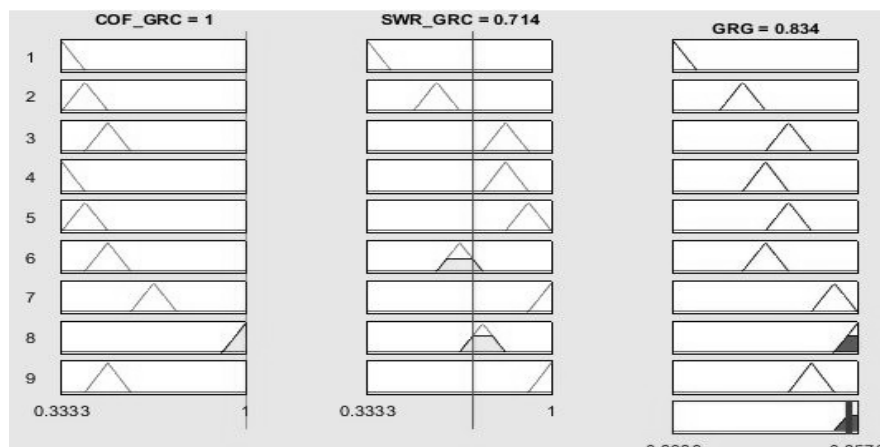


Fig. 9. Fuzzy logic rules viewer.

The GFRG values of all the experiments were shown in Table .8 From Table. 8 ,it shows that the experiment 8 combination of parameters will be the optimum combination of parameters having highest grey-fuzzy reasoning grade. So, the optimum combination of parameters were 30 N normal load, 1.046 m/s sliding velocity, 150 m sliding distance, 400 grit size of abrasive paper.

*Table 8. Grey Fuzzy reasoning grades and their Rank.*

Expt.No	Grey Fuzzy Reasoning Grade (GFRG)	Rank
1	0.353	9
2	0.530	8
3	0.661	5
4	0.595	6
5	0.674	4
6	0.585	7
7	0.792	2
8	0.834	1
9	0.704	3

*Table 9. Conformation test results.*

	Optimum process Parameters	
	Prediction	Experiment
Parameter Levels	A3B2C1D3	A3B2C1D3
GFRG	0.834	0.856

Conformation test results are shown in the Table. 9. At optimum combination of parameters (A3B2C1D3) the estimated GFRG is 0.834 and experimental GFRG is 0.856. Therefore gain can be observed in GFRG which shows that we can use grey fuzzy logic algorithm for the multi objective optimization.

**Summary.** In present investigation an algorithm used which is a combination of fuzzy logic and grey relational analysis for the optimization of multiple response process parameters. The following conclusions can be drawn from the present research work.

- The grey fuzzy based system indicates that the highest GFRG can be obtained at 30 N normal load, 0.523 m/s sliding velocity, 450 m sliding distance, 320 grit size of abrasive paper for Aluminium honeycomb reinforced with Polypropylene Composite material.
- The grey fuzzy based system shows that the highest GFRG can be obtained at 30 N normal load, 1.046 m/s sliding velocity, 150 m sliding distance, 400 grit size of abrasive paper for Aluminium honeycomb reinforced with Nylon 6 Composite material.
- The confirmation test also reveals that the grey-fuzzy logic system is applicable for optimization of the multi responses in between the ranges of the process parameters.

## References

- [1] Gunaraj V, Murugan N, Prediction and optimization of weld bead volume for the submerged arc process, Part-1, Journal of Welding 79 (10), 2000, 286-294.
- [2] Gunaraj V, Murugan N, Prediction and optimization of weld bead volume for the submerged arc process, Part-2, Journal of Welding 79 (11), 2000, 331-338.
- [3] Al-Aomar, Raid, A robust simulation-based multi criteria optimization methodology, Simulation Conference, Proceedings of the winter, Vol. 2. IEEE, 2002.
- [4] Wang Jen-Ting, Jean Ming-Der, Optimization of cobalt-based hard facing in carbon steel using the fuzzy analysis for the robust design, International Journal of Advanced Manufacturing Technology 28, 2006, 909-18.
- [5] Asiabanpour B, Palmer K, Khoshnevis B, An experimental study of surface quality and dimensional accuracy for selective inhibition of sintering, Journal Rapid Prototyping, 2004, 10(3), 181-92.

- [6] Wu Ful-Chiang, Optimization of correlated multiple quality characteristics using desirability function, *Quality Engineering*, 2005, 17(1), 119-26.
- [7] Bekhet N.E, Tribological behaviour of drawn polypropylene, *Journal of Wear*, 1999, 55–61.
- [8] Wetzel, Bernd, F. Hauptert, K. Friedrich, M. Q. Zhang, M. Z. Rong, Mechanical and tribological properties of microparticulate and nanoparticulate reinforced polymer composites, *Proceedings of the ICCM-13*, 2001, ID1021.
- [9] Malucelli, Giulio, Francesco Marino, Abrasion resistance of polymer nanocomposites—a review, *Abrasion resistance of materials*, Intech-Open Access Publisher, Rijeka, 2012, 1-18.
- [10] J.L. Deng, Control problems of grey systems, *Systems & Control Letters*, 1982, 288–294.
- [11] J.L. Deng, Introduction to grey system, *Journal of Grey System*, 1989, 1–24.
- [12] P.N. Singh, K. Raghukandan, B.C. Pai, Optimization by grey relational analysis of EDM parameters on machining Al–10% SiCP composites, *Journal of Materials Processing Technology*, 2004, 1658–1661.
- [13] M. Kurt, S. Hartomacioglu, B. Mutlu, U. Koklu, Minimization of the surface roughness and form error on the milling of free-form surfaces using a grey relational analysis, *Journal of Materials science and Technology*, 2012, 205–213.
- [14] S. Pattnaik, D.B. Karunakar, P.K. Jha, Multi-characteristic optimization of wax patterns in the investment casting process using grey-fuzzy logic, *International Journal of Advanced Manufacturing Technology*, 2013, 67 (5-8), 1577-1587.
- [15] P. Asokan, R. Ravi Kumar, R. Jeyapaul, M. Santhi, Development of multi-objective optimization models for electrochemical machining process, *International Journal of Advanced Manufacturing Technology*, 2008, 39, 55–63.
- [16] Y. Tzeng, F. Chen, Multi-objective optimisation of high-speed electrical discharge machining process using a Taguchi fuzzy-based approach, *Journal of Materials and Design* 28 (4) 2007, 11.

# Formation And Distribution of Brittle Structures in Friction Stir Welding of AA 6061 To Copper. Influence of Preheat

Seyed Vahid Safi<sup>1,a</sup>, Hossein Amirabadi<sup>2</sup>, Mohammad Kazem Besharati Givi<sup>3</sup>

1 – M.Sc. student. Mech. Eng., University of Birjand, Birjand, Iran

2 – Assoc. prof., Mech. Eng., University of Birjand, Birjand, Iran

3 – Assoc. prof., Mech. Eng., University of Tehran, Tehran, Iran

a – [vahid.safi@gmail.com](mailto:vahid.safi@gmail.com)



DOI 10.13140/RG.2.1.2620.9684

**Keywords:** friction stir welding, mechanical properties, preheat, intermetallic.

**ABSTRACT.** In this paper, apart from introducing brand – new warm friction stir welding (WFSW) method, the effect of preheating on friction stir welded of copper and aluminum alloys sheets and its influence on improving the mechanical properties of the weld were investigated. Sheets of aluminum alloy 6061 and copper with thickness of 5mm were used. The tool was made of tool steel of grade H13 with a threaded cone shape. Rotational speeds ( $\omega$ ) of 1200-1400 rpm and traverse speeds ( $v$ ) of 50-100 mm/min were used for better understanding the behavior of the tools during the heat input. The sheets were kept in furnace with temperature of 75 °C and 125°C and welding was done afterwards. At last, tensile and micro hardness tests were done to compare the mechanical properties of the welds. Considering to the high thermal conductivity of both copper and aluminum, the reason of increase in strength of the joints could be related to the low temperature gradient between the weld zone and base metal because the heat gets out of the stir zone with lower steep. A significant increase in hardness is observed in the SZ for the following reasons: (i) the presence of concentric grains with intensely refined recrystallization and (ii) the presence of intermetallic compounds. The tensile test results showed 85% increase in the strength of preheated joints. The maximum strength occurs for preheating of 75°C, rotational speed of 1200 rpm and traverse speed of 50 mm/min. In the present study, intermetallic compounds and the precipitates are moved to the grain boundaries during the welding process. These precipitates act as strong obstacles to the movements of dislocations and increase the deformation resistance of material. This phenomenon may result in locking of grain boundaries and consequently decrease of grain size. This grain refinement can improve the mechanical properties of welds. Accordingly, hardness and strength of the material will be increased.

**1. Introduction.** FSW is a process including many actions and interactions between a series of simultaneous thermodynamic processes. These reactions are the results of heat input rate, cooling rate, flow and deformation, dynamic recrystallization and integration of mechanical joints [1]. This method of welding was invented in 1991 by Thomas Wayne et al. in TWI in Cambridge, England [2]. FSW is a relatively new method in metal joining that because of solid state nature of this method (no melting happens at joining) it has some advantages comparing with other fusion welding methods. Low distortion and shrinkage, good mechanical properties, fewer defects and the ability of welding some metals that cannot be welded with fusion welding methods are among the most important advantages of this method [3]. In last few years, this process has been used in aerospace and aviation industries, automotive industries, fuel tanks etc. in most developed countries. During this process, imposes high lateral forces to the material during deformation which causes temperature to increase up to about 70-80% of its melting temperature [4, 5]. Copper has a wide range of applications because of its great thermal and electrical conductivity, corrosion and fatigue resistance and good flexibility. Copper alloys have various set of properties, which is dependent on the addition of elements and heat treatment [6].

Today, aluminum and its alloys have a wide range of applications in defense industry, aerospace, transportation, marine industry, construction industry, packaging and containers etc. some of the properties which made aluminum and its alloys as one of the most economical and popular group of

metals are: Light weight, flexibility, physical properties, mechanical properties, corrosion resistance [7]. During the improvement of FSW process, the conventional fusion welding methods for similar and dissimilar materials were used. There are a few studies about FSW for dissimilar materials at the moment. FSW of dissimilar materials such as aluminum and copper causes the formation of intermediate brittle phases of Al/Cu, which still needs to be studied in the future [8, 9].

Ouyang et al [10]. Also studied the FSW on dissimilar metals such as AA6061 (T6) and copper. They showed that joining of AA6061 to copper due to the brittle nature of intermetallic compounds in the weld nugget, is hard. Mechanical mixture zone of dissimilar joint of AA6061 to copper is mainly consisted of various intermetallic compounds including CuAl<sub>2</sub>, CuAl and Cu<sub>9</sub>Al<sub>4</sub> with few amount of  $\alpha$ -Al and FCC solid solution of aluminum in copper.

On the other hand Galvao et al [11]. observed that welding with higher  $\omega/v$ , increase the heat input and causes the formation of mixture zones from materials with higher size and more homogenous. The morphology of stir zone, type and the amount of intermetallic structures which are formed because of thermo mechanical induction solid state are highly dependent to welding parameters. In FSW of dissimilar metals, pin is an important factor in compare to the two metals.

Ratnesh and Pravin [12] welded AA6061 to copper with FSW. They obtained good joints with changing the central line of the pin into the copper and in the advancing direction. They reported that ultimate tensile strength of aluminum in copper joint is low due to the presence of intermetallic compounds. Increase in the rotational speed lowers the tensile strength, which is mainly due to the increase in the amount of intermetallic compounds, which are formed in the aluminum-copper interface. Higher hardness in the stir zone in compare to the base metals is due to the formation of hard and brittle compounds such as CuAl<sub>2</sub>, CuAl and Cu<sub>9</sub>Al<sub>4</sub>.

Akinalbi et al [13]. observed that interface of the joint are recognized with lamellar mixture of aluminum and copper which are apparent in the structure and are due to heat input from the stir action of the pin during the FSW process. They also observed that decrease in grain size towards the stir zone of the welds increases.

Recent researches show that with placing the copper sheet, which has higher melting temperature in the advancing side, a weld with good compounds can be obtained. However, many of these studies show the presence of intermetallic compounds during FSW of aluminum with copper, but more study is needed on new formed phases for better understanding the weld joint. Optimizing the parameters of the process to decrease the formation of intermetallic compounds in the interface is also required.

**2. Experimental procedure.** Dissimilar FSW of 6061 aluminum alloy and pure copper sheets both with the thickness of 5 mm was performed. The specimens were cut to the dimension of 70 mm×200 mm by wire cut. Due to the different behaviors of aluminum alloy and pure copper, in addition to the welding and also complication of condition simultaneous with applying preheating condition, it has been attempted to obtain more appropriate analysis of condition dominant in dissimilar joints welding by considering a set of parameters affecting welding process. That is why a tool with frustum threaded pin and also pin tendency towards copper sheet (Fig. 1) in 3 different travel and rotation speeds have been used.

Parameters employed in dissimilar joining of copper and 6061 aluminum alloy sheets are shown in Table 1. The joints were performed in 3 different temperature domains including room temperature, 75 °C and 125 °C.

After welding, three tensile test samples were cut from each welded sheet in a vertical direction to the weld line using wire cut to investigate the strength of the joints. The tensile test samples were prepared according to ASTM E8M standard. The tests were carried out using a Hounsfield tensile testing machine under the crosshead speed of 1 mm min<sup>-1</sup> at room temperature. Microstructural analysis was performed on the cross section perpendicular to the welding direction. A solution of Fe (NO<sub>3</sub>)<sub>3</sub> (5g) + HCL (25 ml) + H<sub>2</sub>O (75 ml) was used to etch the copper side of the joints, while the aluminum side was etched by a reagent with a solution of 25ml HNO<sub>3</sub> and 75ml H<sub>2</sub>O for 60 s. Optical

and scanning electron microscopy (SEM) equipped with energy dispersive X-ray spectroscopy (EDS) were used in order to observe the microstructure and characterize the intermetallic compounds at the joint interface. Furthermore, EDS line scan analysis was performed to follow the compositional change across the intermetallic compounds existing at the interface of aluminum and copper sides of the interface. Micro hardness measurements were also taken from the cross sections of both aluminum and copper sheets at the welded area perpendicular to the welding direction by applying load of 25 gf for 20 s duration loading time.

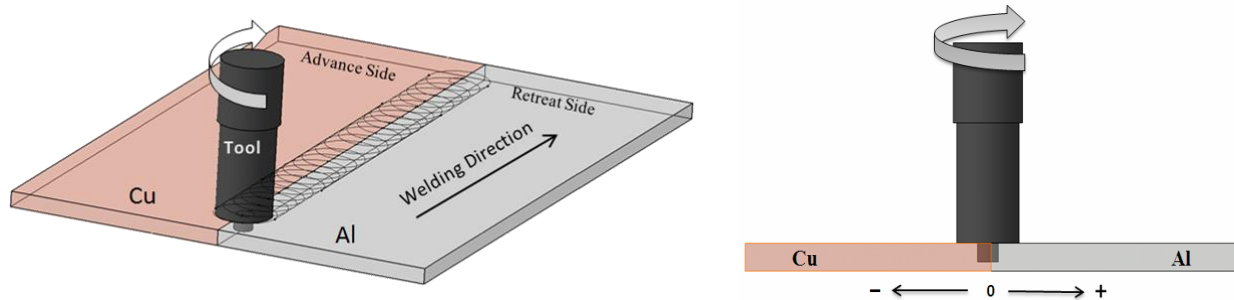


*Fig. 1. Schematic illustration showing set-up of dissimilar FSW.*

*Table 1. Parameters employed for dissimilar joining of copper and 6061 aluminum alloy sheets*

<i>Frustum threaded pin</i>	<i>Geometry of tool pin</i>
18- 6 - 4.8 mm	Shoulder diameter, Pin diameter, Pin length
1400 -1300-1200 rpm	Tool rotation speed
50-75-100 mm/min	Tool travel speed
3 degree	Tilt angle
2 mm toward copper sheet	Tool offset

### 3. Result and Discussion.

**3.1 Joints appearance.** Fig. 2 shows surface appearances and cross sections of Al/Cu joints produced at different traverse and rotational speeds as it is observed, the weld surface does not contain any kind of defect and onion ring structure is clearly observable as well.

As can be observed in Fig. (2-e), within the stir zone, the dominant phase is aluminum and fine and coarse particles of copper have been distributed within the aluminum matrix. Full turbulence of material and displacement of copper toward aluminum is indicative of adequate flow in the stirring zone. Welding area of welded joints is similar to the common form of nugget zone in FSW process that is as elliptical. In the Fig. (2-d), an image of optimal cross sections ( $\omega = 1200$   $v = 50$ ) can be observed. The boundary of Al/Cu is completely continuous and free of any hole or discontinuities. The presence of small particles of copper in the aluminum side indicates that conditions have been favorable for adequate stirring by means of tool in the weld zone. However, in this case, because of the placement of copper on the advance side, the situation is different (Fig. 2-f). In this case, the continuity of copper and stir zone is not desirable and in the border of copper, discontinuity and crack are observed. Moreover, there is several holes in the nugget zone. Because of the discontinuity in the boundary between the copper and the stir zone, the created joints is so weak in terms of mechanical property and can be easily fractured in the boundary of Al/Cu.

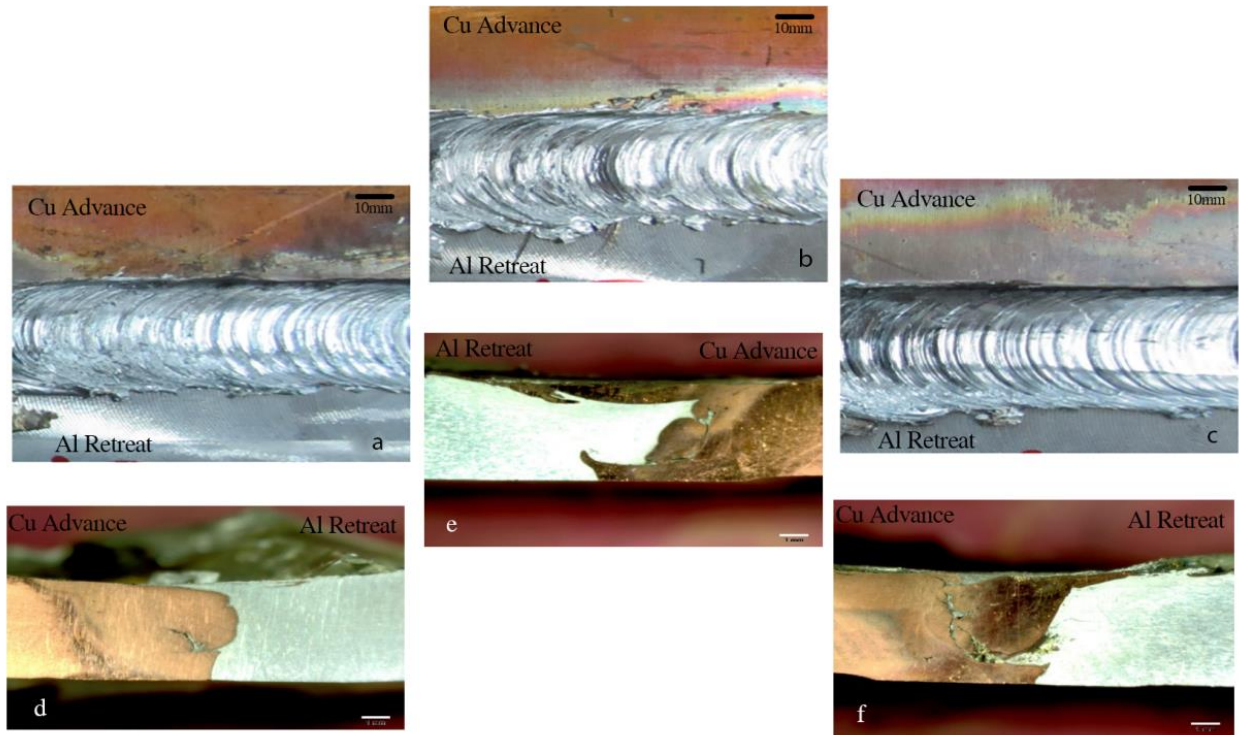


Fig. 2. Macroscopic view of weld surface and cross sections of joints at the welding conditions of: (a, d):  $\omega=1200$   $v=50$ ; (b, e):  $\omega=1300$   $v=75$  and (c, f):  $\omega=1400$   $v=100$ .

**3.2 Material flow.** In order to study the flow behavior of materials more precisely, the microstructures of the nugget zone were examined in detail by SEM and results are shown in Fig. 3. Different phases were evidenced and corresponding EDS analysis were carried out. The EDS results were presented in table 2.

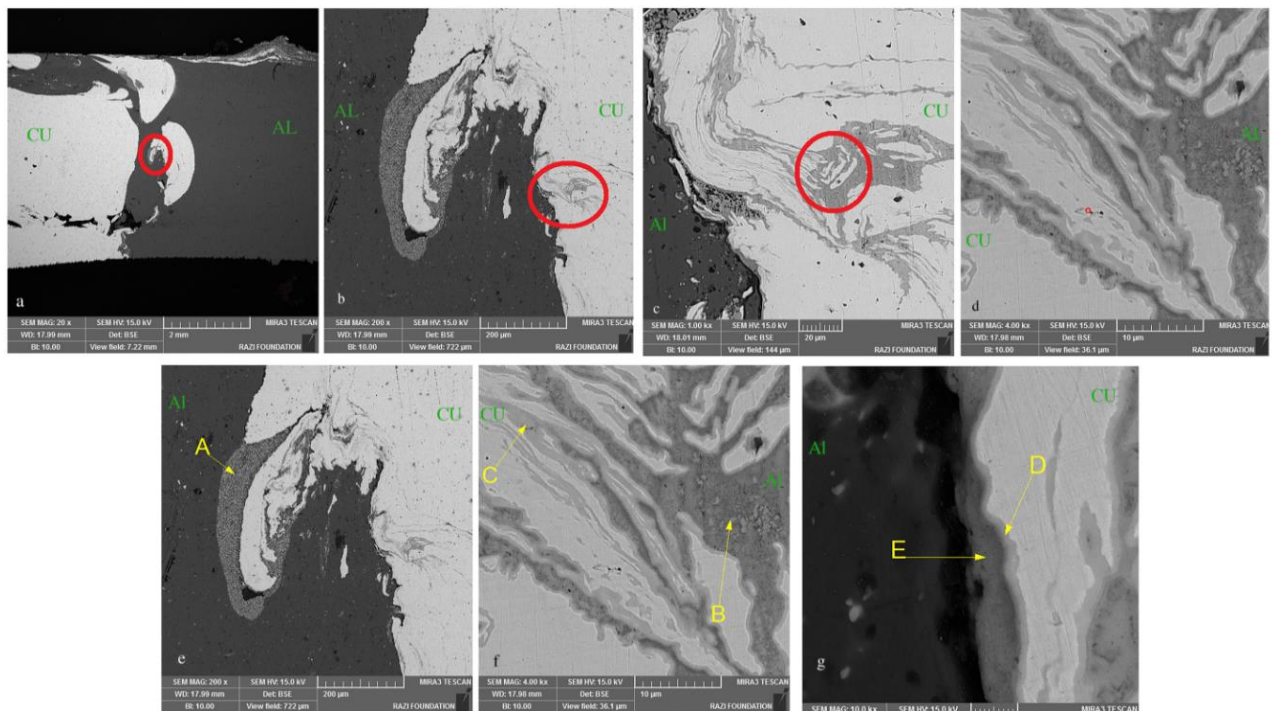


Fig. 3. SEM images of the dissimilar Al/Cu joints interface

Table. 2. EDS analysis results of reaction layer pointed in Fig. 3 (at-%)

Position	Al	Cu	Possible phases
A	83/48	16/52	Al+Al <sub>2</sub> Cu
B	11	84/45	Solid Solution Cu(Al)
C	39/43	60/57	Al <sub>2</sub> Cu <sub>3</sub>
D	43/56	56/44	AlCu
E	32/15	64/44	Al <sub>4</sub> Cu <sub>9</sub>

As can be observed in Fig. (3-a), rotation of tool in the interface of the joint has caused enough stirring and mixing of the copper and aluminum, that this mixture along with heat caused by the process of preheating sheets, plastic deformation and friction have caused the separation of coarse particles of copper and locating them in aluminum matrix. The result of this reaction is penetration of copper and aluminum into each other particles together and formation of intermetallic compounds. In Fig. (3- b), which is an image with a larger magnification compare with Fig. (3- a), the intermetallic compounds can be clearly observed. Compounds that as the small and scattered parts have been distributed in the boundary of the joint. In Fig (3-c), the sequential layers of copper and intermetallic compounds are observed that reflects this fact that the aluminum particles are isolated from the aluminum sheet and they convert to intermetallic compounds in the side of copper sheet because of suitable condition in the terms of the amount of heat and enough time to react. Fig (3-d) shows the presence of halos with different color besides copper layers that indicates the formation of different intermetallic compounds in those areas. By an exact investigation of the joint area using EDS of chemical composition of present components, the presence of fine particles of metallic compounds in aluminum matrix that have been distributed heterogeneously (Fig. 3-e). According to the results of the analysis carried out, the points of B and C (Fig. 3-f) are two different intermetallic compounds. Point B contains 5.13 wt-% of aluminum and 92.67 wt-% of copper, while point C includes 21.65 wt-% aluminum and 78.35 wt-% of copper that indicates the fact that the conditions in point C is much more favorable in terms of time and the amount of heat to create intermetallic compounds.

Compounds created in the D and E is directly related to the aluminum particles in the copper (Figure 3. g). The reason for this phenomenon and formation of different intermetallic compounds can be stated in a way, that atoms isolated from copper sheet in the aluminum side and isolated aluminum atoms in the copper side, according to the condition of joint such as the inlet temperature and time, react with each other in the interface of the joint and cause formation of intermetallic layers with different colors, that this difference in contrast is contributed to the differences in the chemical composition of these components. Then this difference in chemical composition occurs because of the penetration atoms into the interface of the joint. Therefore, it can be concluded that formation of intermetallic compounds depends on the permeability of atoms and welding conditions. The newly formed isolated structures and solid solution may be related to the local diffusion induced by the preheating effect on the nugget zone. Based on the EDS analysis results, typical intermetallic were observed in the lower part of the weld, including AlCu (D), Al<sub>2</sub>Cu<sub>3</sub> (C), and Al<sub>4</sub>Cu<sub>9</sub> (E).

### 3.3 Mechanical properties.

**3.3.1 Micro hardness distributions.** The results of the dissimilar Al/Cu joints hardness test can be observed in Fig. 4.

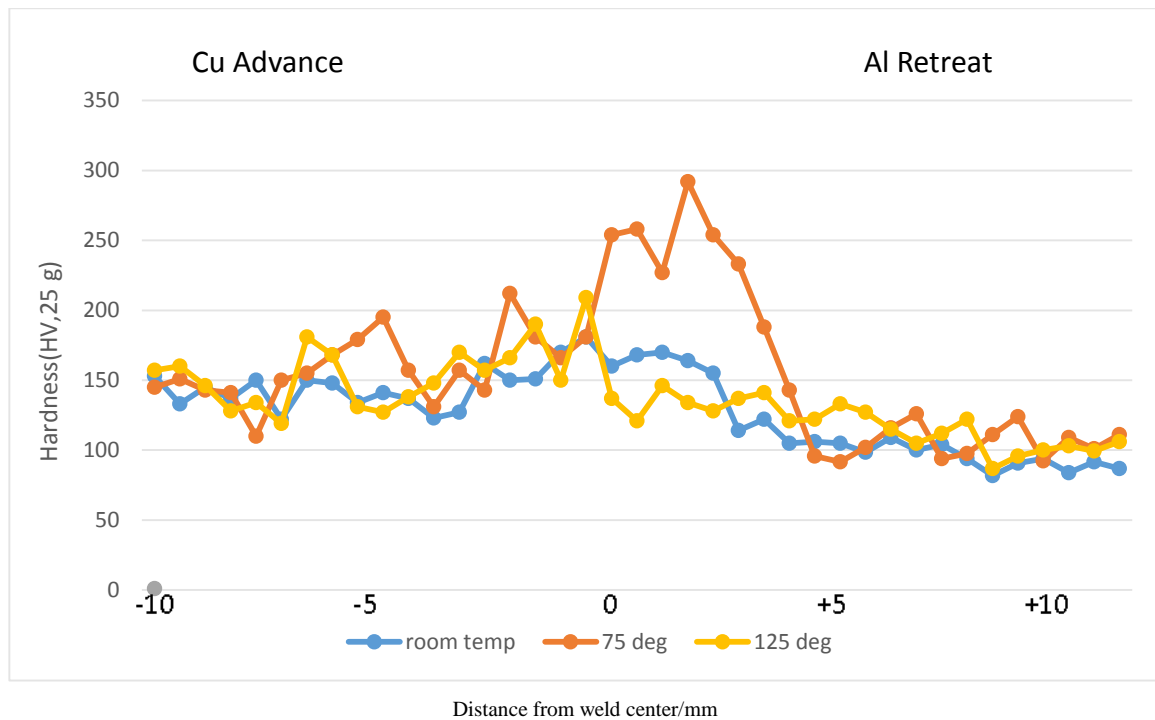
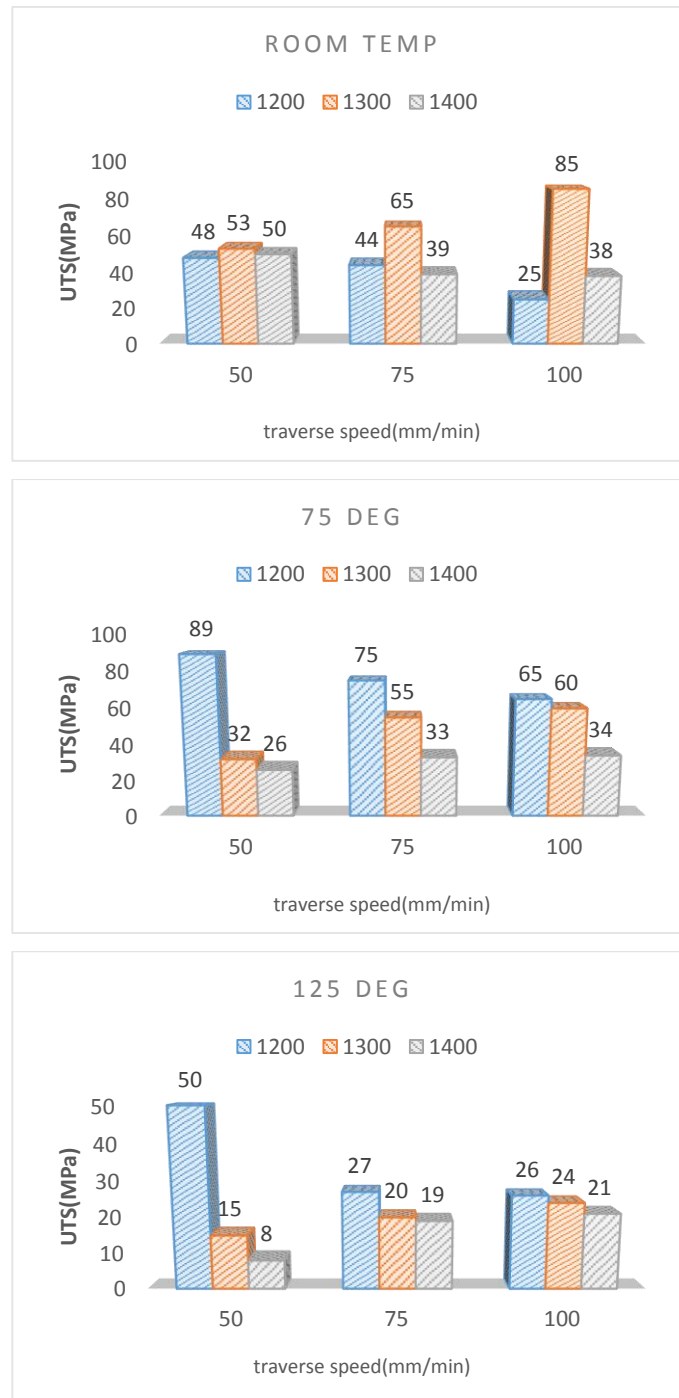


Fig. 4. Hardness profiles along the traverse cross section of Al/Cu joint ( $\omega=1200$ ,  $v=50$ ) at three different preheating temperatures

The above values signify different welding states including constant traverse and rotational speed, and varied preheating conditions. The results suggest that in contrast to the base metal a significant increase in hardness is observed in the SZ for the following reasons: (i) the presence of concentric grains with intensely refined recrystallization and (ii) the presence of intermetallic compounds. TMAZ has less hardness compared to the SZ, but due to the presence of different grading, it enjoys more hardness compared to the base metal and the HAZ zone. Observations are indicative of the fact that, by the application of preheating conditions, the rate of hardness significantly increases in the stir zone, and reaches its maximum value at 75 degrees centigrade. One of the mechanisms increasing the hardness and strength of the materials is precipitation hardening. In this mechanism, some of the alloying elements combine with each other and form fine precipitates. These precipitates act as strong obstacles to the movements of dislocations and increase the deformation resistance of material. Accordingly, hardness and strength of the material will be increased. In the present study, intermetallic compounds and the precipitates are moved to the grain boundaries during the welding process. This phenomenon may result in locking of grain boundaries and consequently decrease of grain size. This grain refinement can improve the mechanical properties of welds. Locking of grain boundaries decreases the grain growth and grain boundary movement during the plastic deformation, which in turn delays the occurrence of recrystallization. Moreover, in this condition, the recrystallization temperature is probably higher than the temperature at which the precipitates are formed. Another possible explanation is that the recrystallization process needs noticeable amount of time, which is not provided during the welding process. Preheating of the specimens at 75 °C provides the driving force for precipitates to move to the metallurgical defects such as grain boundaries and prevent the grain growth during the welding process. Therefore, the joint strength will be increased due to the formation of finer grain by increasing of the preheating temperature from 75 to 125 °C.

**3.3.2 Tensile strength.** Tensile test results are presented in Fig. 5 according to the applied travel speed, rotational speed and preheating temperature. By considering to the tensile test results given in Fig. 5, it can be found that the maximum strength for the specimens welded at room temperature is related to the rotation and travel speeds of 1300 rpm and 100 mm/min, respectively. Fig. 5 shows the effect of traverse speed on UTS. Welding speed has an inverse effect on tensile strength. Lower

welding speed leads to greater amount of heat supplied to materials and therefore, it improves plastic deformation of the material and the formation of the effective weld joint. However, increase in heat caused loss of strength. Different behaviors of aluminum alloys and pure copper toward preheating can be articulated as the main reason of this phenomenon. Because in a condition that heat input is suitable for copper, aluminum alloy shows negative reaction to this heat or in the similar case, when the generated heat to the welding area is appropriate for aluminum alloy, this amount of heat is inadequate for copper stir and consequently suitable joint is not achieved. As a result, for dissimilar joining of 6061 aluminum alloy and pure copper, a mediate condition toward different behaviors of welding alloys should be considered. It was found from the result that the welding speed have more signification effect on tensile strength.



*Fig. 5. Tensile test result for dissimilar Al/Cu joints*

According to previous researches, ratio of tool rotation speed to its travel speed plays an important role on turbulence of the plasticized material and consequently on microstructure and mechanical properties of joints due to having direct impact on rates of generated heat. That is why this parameter is known as one of the most important process parameters [17]. Increase in  $\omega/v$  ratio causes the decrease of tool advancing length in each rotation. In another word, in a specified length of joint, tool will have more rotation number. This issue will have an especial effect on materials flux in stir zone. In fact, stir of materials will be increased by decreasing the advancing speed and increasing the tool rotation speed. Changes in  $\omega/v$  ratio in welding process will have a considerable impact on temperature peak and also its distribution. In fact, this is an important factor in microstructural changes and thereby the eventual properties of these kinds of joints. As a result, changes in  $\omega/v$  variable are along with changes in joint quality.

The reasons of these changes can be justified in a way that reduction of  $\omega/v$  ratio will lead to decrease in amount of heat interred in welding zone. Because the tool rotation number in one millimeter of weld will be decreased and so, friction heat and heat derived from plastic work (due to strain decreasing derived from  $\omega$  decrease) will be reduced. In this case, material flux around the tool will be decreased and extent of turbulence zone will be reduced.

**Summary.** In this study, effect of preheating on mechanical properties of dissimilar friction stir welded Al/Cu joints have been investigated. The following results were obtained:

- Preheating of Al/Cu dissimilar joints improved the mechanical properties of the welds.
- The hardness at the copper side of the nugget was higher than that at the aluminum side and preheating has an effective role to improve it as well.
- Based on the EDS analysis results, typical intermetallic were observed in the lower part of the weld, including AlCu, Al<sub>2</sub>Cu<sub>3</sub> and Al<sub>4</sub>Cu<sub>9</sub>.
- WFSW process is a novel method to introduce metallurgical and mechanical changes in materials because of the uniform distribution of the particles in the stir zone.
- Full stir of aluminum and copper was observed at the interface. Due to the presence of aluminum particles in copper on the advancing side, flow of materials is upward on the bottom of the welded plates, while it is downward in the retreating side.

## References

- [1] R. Sakano, K. Murakami, K. Yamashita, T. Hyoe, M. Fujimoto, M. Inuzuka, U. Nagao, H. Kashiki, Kobe, Japan, 2001. Development of spot FSW robot system for automobile body members, in: Proceedings of the 3rd International Symposium of Friction Stir Welding
- [2] Thomas WM, Nicholas ED, Needham JC, Murch MG, Temple-Smith P, Dawes CJ. Friction stir butt welding. International Patent Application No. PCT/GB92/02203; 1991.
- [3] Montheillet, D. Allehaux, 2006, "Mechanical and thermal modelling of Friction Stir Welding", Journal of Materials Processing Technology, 171, pp.348–357.
- [4] S. Benavides, Y. Li, L. E. Murr, D. Brown, J. C. McClure, 1999, Scripta Mater. Vol 41, pp. 809
- [5] Y. Li, E. A. Trillo, L. E. Murr, J. 2000, Mater. Sci. Lett. Vol 19, pp. 1047
- [6]. Kundig K. J. A., Cowie J. G. Copper and copper alloys. In: Myer K, editor. Mechanical engineers' handbook. Wiley Interscience; 2006. p. 117-220.
- [7] T. Chen, "Process parameters study on FSW joint of dissimilar metals for aluminium-steel", journal of materials science, Vol.44, 2009, pp.2573-2580.
- [8] B. S. Yilba, A. Z. Sahin, N. Kahraman, A. Z. Al-Garni, "Friction stir welding of St-Al and Al-Cu materials" J. Mater. Process. Technol., 1995, 49, 431-443.

- [9] J. Ouyang , E. Yarrapareddy , R. Kovacevic , “Microstructural evolution in the friction stir welded 6061 aluminium alloy ( T6- temper condition) to copper” , J. Mater. Process. Technol., 2006, 172, 110-122.
- [10] Jiahu Ouyang, Eswar Yarrapareddy, Radovan Kovacevic, “ Microstructural evolution in the friction stir welded 6061 aluminum alloy (T6-temper condition) to copper” Journal of Materials Processing Technology, 2006, 172, pp 110–122.
- [11] I. Galvao, J. C. Oliveira, A. Loureiro and D. M. Rodrigues, “Formation and distribution of brittle structures in friction stir welding of aluminium and copper: influence of process parameters” Science and Technology of Welding and Joining, 2011, 16, No 8, pp. 681- 689.
- [12] Ratnesh K. Shukla , Pravin K. Shah , “ Investigation of Joint Properties of Friction Stir Welding of Aluminum 6061 Alloy to Copper” International Journal of Engineering Research and Technology, 2010, 3, Number 3, pp. 613—620.
- [13] Esther T. Akinlabi, Stephen A. Akinlabi, “Effect of Heat Input on the Properties of Dissimilar Friction Stir Welds of Aluminium and Copper” American Journal of Materials Science, 2012, 2(5), pp. 147- 152.
- [14] M. Abbasi. Gharacheh, A. H. Kokabi, G. H. Daneshi, B. Shalchi and R. Sarrafi, “ The Influence of the Ratio of “Rotational Speed/Traverse Speed” (  $\omega/v$  ) on Mechanical Properties of AZ31 Friction Stir Welds” , International Journal of Machine Tools and Manufacture, Pages 1983-1987, December 2006.

## Isothermal Pneumo-Forming of Hemispherical Parts Made Out of Anisotropic Materials In Short-Term Creep Mode

S.N. Larin<sup>1</sup>, V.I. Platonov<sup>1</sup>, Nuzhdin G.A.<sup>2</sup>

1 – Tula State University, Tula, Russia

2 – quality assurance company “Konsersium”, Moscow, Russia



DOI 10.13140/RG.2.1.3033.6408

**Keywords:** anisotropy, mathematical model, high-strength materials, domed parts, pneumo-forming, creep, pressure, stress, thickness, damage rate, failure.

**ABSTRACT.** Provided here are results of theoretical and experimental research of strained and stressed state, force modes, geometrical sizes for the blanks, and limit possibilities of deformation during isothermal blow molding of hemispheric parts of anisotropic material in creeping mode. Determined is the effect for the researched parameters of the studied deformation process, produced by anisotropy of mechanical properties, loading conditions and blank's geometric dimensions. Comparison of the theoretical and experimental data regarding the relative blank thickness in the blank dome and base points, and of data regarding the relative height of the blank, point to their satisfactory agreement (up to 10 percent). Recommendations have been developed regarding calculation of scientifically-based technological parameters for operations of isothermal straining of semi-spherical components made out of highly strong anisotropic materials in the mode of short-time creeping. The recommendations were used during development of technological processes of manufacture -- in the mode of short-time creeping and out of highly strong anisotropic materials -- of semispherical components conforming to the operational technical requirements. The technological processes provide for increasing specific strength by 1,5 – 1,7 times, for decreasing the mass by 1,5 times, for reducing labor content by 2-3 times, and for growth of capacity factor – from 0,3 to 0,9.

**Introduction.** Spherical sheet domes make bodies for tanks for fuel and liquid nitrogen, which are used in aviation and space technologies. The conventional methods of their manufacture are in the mode of multistage squeeze drawing with transitional thermal treatment rounds, or else it is hammer stamping in subpress dies, these being highly labor-consuming operations. Isothermal deformation of domed parts with gas of sheet high-strength aluminum and titanium alloys has considerable advantage over the traditional methods of processing, and it is quite promising for its industrial use [1-5].

**Materials that are subjected to processes of plastic straining, possess, as a rule, anisotropy of mechanical properties. Anisotropy of mechanical properties may produce both positive or negative effect upon stable procedure of technological processes of plastic deformation under various thermomechanical modes [1-19].**

**Equations.** Let us consider straining of a round sheet blank with radius  $R_0$  and with thickness  $h_0$  by free bulging in the mode of viscous flow of material as influenced by excessive gas pressure  $p = p_0 + a_p t^{n_p}$  into a spherical matrix (Fig. 1). Here  $p_0, a_p, n_p$  – are pressurizing constants.

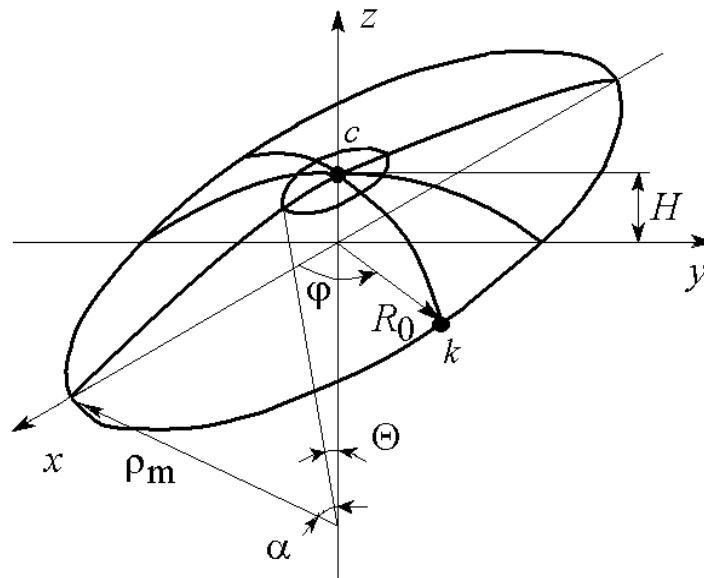


Fig. 1. Diagram for calculation of strained condition of middle surface of blank in meridian plane

The blank is fixed along the outer contour. The blank material is taken as transversal-isotropic with anisotropy ratio  $R$ ; the stressed state of the dome is plane, i.e., the stress is perpendicular to the plane of the sheet and equals zero ( $\sigma_z = 0$ ). We consider straining in the meridian plane of the dome as straining a membrane. Because of the symmetry of the material's mechanical properties, relative to the blank axis and the character of action of the external forces, -- the strain stresses and speeds, that are meridian, circumstantial and normal to the middle surface of the blank, are the major ones.

The middle surface of the blank remains a part of the spherical surface at any stage of straining. Taking place in any meridian section of the dome is radial flow of material relative to the new center at every stage of straining.

According to the adopted allowance, the radiuses of curvature of the meridian section  $\rho_m$  of the middle surface and of the slashing of the dome by the taper surface that is perpendicular to the meridian arc,  $\rho_t$ , are found according to the following formula.

$$\rho_m = \rho_t = \rho = \frac{H^2 + R_0^2}{2H}, \quad (1)$$

where  $H$  – is the height of the dome at a given moment of straining.

**Since the trajectories of the points of the middle surface are orthogonal at this moment to the profile in formation, straining speeds in the pole of the meridian surface (point “c”) shall be determined in the meridian sections as**

$$\xi_{tc}^c = \frac{2H\dot{H}}{H^2 + R_0^2}; \quad \xi_{mc}^c = \frac{2H\dot{H}}{H^2 + R_0^2}; \quad \xi_{zc}^c = \frac{\dot{h}}{h}, \quad (2)$$

where  $\dot{H} = dH/dt$ ;  $\dot{h} = dh/dt$ .

The blank is fixed in the contour (point “k”), i.e., the strain speed along the contour equals zero  $\xi_{tk}^c = 0$ , and according to the associated flow law, we have

$$\xi_{tk}^c = 0; \sigma_{tk} = \frac{R\sigma_{mk}}{1+R}; \xi_{zk}^c = -\xi_{mk}^c, \quad (3)$$

where  $R$  – is the normal anisotropy factor for viscous flow of material.

Further in the text we make no limitations about changing the shell thickness along the circumference arc in the meridian section. In this case the speed for the strain in the meridian  $\xi_m^c$ , circumferential direction  $\xi_t^c$  and the thickness strain  $\xi_z^c$  of the shell is found after the following formulas accordingly

$$\xi_m^c = \left( \frac{\sin \theta}{\theta \sin \alpha} - \operatorname{ctg} \alpha \right) \dot{\alpha}; \xi_t^c = \left( \frac{\cos \theta}{\sin \alpha} - \operatorname{ctg} \alpha \right) \dot{\alpha}; \xi_z^c = \frac{\dot{h}}{h}. \quad (4)$$

where  $\theta$  – is here actual angle between the blank’s vertical axis of symmetry and radius-vector determining the position of point in the section of middle surface by diagonal plane;  $\dot{\alpha} = d\alpha/dt$ .

It was assumed during the straining of the shell that there takes place in the meridian plane during every stage of straining a radial flow of point of middle surface, that is relative to the new center at moment  $t + dt$ , i.e., in the direction of  $\theta + d\theta$ .

Connection between angle  $\alpha$  and straining time  $t$ , when functional connection is assumed  $H = H(t)$ , is found as follows

$$\alpha = 2 \operatorname{arctg} \frac{H(t)}{R_0}. \quad (5)$$

The thickness of the meridian plane dome of the shell ( $\theta = 0$ ) is found from the following formula

$$h = h_0 / \left( 1 + \frac{H^2(t)}{R_0^2} \right)^2. \quad (6)$$

The changing thickness of the shell from straining time  $t$  at the spot of its fixation ( $\theta = \alpha$ ) is found after the following formula

$$h = h_0 \frac{H(t)}{R_0 \left( 1 + \frac{H^2(t)}{R_0^2} \right)^{\operatorname{arctg} \frac{H}{R_0}}}. \quad (7)$$

Cutting elements from the membrane by meridian planes and cone surfaces in the vicinity of the point under consideration, and assuming that the stresses are evenly distributed throughout the thickness of

the element, we write down the equation of equilibrium of momentless shell loaded with uniform pressure  $p$ , as follows:

$$\frac{\sigma_m}{\rho_m} + \frac{\sigma_t}{\rho_t} = \frac{p}{h}; \quad \sigma_{mx} = \frac{p\rho_t}{2h}. \quad (8)$$

Solving them together and taking account of  $\rho_m = \rho_t$ , we find

$$\sigma_m = \sigma_t = \frac{p\rho}{2h}. \quad (9)$$

The equivalent speed of straining  $\xi_e^c$  and equivalent stress  $\sigma_e$  in the apex of the dome (point “c”) and in the point of fixation of the shell over the entire circuit (point “k”) are computed respectively for anisotropic material after the following formulas:

$$\xi_{ec}^c = \frac{2}{\sqrt{3}} \sqrt{2+R} \xi_{mc}^c; \quad \sigma_{ec}^c = \frac{\sqrt{3}}{2\sqrt{2+R}} \sigma_{mc}^c; \quad (10)$$

$$\xi_{ek}^c = \left\{ \frac{2}{3} \frac{(2+R)(R+1)}{2R+1} \right\}^{1/2} \xi_{mk}^c; \quad \sigma_{ek}^c = \left\{ \frac{3}{2} \frac{2R+1}{(2+R)(R+1)} \right\}^{1/2} \sigma_{mk}^c. \quad (11)$$

Let us consider a case of slow isothermal straining of a shell made out of material for which hold constitutive equations of the energy theory of creep and creep damage [4]

$$\xi_e^c = \frac{B(\sigma_e/\sigma_{e0})^n}{(1-\omega_A^c)^m}; \quad \dot{\omega}_A^c = \frac{\sigma_e \xi_e^c}{A_{np}^c}, \quad (12)$$

where  $B$ ,  $n$ ,  $m$  – are material invariables depending on the test temperature;

$\omega_A^c$  – is the material damage rate for viscous deformation in the energy failure models;

$A_{np}^c$  – is specific fracture work for mode of viscous flow;

$\dot{\omega}_A^c = d\omega_A^c/dt$ ;  $\xi_e^c$  and  $\sigma_e$  – are equivalent straining speed and strain;

$\sigma_{e0}$  – is equivalent stress dividing the viscous and viscoplastic flows of material.

The value of the specific fracture work  $A_{np}^c$  for viscous flow of anisotropic material is found from

$$A_{np}^c = D(b_0 + b_1 \cos \alpha + b_2 \cos \beta + b_3 \cos \gamma),$$

where  $D, b_0, b_1, b_2, b_3$  – are material constants;

$\sigma = (\sigma_1 + \sigma_2 + \sigma_3)/3$  – is mean stress;  $\sigma_1, \sigma_2$  and  $\sigma_3$  – are primary stresses;

$\alpha, \beta, \gamma$  – are orientation angles of the first main stress axis  $\sigma_1$  as relative to the main axes of anisotropy  $x, y$  and  $z$  respectively.

**Since the value of pressure  $p$  at every moment of straining is distributed evenly over the surface of the shell, we shall be finding its value in the apex of the shell dome (point “c”).**

By substituting into the first material state equation (12) its constituent values  $\sigma_e$  and  $\xi_e^c$ , found after formulas (10), and taking account of formulas (1), (4), (9), we receive

$$p^n dt = \frac{\sigma_{e0}^n (1 - \omega_{Ac}^c)^m 2^{2n+2} (2+R)^{\frac{n+1}{2}} H^{n+1} h^n dH}{3^{\frac{n+1}{2}} B (H^2 + R_0^2)^{n+1}}. \quad (13)$$

Shell thickness  $h$  is found after formula (6).

We now find the value of the damage accumulation  $\omega_{Ac}^c$ . By substituting into the second state equation (12) formulas (10), account being taken of (1), (4) and (9), we obtain

$$\dot{\omega}_{Ac}^c = \frac{p \left( 1 + \frac{H^2}{R_0^2} \right)^2}{h_0 A_{np}^c} \dot{H}. \quad (14)$$

This equation is fitfully used if the pressurizing provides for  $p = const$ .

If we substitute the first state equation into the second one, we shall have a different type of equation for finding the damage rate

$$\dot{\omega}_{Ac}^c = \frac{\sigma_{e0}^n (1 - \omega_{Ac}^c)^{m/n} (\xi_{ec}^c)^{\frac{n+1}{n}}}{A_{np}^c B^{1/n}}. \quad (15)$$

This equation can be comfortably used if  $\xi_{ec}^c = \xi_{e1}^c = const$ . In the latter case integration of equation (15) results in a formula of the following type:

$$\omega_{Ac}^c = 1 - \left[ 1 - \frac{n-m}{n} \frac{\left( \xi_{e1}^c \right)^{\frac{n+1}{n}} \sigma_{e0} t}{A_{np}^c B^{1/n}} \right]^{\frac{n}{n-m}}. \quad (16)$$

Destruction time  $t_*$  is found from assumption  $\omega_{Ac}^c = 1$

$$t_* = \frac{A_{np}^c B^{1/n} n}{\sigma_{e0} (n-m) \left( \xi_{e1}^c \right)^{\frac{n+1}{n}}}. \quad (17)$$

Pressure  $p$ , which is necessary for creating the straining conditions, shall be computed after the following formula

$$p(t) = \frac{\sigma_{e0} \left( 1 - \omega_{Ac}^c \right)^{m/n} 2^2 (2+R)^{1/2} H h}{\sqrt{3} B^{1/n} \left( H_0^2 + R_0^2 \right)} \left( \xi_{e1}^c \right)^{1/n}. \quad (18)$$

Functional connection  $\omega_A^c = \omega_A^c(t)$  is found as per formula (16), while  $H = H(t)$  can be found from the following equation

$$t = \frac{2\sqrt{2+R}}{\sqrt{3}} \frac{\ln \frac{H^2 + R_0^2}{H_0^2 + R_0^2}}{\xi_{e1}^c}. \quad (19)$$

Limiting dome height  $H_*$  can be found by equation (19) with  $t = t_*$ .

Function setting  $H = H(t)$  allows us to find  $\omega_A^c = \omega_A^c(t)$  from formulas (15) or (16), whereas function  $p = p(t)$  is calculated after formula (13).

The same procedure is used for finding the stressed and strained conditions of the blank in the point of fixation of the shell (point “k”), and also found are the principal equations and correlations for the solving of the problem with the assumption that the behavior of the material is subject to equations of the kinetic theory of creep and creep damage under the known law of time-pressure  $p = p(t)$  and under permanent equivalent strain rate in the blank dome  $\xi_{e1}$ .

There have been developed the calculation algorithm for the force and strain parameters of the studied technological process, and the computer software.

**Discussion of results. Evaluated were the stressed and strained conditions, the material flow kinematics, the force modes and frontiers of the studied process of strain – as relating to accumulated microscopic damages, and depending on anisotropy of the mechanical properties**

of the source material, on the stress sequence, and on the geometric dimensions of the blank and of the ready item.

Calculation was performed for titanium alloy LT31 under  $T = 860^\circ\text{C}$ , the behavior of which is subject to the energy theory of creep and creep damage, and for titanium alloy 4AL-3MO-1V under  $T = 950^\circ\text{C}$ , the behavior of which is subject to the kinetic theory of creep and creep damage. Mechanical characteristics of these materials during deformation under conditions of viscous flow of material are shown in the work [3, 4].

The curves for changing values of gas pressure  $p$ , for relative values of blank thickness in the dome  $\bar{h}_c = h_c/h_0$  and at the place of its attachment  $\bar{h}_k = h_k/h_0$ , for the height of the dome-shaped blank  $\bar{H}' = H/R_0$ , for strain time  $t$  for titanium alloy LT31 ( $T = 860^\circ\text{C}$ ) under permanent value of the equivalent strain rate in the blank dome  $\xi_{el}$  --are shown in Fig. 2. Experimental data are shown here with dots.

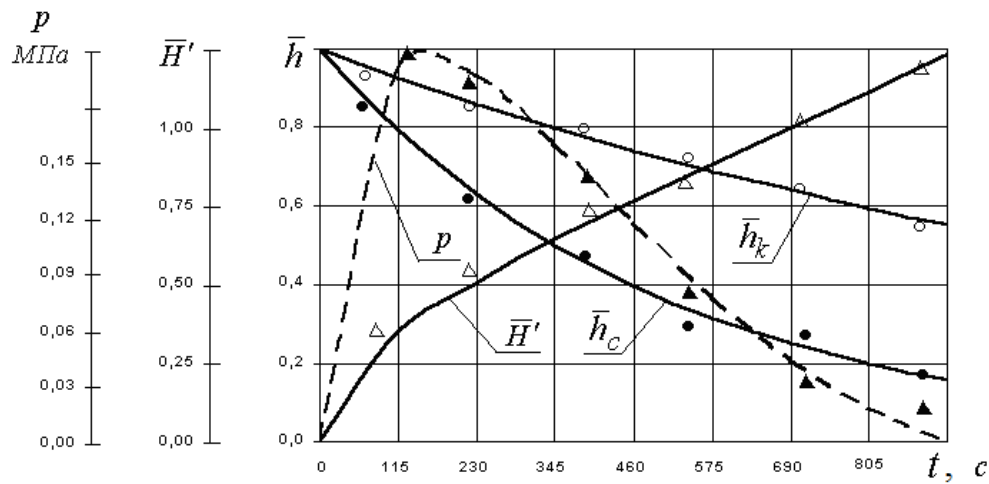


Fig. 2. Changes of  $p$ ,  $\bar{H}'$  and  $\bar{h}$  in studied points of blank as depending on  $t$  of titanium alloy LT31 ( $\bar{R}_0 = 300$ ;  $\xi_{el} = 0,002 \text{ 1/c}$ )

It follows from analysis of the calculation results and graphic dependencies that, as there grows to a certain limit the strain time  $t$ , there takes place a steep increase in the relative height of the blank  $\bar{H}'$  and reduction in the relative thickness of the blank in the dome  $\bar{h}_c$  and in the place of its fixation  $\bar{h}_k$ . Further increase in the time of straining  $t$  results in a smooth changing of the values under study. At time moment  $t$ , close to the destruction of the blank, there takes place a sudden change of the relative values of  $\bar{H}'$ ,  $\bar{h}_c$  and  $\bar{h}_k$ . This is linked to the intensive accumulation of micro-damages at the concluding stage of the process.

It has been found that change of the relative thickness in the blank dome proceeds in a more intensive manner as versus changing the relative thickness at the place of its fixation. As the  $t$  straining time grows, that difference grows too and may reach as much as 50%.

It was shown that for the purpose of ensuring a permanent equivalent speed of strain in the blank dome, the law of changing pressure  $p$  during time of straining  $t$  has a complicated character. At the initial moment of deformation we observe a sudden growth of pressure  $p$ , since there takes place a

substantial change of half-sphere radius  $\rho_m$ . Further extension of the straining time  $t$  is accompanied with reduction in the magnitude of the gas pressure  $p$ .

Comparison of theoretical and experimental data for the relative thickness in the dome of blank  $\bar{h}_c$  and at the place of its fixation  $\bar{h}_k$ , as well as the data for relative height of blank  $\bar{H}'$  points to their satisfactory coincidence (up to 10%).

It is defined, that destruction of the blank during isothermal staining takes place in blank dome where there happens the maximum thinning of the blank.

Dependence of change in destruction time  $t_*$ , of relative height  $\bar{H}'_*$  and of thickness in the blank dome  $\bar{h}_*$  at the moment of destruction as determined after the magnitude of accumulated micro-damages with  $\omega_A^c = 1$ , -- on the magnitude of the standing equivalent speed of strain in the blank dome  $\xi_{e1}$  and on anisotropy ratio  $R$  is shown in Fig.3 and Fig.4 respectively. It is shown that increasing the parameters of stress sequence  $a_p$ ,  $n_p$  and increasing the magnitude of the permanent equivalent speed of strain in the blank dome  $\xi_{e1}$ , result in decreasing destruction time  $t_*$  and blank relative height  $\bar{H}'_*$ , and result also in increasing the relative thickness in the blank dome  $\bar{h}_*$ .

It follows from the curves' analysis (Fig. 4) that normal anisotropy factor  $R$  produces a substantial effect upon the magnitude of the destruction time and upon the relative values  $\bar{H}'_*$ ,  $\bar{h}_*$ . As there grows the anisotropy factor  $R$ , the relative value  $\bar{h}_*$  grows steeply, while destruction time  $t_*$  and blank relative height  $\bar{H}'_*$ , abruptly drop in magnitude. It was found, that failure to take account of anisotropy of blank's mechanical properties during analysis of the process of isothermal deformation of a spherical shell results in a measurement error in the evaluation of destruction time  $t_*$  in the order of 35%, and this results in an error of 15% in the evaluation of the relative height  $\bar{H}'_*$  and of the thickness in the blank dome  $\bar{h}_*$  during the destruction moment.

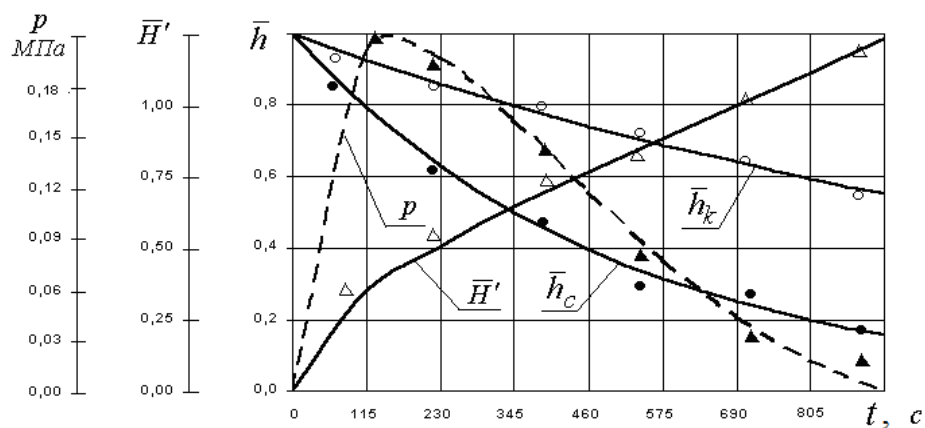


Fig. 3. Dependence on  $\xi_e$  of changing  $t_*$  and  $\bar{H}'_*$ ,  $\bar{h}_*$  in blank dome, titanium alloy LT31 ( $\bar{R}_0 = 300$ )

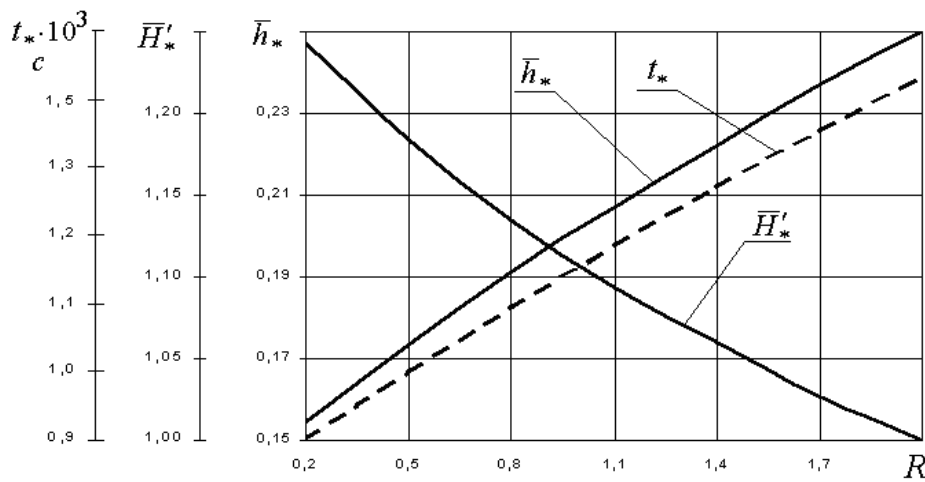


Fig. 4. Dependence on  $R$  of changing  $t_*$  and  $\bar{H}'_*$ ,  $\bar{h}_*$  (kinetic theory;  $\bar{R}_0 = 300$ ;  $p_0 = 0,013 \text{ MPa}$ ;  $a_p = 4 \cdot 10^{-3} \text{ MPa} / c^{n_p}$ ;  $n_p = 0,6$ )

Calculation analysis shows that the limitations of deformation under conditions of viscous flow of material whose behavior obeys the kinetic theory of creep and creep damage (alloy 4AL-3MO-1V), do not depend on the loading conditions of the blank. Shown is the substantive dependence of destruction time  $t_*$  on loading parameters  $a_p$ ,  $n_p$  and on the magnitude of the permanent equivalent strain rate  $\xi_{el}$ . Increasing the loading parameter  $a_p$  from  $0,2 \cdot 10^{-3} \text{ MPa} / c^{n_p}$  to  $1,4 \cdot 10^{-3} \text{ MPa} / c^{n_p}$ , and increasing  $n_p$  from 0,5 to 0,8 under fixed other parameters, results in the reduction of the destruction time  $t_*$  by 1,8 times.

There has been shown substantive effect of the geometric dimensions of the blank upon the values of the destruction time  $t_*$ . It was found that increasing the relative size of the blank radius  $\bar{R}_0 = R_0 / h_0$  from 200 to 800 results in reduction of the destruction time by more than 4 times over.

**Summary.** There has been carried out experimental research of operations of isothermal straining of hemispherical parts of high-strength anisotropic materials in the mode of short-time creeping. It was experimentally shown that in case of direct one-stage molding, there forms significant unevenness in the width of the wall along the generatrix from the flange radius to the dome center ( $h/h_0$ ). In case of shells of alloys LT31 it was on an average 0,4; and was 0,33 for shells made out of alloy AA5052. In order to lessen the unevenness in the wall thickness, it is recommended to use two-stage stamping with an insert (reversal). Comparison of theoretical and experimental data on relative thickness in the blank dome and in the basic points, as well as comparison of the blank's relative heights, points to their satisfactory coincidence (up to 10 %).

Recommendations have been developed for calculating scientifically-based technological parameters for operations of isothermal straining of semispherical components made out of highly strong anisotropic materials in the mode of short-time creeping. The technological processes are based on observing the proper sequence of operations with the provided blanks in one operating position: heating, vacuuming – forming – thermal stabilization – cooling.

The above recommendations were used for developing technological processes of manufacturing semispherical components meeting the operational technological requirements, the components were made out of highly strong anisotropic materials in the mode of short-time creeping. Samples of dome-

shaped critical-task components made out of titanium alloys 4AL-3MO-1V, manufactured by isothermal stamping in the mode of short-time creeping, are shown in Fig. 5.



*Fig. 5. Samples of dome-shaped components made out of titanium alloys 4AL-3MO-1V (a) and BT23 (b)*

The described technological processes provide for: greater specific strength – 1,5 ... 1,7 times; weight reduction - 1,5 times; lower labor consumption - 2...3 times; greater capacity factor (from/to) - 0,3/0,9.

This research was carried out as per basic part of state task №2014/227 for scientific research, issued by the Ministry of Education and Science of the Russian Federation for 2014-2020, and as per grant RFFI № 14-08-00066 a, № 16-48-710016 and 16-08-00020 .

## References

- [1] K.I .Romanov, Mechanics of hot metal forming, M .: Engineering, 1993. 240 pp.
- [2] N.N. Malinin, Applied theory of plasticity and creep, M .: Mechanical engineering, 1975. 400 p.
- [3] S.P. Yakovlev, V.N .Chudin, S.S .Yakovlev, J.A. Sobolev, Isothermal deformation of high anisotropic materials, M .: Engineering, 2004. 427 pp.
- [4] S.S. Yakovlev, V.N. Chudin, J.A. Sobolev, S.P. Yakovlev, V.I. Tregubov, S.N. Larin, Isothermal pneumo-forming of anisotropic high-strength sheet materials, M .: Engineering, 2009. 352 pp.
- [5] E.I. Semenov, Forging and Stamping: Reference: In 4 volumes. V.4. Stamping, M .: Engineering, 2010. 732 pp.
- [6] Y.M.Aryshensky, F.V. Grechnikov, Theory and calculations of plastic deformation of anisotropic materials, M .: Metallurgy, 1990. 304 pp.
- [7] F.V.Grechnikov, Straining of anisotropic materials, M .: Engineering, 1998. 446 pp.
- [8] V.D. Golovlev, Calculation of stamping processes, M .: Engineering, 1974. 136 pp.
- [9] S.P.Yakovlev, V.D. Kuhar, Punching anisotropic blanks, M .: Engineering, 1986. 136 pp.
- [10] S,P.Yakovlev, S.S. Yakovlev , V.A. Andreichenko, Forming anisotropic materials, Kishinev: Quant, 1997. 332 p.10.
- [11] S.S.Yakovlev, O.V. Pylypenko, Isothermal extract anisotropic materials, M .: Engineering, 2007. 212 pp.

- [12] S.S.Yakovlev, V.I.Tregubov, Theory and technology of manufacturing large-sized axisymmetric critical parts of highly anisotropic materials, Tula: Tula State University Publishing House, 2011. 230 pp.
- [13] S.S.Yakovlev, V.D.Kuhar, V.I.Tregubov, Theory and technology of forming anisotropic materials, M.: Engineering, 2012. 400 pp.
- [14] S.S.Yakovlev, V.I.Tregubov, S.P.Yakovlev, Rotating hood with wall thinning rotationally symmetric parts of anisotropic round billets - specialized equipment, M.: Engineering, 2009. 265 pp.
- [15] S.S.Yakovlev, V.I.Tregubov, Theory and technology of manufacturing large-sized axisymmetric critical parts of highly anisotropic materials, Tula: Tula State University Publishing House, 2011. 230 pp.
- [16] S.S.Yakovlev, V.D.Kuhar, V.I.Tregubov, Theory and technology of forming anisotropic materials, M.: Engineering, 2012. 400 pp.
- [17] S.S. Yakovlev, V.I.Tregubov, V.D. Kuhar, V.Y.Travin, Deep drawing of anisotropic materials, Tula: Tula State University Publishing House, 2013. 225 pp.
- [18] S.S.Yakovlev, V.I.Tregubov, G.A.Nuzhdin, Plastic flow of anisotropic hardening material with strength differential effect, Tula: Tula State University Publishing House, 2014. 115 pp.
- S.S. Yakovlev, K.S. Belts, V.I.Tregubov, Stability of anisotropic sheet metal and of pipe blanks during plastic deformation, Tula: Tula State University Publishing House, RARAN, 2014. 222 pp.

# MHD Stagnation Point Flow in a Boundary Layer Of a Nano Fluid Over a Stretching Sheet in the Presence of Viscous Dissipation and Chemical Reaction

Ch. Achi Reddy <sup>1,a</sup> & B. Shankar <sup>2</sup>

1 – M.L.R. Institute of Technology, Dundigal, Hyderabad, 500 043, India

2 – Professor, Department of Mathematics, Osmania University, Hyderabad, 500 007, India

a – [achireddy.ch@gmail.com](mailto:achireddy.ch@gmail.com)



DOI 10.13140/RG.2.1.2022.4881

**Keywords:** boundary layer flow, exponentially stretching sheet, chemical reaction and viscous dissipation.

**ABSTRACT.** The paper shows an attempt of numerical investigation on the effect of viscous dissipation and Chemical reaction on a viscous, steady and incompressible fluid over an exponentially stretching sheet within a specified boundary layer. As a formal approach, the model has been adopted with the governing equations and the simulation is carried out with the Keller Box method. The pattern or the profiles of the skin friction coefficient and the heat and mass transfer rates are achieved in execution of mathematical model have been presented in the paper. The enhancement in magnetic parameter leads to a considerable reduction in velocity and Chemical reaction parameter is predominant in controlling the profile of concentration. An increase in Eckert number is observed to cause the enhancement in the temperature profile whereas it decreases the concentration profile. The results obtained in the simulation of Keller box method are in well agreement with realistic situation of the scientific scenario.

**1. Introduction.** The importance of stagnation point flow has drawn the attention of many researchers due to its growing application in industry. The fluid is said to have reached its stagnation point when local Velocity of the fluid becomes zero. In some situations, flow is stagnated by a solid wall while in others; there is a line interior to a homogeneous fluid domain or the interface between two immiscible fluids [1-3]. A good amount of research is done drawing the attention of several researchers [4-12].

In 1993, during an investigation of new coolants and cooling technologies at Argonne National Laboratory in U.S. Chai invented a new type of fluid called Nano fluid [13]. Nano fluids are fluids that contain small volumetric quantities of nanometre sized particle, Called nanoparticles. The nanoparticles used in Nano fluids are typically made of metals, oxides, carbides, or carbon nanotubes. Common base fluids include water, ethylene glycol and oil. Nano fluids commonly contain up to a 5% volume fraction of nanoparticles to see effective heat transfer enhancements [25-27].

Nano fluids are studied because of their heat transfer properties: they enhance the thermal conductivity and convective properties over the properties of the base fluid. Typical thermal conductivity enhancements are in the range of 15-40% over the base fluid and heat transfer coefficient enhancements have been found up to 40%. Increasing the thermal conductivity of this magnitude cannot be solely attributed to the higher thermal conductivity of the added nanoparticles, and there must be other mechanisms attributed to the increase in performance [28-29].

Stagnation point flow appears in virtually all fields of science and engineering. A flow can be stagnated by a solid wall or a free stagnation point or a line can exist in the interior of the fluid Domain. The study of stagnation point flow as pioneered by Hiemenz in 1911 [15] who solved the two dimensional stagnation point problem using a similarity transformation.

Magyari and Keller [16] investigated the steady boundary layers flow on a stretching continuous surface with exponential temperature distribution while Partha et al. [17] analysed the effects of viscous dissipation on the mixed convection heat transfer from an exponentially stretching surface.

In the present study we have investigated the viscous dissipation for different values of velocity ratio parameter and observed that the nanoparticle volume decreases with the increase of chemical reaction parameter for  $\gamma = 0.1$  and  $2.1$ .

**2. Mathematical Formulation.** Consider a steady, two-dimensional boundary layer stagnation-point flow of a Nano fluid over an exponentially stretching sheet, the stretching and free stream velocities are assumed to be of the forms  $u_w(x) = ae^{x/l}$ , and  $u_\infty(x) = be^{x/l}$ , respectively. Where  $a > 0$  and  $b$  are constants,  $x$  is the coordinate measure along the stretching surface and  $l$  is length of the sheet. A non-uniform transverse magnetic field of strength  $B(x) = B_0 e^{x/2l}$  is imposed parallel to the  $y$ -axis, where  $B_0$  is a uniform magnetic field strength. It is assumed that the induced magnetic field due to the motion of an electrically conducting field is negligible. Further, it is also assumed that the external electric field is zero and the electrical field due to polarization of charges is negligible [22].

Figure (1) shows that the temperature  $T$  and the Nano-particles fraction  $C$  take forms  $T\omega(x)$  and  $C\omega(x)$ , respectively whereas the ambient values of temperature  $T_\infty$  and Nano-particle fraction  $C_\infty$  are obtained when  $y$  tends to infinity.

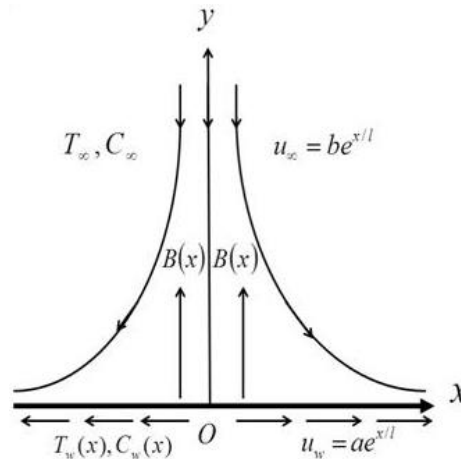


Fig. 1. Physical flow model and coordinate system.

The governing boundary layer equations of the conservation Law of mass, momentum, energy and concentration in the flow as follows:

$$\frac{\partial u}{\partial x} + \frac{\partial v}{\partial y} = 0 \quad (1)$$

$$u \frac{\partial u}{\partial x} + v \frac{\partial u}{\partial y} = u_\infty \frac{du_\infty}{dx} + \frac{u}{\rho_f} \frac{\partial^2 u}{\partial y^2} + \frac{\sigma B^2(x)}{\rho_f} [u_\infty - u], \quad (2)$$

$$u \frac{\partial T}{\partial x} + v \frac{\partial T}{\partial y} = \alpha \frac{\partial^2 T}{\partial y^2} - \frac{1}{(\rho c)_f} \frac{\partial q_r}{\partial y} + \tau \left[ D_B \frac{\partial C}{\partial y} \frac{\partial T}{\partial y} + \frac{D_T}{T_\infty} \left( \frac{\partial T}{\partial y} \right)^2 \right] + \frac{\mu}{(\rho c_p)_f} \left( \frac{\partial u}{\partial y} \right)^2 \quad (3)$$

$$u \frac{\partial C}{\partial x} + v \frac{\partial C}{\partial y} = D_B \frac{\partial^2 C}{\partial y^2} + \frac{D_T}{T_\infty} \frac{\partial^2 T}{\partial y^2} - \kappa(C - C_\infty) \quad (4)$$

Here  $u$  and  $v$  – are the velocity components in the  $x$  and  $y$  directions respectively,

$\mu$  – is the viscosity;

$\rho$  – is the density of the base field;

$\sigma$  – is the electrical conductivity.

$$\alpha = \frac{\kappa}{(\rho c)_f},$$

where  $k$  – is the thermal conductivity;

$(\rho c)_f$  – is the heat capacitance of the base fluid.

$$\tau = \frac{(\rho c)_p}{(\rho c)_f},$$

where  $(\rho c)_p$  – is the heat capacitance of the nanoparticle;

$D_B$  – is the Brownian diffusion coefficient;

$D_T$  – is the thermophoresis diffusion coefficient;

$q_r$  – is the radiation flux.

The Rosseland approximation is defined as [23, 24];

$$q_r = -\frac{4\sigma^*}{3k^*} \frac{\partial T^4}{\partial y} \quad (5)$$

where  $\sigma^*$  – is the Stefan-Boltzmann constant;

$k^*$  – is the mean absorption coefficient.

It is assumed that the temperature difference between the free stream  $T_\infty$  and local temperature  $T$  is small enough expanding  $T^4$  in a Taylor series about  $T_\infty$  and neglecting higher order terms results.

$$T^4 \cong 4T_\infty^3 T - 3T_\infty^4 \quad (6)$$

After substituting Eqs. (5) and (6) in Eq. (3), it will be reduces to

$$\begin{aligned}
 u \frac{\partial T}{\partial x} + v \frac{\partial T}{\partial y} = & \left[ \alpha + \frac{16\sigma^* T_\infty^3}{3\kappa^* (\rho c)_f} \right] \frac{\partial^2 T}{\partial y^2} + \\
 & \tau \left[ D_B \frac{\partial C}{\partial y} \frac{\partial T}{\partial y} + \frac{D_T}{T_\infty} \left( \frac{\partial T}{\partial y} \right)^2 \right] + \frac{\mu}{(\rho c_p)_f} \left( \frac{\partial u}{\partial y} \right)^2
 \end{aligned} \quad (7)$$

The subjected boundary conditions are

$$\left. \begin{aligned}
 u = u_\omega(x) = ae^{x/l}, v = 0, T = T_\omega(x), C = C_\omega(x), & \quad \text{at} \quad y = 0 \\
 u \rightarrow u_\infty(x) = be^{x/l}, v \rightarrow 0, T \rightarrow T_\infty, C \rightarrow C_\infty, & \quad \text{as} \quad y \rightarrow \infty
 \end{aligned} \right\} \quad (8)$$

The prescribed temperature and concentration on the surface of the sheet is assumed to be  $T_\omega(x) = T_\infty + T_0 e^{x/2l}$  and  $C_\omega(x) = C_\infty + C_0 e^{x/2l}$  where  $T_0, C_0$  are the reference temperature and concentration respectively, now, the non-linear partial differential equations for the purpose of a stream function  $\psi = \psi(x, y)$  is defined as

$$u = \frac{\partial \psi}{\partial y}, v = -\frac{\partial \psi}{\partial x}, \quad (9)$$

where the continuity Eq. (1) is satisfied identically. A similarity transformation is defined as [20] follows

$$\begin{aligned}
 \psi = \sqrt{2lva} e^{x/2l} f(\eta), \quad \theta(\eta) = \frac{T - T_\infty}{T_\omega - T_\infty} \\
 \phi(\eta) = \frac{C - C_\infty}{C_\omega - C_\infty}, \quad \eta = y \sqrt{a/2vl} e^{x/2l}
 \end{aligned} \quad (10)$$

As such Eq. (10), Eqs. (2), (4) and (7) reduce to the following system of nonlinear ordinary differential equations.

$$f''' + ff'' - 2f'^2 + 2\varepsilon^2 + M(\varepsilon - f') = 0 \quad (11)$$

$$p_{rN} \theta'' + f\theta' - f'\theta + Nb \phi' \theta' + Nt \theta'^2 + E_C f''^2 = 0 \quad (12)$$

$$\phi'' + Lef\phi' - Lef'\phi + Nt_b \theta'' - \gamma \phi L e = 0 \quad (13)$$

where

$$\varepsilon = b/a, \quad v = \frac{\mu}{p_f}, \quad M = \frac{2l\sigma B_0^2}{ap_f} \quad (14)$$

$$Nb = \frac{\pi D_B (C_\omega - C_\infty)}{\nu},$$

$$Nt = \frac{\pi D_T (T_\omega - T_\infty)}{\nu T_\infty}, E_c = \frac{u_\omega^2}{(Cp)_f (T_\omega - T_\infty)}, \gamma = \frac{2lk}{u_\omega},$$

where, prime denote the differentiation with respect to  $\eta$ ,  $B$  – is the velocity ratio parameter;

$\nu$  – is the kinematic viscosity of the fluid;

$P_r$  – is the Prandtl number;

$Le$  – is the Lewis number;

$M$  – is the magnetic parameter;

$A$  – is the heat source parameter,

$S$  – is the suction parameter.

$$P_{rN} = \frac{1}{P_r} \left( 1 + \frac{4}{3} N \right),$$

where

$$N = \frac{4\sigma^* T_\infty^3}{kk^*} \text{ is the radiation parameter,}$$

$$Nt_b = \frac{Nt}{Nb},$$

where  $Nb$  – is the Brownian motion parameter and  $Nt$  is the thermophoresis parameter;

$Ec$  – Eckert number;

$\gamma$  – is chemical reaction parameter;

The corresponding boundary conditions Eq. (8) are transformed into

$$\begin{aligned} f(\eta) = 0, f'(\eta) = 1, \theta(\eta) = 1, \phi(\eta) = 1 \quad \text{at} \quad \eta = 0, \\ f'(\eta) \rightarrow \varepsilon, \theta(\eta) \rightarrow 0, \phi(\eta) \rightarrow 0 \quad \text{as} \quad \eta \rightarrow \infty \end{aligned} \quad (15)$$

The parameters of practical interest in the formulated problem are velocity, heat and mass transfer respectively, which are presented in terms of Skin friction  $C_f$ , Nusselt number  $Nu$  and Sherwood numbers  $Sh$ . Using the transformed variables (10), the non-dimensional expressions for the Skin friction coefficient  $C_{fx}(0) = f''(0)$ , the reduced Nusselt number  $-\theta'(0)$  and the reduced Sherwood number  $-\phi'(0)$  respectively are defined as;

**Skin friction Coefficient.** The Skin friction coefficient  $C_f$  is defined by

$$C_f = \frac{\tau_\omega}{\frac{1}{2} \rho U_\omega^2},$$

where  $\tau_w$  – is the local wall Shear stress;

$\rho$  – is the fluid density.

$$\sqrt{\text{Re}_x} \cdot C_f = f''(0)$$

**Nusselt Number.** In heat transfer at a boundary within a fluid, the Nusselt number (Nu) is the ratio of convection to conductive heat transfer across the boundary

$$\begin{aligned} Nu_x &= \frac{\text{convective heat transfer}}{\text{conductive heat transfer}} = \frac{xq_w}{K(T_w - T_\infty)} \\ -\theta'(0) &= \frac{Nu_x}{\sqrt{\text{Re}_x}} \end{aligned} \quad (16)$$

**Sherwood Number.** The Sherwood number (Sh) is also called the mass transfer Nusselt number. It represents the ratio of convective to diffusive mass transport

$$\begin{aligned} Sh_x &= \frac{\text{Convective mass Transfer coefficient}}{\text{Diffusive mass Transfer coefficient}} = \frac{xJ_w}{D_B(C_w - C_\infty)} \\ \frac{Sh_x}{\sqrt{\text{Re}_x}} &= -\phi'(0) \end{aligned}$$

where  $\text{Re}_x = u_w(x) \cdot \frac{x}{\nu}$  is the local Reynolds number based on the stretching velocity.

**3. Numerical Procedure.** The equations (11) - (14) subject to the boundary conditions (15) are solved numerically using an implicit finite - difference scheme known as Keller box method. The method has the following four basic steps.

1. Reduce equations (11) - (14) to first order equations.
2. Write the difference equations using central differences.
3. Linearize the resulting algebraic equations by Newton's method and write them in matrix -vector.
4. Use the Block - tridiagonal elimination technique to solve the linear system.

#### 4. Results and Discussion.

Table 1. Comparison of the reduced Nusselt number  $-\theta'(0)$  when  $Nb = Nt = Le = \varepsilon = 0$ 

$Pr$	$M$	$N$	[19] $-\theta'(0)$	[20] $-\theta'(0)$	[21] $-\theta'(0)$	Present results $-\theta'(0)$
1	0	0	0.9548	0.9548	0.9548	0.9548
2	0	0	1.4714	1.4714	1.4714	1.4715
3	0	0	1.8691	1.8691	1.8691	1.8692
1	0	1.0	0.5315	0.5312	0.5312	0.5311
1	1.0	0	---	0.8611	0.8611	0.8611
1	1.0	1.0	---	0.4505	0.4505	0.4505

 Table 2. Values of the reduced Nusselt number  $-\theta'(0)$ , reduced Sherwood number  $-\phi'(0)$ , and the skin friction coefficient  $C_{fx}(0)$  for various values of Eckert number.

$Nb = Nt = M = \varepsilon = \gamma = 0.1$			$-\theta'(0)$	$-\phi'(0)$	$C_{fx}(0)$
$Ec$	$Le$	$N$			
0.1	10	1.0	0.5176	3.6996	1.2856
0.2	10	1.0	0.4976	3.7107	1.2856
0.3	10	1.0	0.4776	3.7219	1.2856
0.4	10	1.0	0.4375	3.7442	1.2856

 Table 3. Values of the reduced Nusselt number  $-\theta'(0)$ , reduced Sherwood number  $-\phi'(0)$ , and the skin friction coefficient  $C_{fx}(0)$  for various values of Chemical Reaction parameter.

$\gamma$	$Nb = Nt = M = \varepsilon = Ec = 0.1$			$-\theta'(0)$	$-\phi'(0)$	$C_{fx}(0)$
	$Pr$	$Le$	$N$			
0.1	1.00	10	1.0	0.5176	3.6996	1.2856
0.2	1.00	10	1.0	0.5175	3.8407	1.2856
0.3	1.00	10	1.0	0.5174	3.9757	1.2856
0.4	1.00	10	1.0	0.5172	4.1055	1.2856

The system of ordinary differential equations [11-13] has been solved numerically using Keller-box method. From the numerical computation, the main physical quantities of interest namely the local Skin friction coefficient, the local Nusselt number and the local Sherwood number are obtained and the results are presented in Table 2 and Table 3.

From Table 2 it is observed that with the increase in Eckert number, there is a decrease in rate of heat transfer and increase in mass transfer.

From Table 3 it is observed that with increase in chemical reaction parameter, there is no significant change in rate of heat transfer but there is an increase in the rate of mass transfer.

Figure 2 shows the effects of the magnetic Parameter  $M$  on the flow field velocity  $f'(\eta)$  for three different values of the Velocity ratio parameter  $\varepsilon$ ,  $\varepsilon = 0.1, 1$  and  $2.1$ .

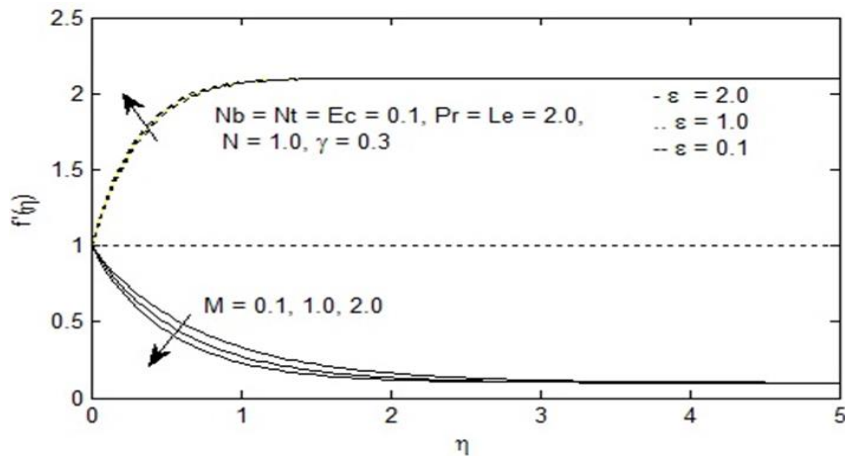


Fig.2. Velocity profile against  $\eta$  for different values of  $M$

When  $\varepsilon=0.1$  the velocity profile and the boundary layer thickness decrease with an increase in  $M$ . When  $\varepsilon=2.1$ , higher value of the Lorentz force further reduces the velocity and consequently the thickness of boundary layer reduces. When  $\varepsilon=1$ , there is no influence of magnetic field  $f'(\eta)$  and  $f'(\eta)$  attains a constant value of 1 for any value of  $\eta$  indicating that there is no boundary layer of fluid, as shown by a dotted line in Fig 2. This means that in the case when the external stream velocity becomes equal to the stretching velocity. The flow is not influenced by the different values of the incorporated flow parameters. When  $\varepsilon=2.1$  the flow velocity increases indicating the decrease in thickness of boundary layer with an increase in  $M$ . As compared to  $\varepsilon=0.1$  case, the boundary layer thickness decreases causing an inverted boundary structure.

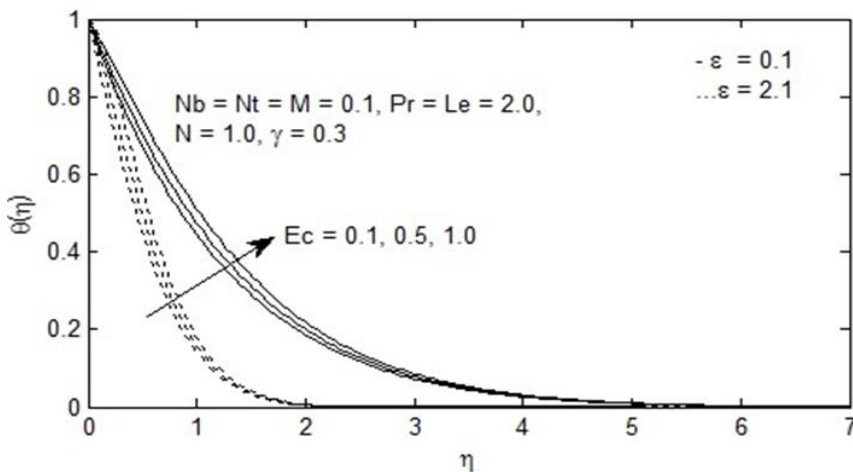


Fig. 3. Temperature profile against  $\eta$  for different values of  $Ec$

Figure 3 shows an increase in Nano fluid Temperature with increases in the viscous dissipation parameter, Eckert number. Which can be attributed to the action of viscous heating. Concentration increases with an increase in the viscous dissipation parameter, Eckert number as shown in Fig. 4

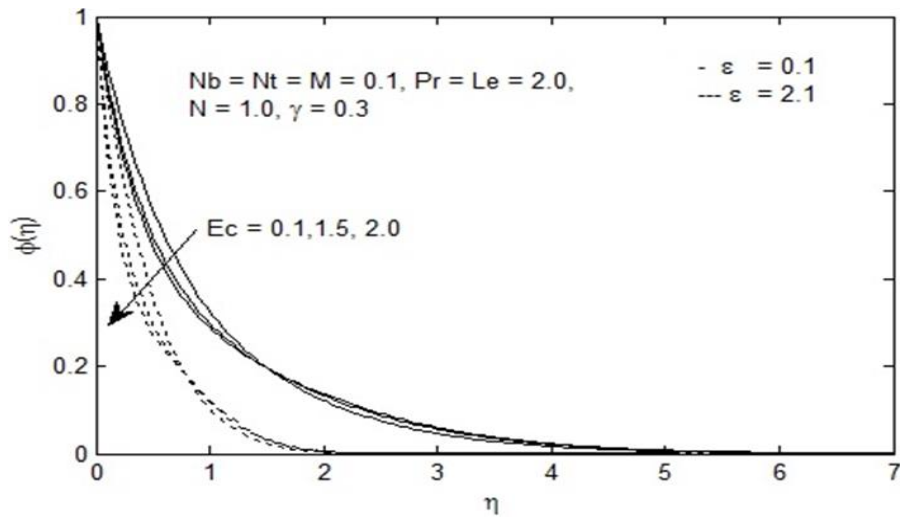


Fig. 4. Concentration profile against  $\eta$  for different values of  $E_c$

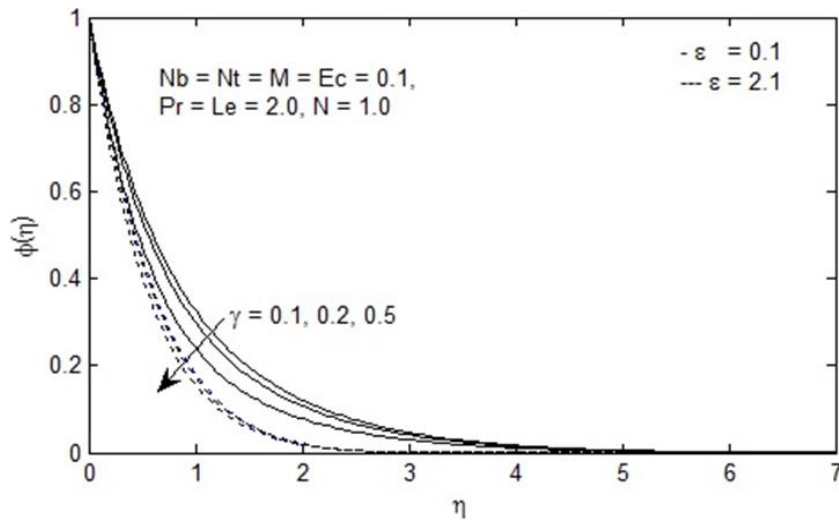


Fig. 5. Concentration profile against  $\eta$  for different values of  $\gamma$

The influence of chemical reaction parameter  $\gamma$  on concentration profile is shown in Fig. 5. Concentration decreases with an increase in the chemical reaction parameter indicating that the nanoparticle volume fraction decreases with the increase of chemical reaction parameter, while effect chemical reaction parameter  $\gamma$  is not significant on the temperature profile.

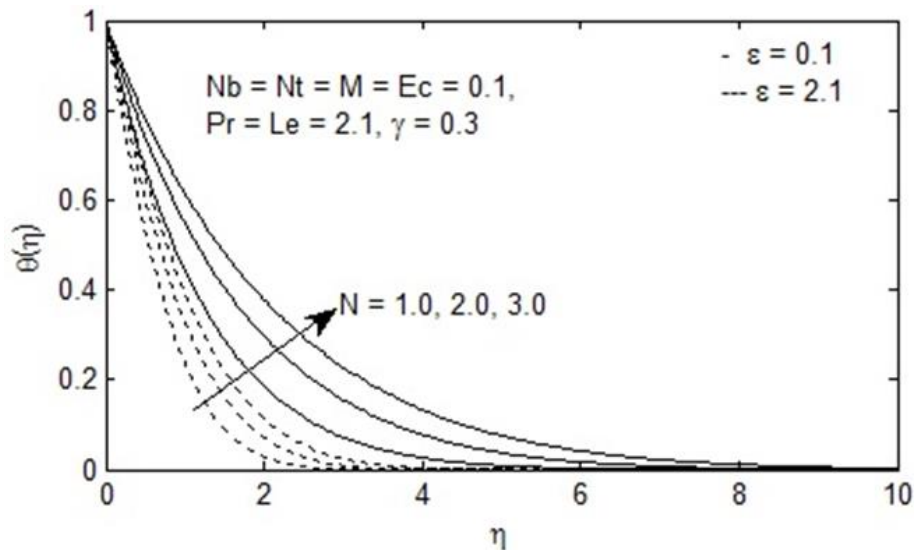


Fig. 6. Temperature profile profile against  $\eta$  for different values of  $N$

**Summary.** A numerical study corresponding to the flow and heat transfer in a steady flow region of Nano fluid over an exponential stretching surface and effects of Chemical reaction parameter and Eckert number are examined and discussed in detail. The main observations of the present study are as follows.

- (I) An increase in the magnetic parameter is to reduce the velocity profile;
- (II) An increase in the Eckert number increases the temperature profile while it reduces the concentration profile;
- (III) With increasing values of Chemical reaction parameter ( $\gamma$ ) the concentration profile decreases.

## References

- [1] K. Hiemenz. Die Grenzschicht an einem inden gleichförmigen Flüssigkeitsstrom eingetauchten geraden Kreiszylinder. Dingler's Polytech. J. 1911; 326, 321-4.
- [2] T.R. Mahapatra and A.S. Gupta. Heat transfer in stagnation-point flow towards a stretching sheet. Heat Mass Tran. 2002; 38, 517-21.
- [3] T.R. Mahapatra and A.S. Gupta. Stagnation-point flow towards a stretching surface. Can. J. Chem. Eng. 2003; 81, 258-63.
- [4] R. Nazar, N. Amin, D. Filip and I. Pop. Stagnation point flow of a micropolar fluid towards a stretching sheet. Int. J. Nonlinear Mech. 2004; 39, 1227-35.
- [5] Y.Y. Lok, N. Amin and I. Pop. Non-orthogonal stagnation point flow towards a stretching sheet. Int. J. Nonlinear Mech. 2006; 41, 622-7.
- [6] S. Nadeem, A. Hussain and M. Khan. HAM solutions for boundary layer flow in the region of the stagnation point towards a stretching sheet. Comm. Nonlinear Sci. Numer. Simulat. 2010; 15, 47581.
- [7] F. Labropulu, D. Li and I. Pop. Non-orthogonal stagnation-point flow towards a stretching surface in a non-Newtonian fluid with heat transfer. Int. J. Therm. Sci. 2010; 49, 1042-50.
- [8] A. Ishak, Y.Y. Lok and I. Pop. Stagnation-point flow over a shrinking sheet in a micropolar fluid. Chem. Eng. Comm. 2010; 197, 1417-27.
- [9] N. Bachok, A. Ishak and I. Pop. Boundary-layer flow of nanofluid over a moving surface in a flowing fluid. Int. J. Therm. Sci. 2010; 49, 1663-8.

- [10] M. Patel and M.G. Timol. Orthogonal stagnation point flow of a power law fluid towards a stretching surface. *Int. J. Appl. Math. Mech.* 2011; 7, 31-7.
- [11] N. Bachok, A. Ishak and I. Pop. On the stagnation point flow towards a stretching sheet with homogeneous-heterogeneous reactions effects. *Comm. Nonlinear Sci. Numer. Simulat.* 2011; 16, 4296-302.
- [12] S.U.S. Choi, Z-G. Zhang, W. Yu, F.E. Lockwood and E.A. Grullce, *Appl. Phys. Lett.* 79, 2252 (2001).
- [13] E. Magyari and B. Keller, "Heat and mass transfer in the boundary layers on an exponentially stretching continuous surface", *Journal of Physics D*, Vol. 42, no. 5, pp. 577-585, 1999.
- [14] M.K. Partha, P.V.S.N. Murthy, and G.P. Rajasekhar, "Effect of viscous dissipation on the mixed convection heat transfer from an exponentially stretching surface", *Heat and Mass Transfer*, Vol., 11, no. 4, pp. 360-366, 2005.
- [15] M. Shakhaoath Khan, I. Karim, and M. Sirajual Islam, "Possessions of chemical reaction on MHD heat and mass transfer nanofluid flow on a continuously moving surface," *The American Chemical Science Journal*, Vol. 4, no. 3, pp. 401-415, 2014.
- [16] B. Bidin and R. Nazar. Numerical solution of the boundary layer flow over an exponentially stretching sheet with thermal radiation. *Eur. J. Sci. Res.* 2009; 33, 710-7.
- [17] A. Ishak. MHD boundary layer flow due to an exponentially stretching sheet with radiation effect. *Sains Malays.* 2011; 40, 391-5.
- [18] C.H. Chen. Effects of magnetic field and suction or injection on convection heat transfer of nonNewtonian power law fluids past a power law stretched sheet with surface heat flux. *Int. J. Therm. Sci.* 2008; 47, 954-61.
- [19] R.D. Cess. The interaction of thermal radiation with free convection heat transfer. *Int. J. Heat Mass Tran.* 1966; 9, 1269-77.
- [20] F.M. Hady, F.S. Ibrahim, S.M. Abdel-Gaied and M.R. Eid. Radiation effect on viscous flow of a nanofluid and heat transfer over a nonlinearly stretching sheet. *Nanoscale Res. Lett.* 2012; 7, Article ID 229.
- [21] E.I. Aziz, M.A. 2009, "Viscous dissipation effect on mixed convection flow of a micropolar fluid over an exponentially stretching sheet", *Con. J. Phys.* 87: 359-368.
- [22] Partha, M.K. Murthy, P.V.S.N. and Rajasekhar, G.P., 2005: "Effects of viscous dissipation on the mixed convection heat transfer from an exponentially stretching surface". *Heat Mass Transfer* 41: 369-366.
- [23] M.S. Khan, I. Karim, L.E. Ali, and A. Ismail, "Unsteady MHD free convection boundary-layer flow of a nanofluid along a stretching sheet with thermal radiation and viscous dissipation effect," *International Nano Letters*, vol. 2, article 24, 2012.
- [24] M.A. Hamad, I. Pop, and A.I. Ismail, "Magnetic field effects on free convection flow of a nanofluid past a vertical semi-infinite flat plate," *Nonlinear Analysis. Real World Applications*, Vol. 12, no. 3, pp. 1338-1346, 2011.
- [25] K. Jafar, R. Nazar, A. Ishak, and I. Pop, "MHD flow and heat transfer over stretching/shrinking sheets with external magnetic field, viscous dissipation and Joule effect," *The Canadian Journal of Chemical Engineering*, vol. 90, no. 5, pp. 1336-1346.
- [26] M. Ganeswara Reddy, "Influence of the thermal radiation, viscous dissipation and hall current on MHD convection flow over a stretched vertical flat plate," *Ain Shams Engineering Journal*, Vol. 4, no. 1, pp. 169-175, 2011.

[27] K. Vajravelu and A. Hadjinicolaou, “Heat transfer in a viscous fluid over a stretching sheet with viscous dissipation and internal heat generation”, *International Communications in Heat and Mass Transfer*, vol. 20, no. 3, pp. 417-430, 1993.

[28] F.H. Hady, E.S. Ibrahim, S.M. Abdel-Gaied, and M.R. Eid, “Radiation effect on viscous flow of a nanofluid and heat transfer over a nonlinearly stretching sheet”, *Nanoscale Research Letters*, vo. 7, article 229, 2012.

A. Postelnicu, “Influence of chemical reaction on heat and mass transfer by natural convection from vertical surfaces in porous media considering Soret and Dufour effects,” *Heat and Mass Transfer*, vol. 43, no.6, pp. 595-602, 2007.

# Quality Characteristics of Cutting Surfaces in the Milling of the Titanium Alloy Ti10V2Fe3Al

Michael Storchak<sup>1</sup>, Lucas Saxarra<sup>1</sup>, Like Jiang<sup>2</sup>, Yiping Xu<sup>2</sup>, Xun Li<sup>3</sup>

1 – Institute for Machine Tools, University of Stuttgart, Holzgartenstraße 17, 70174 Stuttgart, Germany

2 – Changhe Aircraft Industries Group Limited Corporation, Jingdezhen, 333002, China

3 – School of Mechanical Engineering and Automation, Beihang University, Beijing 100191, China



DOI 10.13140/RG.2.1.4655.1925

**Keywords:** Machining of titanium alloy, surface roughness, microhardness, residual stress, simulation.

**ABSTRACT.** As titanium alloys have unique mechanical properties, the  $\alpha$ -titanium alloy Ti10V2Fe3Al (Ti-1023) is widely used by the aerospace industry, among other things, when producing critical components such as parts of the fuselage and the wings as well as various rotating components due to its extremely high ratio of strength to density, its great resistance to fatigue, its excellent resistance to corrosion and fracture toughness. Within the group of titanium materials, the alloys of the  $\alpha$ -phase are among the materials which are most difficult to machine. In particular, this concerns milling processes widely used in the production of various complicated components. In order to be able to successfully apply the machining process of the titanium alloy Ti-1023, optimum cutting parameters of the tool have to be used, guaranteeing a required machining quality. This paper presents the results of experimental tests into the formation of quality characteristics such as roughness and microhardness as well as residual stresses and their simulation depending on cutting parameters such as cutting speed, feed and radial depth of cut. To analyse more closely how the cutting parameters affect the quality characteristics in milling, the individual dependences of the effects were described in exponential equations. The exponents for the exponential equations were established according to the Gaussian elimination method. The experimental results obtained and the developed FEM cutting models serve as a basis for further optimising the machining processes of titanium alloys.

**Introduction.** Different titanium alloys are used in broad ranges of technology. The  $\alpha$ -titanium alloy Ti10V2Fe3Al (Ti-1023) is widely used by the aerospace industry, among other things, when producing critical components such as parts of the fuselage and the wings as well as various rotating components, due to its extremely high ratio of strength to density, its great resistance to fatigue, its excellent resistance to corrosion and fracture toughness [1]. Thanks to its unique physical-mechanical properties, this titanium alloy is gaining more and more importance besides the  $\alpha+\beta$ -alloy Ti6AlV4, which is commonly used in industry and commerce [2]. Within the group of titanium materials, the alloys of the  $\beta$ -phase are among the materials which are most difficult to machine. Especially material removal is characterised by low cutting speeds, small feeds and short tool lives, depending on the material precipitation condition [3].

These difficulties in the machining of the titanium alloy Ti-1023 have a great effect on guaranteeing the physical-mechanical [4], [5] and the geometrical quality characteristics [6] of the machined components' surface layers. This concerns particularly milling processes commonly used when producing various complicated components [7]. The cutting parameters have the greatest effect on the formation of the quality characteristics in the machining of titanium alloys as well as other materials. This paper presents the results of experimental tests into the formation of quality characteristics such as roughness, microhardness and residual stresses as well their simulation depending on cutting parameters such as cutting speed, feed and radial depth of cut of the milling cutter.

**Test set-up. Milling process.** The experimental analyses of the milling process were conducted on the machining centre Hermle UWF 1202 H. The test set-up for milling is shown in Fig. 1. The

workpiece made out of the titanium alloy Ti-1023 has a dimension of 20 mm □ 20 mm □ 60 mm and is clamped in a six-component dynamometer, type 9129AA, by Kistler by means of a clamping system. It was milled on a rectangular track along the cross-section of the workpiece in four steps with varying real depth of cut  $a_e$  of 0,5 mm, 1,0 mm, 1,5 mm and 2,0 mm (see Fig. 1). A cemented carbide end milling cutter with five teeth, D20R3H30Q90L130 by Widia, was used as tool. The three components of the resultant force  $F_x$ ,  $F_y$  and  $F_z$  as well as the milling moment  $M_z$  around the rotational axis of the milling cutter were measured during machining.

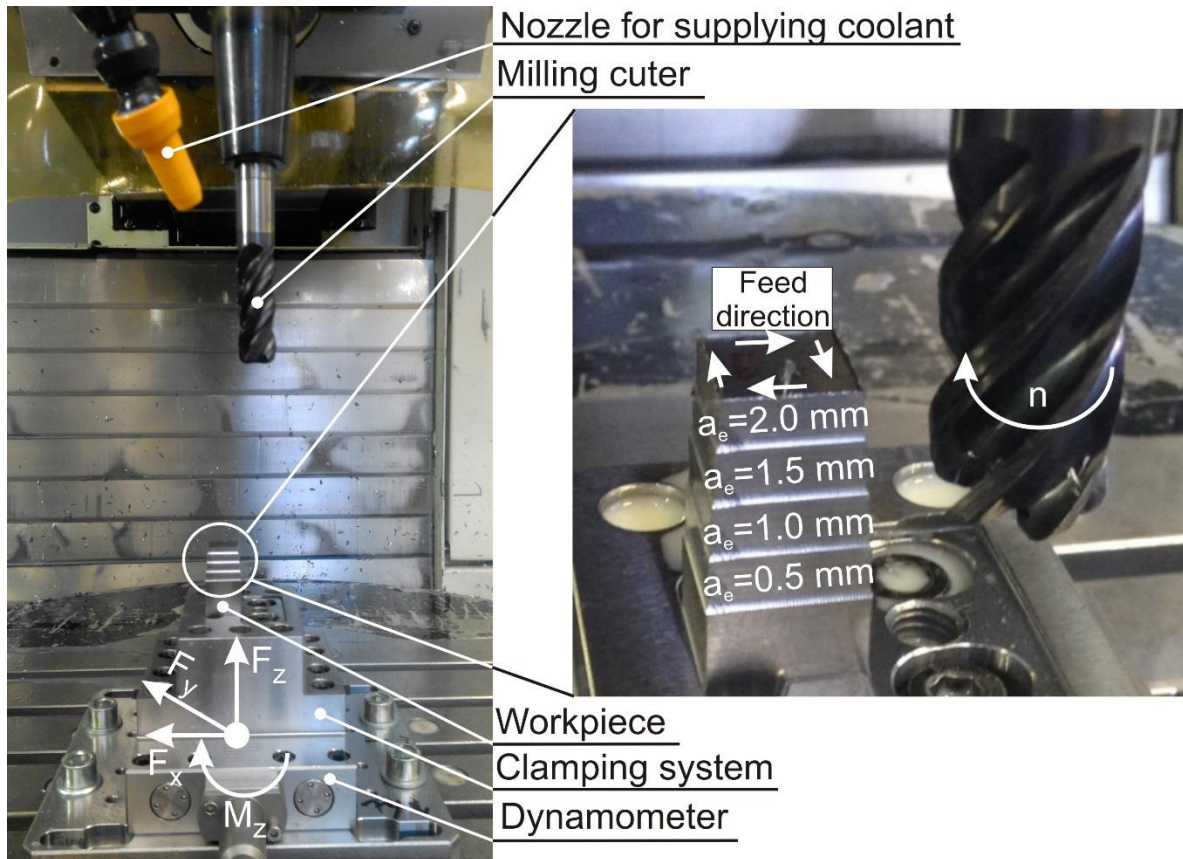


Fig. 1. Test set-up for analysing milling processes

**Surface roughness.** The roughness of machined surfaces was measured with a stylus profiler SV-C3200 by Mitutoyo. The measurements were carried out according to the scheme presented in Fig. 2. For a statistical safeguarding, each milled surface was separately scanned several times lengthwise and crosswise. Then the average of the obtained results was taken. The following parameters were established in the roughness measurements [8]:

- centre line average height –  $R_a$ ;
- average roughness height –  $R_z$ ;
- average depth of surface smoothness –  $R_p$ ;
- height root mean square –  $R_q$ ;
- roughness height –  $R_t$ ;
- average roughness width –  $RS_m$ ;
- material ratio –  $Rmr$ , from which the material ratio curve or rather the Abbott curve was made up to characterise the vertical material distribution of a surface.

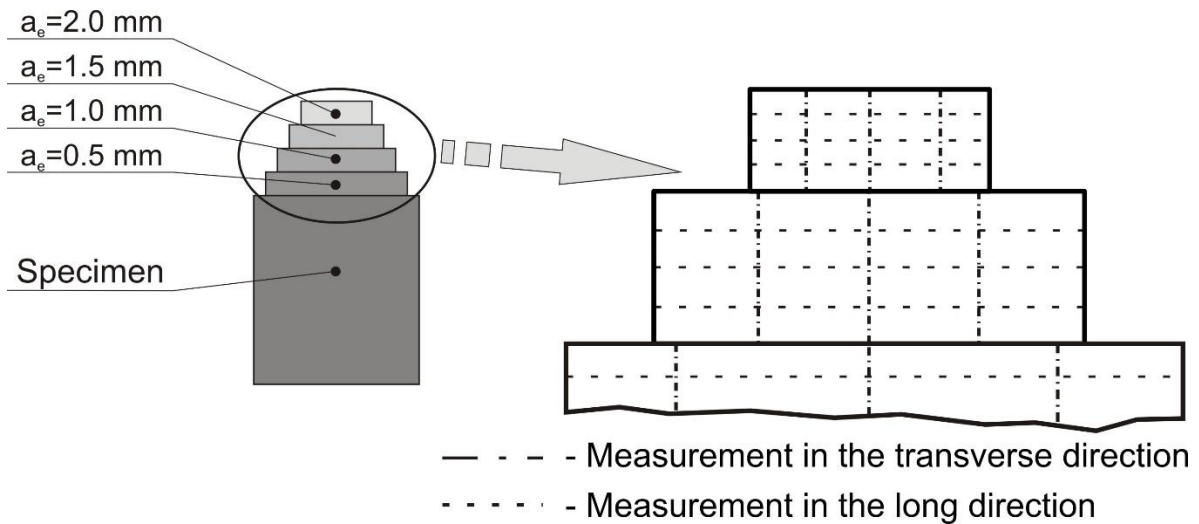


Fig. 2. Scheme of roughness measurement

**Microhardness.** The microhardness was established with the measuring system Picodentor HM500 by Fischer according to DIN EN ISO 14577 - Fig. 3.

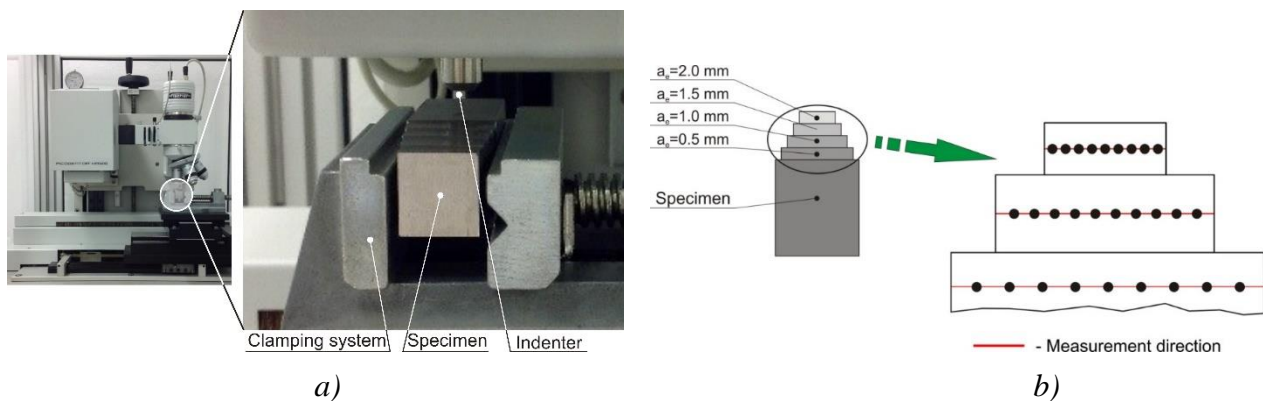


Fig. 3. Set-up (a) and scheme (b) for measuring microhardness

A standardised indenter here is pressed into the microstructure of the test specimen with a predetermined test force [9]. During the entire process, the applied force is recorded with a load cell and the penetration depth arising here is detected with a position-measuring system for each individual test method - Fig. 4.

For guaranteeing the reproducible measuring results, it is necessary at the beginning to define the optimum number of measuring points for each milled surface to be tested. After evaluating the variation coefficient, it showed that an optimum result is achieved with ten measuring points. The maximum test force was 500 mN, the load well time was 20 s and the delay under load was 5 s in the measurements. Not only the Vickers hardness  $HV$ , but also the elastic penetration work  $W_e$ , the plastic penetration work  $W_p$  and the total penetration work  $W_t$  were established in the tests.

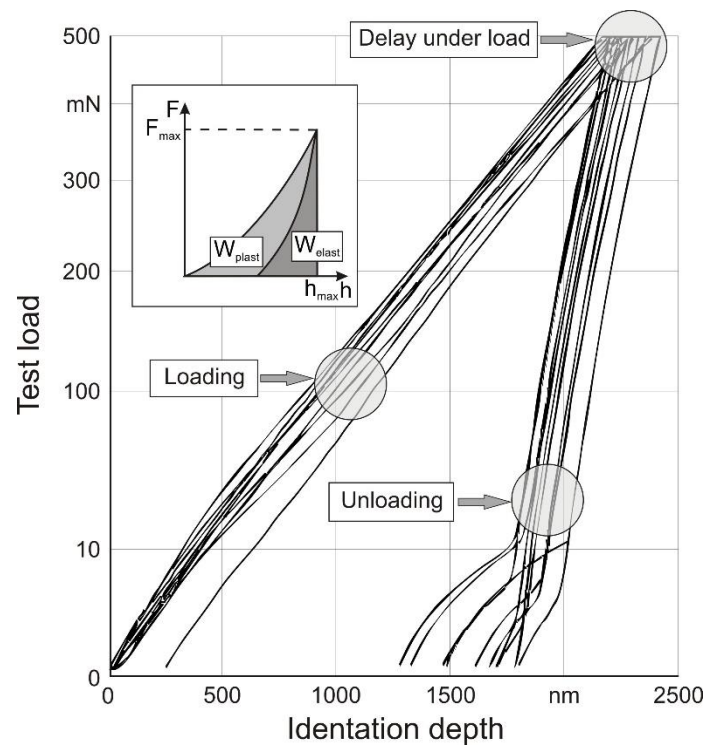


Fig. 4. Curves of indenting load when measuring microhardness

**Residual stress.** The residual stresses were analysed at given positions of the specimens, which were machined at varying cutting parameters and with or without supplying coolant. The cutting method was used for this. Strain gauges of the FLA-3-11 type were centrally mounted onto the machined surfaces, before the specimens were sawed up. The machined surfaces were cut at a distance of 1 mm to the edge of the sample. Afterwards, the strains caused by cutting were determined with a measuring bridge, type P3500 by Micro Measurements Group. The residual stress caused was calculated from the strain difference to the initial condition using a Young's modulus of  $E = 106$  GPa and a Poisson's ratio of  $\mu = 0,36$ .

**Results of milling process analyses.** The cutting parameters of cutting speed  $V_C$ , feed  $f_z$  and radial depth of cut  $a_e$  were varied in the experimental tests regarding the milling process of the titanium alloy Ti-1023. The axial depth of cut was 7 mm in all analyses of the milling process.

The tests were carried out using factorial design of experiments. To be able to detect a definite behaviour of quality characteristics such as the roughness and the microhardness of surface layers in the machining of the titanium alloy Ti-1023 depending on the analysed cutting parameters, such dependences are represented in the form of an exponential equation:

$$Q = C \times V_C^x \times f^y \times a_e^z, \quad (1)$$

where  $Q$  – is the corresponding quality characteristic;

$C$  – is the constant;

$x$ ,  $y$  and  $z$  – are the exponents for the cutting parameters.

Based on the experimental tests of the quality characteristics, the exponents for the exponential equations were established according to the Gaussian elimination method [10]. The analysis of the exponents, presented below, guarantees that a clear effect of the respective cutting parameters on the quality characteristics to be examined can be established.

**Kinetic characteristics.** The three parameters of cutting speed, feed and radial depth of cut were varied in the experimental analyses regarding the milling process of the titanium alloy Ti-1023. Cutting speed was changed in five steps of 30 m/min, 45 m/min, 60 m/min, 90 m/min and 120 m/min. Feed was varied in four steps of 0,06 mm/tooth, 0,08 mm/tooth, 0,1 mm/tooth and 0,12 mm/tooth, and the radial depth of cut was changed in four steps of 0,5 mm, 1,0 mm, 1,5 mm and 2,0 mm.

As an example, Fig. 5 shows how the radial force  $F_x$  (see Fig. 5, a) and the axial force  $F_z$  (see Fig. 5, b) depend on the radial depth of cut of the milling cutter and the cutting speed at a feed  $f_z$  of 0,12 mm/tooth. Both the radial force  $F_x$  and the axial force  $F_z$  increase with growing radial depth of cut. The increase here is proportional to the growing material removal. As cutting speed increases, it can partly be seen that the components of the resultant force rise. This increase does, however, not apply to all analysed values of the cutting parameters and does not maintain its character in the entire examined range.

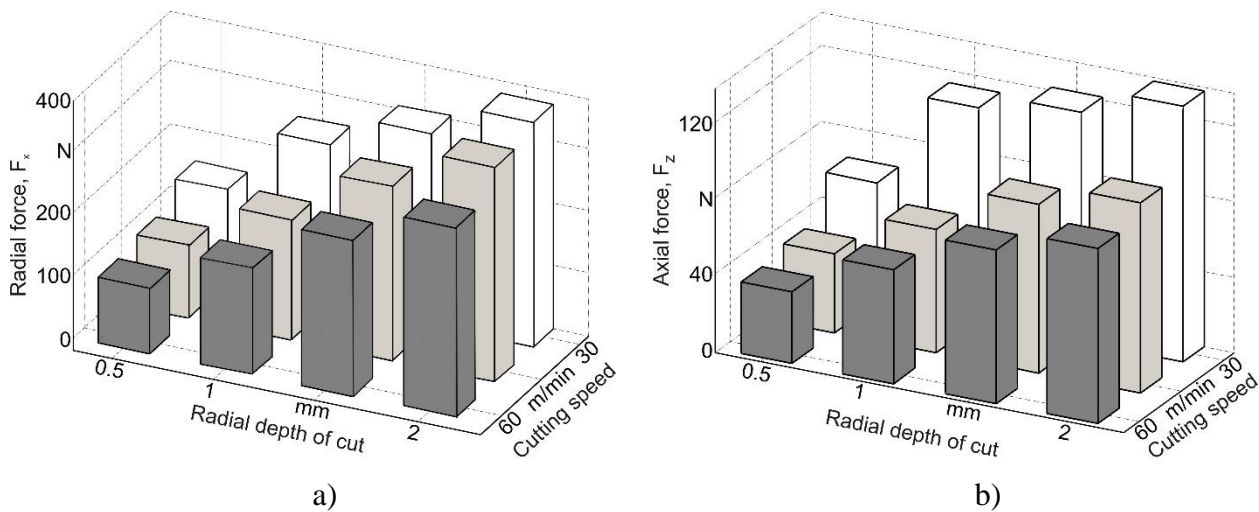


Fig. 5. Dependence of radial  $F_x$  (a) and axial  $F_z$  (b) forces on the radial depth of cut and the cutting speed

Hence, on the basis of the performed tests, it cannot be clearly found that changing the cutting speed affects the kinetic machining characteristics in milling.

**Surface roughness.** As examples, the presented results showed how roughness, namely the height parameters  $R_a$  and  $R_z$  as well as the step parameter  $RS_m$  of the surfaces machined crosswise, depends on the cutting parameters.

Based on all measurements, the exponential equation (2) was made up, enabling an analysis of how the cutting parameters affect the centre line average height  $R_a$  of the machined surfaces:

$$R_a = 35,8 \times V_c^{-0,045} \times f_z^{1,641} \times a_e^{0,038} \text{ } [\mu\text{m}]. \quad (2)$$

According to Equation (2), feed  $f_z$  has the greatest effect on the centre line average height  $R_a$ . As feed increases,  $R_a$  rises here by an exponent of 1,641. The cutting speed and the radial depth of cut of the milling cutter have a considerably smaller effect. Here  $R_a$  decreases slightly with increasing cutting speed and rises slightly with growing radial depth of cut. Fig. 6 illustrates this regularity with a few exceptions by showing how the centre line average height  $R_a$  depends on cutting speed and feed at a radial depth of cut of 2 mm (Fig. 6, a) as well as on cutting speed and the radial depth of cut at a feed of 0,1 mm/tooth (Fig. 6, b).

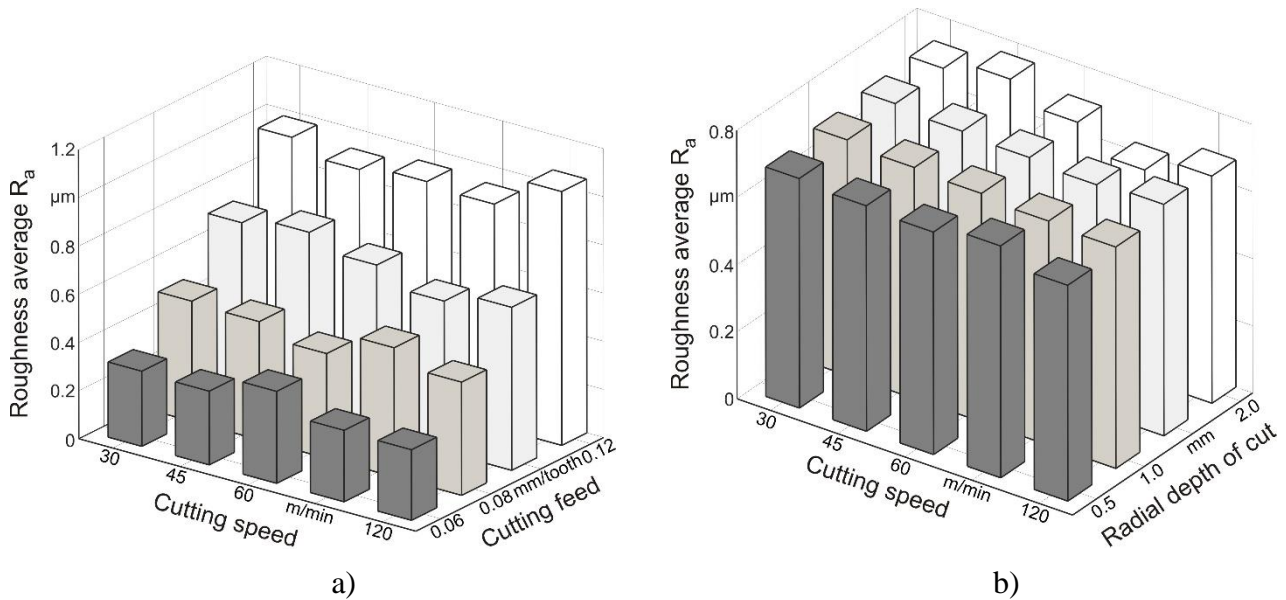


Fig. 6. Centre line average height  $R_a$  depending on cutting speed and feed (a) as well as on cutting speed and radial depth of cut (b)

How the cutting parameters affect the average roughness height  $R_z$  was analysed analogously to the previous case, using equation (3):

$$R_z = 303,4 \times V_C^{-0,042} \times f_z^{1,895} \times a_e^{0,052} [\mu\text{m}]. \quad (3)$$

Here feed also affects  $R_z$  much more than cutting speed and the radial depth of cut of the tool, and this character is maintained like in the previous case. This effect is confirmed by Fig. 7, which illustrates how the average roughness height  $R_z$  depends on cutting speed and feed at a radial depth of cut of 2 mm.

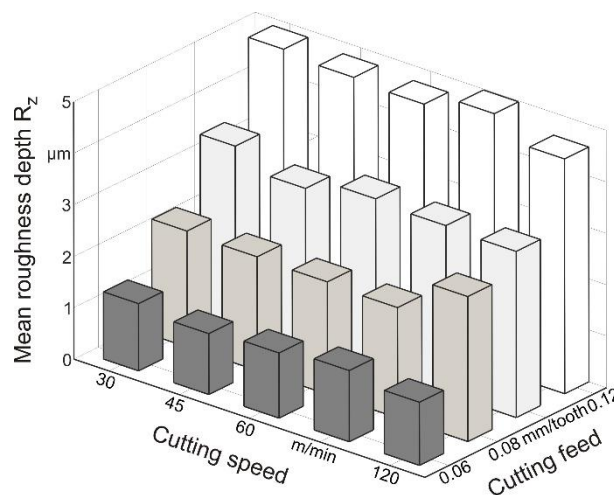


Fig. 7. Average roughness height  $R_z$  depending on cutting speed and feed

Analysing the measured dependences of the average roughness width  $RS_m$  on the varied cutting parameters resulted in the following exponential equation:

$$RS_m = 1,25 \cdot e + 04 \times V_c^{0,124} \times f_z^{1,345} \times a_e^{0,012} [\mu m]. \quad (4)$$

It follows from this equation that feed  $f_z$  has the greatest effect on  $RS_m$  with an exponent of 1,345. The average roughness width here increases with growing feed.  $RS_m$  also increases slightly with rising radial depth of cut and even more with growing cutting speed. Fig. 8 illustrates this dependence, using the variation in cutting speed and feed at a radial depth of cut of 2 mm as an example.

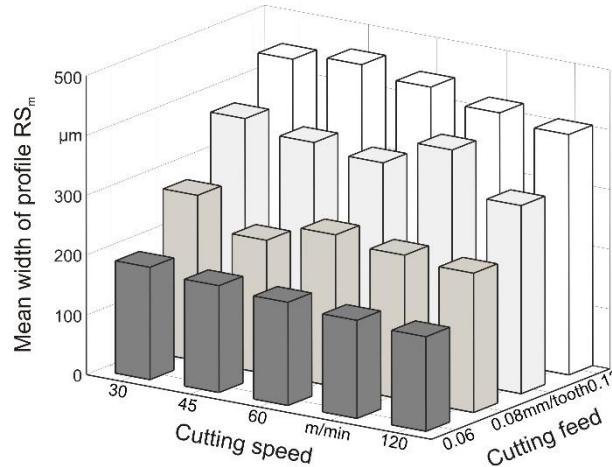


Fig. 8. Average roughness width  $RS_m$  depending on cutting speed and feed

The dependences for other values of the radial depth of cut show a similar behaviour, which corresponds to the established exponential equation (4). It can be noticed here that the values calculated with the exponential equations (2) – (4) are only valid for the analysed range of changes in the cutting parameters. The character of how the cutting parameters affect the roughness of the machined surfaces should, however, be maintained outside the examined range as well.

**Microhardness.** How the analysed cutting parameters affect the microhardness of the machined boundary layers is described with the exponential equations (5), (6) and (7), which were developed owing to the evaluation of all experimental tests performed. Equation (5) here represents how microhardness depends on the examined cutting parameters. Equation (6) describes the elastic penetration work and equation (7) represents the plastic penetration work depending on the examined cutting parameters.

$$HV = 345.1 \times V_c^{0.066} \times f_z^{0.039} \times a_e^{-0.061} [\text{MPa}], \quad (5)$$

$$W_e = 0.0958 \times V_c^{0.029} \times f_z^{0.021} \times a_e^{-0.012} [\mu J], \quad (6)$$

$$W_p = 0.3981 \times V_c^{-0.081} \times f_z^{-0.03} \times a_e^{0.066} [\mu J]. \quad (7)$$

As examples, Fig. 9 illustrates how microhardness depends on cutting speed and the radial depth of cut of the milling cutter at a feed of 0,1 mm/tooth (Fig. 9, a) as well as on cutting speed and feed at a radial depth of cut of 1,5 mm (Fig. 9, b).

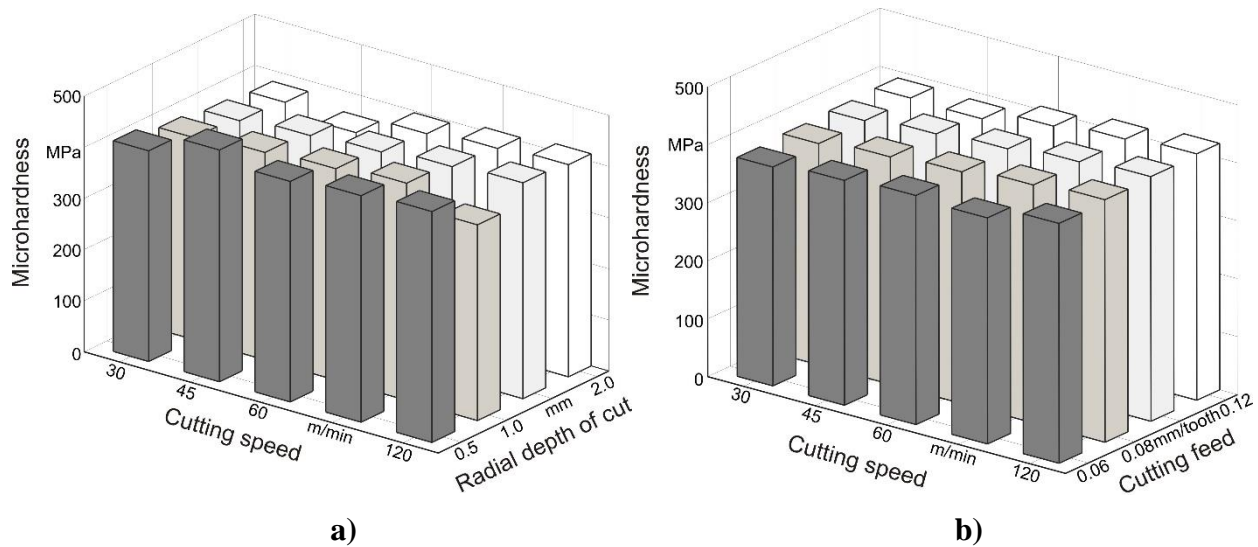


*Fig. 9. Microhardness depending on the radial depth of cut and feed (a) as well as on cutting speed and feed (b)*

The diagrams show that microhardness decreases as a function of the radial depth of cut and increases slightly with growing cutting speed. The analysis of the exponential equations (5) – (7) guarantees further, more precise evaluations of the obtained results. It shows very clearly that microhardness decreases with increasing radial depth of cut. This involves an increase in elastic and plastic penetration work. Furthermore, it can be observed that there is a steady increase in microhardness with growing cutting speed. The elastic penetration work continuously increases then, reaching its maximum at a high cutting speed and a great feed. Although the elastic penetration work rises, the plastic penetration work steadily decreases as cutting speed increases. The growing feed causes a slight increase in microhardness and the plastic penetration work as well as a decrease in the elastic penetration work. At last, it could be detected that the machining direction showed hardly any influence on the surface quality or the microhardness of the boundary layers after a machining process.

When analysing the experimentally determined dependence of the quality characteristics on the cutting parameters, it showed that the character of the dependences reacts very sensitively to the condition of the tool and is considerably influenced by this condition. Hence, these dependences are very strongly influenced by tool wear. This guarantees that the machining quality varies in different stages of the tool's service life. Hence, the same tool differs, for example, in the roughness of the machined workpiece surfaces, in the microhardness of the boundary layers, in residual stress, resultant forces and cutting temperatures, etc. along the whole path length. Fig. 10 shows how the radius of cutting edge rounding and the wear land on the flank face of the wedge vary along the whole path length of the tool. It can be detected that the predominant kind of wear is represented by the breakaways of the cutting edge. At the beginning, these breakaways make up a relatively small part of the cutting edge. However, these breakaways and their proportion are later growing until they are very large at the end of the tool life. Thus the radius of cutting edge rounding, the wear land on the flank face of the wedge and the resultant forces increase considerably at this moment in the tool life. This changes not only the absolute value of the quality characteristics such as roughness and microhardness but also the character of their dependence on the cutting parameters. That is the reason why the wear condition of the tool has to be taken into account in experimental analyses for establishing dependences, so that the tool wear must remain constant during the tests. In the present case, such tests were carried out up to a path length of the milling cutter between 3000 and 3200 mm.

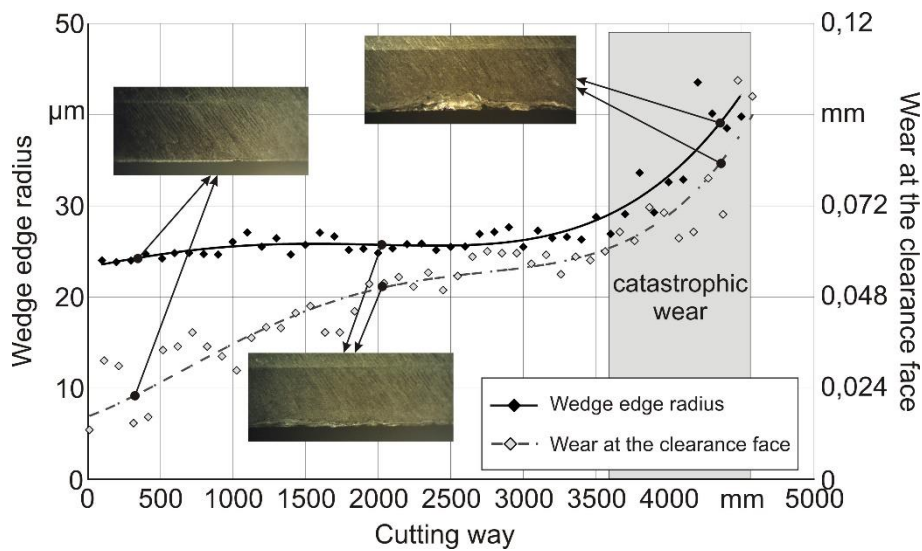


Fig. 10. Wedge edge radius and wear on the flank face depending on the cutting way

**Residual stress.** The residual stress in the boundary layers of the machined specimens was established by experiment and numerically modelled with FEM. Afterwards, the results were compared.

**Experiment.** Fig. 11 illustrates how cutting speed affects dry and wet cutting by cutting feed 0,1 mm/tooth and radial depth of cut 1,5 mm. It can be observed that the residual stress in wet cutting is in the negative range or rather proves itself as compressive stress. The only exception is the machining process at a cutting speed of 120 m/min. That there are compressive stresses after wet cutting can be attributed to the predominant hardening of the machined material. In the machining process with a cutting speed of 120 m/min, the softening of the machined material predominates due to the considerably greater effect of the cutting temperature. Thus, compressive stress is transformed into tensile stress at this cutting speed.

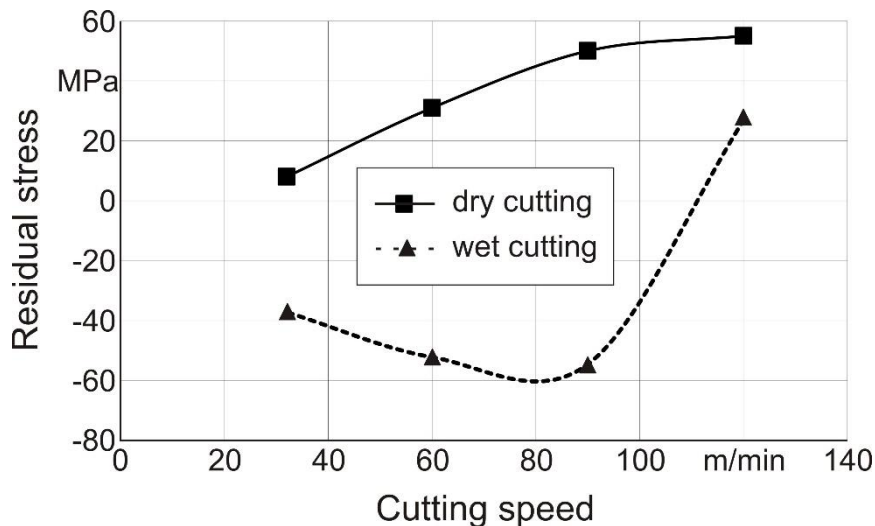


Fig. 11. Residual stress depending on cutting speed in wet and dry cutting

Due to a considerably higher cutting temperature than in wet cutting, the machined material is hardened at all cutting speeds during the machining without supplying coolant. This leads to tensile stresses. Consequently, the residual stresses in dry machining are within the range of tensile stresses for all analysed cutting speeds.

**Simulation.** For the numerical modelling of the residual stresses, FEM models were created for the orthogonal cutting and the milling of the titanium alloy Ti-1023. The commercially available FEA software DEFORM 2D/3D<sup>TM</sup> was used for creating the cutting models [11]. The simulation is based on the implicit Lagrange formulation of networks. It is assumed for both models that the material of the workpiece is isotropic of the elastoplastic type and the material of the tool is absolutely rigid. The material model of the workpiece is represented as a Johnson-Cook model, which is well-acknowledged for the modelling of different cutting processes [12]. The material model of the tool is determined by the model of the software's internal database. The damage mechanism is reproduced with the Cocroft & Latham model in the modelling of the cutting processes [13].

The conditions regarding the thermomechanical interactions of the workpiece with the tool and with itself remained unaltered during the entire simulation in the modelling of all cutting processes. In the modelling of all cutting processes, the friction model in the tool-workpiece contact is assumed to be of the shear type with a constant value of 0,6 and as Coulomb model with a constant value of 0,15 in the contact of the tool with itself.

Fig. 12, a shows the geometry of the FEM model for orthogonal cutting. The figure also presents the geometry of the wedge, the relative positioning and movement of tool and workpiece as well as the boundary conditions used. The boundary conditions are established by fixing workpiece and tool and by giving the thermal conditions at the boundaries of the respective objects. The bottom of the workpiece is rigidly fixed in the X- and Z-directions (see Fig. 12, a). The right-hand side of the tool is rigidly fixed in the Z-direction. The conditions of the room temperature (RT) are given at the bottom and the left-hand side of the workpiece as well as at the left-hand side and the top of the tool. The absolute movement against the X-direction is given to the tool.

The material and fracture model parameters for workpiece were established due to the flow curves obtained by the tensile and compression tests in the examinations with the specimens of the titanium alloy Ti-1023 [14], [15]. In addition, the values for the cutting processes were stated more precisely using the inverse method [16], [17]. For both cutting models, the following values were used as coefficients of the Johnson-Cook model:  $A=976.9$  MPa;  $B=502.3$  MPa;  $C=0.028$ ;  $n=0.22$ ;  $m=1$ . It was assumed here that the critical breaking stress according to the Cocroft&Latham model is 260 MPa. The softening or rather the load-carrying capacity of the elements here was 10% after breaking.

Fig. 12, b presents the geometry of the FEM model for milling. The figure also shows the geometry of the milling cutter, the relative positioning and movement of tool and workpiece as well as the boundary conditions used. The workpiece is rigidly fixed analogously to the FEM model for oblique cutting (see Fig. 12, b). The milling cutter is rigidly fixed in the Z-direction. The thermal conditions of tool and workpiece are given. The absolute rotating motion at a rotational speed  $n$  and the translational movement at a feed speed  $V_f$  against the X-direction are given to the tool.

Fig. 13 depicts the simulation of the residual stresses, showing how stress is distributed in the workpiece in the respective direction. Fig. 13, a presents the simulation of the orthogonal cutting process at the cutting speed 32 m/min and cutting depth 0,3 mm, whereas Fig. 13, b illustrates the simulation of the milling process at the cutting speed 90 m/min, cutting feed 0,1 mm/tooth and radial depth of cut 1,5 mm. The height of the stresses is shown in the scale on the right-hand side.

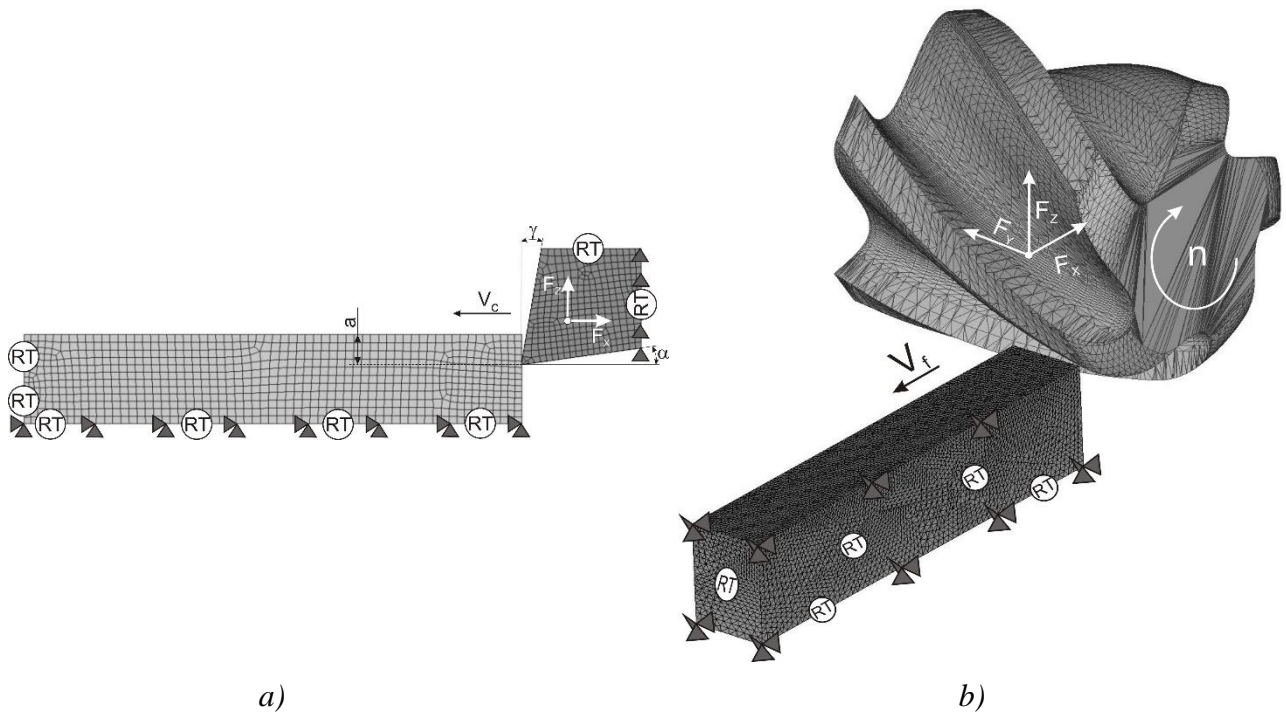


Fig. 12. Initial geometry and boundary conditions of the orthogonal cutting model (a) and of the milling model (b)

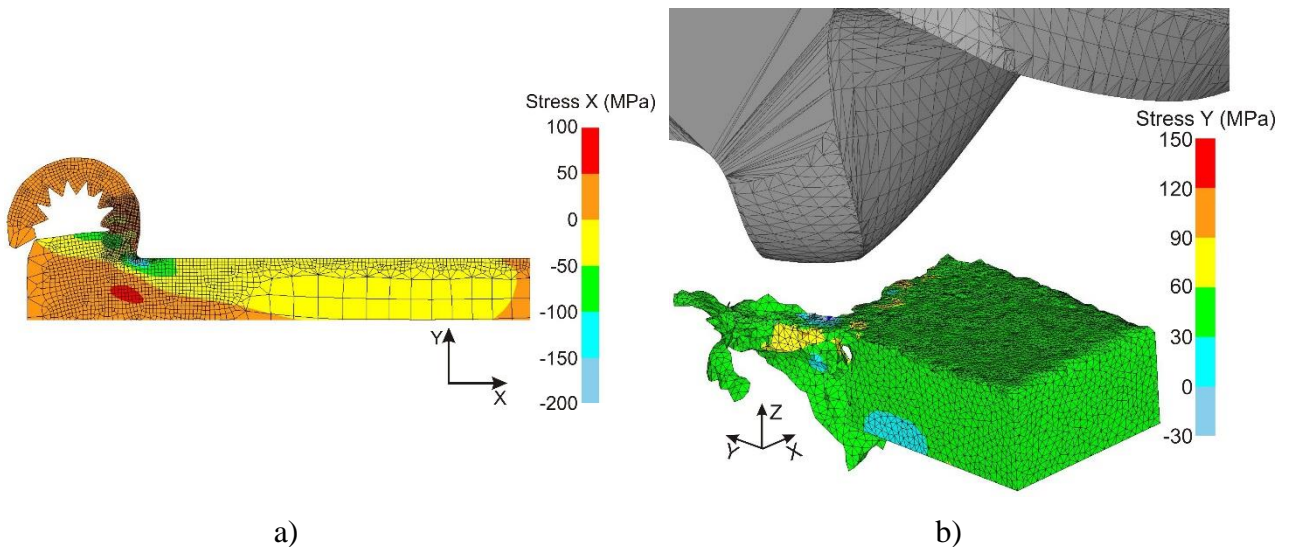


Fig. 13. Simulation of stress distribution in orthogonal cutting (a) and milling (b)

Fig. 14 compares the experimental and the simulated residual stresses when milling at different cutting speeds without supplying coolant. As can be inferred from the figure, the greatest difference between simulated and experimental data was the relative value of 32%.

It will surely be possible to eliminate the error by modelling the thermomechanical interactions in the shear zones as well as the fracture processes more precisely. Finally yet importantly, the mechanical properties of the machined material that are suitable for the cutting process will have to be determined more exactly here.

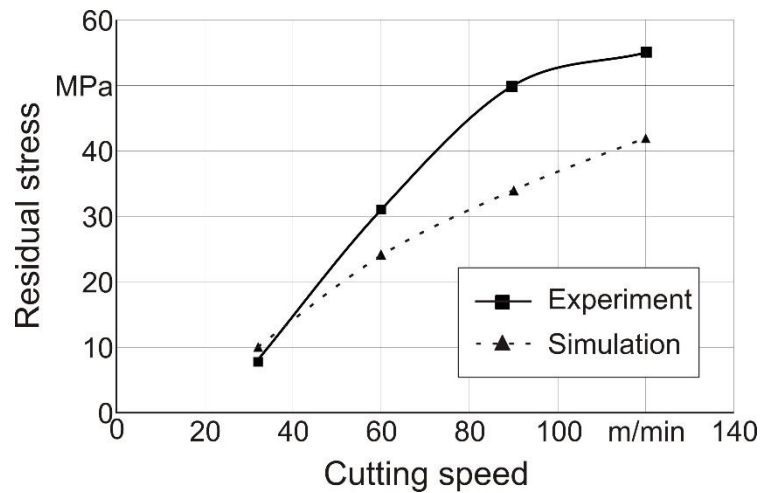


Fig. 14. Comparison between experimental and simulated residual stress in milling

**Summary.** This paper presents the results of experimental tests into the formation of quality characteristics such as roughness and microhardness as well as residual stresses and their simulation depending on cutting parameters such as cutting speed, feed and radial depth of cut.

To analyse more closely how the cutting parameters affect the quality characteristics in the milling of the titanium alloy Ti-1023, the individual dependences of the effects were described in exponential equations. The exponents for the exponential equations were established according to the Gaussian elimination method. The analysis of the exponents guarantees that a clear effect of the respective cutting parameters on the quality characteristics to be examined can be established. The values calculated with the exponential equations are only valid for the analysed range of changes in the cutting parameters. The character of how the cutting parameters affect the quality characteristics of the machined surfaces should, however, be maintained outside the examined range as well.

It was found out that feed  $f_z$  has the greatest effect on the centre line average height  $R_a$ . The cutting speed and the radial depth of cut of the milling cutter have a considerably smaller effect. Here  $R_a$  decreases slightly with increasing cutting speed and rises slightly with growing radial depth of cut. Feed also affects  $R_z$  much more than cutting speed and the radial depth of cut of the tool, and this character is maintained like in the dependences of  $R_a$  on the cutting parameters. When taking the dependences of the average roughness width  $RS_m$  on the changed cutting parameters into account, it could be found that feed  $f_z$  also has the greatest effect on  $RS_m$ . The average roughness width here increases with growing feed.  $RS_m$  also increases slightly with rising radial depth of cut and even more with growing cutting speed.

The microhardness in the boundary layers of milled specimens decreases with increasing radial depth of cut. This involves an increase in elastic and plastic penetration work. Growing cutting speed leads to a steady increase in microhardness. The elastic penetration work continuously increases then, reaching its maximum at a high cutting speed and a great feed. Although the elastic penetration work rises, the plastic penetration work steadily decreases as cutting speed increases. The growing feed causes a slight increase in microhardness and the plastic penetration work as well as a decrease in the elastic penetration work.

Experimental tests of the residual stress in wet cutting showed that it is in the negative range or rather proves itself as compressive stress. The only exception is the machining process at a cutting speed of 120 m/min. Due to a considerably higher cutting temperature than in wet cutting, the machined material is hardened during the machining without supplying coolant. This leads to tensile stresses at all cutting speeds.

The developed FEM cutting models of orthogonal cutting and milling guarantee simulating the residual stress in the machined workpiece. Comparing the simulated and the measured residual

stresses in the machining without supplying coolant shows a satisfactory agreement with a greatest relative error of 32% and confirms that the created FEM cutting models are valid.

The experimental results obtained and the developed FEM cutting models serve as a basis for further optimising the machining processes of titanium alloys.

**Acknowledgements.** The presented results were gained in the project 2013DFB70110, which was funded by the International Science & Technology Cooperation Program of China. The authors would like to thank the Government of the Republic of China for this support, which is highly appreciated.

## References

- [1] Boyer, R., & Briggs, R. (2005). The Use of  $\beta$  Titanium Alloys in the Aerospace Industry. *Journal of Materials Engineering and Performance*, 14(6), 681-685. doi: 10.1361/105994905x75448.
- [2] Biermann, D.; Machai, C. (2010). Die Alternative zu Ti-6Al-4V. *Werkstatt und Betrieb*, 143(4), 56–58.
- [3] Machai, C., & Biermann, D. (2011). Machining of  $\beta$ -titanium-alloy Ti-10V-2Fe-3Al under cryogenic conditions: Cooling with carbon dioxide snow. *Journal of Materials Processing Technology*, 211(6), 1175-1183. doi:10.1016/j.jmatprotec.2011.01.022.
- [4] Yang, H. C., Chen, Z. T., & Jiang, L. K. (2013). Experimental Study on Hardness of Titanium Alloy Ti-1023 by Milling. *AMR Advanced Materials Research*, 690-693, 2446-2449. doi:10.4028/www.scientific.net/amr.690-693.2446.
- [5] Changfeng, Y., Daoxia, W., Liang, T., Junxue, R., Kaining, S., & Zhenchao, Y. (2013). Effects of cutting parameters on surface residual stress and its mechanism in high-speed milling of TB6. *Proceedings of the Institution of Mechanical Engineers, Part B: Journal of Engineering Manufacture*, 227(4), 483-493. doi:10.1177/0954405413475771.
- [6] Houchuan, Y., Zhitong, C., & Zitong, Z. (2014). Influence of cutting speed and tool wear on the surface integrity of the titanium alloy Ti-1023 during milling. *The International Journal of Advanced Manufacturing Technology Int J Adv Manuf Technol*, 78(5-8), 1113-1126. doi:10.1007/s00170-014-6593-x.
- [7] Wagner, V., & Duc, E. (2014). Study of Ti-1023 milling with toroidal tool. *The International Journal of Advanced Manufacturing Technology Int J Adv Manuf Technol*, 75(9-12), 1473-1491. doi:10.1007/s00170-014-6217-5.
- [8] DIN EN ISO 4287. (1997). Geometrical Product Specifications (GPS) - Surface texture: Profile method - Terms, definitions and surface texture parameters.
- [9] DIN EN ISO 14577. (2015). Instrumented indentation test for hardness and materials parameters, 2015.
- [10] Beutelspracher, A. *Lineare Algebra*. (2014). Eine Einführung in die Wissenschaft der Vektoren, Abbildungen und Matrizen. Springer Spektrum, 386.
- [11] Deform-User Manual SFTC-Deform V11.0.2. (2014). Columbus (OH), USA.
- [12] Johnson, G. R.; Cook, W. H. (1983). A constitutive model and data for metals subjected to large strains, high strain and high temperatures. *Proc. 7th Int. Symp. On Ballistics*, The Hague, Netherlands, 541–547.
- [13] Cockroft, M. G.; Latham, D. J. (1968). Ductility and workability of metals. *Journal of the Institute of Metals*, 96, 33–39.
- [14] Robertson, D. G., & Mcshane, H. B. (1998). Analysis of high temperature flow stress of titanium alloys IMI 550 and Ti-10V-2Fe-3Al during isothermal forging. *Materials Science and Technology Mats. Sci. Tech.*, 14(4), 339-345. doi:10.1179/026708398790301403.

- [15] Bao, R., Huang, X., & Cao, C. (2006). Deformation behavior and mechanisms of Ti-1023 alloy. *Transactions of Nonferrous Metals Society of China*, 16(2), 274-280. doi:10.1016/s1003-6326(06)60046-0.
- [16] Shrot, A., & Bäker, M. (2012). Determination of Johnson–Cook parameters from machining simulations. *Computational Materials Science*, 52(1), 298-304. doi:10.1016/j.commatsci.2011.07.035.
- [17] Klocke, F., Lung, D., & Buchkremer, S. (2013). Inverse Identification of the Constitutive Equation of Inconel 718 and AISI 1045 from FE Machining Simulations. *Procedia CIRP*, 8, 212-217. doi:10.1016/j.procir.2013.06.091.

## A Comparison between Dual Phase Steel and Interstitial Free Steel Due To the Springback Effect

E.A. Silva <sup>1</sup>, L.F.V.M. Fernandes <sup>2</sup>, N.A.S. Sampaio <sup>3,4</sup>, R.B. Ribeiro <sup>2,5</sup>, J.W.J. Silva <sup>2,3</sup>,  
M.S. Pereira <sup>1</sup>

1 – Universidade Estadual Paulista – UNESP, Campus de Guaratinguetá, SP, Brazil

2 – Faculdades Integradas Teresa D'Ávila – FATEA, Redes Salesianas, Lorena, SP, Brazil

3 – Associação Educacional Dom Bosco – AEDB, Resende, RJ, Brazil

4 – Universidade do Estado do Rio de Janeiro – UERJ/FAT, Resende, RJ, Brazil

5 – Faculdade de Tecnologia do Estado de São Paulo – FATEC, Cruzeiro, SP, Brazil



DOI 10.13140/RG.2.1.3749.7205

**Keywords:** springback, dual-phase steel, interstitial free steel, aspect ratio.

**ABSTRACT.** This is a study of the springback effect on two kinds of high strength steel, which are: dualphase and interstitial free, currently used as feedstock in the production of vehicles. The mechanical characterization of the springback effect was performed by means of a mechanical conformation test, called three-point air bending, performed by adapting it to the unconstrained cylindrical bending test. It was also evaluated the mechanical properties of the material defined by the tensile test in order to determine its tensile strength, yield strength, and elongation. Furthermore, it was performed a microstructural characterization of advanced steels by identifying and quantifying the present phases in coexistence by means of digital image processing. The results indicate that the springback effect in the dual-phase steel has the highest springback rates due to its high mechanical strength, and it causes a decrease in the aspect ratio of the grains that suffered mechanical conformation attempting to return it to its original form. On the other hand, the springback effect has the lowest rates, and the change in aspect ratio depends only on the interstitial free steel elongation capacity due to its lower mechanical strength.

**1. Introduction.** From the 1950's, there was a concern of the automotive industry to produce steel with high formability and low price, and this influenced in changes in vehicle models. In the 1970's, due to the oil crisis, many countries took serious measures to reduce and rationalize energy consumption. The automobile industry then had to find solutions, bringing developments in aerodynamics and reducing vehicles weight. In addition, in all countries, there can be no growth in the automotive sector without giving due importance to the steel mills [1].

The automobile industry has taken steps such as reducing the size of vehicles, replacement of materials, which are traditionally used for aluminum and plastic, and replacement of carbon steels. As a result, steelmakers aimed primarily to promote the assembly of advanced materials with high strength, ensuring an increased structural integrity, an increased resistance to shock, with a lower cost to the final product [2].

A system sets the conventional high-strength steel (HSS) as those having yield strength between 210 and 550 MPa and tensile strength between 270 and 700 MPa, while the high strength advanced steel (AHSS) has a yield strength that is greater than 550 MPa, and tensile strength greater than 700 MPa [3].

The main difference between the HSS and the AHSS is their microstructure. HSS steels are ferritic-pearlitic, of a single phase. AHSS are steels which mainly contain a microstructure with a different phase than ferrite, for example, martensite, bainite, austenite and/or retained austenite in sufficient quantities to produce their own mechanical properties. However, the widespread use of AHSS in the

automotive industry is limited due to challenges in formability, metal sheet, tool life, and to the springback effect. It is a major problem that compromises the mass production of automotive structural components with AHSS [4].

According Ramezani [5], it is a partially undesirable change occurring in steel sheets as a result of the constraints removal after their conformation process. The two types of steels studied in this work are among the major steels used by automobile industries nowadays because they are high strength steels, being dual-phase steel (DP), which is an AHSS, and interstitial free steel (IF), which is a HSS.

## **2. Experimental procedure.**

**2.1. Metallography before the conformation.** The following metallographic preparation processes are standardized by ASTM ID: E 3-10 (2007). Test specimens were made from DP and IF steels as delivered at the dimensions of 10 mm long, 10 mm wide, 0.8 mm thick.

After sectioning in the longitudinal direction of rolling, the specimens were subjected to hot embedding with bakelite. During the grinding, the following abrasives were used: 220, 320, 400, 600, 1000, and 1200 mesh. The polishing was performed in an OP-U solution and distilled water, subjecting the specimens to a rotation of 600 rpm. The chemical etching was done with a 2% Nital solution to reveal the grain boundaries of ferrite and constituents [6].

The micrographs were obtained using the NIKON optical microscope, model EPIPHOT 200. The image processing was done using the Image J 1.45 software. All images were standardized in the same luminosity conditions and gray shades scale with the use of tools to enhance contrast, normalize and equalize histogram.

**2.2. Mechanical conformation tests.** Test specimens were made from the same material as delivered and sectioned at the following dimensions: 80 mm long, 30 mm wide, and 0.8 mm thick. Such dimensions of the specimens were made according to the parameters defined for the unconstrained cylindrical bending test presented at the Numisheet conference 2002 [7].

The specimens were subjected to a test called the three-point air bending. This experiment was made in adapting the method to the unconstrained cylindrical bending test, in which the specimen is subjected to a punch with the cylindrical body.

The punch had a 5 mm radius and the distance between the supports of the die was 13 mm, according to the ASTM ID: E 290-09 standards to a sample thickness of about 1 mm. The three-point air bending was performed in a universal Shimadzu testing machine, Autograph AG-X, model 50 kN.

The specimens were subjected to conformation until the internal angle of bending reached a predetermined value. The values selected for the internal angle bending were: 30, 60, 90 and 120 degrees, respectively, for each bend, using three replicates for each angle in the same material. The punch was removed from the material 20 seconds after reaching the bending angle, and then, the new bend angle measurement was made to determine whether there was a springback effect or not. For this measurement, it was used the Image J 1.45 software for processing images photographed on an Olympus digital camera. Such measurements continue to be made for a period of 12 h, 24 h, 48 h and 72 h after conformation. Completed the 72 h after the mechanical bending, the resulting bending angle was subtracted from the initial angle of bending which were of 30°, 60°, 90° or 120°, respectively, and this subtraction resulted in a total springback angle ( $\theta_1 + \theta_2$ ), as shown in Figure 1.

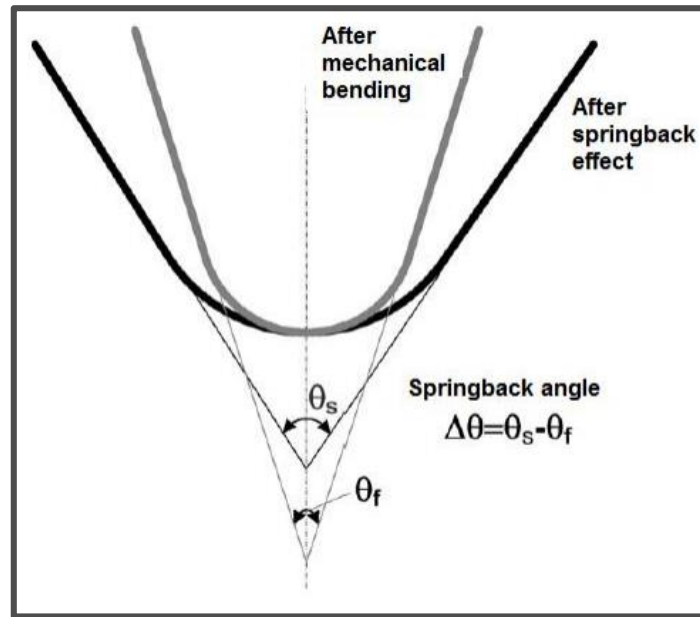


*Fig. 1. Definition of springback angle [8].*

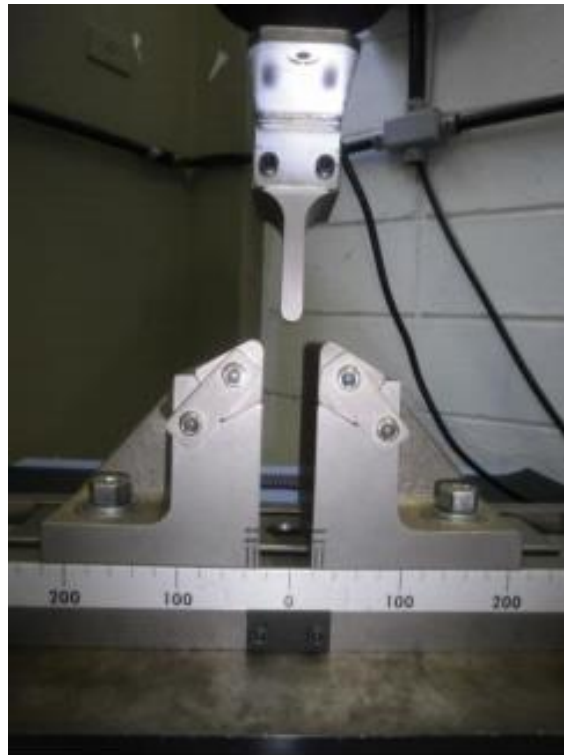


*Fig. 2. Device mounted universal testing machine for testing three-point bending in air.*

**2.3. Metallography after the conformation.** Test specimens were made from materials that were subjected to a mechanical bending test after 72 hours of evaluation at the following dimensions: 10 mm length x 10 mm wide x 0.8 mm thick. The region of the steel plates chosen to obtain the specimens was the one where a curvature was formed due to bending. The specimens were cut in a longitudinal direction, i.e., in the direction of the steel plates lamination by dividing them in the middle. This material was embedded in order to expose its inner surface in order to obtain samples of the region that was deformed during the bending.

The metallographic followed in the same manner as in the pre-conformation test, with the use of hot embedding and polishing, and the chemical etching was made with a 2% Nital solution. The 30 analyzed pictures were for each treatment.

### 3. Results and discussion.

With respect to the mechanical properties, shown in Table 1, they were obtained by tensile tests, extracting the specimens in a transverse direction at 45°, and in the rolling direction of the material. In table I, the tensile strength was designed by RT in MPa, yield strength by LE in MPa, and elongation by Elong in %.

Table 1. Mechanical properties of materials dual-phase steel (DP) and interstitial free steel (IF)

Material	RT (MPa)	LE (MPa)	Along (%)
DP	623.6 ± 2.9	407.3 ± 3.6	23.4 ± 1.4
IF	298.0 ± 2.1	147.9 ± 3.8	40.9 ± 1.9

As shown in Figure 3, the dual-phase steel showed the greatest springback angle (between 7 and 9 degrees), and the interstitial free steel had lower angles (between 4.5 and 6 degrees).

Thus, Figure 3 shows the results that can be compared with W.Gan's work, whereby it was concluded that materials with higher yield strength tend to have greater springback effect, as compared to other materials with lower yield strength [9].

Moreover, as shown in Figure 2, the angular variation of the springback effect was increased from 120° to 30°. This means that as the extent of the internal angle bending was being reduced from 120°, 90°, 60° to 30°, an increase in the springback effect occurred.

According to the dual-phase steel, a decrease in the internal angle bending causes a greater springback effect.

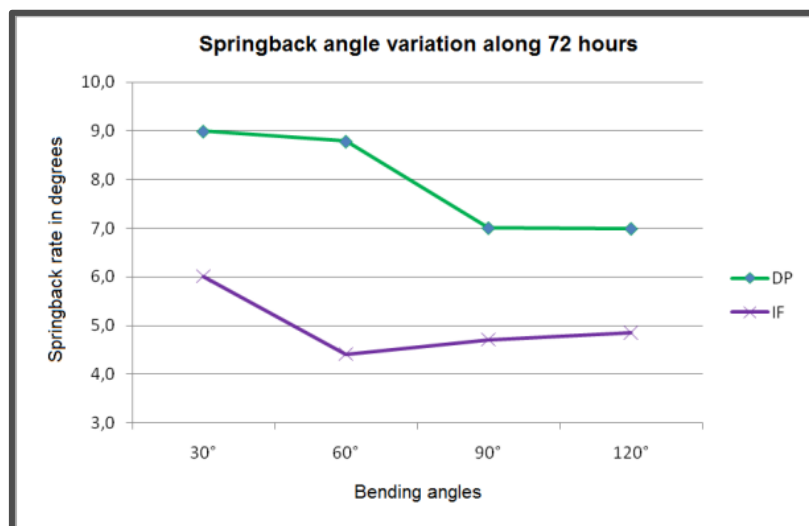


Fig. 3. Angle variation of the springback effect for different bending angles after 72 hours

The ANOVA was used as a statistical tool for interpreting the results. It means a variance analysis, and it is a test of treatment average comparison. It was used a two-factor ANOVA type with repetition, submitted to an F test, at a significance level of 5%.

According to Table II, the time and degree factors significantly influenced the results of springback effect in the dual-phase steel. It can be verified that, according to F Test, - p value was lower than 0.05 which were different from each other in average. The same is not true for the interactions where the - p value is greater than 0.05, indicating that the treatment time and degree did not cause interactions together with the results.

Table 2. Analysis of variance of springback effect to dual-phase steel

Source of variation	SQ	gl	MQ	F	Value-P	F-critic
Time	9.487148	4	2.371787	3.188721	0.023015831	2.605975
Degree	59.80007	3	19.93336	26.79916	1.14078E-09	2.838745
Interactions	1.196571	12	0.099714	0.13406	0.999686828	2.003459
Inside	29.75221	40	0.743805			
Total	100.236	59				

Examining Table III, where an analysis of variance for the aspect ratio is shown, - p value is less than 0.05, thus the variation in the aspect ratio for the dual-phase steel differentiates along the treatment degrees at a significance level of 5%.

Table 3. Analysis of variance of the aspect ratio after 72 hours of the springback effect, considering the four internal angles of bending applied to the dual-phase steel from 30 photos

ANOVA						
Source of variation	SQ	gl	MQ	F	Value-P	F-critic
Among groups	0.03813	4	0.009533	2.631578	0.036708	2.434065
Within groups	0.525241	145	0.003622			
Total	0.563372	149				

An analysis of variance for the interstitial free steel subjected to the springback effect is shown in Table IV which indicates that the difference between the means were significant only for the factor degree, and this is the only one where the - p value is less than 0.05. The time factor and the interactions between time and degree did not have an influence on the springback effect.

Table 4. Analysis of variance of springback effect to interstitial free steel.

Source of variation	SQ	gl	MQ	F	Value-P	F-critic
Time	3.204853	4	0.801213	0.535429	0.710460251	2.605975
Degree	24.25645	3	8.085484	5.403309	0.003232364	2.838745
Interactions	0.260574	12	0.021714	0.014511	0.999999999	2.003459
Inside	59.8558	40	1.496395			
Total	87.57768	59				

Table 5 has an analysis of variance to evaluate the influence of the springback effect in the aspect ratio. It was concluded that this effect caused a significant change in aspect ratio, since the - p value was less than 0.05.

Table 5. Analysis of variance of the aspect ratio after 72 hours of the springback effect, considering the four internal angles of bending applied to the interstitial free steel from 30 photos.

ANOVA						
Source of variation	<i>SQ</i>	<i>gl</i>	<i>MQ</i>	<i>F</i>	Value- <i>P</i>	<i>F-critic</i>
Among groups	3.56368	4	0.89092	2.551933382	0.041591	2.434065
Within groups	50.62177	145	0.349116			
Total	54.18545	149				

As shown in Figure 4, the aspect ratio for the 180° angle refers to the material as delivered before suffering mechanical bending. In this graph, it is seen that the treatment is the most different from the others which was at 120°, thus obtaining a greater aspect ratio. As for the other treatments, the aspect ratio values are closer to the material as delivered.

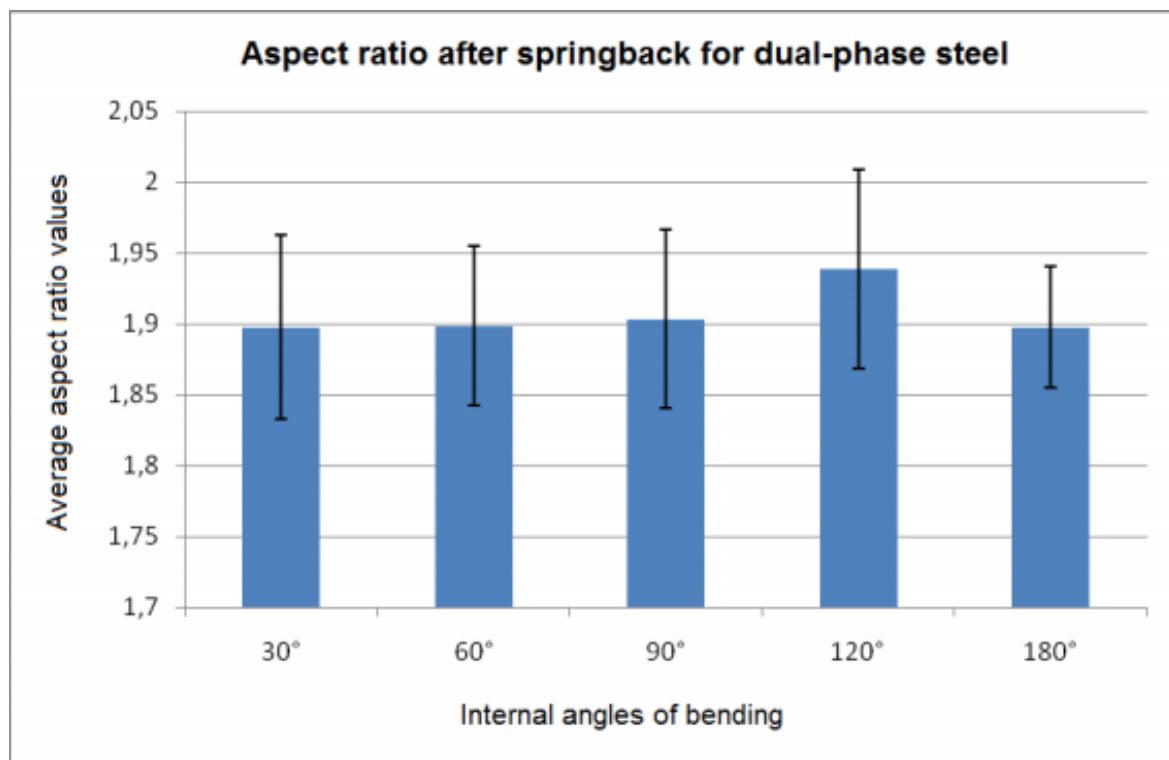


Fig. 4. Average aspect ratio values and their standard deviation of vertical bars 72 hours after removal of constraints obtained from 30 pictures for each internal angle of bend of 30° to 120°, and 180° to material as received.

To view the mechanical influence of the springback effect on the conformation and aspect ratio, it is mounted the graph of Figure 5 from which it is observed that the treatment at 30° was the only one that had the highest mean values of the aspect ratio.

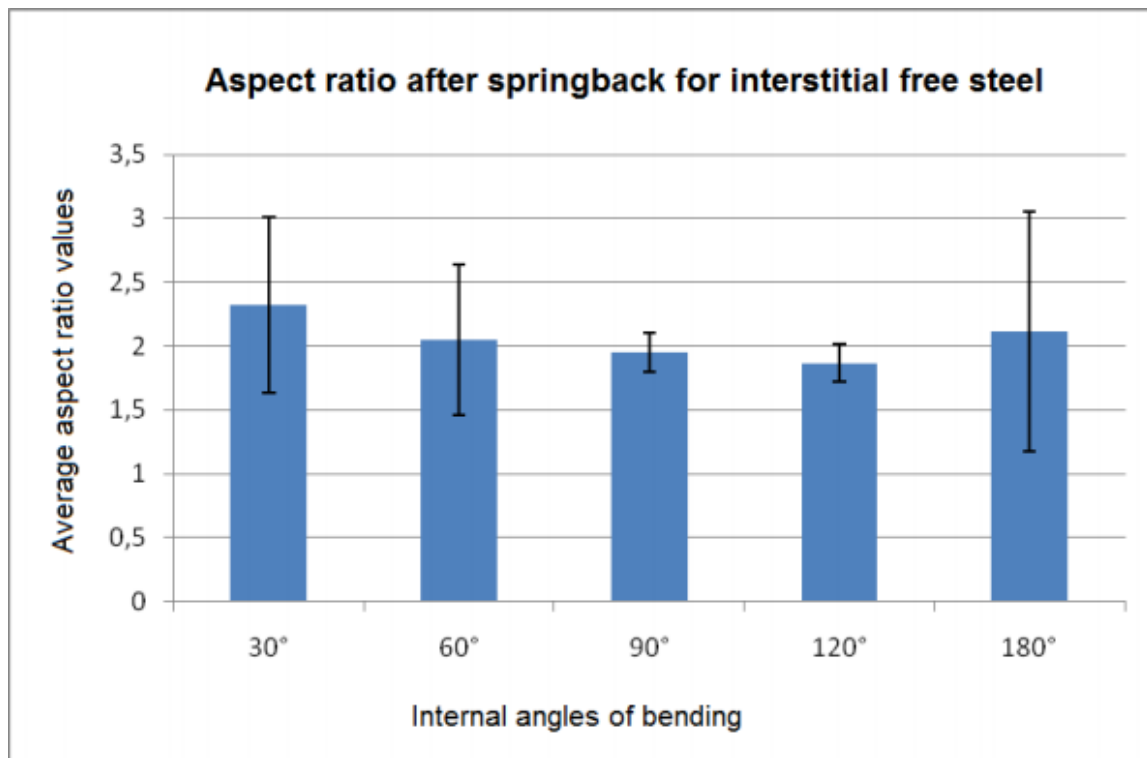


Fig. 5. Average aspect ratio values and their standard deviation of vertical bars 72 hours after removal of constraints obtained from 30 pictures for each internal angle of bend of 30° to 120°, and 180° to material as received.

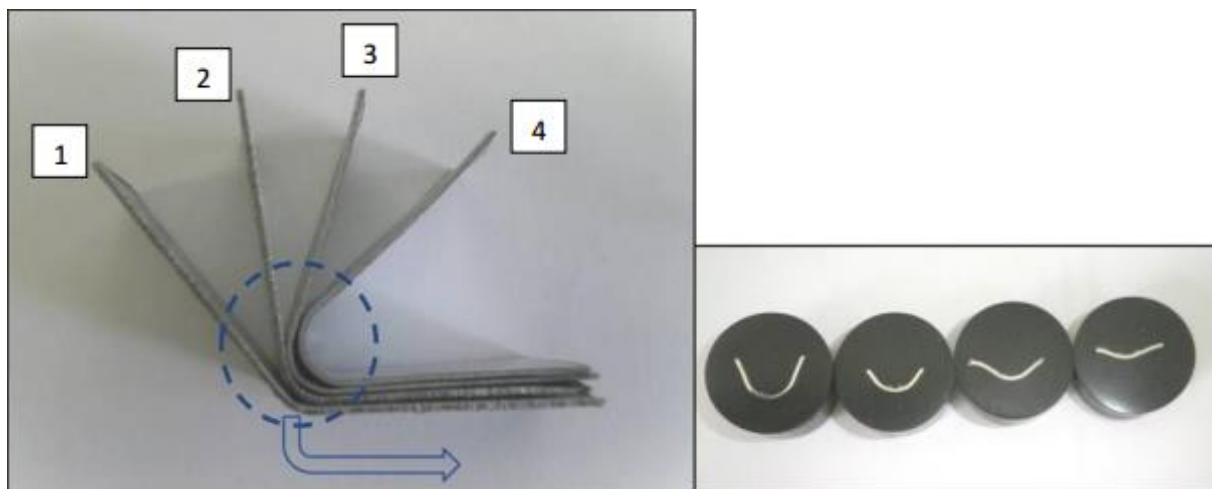
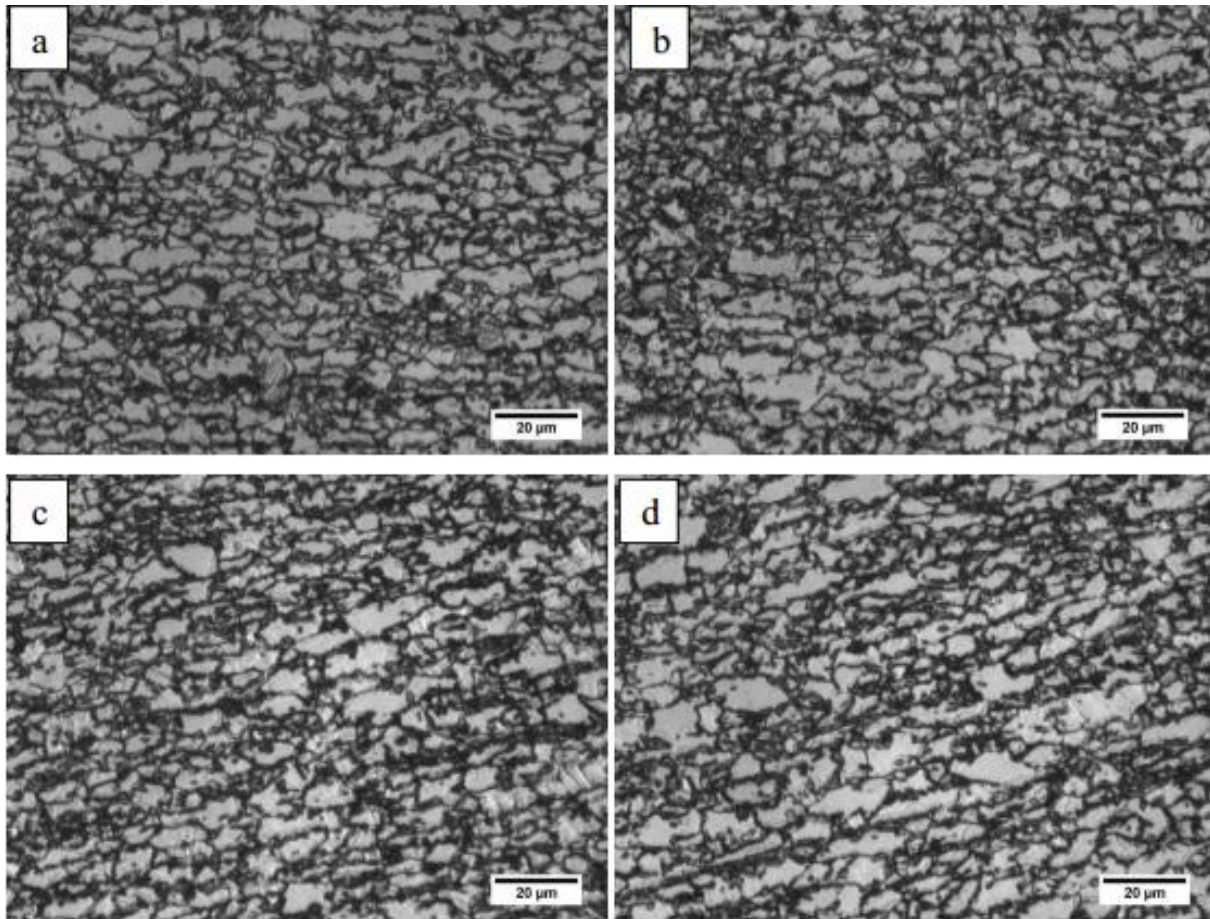


Fig. 6. Samples of sheets, for illustration, already subject to three-point bending in air and subsequent springback effect for 72 hours, where the numbers refer to the values of angles of bending applied, with (1) was 120°, (2) was 90° (3) was 60° and (4) was 30° and the region conformed subjected to the mounting respectively of 30° to 120°.

Figure 7 from (a) to (d) are images of the dual-phase steel microstructure obtained by an optical microscopy. It is observed the presence of martensite microstructure (dark portion) in all images, like islands immersed in the matrix of ferrite (light portion). Images (c) and (d) differ from each other because it is observed the presence of more elongated ferrite grains in its transverse direction. Thus, the material subjected to the treatment at 120° presented the highest aspect ratio.



*Fig. 7. Optical microscopy images dual-phase steel as received and subjected to mechanical bending, where (a) and (b): material as received; (c) and (d): 120°, increase of 500X, reagent Nital 2%.*

In Figure 8 from (a) to (d), which are images of the microstructure of the interstitial free steel, is noted the presence of ferrite microstructure. Images (c) and (d) show more elongated ferrite grains in one direction. These grains have also to be flatter when compared to the images above, and the images obtained from the treatment at 30° have the highest aspect ratio.

An evidence that the variation in the aspect ratio is influenced by the springback effect and not only by the elongation rate of the steel that can be obtained by analyzing the dual-phase steel which presents the lowest elongation rate among the two materials. Thus, if the aspect ratio were influenced only by the elongation rate, all other treatments of bending for this steel would have aspect ratios which are statistically identical to the material as delivered.

However, for the treatment at 120°, its aspect ratio was statistically higher than that of the material as delivered, since this treatment was the one that had the lowest springback effect which was not sufficient to negate the effects of conformation. In all bending treatments, the dual-phase steel lengthened, but the high springback effect of treatments at 90°, 60° and 30° were sufficient to return the grains to their original shapes, resulting in the similar aspect ratios of the material as delivered.

Therefore, in the dual-phase steel, the aspect ratio variation is independent on the elongation rate of the grains because a severe reduction of the internal bending angle causes a high aspect ratio for the mechanical conformation. This aspect ratio decreases after the springback effect, and it increases with a decrease in the internal bending angle due to high yield strength.

By establishing a relationship between the microstructure and the springback effect for the interstitial free steel, it is possible to say that the greatest springback effect occurred in the treatment at 30°, and this treatment had the highest average aspect ratio in its individual grains.

Therefore, it is possible to observe that in the interstitial free steel, the springback effect did not cause a decrease in the grain aspect ratio, as with the dual-phase steel.

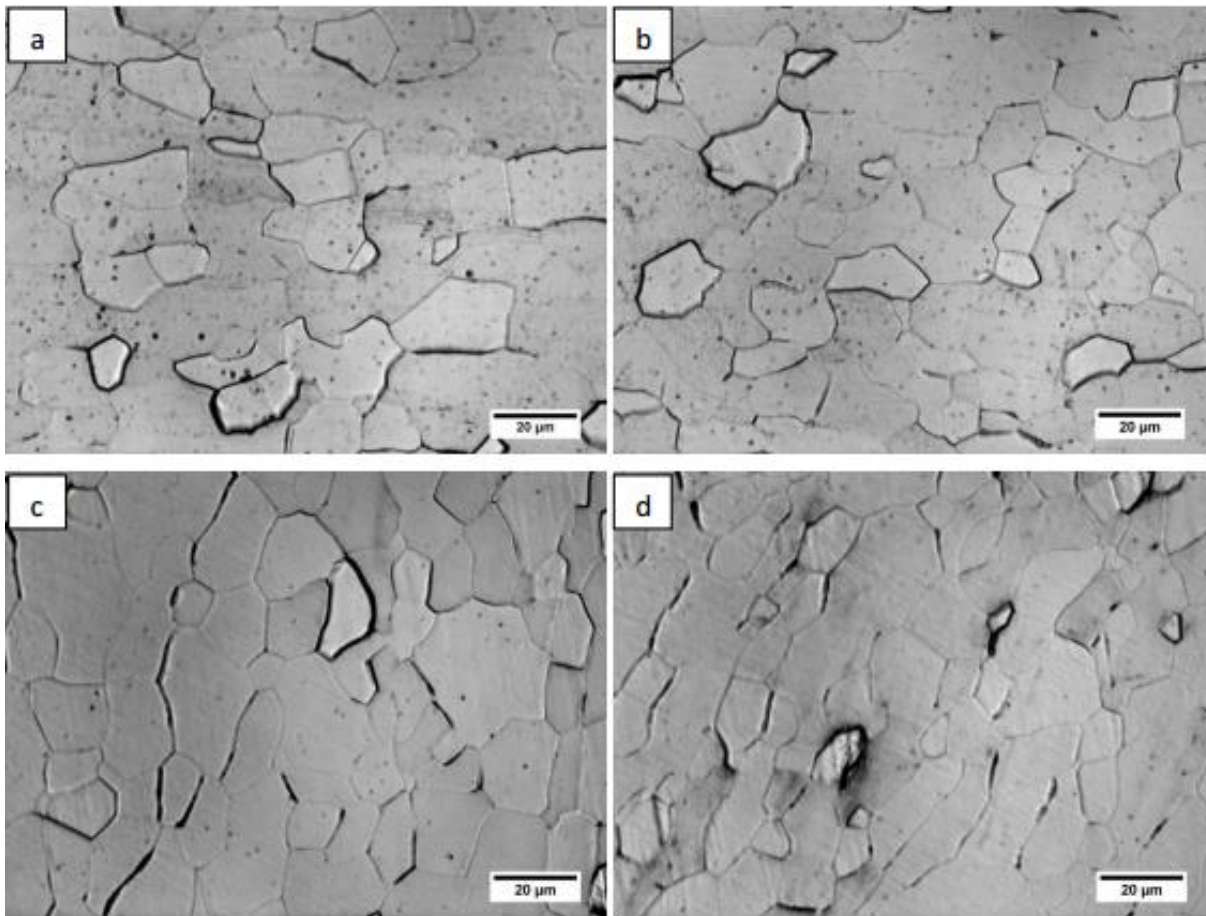


*Fig. 8. Optical microscopy images interstitial free steel as received and subjected to mechanical bending, where (a) and (b): material as received; (c) and (d): 30°, increase of 500X, reagent Nital 2%.*

The interstitial free steel has the lowest limits of yield strength and tensile strength compared to the aforementioned steel. Moreover, it has an elongation rate of 17% which is higher than with the dual-phase steel. Because of a lower mechanical strength of the interstitial free steel in comparison to the previous steel, only during the application of the treatment at 30° which is the acutest internal angle resulted in a significantly different amount of springback effect from the other treatments.

The interstitial free steel is less resistant from the previous one. Its springback effect is less evident, and it can be said that its grains have a lower need for stress relief after the bending when compared with the most resistant steel, and its grains begin to present a greater need to relieve stress only in the acutest internal angles, causing a greater springback effect.

**Summary.** It follows that for the dual-phase steel, more springback effect causes a lower aspect ratio of grains, and a lower springback effect causes a greater aspect ratio of grains which shows that it is a high strength steel. And the opposite occurs for the interstitial free steel with which a greater springback effect accompanied by a greater aspect ratio of grains.

In the dual-phase steel, the aspect ratio is directly proportional to the internal angle of bending. An internal angle decrease increases the springback effect which causes a decrease in the aspect ratio. In this steel, the variation in the aspect ratio depends only on the ability of mechanical resistance.

In the case of the interstitial free steel, the variation of the aspect ratio of their grains is inversely proportional to the internal angle of bending. Thus, the decreasing internal angle increases their aspect ratio. Therefore, for this steel, as opposed to dual-phase steel, the variation of aspect ratio depends on its elongation ability.

**Acknowledgement.** The authors thank the department of materials and technology of FEG/UNESP and research promotion agency called CAPES. The authors would also like to acknowledge the English language review service performed by FDCT – Foundation for Scientific and Technological Development.

## References

- [1] A.L. Nogueira, M.J. Silva, Da carroça ao ultraleve reduction. *Metalurgia & Materials*, vol. 57, n.511, agosto de 2001.
- [2] K. Kishida, High strength steel sheets for light weight vehicle. *Nippon Steel Technical Report*, n.81, p. 12-16, janeiro de 2000.
- [3] S. Keeler, Advanced high strength steel (AHSS) application guidelines. AHSS - World Auto Steel, versão 4.0, 163p., 15 de março de 2009. Disponível em: <[www.worldautosteel.org](http://www.worldautosteel.org)>.
- [4] F. Placidi, R. Vadori, F. Cimolin, F. Campana, An efficient approach to springback compensation for ultra high strength steel structural components for the automotive field. *New Developments*. 2008.
- [5] M. Ramezani, Z. M. Ripin, R. Ahmad, Modelling of kinetic friction in V-bending of ultra high strength steel sheets. *Int J Adv Manuf Technol*, Nibong Tebal, v.46, p.101-110, 2010.
- [6] G. F. Vander Voort, *Metallography, Principles and Practice*. New York: McGraw-Hill, 1999. 752p.
- [7] Numisheet 2002. *Proceedings of the 5th International Conference on Numerical Simulations of 3-D sheet Metal Forming Processes*, D-Y. Yang et al. (eds.), Jeju Island, Korea, 2002. Available at:<[www.numsheet2002.org](http://www.numsheet2002.org)>.
- [8] M. G. Lee, S. J. Kim, R. H. Wagoner, K. Chung, H. Y. Kim, Constitutive modeling for anisotropic/asymmetric hardening behavior of magnesium alloy sheets: Application to sheet springback. *International Journal of Plasticity*. Changwon. v.25, p.70-104, 2009.
- [9] W.Gan, S.S. Babu, N. Kapustka, R. H. Wagoner, Microstructural Effects on the Springback of Advanced High Strength Steel. *Metallurgical and Materials Transactions A*, Columbus, v.37A, p.3221-3231, 2006.

## II. Mechanical Engineering & Physics

M M S E J o u r n a l V o l . 4



## On Application of the Ground Effect For Highspeed Surface Vehicles

Kravets Viktor V.<sup>1</sup>, Kravets Vl.V.<sup>2</sup> & Fedoriachenko S.A.<sup>3, a</sup>

1 – professor, National Mining University, Ukraine

2 – associated professor, Dnepropetrovsk National University of Railway Transport named after Academician V. Lazarian, Ukraine

3 – associated professor, National Mining University, Ukraine

a – [serg.fedoryachenko@gmail.com](mailto:serg.fedoryachenko@gmail.com)



DOI 10.13140/RG.2.1.1034.5365

**Keywords:** ground effect, screen effect, concept, driving efficiency, energy consumption, high-speed motion.

**ABSTRACT.** The paper describes a new approach for driving efficiency estimation. Authors proposed a new approach to assess the energy consumption for vehicle, which are able to reach high speed. Also, there is proposed a new concept of vehicle, which technology based on the ground effect. The concept compounds the automotive and aircraft's solutions in order to reach high driving speed, driving efficiency and low energy consumption per cargo unit. As a result, the defined performance indicators for the transport systems opens up the possibility to formulate and solve optimization problems of structural and parametric synthesis of new types of transport, provide the analytical tools to make informed decisions in the process of design and construction, provide an overall controlled evolution of transport systems.

It is well-known, that the speed range 150-600 km/h for the vehicles of air and ground transport is not developed to its maximum. Therefore, this a gap, which can be filled with a new kind vehicle. Some countries are still working under the idea of such vehicles and are going to develop a new kind, which technical-economic performance and exploitation characteristics will satisfy the market demands.

One of the most perspective kinds of ground transport is well-known in aviation ground-effect craft (Ekranoplane), which technology is based on the ground effect.

Through the years, specialized military institutions were involved in the projects in order to solve sophisticated issues in aerodynamics, strength, safety and exploitation reliability of ground-effect craft. As a result, several ground-effect crafts (GEC) have been designed and produced (Strizh, Volga-2, Lun) (fig. 1).



*Fig. 1. Ground-effect craft Lun*

Such companies as Vehicle Research Corp., General Dynamic, Kawasaki, Lockheed etc, have developed several projects of GEC. There are well-known projects «Columbia», «Aerofoilboat» X-112, X-113, X-114.

To the date, many SMEs worldwide make an effort to develop multifunctional vehicle, which will satisfy the market needs in the niche of such transport. However, those vehicles, the implementation of which has reached the current sample piece or small batch production, pronounced structural features of aircraft and have no specific layout solutions for the automotive structure. This significantly decrease the market prospects of these models. In fact – they are aircrafts, adapted for the auto roads of general purpose, with the performance inherited from the automotive industry, as you can see from the photos, below (Figure 2).



*Fig. 2. GEC prototypes*

For a theoretical study [1-5] for a multifunctional vehicle (MFV) it seems appropriate to start from the classical measures of mechanical motion – the amount of motion, proposed by Descartes and kinetic energy (Leibniz introduced as a "living force") and Helmholtz. It is also known that the increase in speed is the objective tendency for existing terrestrial means of transportation of cargoes and passengers. An integral, averaged vehicle performance indicator can be the amount of energy and its cost value spent per moving mass and speed along the route in the real external disturbances and influence:

$$E_Q = \frac{P \tau}{M L}, \quad (1)$$

where  $P$  – energy (fuel) consumption;

$M$  – average mass of the vehicle;

$L$  – the traversed path;

$\tau$  – the travelling time.

It is obvious, that  $\frac{L}{\tau} = V$  – is the speed of the vehicle. Than:

$$E_Q = \frac{P}{M V}, \quad (2)$$

where  $M V = Q$  – the average amount of motion for the vehicle:

$$E_Q = \frac{P}{Q}. \quad (3)$$

It is known, that widely used easy performance indicator of the vehicle is determined by the formula:

$$E_L = \frac{P}{L} \quad (4)$$

Moreover, it characterizes the power consumption (or fuel) per the travelling distance unit. Then, the connection between input efficiency index and known one will be described as:

$$E_Q = \frac{\tau}{M} E_L. \quad (5)$$

Note, that the performance indicators of the vehicle are dimensional quantities.

It seems reasonable, to provide invariative factor, which links the average kinetic energy  $T = \frac{M V^2}{2}$  and the energy consumption  $P_E$ , that have the same unit:

$$E_T = \frac{P_E}{T}. \quad (6)$$

Thus, it is not difficult to establish a link with the indicators considered earlier  $E_Q$  и  $E_L$ :

$$E_T = 2 \frac{\tau}{L} E_Q, \quad E_T = 2 \frac{\tau^2}{M L} E_L. \quad (7)$$

Thus, a comparative evaluation of the vehicle efficiency is reduced to finding the minimum value of the imposed indicators  $E_L$ ,  $E_Q$ ,  $E_T$ . Note, that a well-known performance indicator  $E_L$  is easy to define, and  $E_T$  – provide an appropriate value. The most important part of the theoretical study to develop a feasible multifunctional vehicle allows combination the characteristics of the aircraft and the car is a factor of driving performance:

$$K = \frac{G}{X}, \quad (8)$$

where  $G = g M$  – the vehicle mass;

$g$  – gravity constant;

$X = c_x q S$  – resistance force;

$c_x$  – resistance coefficient;

$q = \frac{\rho V^2}{2}$  – dynamic pressure;

$\rho$  – atmospheric density;

$S$  – midsection area.

The meaning of the running quality factor is to assess the value of the total weight, carried by the vehicle to the value of the losses associated with energy dissipation in the process of high-speed traffic, i.e., this ratio is analogue of the coefficient of aerodynamic quality for aircraft:

$$K_y = \frac{Y}{X}, \quad (9)$$

where  $Y$  – lift force.

It is known, that increasing the speed of wheeled vehicles more, then 150 km/h arise a complex of physical processes, affecting the comfort and safety of movement. These processes lead to a number of environmental, economic and technical problems, which include:

- Significant investments to alienate territories, construction and operation of a special road surface;
- Overcoming the resistance forces, mainly aerodynamic;
- Smoothness the support surface, the local irregularities in the curvature of the path plan and profile, a small clearance;
- "Vibrating barrier", arising from vibrations caused by irregularities of the supporting surface;
- "Traction barrier" due to decrease of the grip between wheel and supporting surface etc.

It should also take into account, that driver and passengers affected by many disturbing factors be taken into account, registration, assessment and certification of the relevant criteria and indicators. The most important of these factors are dynamic loads (overload), vibration, acoustic vibrations, micro-climatic conditions, etc. Each of them covers a wide range of problems. In particular, the dynamic loads on the power structure or overload affecting a person due to inertial forces at high-speed-controlled movement along a spatial path defined by the support surface and characterized by the curvature in plan and profile, local irregularities, as well as other random factors.

As an illustration, below follows a graphical analysis of a wide range of speeds on the basis of performance indicator  $K$ . The results of these studies are shown in Figure 3, in the form of dependence of the driving characteristics of the operational speed of the vehicle:

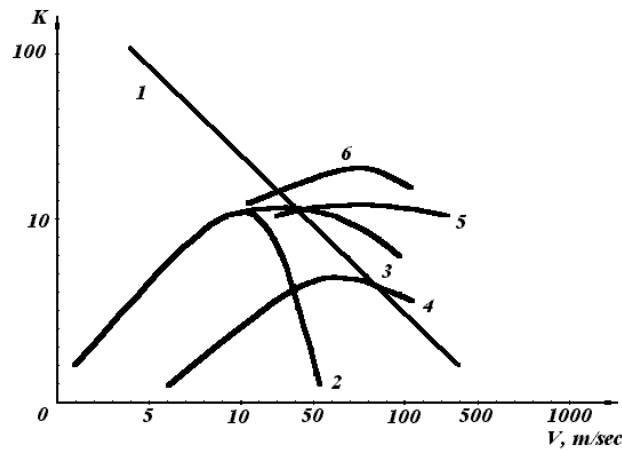


Fig. 3. Graphic curves of the driving performance

As shown on the Fig. 3, factor of driving performance of wheeled vehicles (road, rail) with the increase in speed and decreases monotonically at a speed of 50 m/s does not exceed 10 (curve 1). For example, the maximum driving performance of the helicopter is 7 at a speed 70 m / s (line 4); hydrofoils – 10 at a speed 12 m/s (curve 2); hovercraft – 12 at a rate of 40 to 60 m / s (curve 3), the jet – 15 at a rate of 50 to 500 m/s (curve 5) GEC craft – 40 at a speed of 80 m / s (350 km / h, curve 6).

It should be noted an important feature of the dependences: there is a critical point where the driving characteristics of a wheeled vehicle and GEC matches. This point corresponds to the velocity of 120 km / h and 150 km / h and driving performance coefficient is 20. As follows from this conclusion, there is a necessity to improve research of the GEC craft. A combined transport system can provide stable and high driving quality (20-40), that is not achieved by any known means of transport in the speed range of 150-600 km / h. Creating the proposed combined system of the ground transportation, wholly or partly eliminates the above mentioned technical problems, associated with high-speed movement ("vibrating barrier", "traction barrier" etc.). The support surface for this type of combined transport at high speeds is a combination of conventional pavement, grass or water. Note also the absence of the special road constrictions (bridges etc.) while the motion in the "screen" regime. However, other technical issues might arise at this new technological level. Among these problems are:

- Selection of the optimal aerodynamic shape of the supporting frame, ensuring the highest ground effect and the lowest aerodynamic drag;
- Routing security, stability and control the sub-screen movements;
- Selection of efficient energy sources and ways of its implementation in the operational speed range of 150-600 km / h;

To maintain such vehicle, a dynamical design approach have to used. The vehicle should have efficient aerodynamic shape of the supporting frame. Preliminary proposal of this multifunctional vehicle shown on Fig. 4.

Here, the wedge-shaped body with cross bending is performed to form on top of the discharge surface. Strengthening the screen effect is provided by extension from under the bottom of the unit, which allows increasing the area twice and creates underfloor duct tunnel, which situates a dynamic air cushion when the motion of the device. An additional lift force induces screw propulsion engine. To ensure the manageability and sustainability movement at "sub-screen" regime use airfoils with steering bodies. Resistance movement gives the horizontal wing airfoil, which creates an additional adjustable lift, stabilizing movement and is used to control the formation of forces and moments in the channels of pitch and yaw. Control forces and moments are provided with a front helical boosters, with oncoming traffic screws, placed in the front of the vehicle in a circular nozzle (a gimbal suspension) and two additional engines in the bottom of the body to put forward aerodynamic surfaces. It should be noted, that the screw propeller is most effective at speeds of 200 - 500 km / h, i.e. in the speed range corresponding to the operating mode of GEC craft. To reduce weight, impart

improved aerodynamic shape, strength, processability, surface of the wing-shaped body is made of carbon fiber material, and the lower part and the main structural components are made from light alloys.

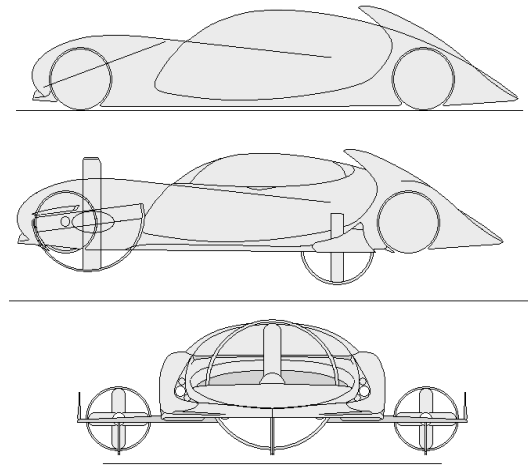


Fig. 4. The main lines of the frame and engines

Taking into account the psycho-physiological abilities of the person, management and routing movement of the vehicle on the movement speeds of over 200 km/h orientation and stabilization systems might be used.

**Summary.** Thus, the search for universal performance indicators (objective functions) transport systems opens up the possibility of formulating and solving optimization problems of structural and parametric synthesis of new types of transport, provides the analytical tools to make substantiated decisions in the process of design and construction, providing an overall controlled evolution of transport systems.

## References

- [1] Kravets V.V., Kravets T.V., *On estimation of the centrifugal, Coriolis and gyroscopic forces in high-speed movement of the train crew*, Applied Mechanics, 2008, Vol.44, pp. 123-132.
- [2] Jian-lin Qian, Chin Dai, *Unsteady flow structure of an airfoil in ground effect*, Journal of Shanghai University, June 2010, Volume 14, Issue 3, pp 228-234.
- [3] Yang Zhigang, Yang Wei, *Complex Flow for Wing-in-ground Effect Craft with Power Augmented Ram Engine in Cruise*, Chinese Journal of Aeronautics 23 (2010) pp.1-8
- [4] Rozhdestvensky K. V. *Wing-in-ground effect vehicles*. Progress in Aerospace Sciences 2006 ; 42 (3): pp. 211-283.
- [5] Yun, Liang, Alan Bliault, and Johnny Doo. *GEC Craft and Ekranoplan: Ground Effect Craft Technology*. New York: Springer, 2010. Internet resource.

# On the Comparison Between the Approximate And Precise Methods of Piled Raft Foundation Analysis

Abbasali Taghavi Ghalesari

1 – Department of Civil Engineering, Babol Noshirvani University of Technology, Babol, Iran



DOI 10.13140/RG.2.1.5128.7446

**Keywords:** piled raft foundation, soil-structure interaction, 3D FE method, approximate method.

**ABSTRACT.** Use of raft foundation to support heavy and tall building may provide the overall safety factor against design loads but the average and differential settlement could exceed the allowable value. On the other hand, utilizing pile group may be an expensive option. In this situation, use of composite pile group and raft foundation that called “Piled Raft Foundation” seems a suitable choice. This foundation is a composite geotechnical system of three bearing components: raft, pile group and soil. The applied load on the raft is transferred to the underlying soil by the contribution of raft and piles. Therefore, considering the interaction effect between the components is essential. It causes some complexities in predicting the behavior of piled rafts. Thus, on this basis, so many different methods were developed. In this study, a comparison between these different methods including approximate and precise methods are presented. Based on the results, a three-dimensional finite element analysis gives perfectly satisfactory results in the prediction of bearing and settlement behavior of piled rafts.

**Introduction.** In recent years, piled raft foundations have been widely used in practice to support heavy and high-rise buildings due to weight and rigidity of the superstructure. When a raft foundation provides the required bearing capacity but the settlement values exceed the allowable limits, an addition of fewer piles in comparison with pile groups could improve the settlement behaviour of the foundation.

The expression of piled raft foundations is in no manner new and has been explained by several authors, including Zeevaert [1], Davis and Poulos [2], Hooper [3], Sommer et al. [4] and Franke [5], among many others.

The mechanism of load transmission in piled raft foundation is so complicated. Thus, different methods from simplified methods to more rigorous methods were developed. In addition to laboratory tests and field studies such as centrifuge test, shaking table test and full-scale modelling, several empirical, analytical and numerical methods have been presented to predict the behaviour of piled rafts under static vertical to dynamic loads. A comparison between the results of different methods of piled raft analysis through some examples is considered in this study. The results of these methods were compared with the results of three-dimensional finite element method as a precise solution. The 3D FE method is capable for considering the interaction effect of the piled raft components.

## Analysis methods.

**Approximation methods.** Hongladaromp et al. [6] presented an approach that considered the soil as an elastic continuum, the raft as a thin plate and the piles as springs. In this method, the interaction effects between the piles were ignored. Poulos [7] presented a program, GARP, based on finite difference method with the consideration of pile-raft interaction. The piles were allowed to reach their ultimate bearing capacities and a local bearing failure was allowed for the raft. A similar method was employed by Russo [8] which the piles and raft were modelled by a series of springs. Boussinesq’s solution was used to calculate the soil displacements. For a single pile, load-settlement curve was assumed hyperbolic to consider the non-linearity of piles. Kitiyodom and Matsumoto [9] presented a method where the piles were modelled by elastic beam elements and the interaction between the

structural elements was estimated by Mindlin's solutions. The lateral and vertical resistances of piles were incorporated in this method. Poulos [10] presented program GASP where the raft was modelled by a strip and piles and soil by springs. Four different interactions between the pile and raft were considered.

**Simplified methods.** Poulos and Davis [11] presented an approach that can be adopted to estimate the load-settlement behaviour. This method is extended by Randolph [12] to estimate the load bearing of piles and raft. The Poulos-Davis-Randolph (PDR) method involves with the stiffness of pile group and raft. The pile-raft interaction factor,  $\alpha_{cp}$  and the load carried by the piles,  $P_{up}$  was computed. By using these factors and programming in mathematical program MATHCAD, a tri-linear load-settlement curve was developed and the calculation of average settlements and pile capacity mobilization was performed.

When the raft satisfies the bearing requirements, piles as settlement reducer are designed. On this basis, Burland [13] developed a step-by-step method to calculate the settlement and bending moment of piled raft.

**Boundary element method.** The boundary element method is based on the discretization of the pile-raft system boundary. Thus, the set of equations to be solved have been decreased. In this method, the partial differential equations are transformed to integral equations. This method is employed by Butterfield and Banerjee [14] to investigate the behaviour of pile group with a rigid cap embedded in an elastic half-space. The interaction effect and soil response were considered by using Mindlin's solution. Franke et al [15] used boundary element method to study the behaviour of piled rafts in high-rise buildings resting on the Frankfurt clay. They also performed a field study on the behavior of these foundations and the measurement of the foundation settlements was presented. El-Mossallamy [16] applied the program GAPR based on the boundary element method to study the behaviour of piled raft foundation in some cases.

**Finite element method.** The finite element method has become a popular and powerful method for studying the behaviour of piled raft foundation due to its realistic results. In this method, both the foundation components and soil should be discretized. Some simplifications such as plane strain and axisymmetric assumptions were made to reduce the computational attempts. One of the first studies using this method was presented by Hooper [3] for the analysis of Hyde Park Barracks. An axisymmetric model is used and the equivalent stiffness is introduced to consider the effect of superstructure stiffening effect. A step-by-step analysis based on this method was presented by Katzenbach and Reul [16], in which the piles were modelled by 3D isoparametric elements and the raft was modelled by shell elements. Prakoso and Kulhawy [18] used finite element program PLAXIS to investigate the piled raft performance with a plane strain model. The analyses include linear elastic and non-linear elastoplastic models. Recently, several authors [19-23] used 3D FE method to study the behaviour of piled raft foundation in different conditions.

**Combined boundary element and finite element method.** In this method, the finite element method for the analysis of the raft is combined with the boundary element method for the analysis of the piles and soil. One example of this method is the study of Poulos et al [24] using elastic-plastic model by combined boundary element and finite element method in some case histories.

**Variational method.** The principle of minimum potential energy is used in this method to analyse the foundation. The interface of raft and soil is the only parts to be discretized. Chow et al. [25] used this method for the analysis of vertically loaded piled raft foundation. The raft was modelled by a thin plate and the pile group was represented by a finite series. The elastic-perfectly plastic behaviour of pile and soil were assumed.

## **Numerical analysis**

**Finite element mesh and boundary condition.** In this paper, in order to compare the results of above-mentioned methods with the three-dimensional finite element method, the behaviour of the

piled raft was investigated by carrying out 3D numerical analyses. The soil and structural elements were discretized to 8-node linear elements. Figure 1 shows a typical finite element mesh used for comparison. Due to load and geometry symmetry, only one-quarter of the problem was modelled. Two symmetric plane and two horizontal fixities were used at lateral boundaries. The base of the model is constrained against translation in three directions. The geostatic stresses were produced to simulate the in-situ condition. Then, a uniform load is applied over the raft area. The long-term response of the soil is considered and so drained effective parameters of the soil were applied.

**Constitutive Modelling.** In this study, Mohr-Coulomb model was used to simulate the soil condition due to its simple and quick responses. In all analyses, average (constant) values of material properties were used for the soil. The structural elements of foundation were modelled with a linear elastic model because they have a great modulus of elasticity in comparison with the soil. At the pile-raft interface, thin-layer elements with the properties of soil material were used. The thickness of these elements were  $0.1D$  ( $D$ =pile diameter) and a slip behaviour between them was assumed.

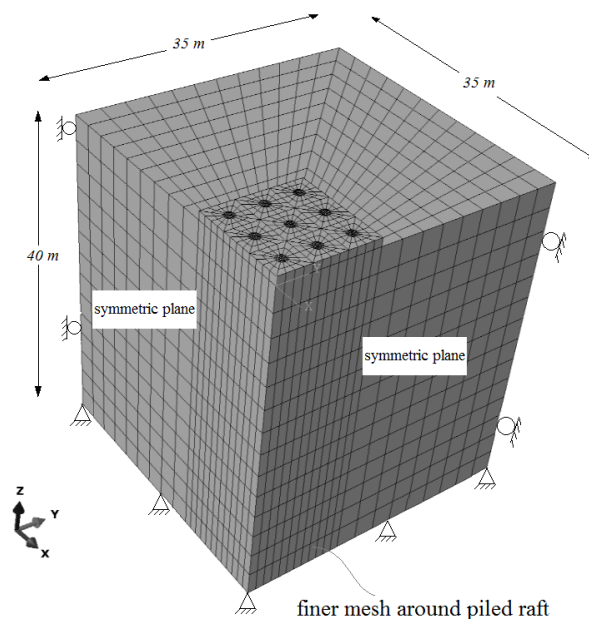


*Fig. 1. Typical Finite Element mesh used for the numerical method.*

**Comparative results and discussion.** In order to investigate the above-mentioned methods and to compare the results of these methods, three typical examples were analyzed and the efficiency of these methods was evaluated.

The geometry and material properties used in the first example are shown in Table 1. This example is based on the study of Chow et al. [25] based on a variational method. A  $3 \times 3$  pile group with the length of 20 m was under a square raft with the 6 m width and 0.5 m thickness. The soil is considered as a linear elastic material. The results of these two methods were presented in Table 2.

Table 1. Geometry and material properties of the first example.

<b>Pile</b>	Young's Modulus ( $E_p$ )	35000 MPa
	Length (L)	20 m
	Radius ( $r_0$ )	0.4
	Spacing (S)	2 m
<b>Raft</b>	Young's Modulus ( $E_r$ )	35000 MPa
	Poisson's ratio ( $\nu_r$ )	0.3
	Thickness ( $t_r$ )	0.5 m
	Width ( $B_r$ )	6 m
<b>Soil</b>	Young's Modulus ( $E_s$ )	280 MPa
	Poisson's ratio ( $\nu_s$ )	0.4
<b>Arrangement</b>	$3 \times 3$	

Table 2. Comparison of the results for the first example.

	$S_{avg}$ (mm)	Pile Load (%)
Chow et al. [25]	8.02	75
Present study	8.16	79

The second example contains a  $5 \times 5$  pile group with a square raft of 27 m width and 2 m thickness. The piles had 30 m length and were embedded in clay soil. The geometry of this case is shown in Figure 2.

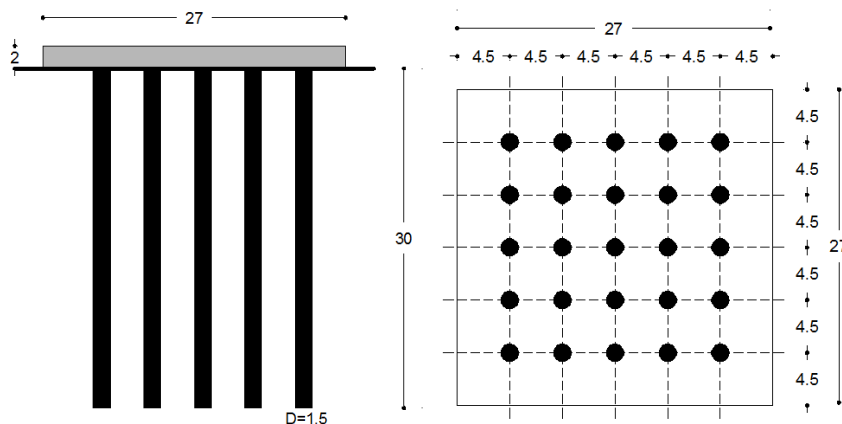


Fig. 2. The geometry of considered case in the second example.

This example had been analyzed by Poulos [7] (GARP program) and El-Mossallamy [16] (boundary element method). A comparison between the results of these analyses with 3D FE method presented in this study for raft, pile group and piled raft is shown in Figure 3. A good agreement between the results of different methods can be recognized. This agreement exists up to reaching the ultimate capacity of pile group. The ultimate pile group capacity, in this case, is defined as a summation of the ultimate capacities of the individual piles. The curves related to 3D FE method and boundary element method are approaching but they are larger than the simplified method. This is due to increasing the horizontal effective stresses around the piles caused by the contribution of the raft contact and hence

increasing the piles ultimate capacity. There is an agreement between the results of boundary element and the simplified methods in the high load ranges. In this case, finite element method underestimates the piled raft capacity and tends to be conservative.

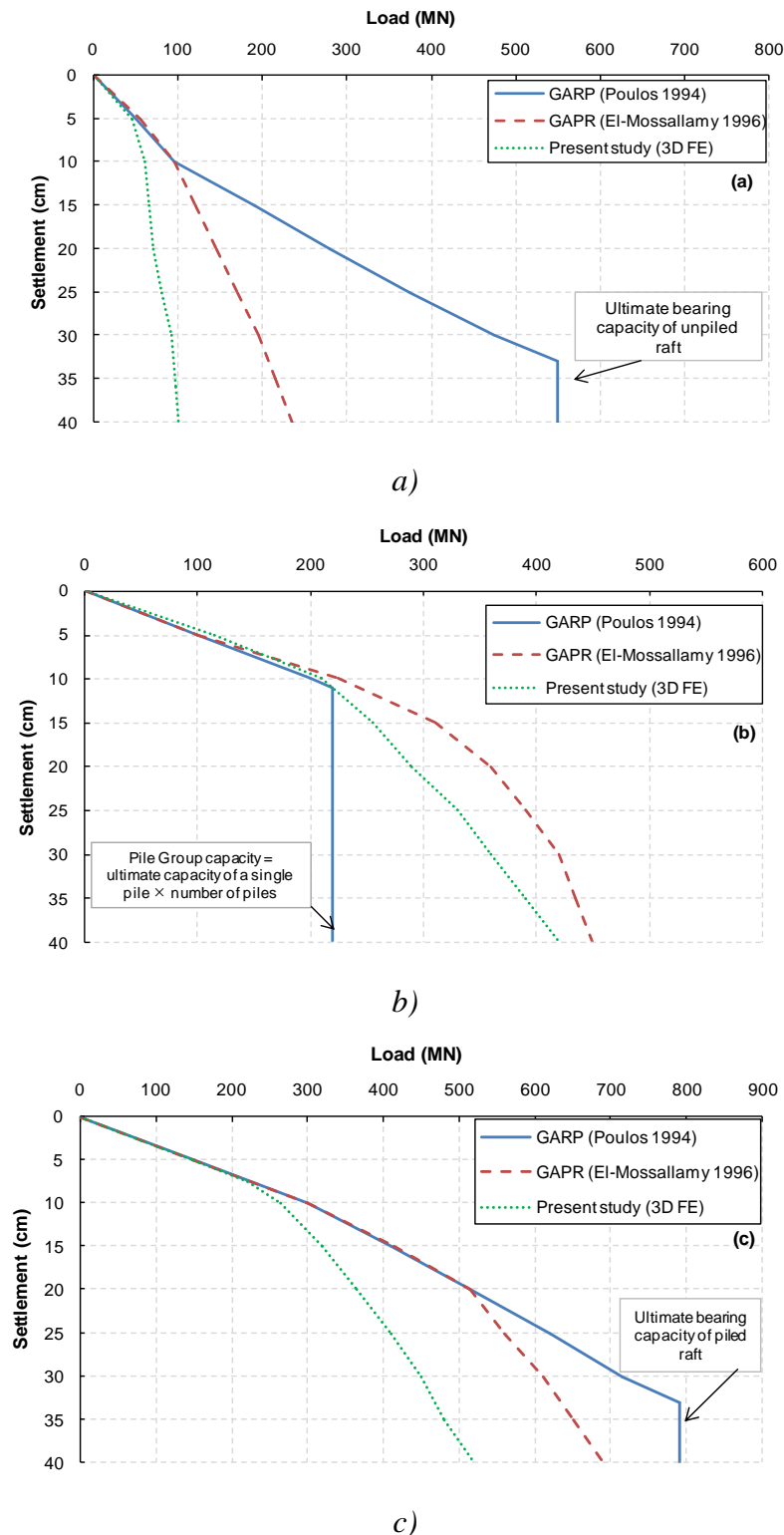


Fig. 3. Load-settlement curve for (a) unpiled raft (b) pile group (c) piled raft

The third example analyzed by 6 different mentioned methods where a  $10 \times 6 \times 0.5$  m raft is supported by a pile group containing 15 piles. Pile, raft and properties soil and load characteristics are shown in Figure 4. Based on finite difference method employing FLAC2D, FLAC3D, plate on spring

approximation method [7] using GARP5, simplified PDR method and strip on spring method using GASP [10], the load-settlement curve of Figure 5 is depicted to compare the results.

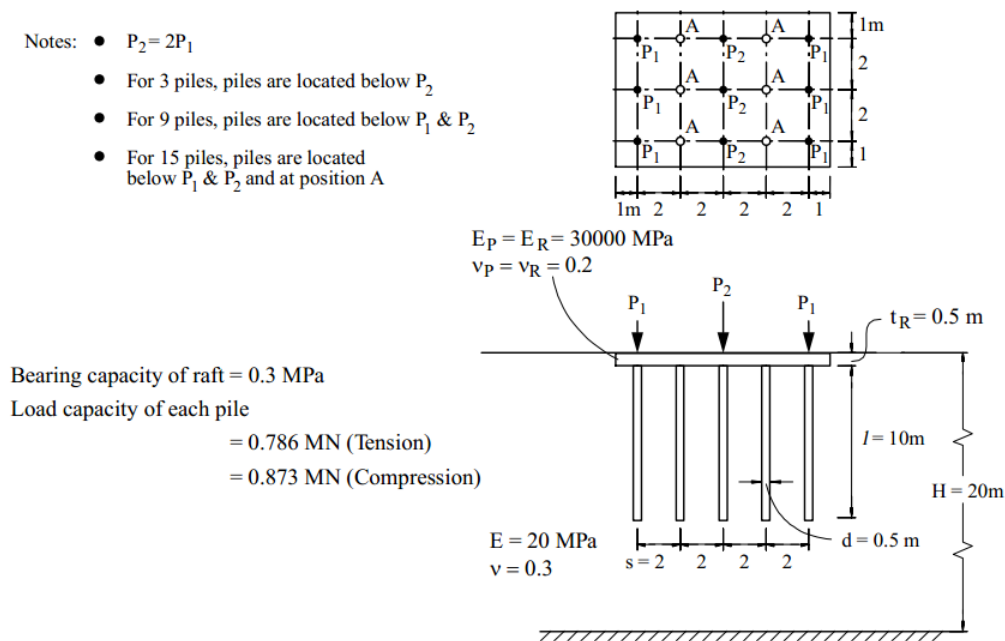


Fig. 4. Pile, raft and soil properties and load characteristics for the third example [26]

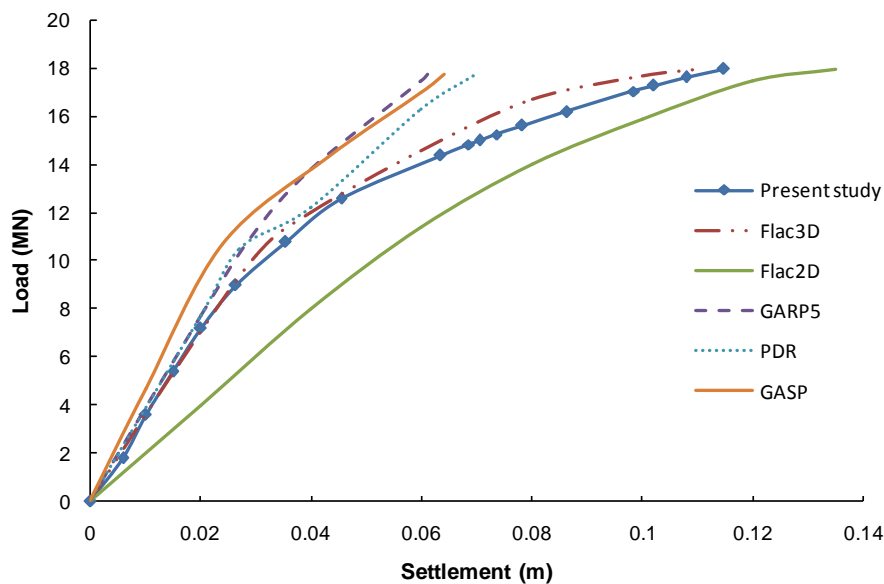
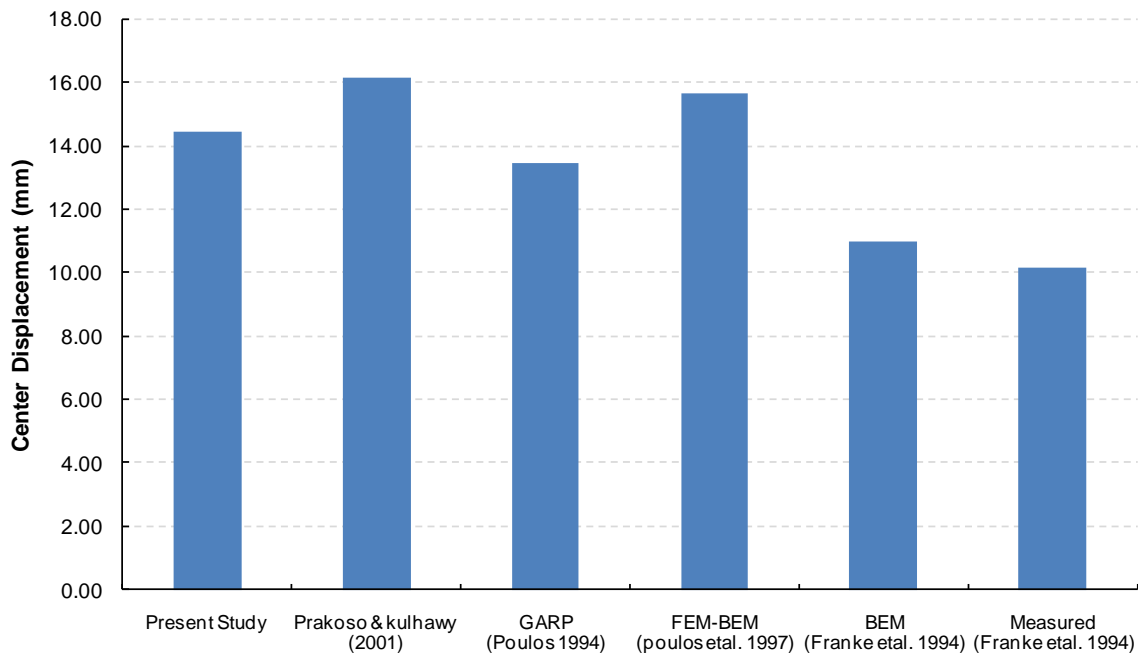


Fig. 5. Comparison of various methods for load-settlement analysis with the present study

As shown in Figure 5, in low load ranges, even the approximation and simplified methods are comparative with the numerical methods (3D FDM and FEM). The latter method gives a softer response than others when the load exceeds 12 MN. It is due to the progress of plastic zone development beneath the raft and so the increase of plastic deformations. However, FLAC2D overestimates the settlements because of the assumptions involved in plane strain modeling. Therefore, 2D plane strain modeling is conservative and cause misleading in the analysis especially when the raft is square.

Moreover, the results of 2D FE [18], approximation method [7], combined BEM and FEM [24], BEM [15] and measurement of Franke et al. [15] were compared with the present method (Figure 6) and a good agreement was observed.



*Fig. 6. Comparison between the approximate, numerical methods and measurements*

**Summary.** In this study, a review of the available methods to consider the behavior of piled raft foundations was performed and a comparison between the results of these different methods with a three-dimensional finite element model is presented. For this purpose, three separate examples for different soil and foundation conditions were considered. Based on the results, analysis of piled raft with the presented 3D FE method gives good and comparative results for the assessment of the performance of foundation.

## References

- [1] Zeevaert, L. (1957). Compensated friction-pile foundation to reduce the settlement of buildings on highly compressible volcanic clay of Mexico City. Proceedings of 4th International Conference of Soil Mechanics and Foundation Engineering, London.
- [2] Davis, E. H., & Poulos, H. G. (1972). The analysis of piled raft systems. Australian Geomechanics Journal. 2(1), 21-27.
- [3] Hooper, J. A. (1973). Observations on the behaviour of a piled raft foundation on London Clay. Proceedings of the Institution of Civil Engineers, 55 (2), 855-877.
- [4] Sommer, H., Wittman, P., & Ripper, P. (1985). Piled raft foundation of a tall building in Frankfurt Clay. Proc. 11th Conf. Soil Mech. Found. Engng, San Francisco 4, 2253-2257.
- [5] Franke, E. (1991). Measurements beneath piled rafts. ENPC Conference, Paris, pp. 1-28.
- [6] Hongladaromp, T., Chen, N. J. & Lee, S. L. (1973). Load distributions in rectangular footings on piles. Geotechnical Engineering, 4(2), 77-90.
- [7] Poulos, H. G. (1994). An approximate numerical analysis of pile-raft interaction. International Journal for Numerical and Analytical Methods in Geomechanics. 18, 73-92.

- [8] Russo, G. (1998). Numerical analysis of piled rafts. *International Journal for Numerical and Analytical Methods in Geomechanics*, 22(6), 477-493.
- [9] Kitiyodom, P., & Matsumoto, T. (2003). A simplified analysis method for piled raft foundations in non-homogeneous soils. *International Journal for Numerical and Analytical Methods in Geomechanics*, 27(2), 88-109.
- [10] Poulos, H. G. (1991). In *Computer methods and advances in geomechanics* (eds Beer et al.), pp. 183-191. Rotterdam: Balkema.
- [11] Poulos, H. G., & Davis, E. H. (1980). *Pile foundation analysis and design*. New York: Wiley.
- [12] Randolph, M. F. (1994). Design methods for pile groups and piled rafts: state-of-the-art report. *Proc. 13th Int. Conf. Soil Mech. Found. Engng*, New Delhi 5, 61-82.
- [13] Burland, J. B. (1995). Piles as settlement reducers. 18th Italian Congress of Soil Mechanics, Pavia.
- [14] Butterfield, R., & Banerjee, P. K. (1971). The problem of pile group-pile cap interaction. *Géotechnique*, 21(2), 135-142.
- [15] Franke, E., Lutz, B., & El-Mossallamy, Y. (1994). Measurements and numerical modelling of high-rise building foundations on Frankfurt Clay. *Geotechnical Special Publication* 40, pp. 1325-1336. New York: American Society of Civil Engineers.
- [16] El-Mossallamy, Y. (1996). Ein Berechnungs-modell zum Tragverhalten der Kombinierten Pfahl-Plattengründung, Dissertation und Mitteilungen des Institutes und der Versuchsanstalt für Geotechnik der Technischen Universität Darmstadt, Heft 36.
- [17] Katzenbach, R., & Reul, O. (1997). Design and performance of piled rafts. *Proceedings of XIV th ICSMFE 97*, Hamburg, Vol. 4, pp. 2253-2256.
- [18] Prakoso, W. A. & Kulhawy, F. H. (2001). Contribution to piled raft foundation design. *Journal of Geotechnical and GeoEnvironmental Engineering*, 127(1), 17-24.
- [19] de Sanctis L, & Mandolini A. (2006). Bearing capacity of piled rafts on soft clay soils. *Journal of Geotechnical and GeoEnvironmental Engineering*, 132(12), 1600-1610. doi 10.1061/(ASCE)1090-0241(2006)132:12(1600)
- [20] Lee J., Kim Y., & Jeong, S. S., (2010). Three-dimensional analysis of bearing behavior of piled raft on soft clay. *Computers and Geotechnics*, 37, 103-114, doi 10.1016/j.compgeo.2009.07.009
- [21] Cho J., Lee J. H., Jeong, S. S., & Lee J. (2012). The settlement behavior of piled raft in clay soils. *Ocean Engineering*, 53, 153-163, doi 10.1016/j.oceaneng.2012.06.003
- [22] Taghavi Ghalesari, A., Barari, A., Fardad Amini, P., & Ibsen, L. B. (2015) Development of optimum design from static response of pile-raft interaction. *Journal of Marine Science and Technology*, 20(2), 331-343, doi 10.1007/s00773-014-0286-x
- [23] Taghavi Ghalesari, A., & Rasouli, H. (2014) The effect of gravel layer on the behavior of piled raft foundations, In *Proc. GeoShanghai 2014, Advances in Soil Dynamics and Foundation Engineering*, ASCE GSP 240, 373-382, doi 10.1061/9780784413425.038
- [24] Poulos, H. G., Small, J. C., Ta, L. D., Sinha, J., & Chen, L. (1997). Comparison of some methods for analysis of piled rafts. *Proceedings of 14th ICSMFE*, Hamburg, 2, 1119-1124.
- [25] Chow, Y. K., Yong, K. Y. & Shen, W. Y. (2001) Analysis of piled raft foundations using a variational approach. *International Journal of Geomechanics*, 1(2), 129-147, doi 10.1080/15323640108500156
- [26] van Impe, W. F. (2001). Methods of analysis of piled raft foundations. *International Society of Soil Mechanics and Geotechnical Engineering*, Technical Committee TC18 on Piled Foundations.

# Dynamic Stress and Strain Analysis for 8x4 Truck Frame

Nagwa Ahmed Abdel-halim<sup>1,a</sup>

1 – Automotive Engineering Department, Faculty of Engineering, Mataria, Helwan University, Cairo, Egypt

a – [Nagwaibrahim2006@yahoo.co.uk](mailto:Nagwaibrahim2006@yahoo.co.uk)



DOI 10.13140/RG.2.1.3829.3363

**Keywords:** 8x4 trucks, king pin inclination, camber, caster, toe-in, truck dynamics, dynamic chassis stress and strain, finite element models and analysis.

**ABSTRACT.** The truck chassis is subjected to lower stresses in rest than it is in movement where the stresses and strains are considerably increased. The current work contains the load cases and boundary conditions for stresses and strains analysis of chassis using finite element analysis. King pin inclination, camber, caster, and toe-in angles of a truck's wheels affect its chassis' longitudinal and transverse stresses and strains. This work concentrates on studying the chassis' stresses and strains when the truck is in longitudinal acceleration motion on asphalted straight road and has adjustable wheel angles for the steerable axles' wheels.

**1. Introduction.** Today wheel alignment is more sophisticated as there are several angles. Therefore, it is important to study the effect of wheel alignment as a factor on the truck chassis stresses and strains. Wheel alignment is often the cause of or at least a contributing factor in changes in the vehicle wheel forces, which is reflected on the values of chassis stresses and strains.

The stress analysis of chassis has been studied using finite element analysis over ANSYS in static and dynamic cases. Shell elements for the longitudinal and cross members, spring elements for suspension, and wheel stiffness have been used. In addition, impact loads have been measured experimentally. The road shocks and the vehicle moving situation have been studied with the adjacent corner of the frame. In addition, the determination of the natural frequencies of the chassis structure has been carried out by using Algor FEMPRO [1-4].

The previous studies investigated many kinds of classical and simple boundary conditions without considering wheel alignment as a factor of the chassis forces [1]. With the present approach, the study of the effect of the steerable wheels' adjustable angles was covered using finite element approach with MATLAB package, which is more efficient and simple. Also, general boundary conditions for the road in addition to most real conditions have been considered in this comprehensive model for the investigation of chassis stresses and strains.

## 2. Basic Concepts

A Mitsubishi FUSO truck, model S52JS4RFAB has been studied in static case after calculated its wheels reaction forces. The truck chassis finite element models were checked in static case for stiffness, deflection, shear and bending stresses, and strain by using MALAB software [5, 6].

In dynamic case, the truck chassis forces are varied under the variation in operation condition. In this study, the structural, construction, and material of the truck tires, and the side air resistance are neglected. Also, the study has been considered the truck's movement is a free rolling case and it moves on straight, hard, and dry road. This study is included the tire alignment as an effected parameter on the frame force.

### 2.1 Influence of Wheel Angles on the Location of Axle Loads [7-9]

The adjusting of the steered wheels' angles is very important to keep the conditions for optimum steer of a vehicle. In addition, it makes the vehicle follows a path which is part of the circumference of its turning circle, which will have a center point somewhere along a line extending the axis of the fixed axle. It keeps the steered wheels at 90 degrees to a line drawn from the circle center through the center of the wheel as represents in Fig. 1 (a), (b).

To show the tire forces in three axes; longitudinal force  $F_x$  (x-axis), vertical load  $F_y$  (y-axis), and lateral force  $F_z$  (z-axis), which can be acting on the center of tire contact a zoomed in picture of a one tire, is shown in Fig. 2.

For static case, the positive kingpin inclination results a moment ( $M_{yk}=F_y w_w/2$ ) around the wheel axis when the vertical wheel load ( $F_y$ ) is shifted to the wheel axis and resolved into two components  $F_y \sin \beta$  (perpendicular on the king pin) and  $F_y \cos \beta$  (parallel to the king pin) as shown in Fig. 3.

A lateral force ( $F_z$ ) will be created due to the vehicle wheel cambered at its top towards the outside by angle ( $\Phi$ ). The reaction force ( $F_{z,c}$ ) of the lateral force ( $F_z$ ) will be appeared at the wheel axis. The reaction force ( $F_{z,c}$ ) will be resolved into two components  $F_{z,c} \cos \beta$  (perpendicular on the king pin) and  $F_{z,c} \sin \beta$  (parallel to the king pin) as shown in Fig. 4.

The toe-in angle ( $\alpha$ ) is that results from change the distance between the vehicle center plane in the longitudinal direction and the line intersecting the center plane of one wheel with the road plane and this angle ( $\alpha$ ) corresponds to the tire slip angle. Fig. 5, 6 represent the plane view of the tire toe-in angle with the kingpin inclination and the tire toe-in, tire camber with the kingpin inclination. Equations 1, 2 describe the forces, which are shown at the center of wheel in Fig. 6.

Fig. 7 details the positive caster angle ( $\tau$ ). It is the angle between the steering axis (EG) projected onto a xy-plane and a vertical drawn through the wheel center. Also, it clears that the kinematic caster trail ( $r_{t,k}$ ), the lateral force trail ( $r_{t,T}$ ), dynamic radius ( $r_{dyn}$ ), the force  $F_{yz}$ , and its components  $F_{yzvk}$ ,  $F_{yzhk}$  which are in equations (3-5).

Fig. 8 shows the plane view of Fig 7. This figure shows how the center of the lateral forces ( $F_{zWA}$ ) moves back by the value of the kinematic caster trail ( $r_{t,\tau}$ ). While the longitudinal forces ( $F_{xWA}$ ) moves outside by the camber offset ( $r_t$ ). Equations 6, 7 contain the values of the above forces.

$$F_{csc} = F_z c \cos \beta - F_y \sin \beta \quad (1)$$

$$F_{ccs} = F_y \cos \beta + F_z c \sin \beta \quad (2)$$

$$F_{yz} = F_{ccs} \quad (3)$$

$$F_{yzvk} = F_{ccs} \sin \tau \quad (4)$$

$$F_{yzpk} = F_{ccs} \cos \tau \quad (5)$$

$$F_{zWA} = F_{csc} \quad (6)$$

$$F_{xWA} = F_{yzvk} \quad (7)$$

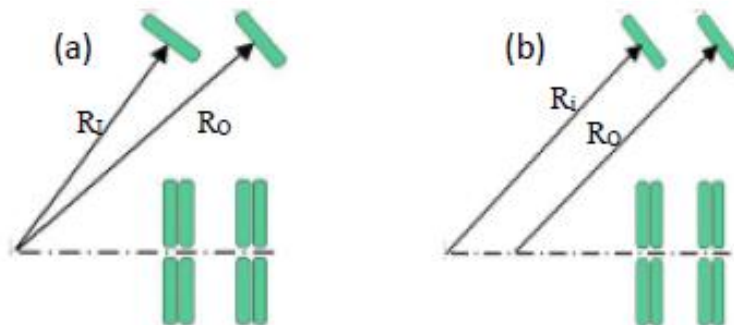


Fig.1. Steering geometry (a) with positive, (b) with zero tire rod angle

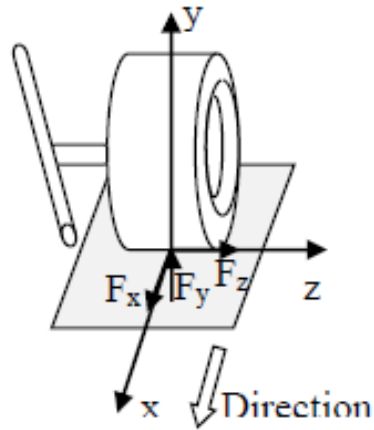


Fig. 2. The tire forces in three axes

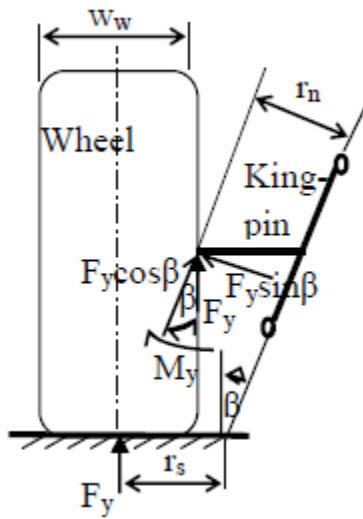


Fig. 3. Side view of the kingpin inclination

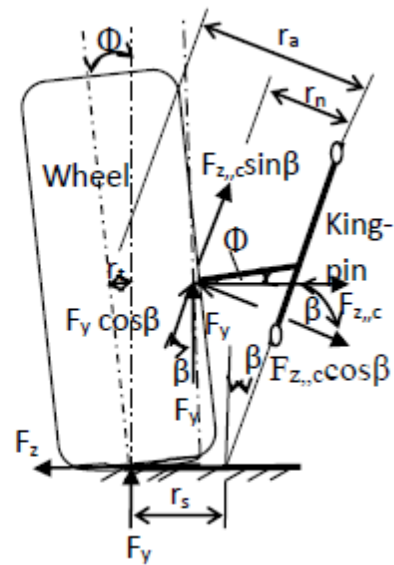


Fig. 4. Side view of camber with kingpin inclination

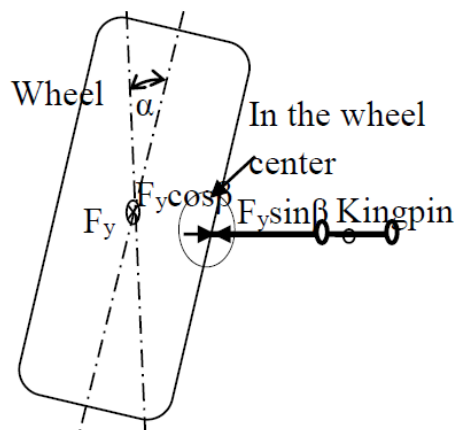


Fig. 5. Plan view of tire toe-in with kingpin inclination

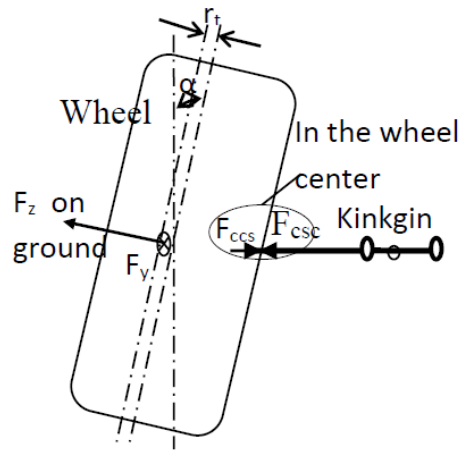


Fig. 6. Plan view of tire camber with toe-in and kingpin inclination

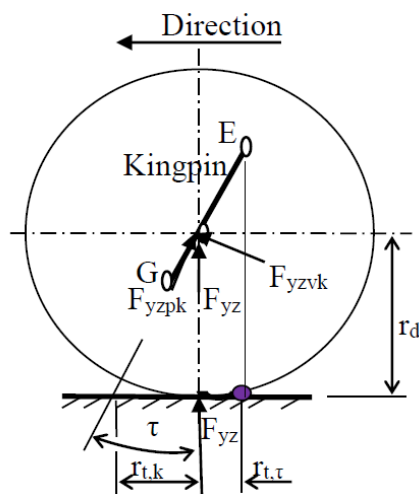


Fig. 7. Side view of the tire with positive caster angle

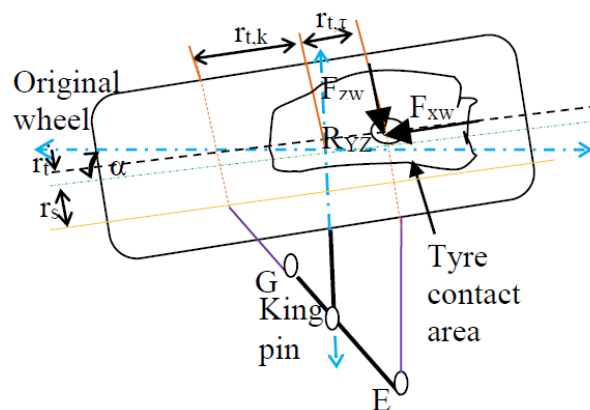


Fig. 8. Plan view of tire with all tire angles

## 2.2 Truck Chassis Dynamic Model [5, 10-13].

The truck used for the study is accelerating on the level ground by acceleration ( $a$ ). The forces of inertia  $F_{in}$ , air resistance  $F_{air}$ , and rolling resistance  $F_r$  of the progressively moving masses directed oppositely to the acceleration. The truck chassis dimensions and forces in dynamic case are viewed in Fig. 9. The longitudinal forces at the wheels contact point with the ground  $A, B, C, D$  can be

computed by sequence of steps. Firstly, the equation of motion along the longitudinal axis of the truck according the force balance method is expressed by equation 8 whereas the front axles' tractive effort is zero because the truck is a rear wheel drive. The tractive effort for the rear axles is calculated as the equations group 9 and the dynamic wheel radius can be determined from equation 10. Secondly, the summation of air, rolling, coefficient of rolling resistance, and inertia resistance forces for the truck components mention in equations (11-14). Thirdly, the distribution of both the inertia and air resistance forces on the contact points of the truck's wheels with the ground can be made by; a) Calculate the percentage of a vertical load of a truck wheel related to the summation the vertical loads of all wheels (equation 15). b) Multiply the percentage of the wheel load and the summation for both the inertia and air resistance forces (group of equations 16). C) Sum the resistance forces at the wheel contact point (group of equations 17).

$$md^2x/dt^2 = aW/g = F_{TC} + F_{TD} - \Sigma R_r - \Sigma R_{air}$$

$$F_{TC} + F_{TD} \geq \Sigma(R_{in} + R_r + R_{air}) \quad (8)$$

$$F_{TC} = M_{emax} i_{gn} i_{f1} \eta_v / n_{w1} r_d, F_{TD} = F_{TC} i_{f2} \quad (9)$$

$$r_d = 0.5D_r + B_t(1 - \lambda_t) \quad (10)$$

$$\Sigma R_{air} = KaB_a H a V^2 \quad (11)$$

$$\Sigma R_r = f(R_{YZA} + R_{YZB} + R_{YZC} + R_{YZD}) \quad (12)$$

$$f = f_0 (1 + V_{max}^2 / 1500) \quad (V \text{ by } m/s) \quad (13)$$

$$\Sigma R_{in} = a/g(\Sigma w) = (\Sigma w) =$$

$$F_{in1} + F_{in2} + F_{in3} + F_{in4} + F_{in5} + F_{in6} + F_{in7} + F_{in8} \quad (14)$$

$$\% R_{YZA} = R_{YZA} / \Sigma (R_{YZA} + R_{YZB} + R_{YZC} + R_{YZD}) \quad (15)$$

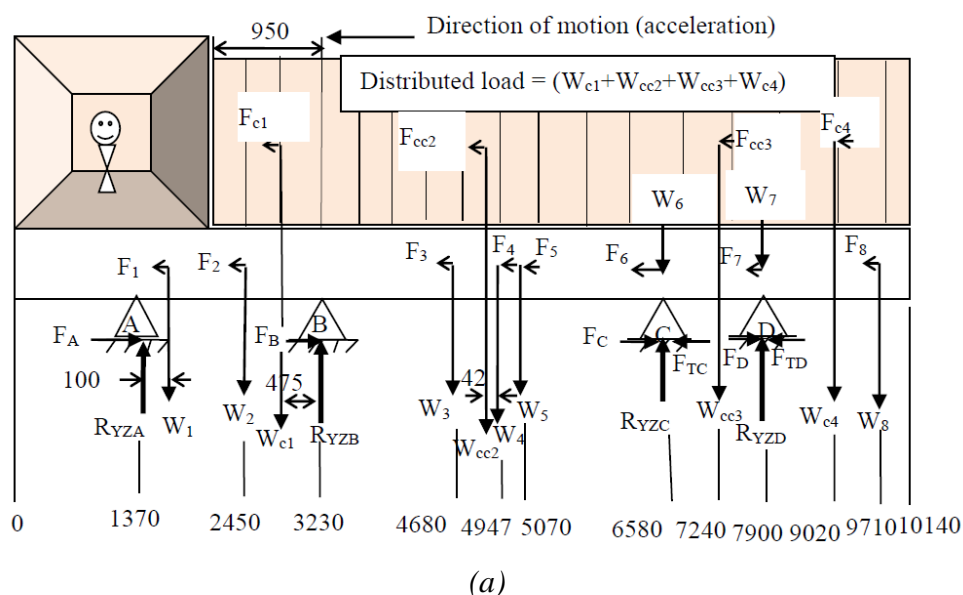
$$(R_{inA} + R_{airA}) = \Sigma(R_{in} + R_{air}) \cdot \% R_{YZA},$$

$$(R_{inB} + R_{airB}) = \Sigma(R_{in} + R_{air}) \cdot \% R_{YZB},$$

$$(R_{inC} + R_{airC}) = \Sigma(R_{in} + R_{air}) \cdot \% R_{YZC},$$

$$(R_{inD} + R_{airD}) = \Sigma(R_{in} + R_{air}) \cdot \% R_{YZD} \quad (16)$$

$$F_A = fR_A + R_{inA} + R_{airA}, F_B = fR_B + R_{inB} + R_{airB}, F_C = fR_C + R_{inC} + R_{airC}, F_D = fR_D + R_{inD} + R_{airD} \quad (17)$$



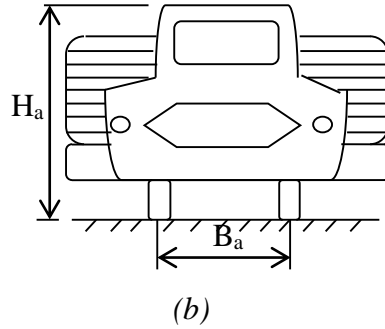


Fig. 9. (a) The truck chassis dimensions and forces in dynamic case, (b) head area of the truck

### 2.3 Influence of Wheel Angles on the Value of Axle Loads [7, 8].

The truck chassis was modeled to study the effect of the wheel angles on the value of vertical reaction, longitudinal, and transverse (lateral) forces. From that point of view the vertical forces at the wheels contact points will be changed for the two front steered axles but didn't change for the two rear drive axles to be become as in equations (18-21). From that and the above paragraph the longitudinal forces at points A, B, C, D will be as illustrated in equations (22-25). The average lateral force results from the wheel camber on the dry road  $F_z$  is represented in equation 26. Therefore, the lateral force at points A, B, C, D are illustrated through equations (27-30).

$$R_{YZA} = R_A \cos \beta + F_{z,c} \sin \beta \quad (18)$$

$$R_{YZB} = R_B \cos \beta + F_{z,c} \sin \beta \quad (19)$$

$$R_{YZC} = R_C \quad (20)$$

$$R_{YZD} = R_D \quad (21)$$

$$F_A = F_{xwA} = f R_{YZA} + \cos \beta (R_{inA} + R_{airA}) \quad (22)$$

$$F_B = F_{xwB} = f R_{YZB} + \cos \beta (R_{inB} + R_{airB}) \quad (23)$$

$$F_C = F_{xwC} = f R_{YZC} + (R_{inC} + R_{airC}) \quad (24)$$

$$F_D = F_{xwD} = f R_{YZD} + (R_{inD} + R_{airD}) \quad (25)$$

$$F_z = F_{z,c} = F_{zw} = F_y \sin \Phi \quad (26)$$

$$F_{zwA} = R_{yZA} \sin \Phi = R_A (\cos \beta + \sin \beta) \sin \Phi \quad (27)$$

$$F_{zwB} = R_{yZB} \sin \Phi = R_B (\cos \beta + \sin \beta) \sin \Phi \quad (28)$$

$$F_{zwC} = R_C f_t \quad (29)$$

$$F_{zwD} = R_D f_t \quad (30)$$

### 3. The Finite Element Model of the Truck Chassis [6, 14-15].

In this study the FEA has been used to analysis the truck chassis beams strength in dynamic case. The same procedure in reference [6] could be repeated. However the truck chassis's beam model forces and supports reactions could be located at the same places but in three dimension axes. And also, the number of elements is five hundred; each element has nearly twenty mm (20.28 mm) length with two nodes at its edges.

#### 3.1 Global Stiffness Matrix ( $K_{NgNg}$ ) and The Deflection Vector ( $\delta_{NgNg}$ ).

The shape of the element stiffness matrix in three dimensions is completely different rather than in one dimension. Each node in this case study has five degrees of freedom namely longitudinal ( $u$ ), vertical ( $y$ ), lateral ( $l$ ) displacements respectively and  $xy$ -plane cross-section (slope) rotation ( $\theta_z$ ),  $xz$ -plane cross-section (slope) rotation ( $\theta_y$ ) respectively. The linear system for Euler-Bernoulli beam has been described in equation 31, 32 for one element ( $L$ ) as a complete element stiffness matrix ( $K_{ij}$ ), nodal variables (displacements and rotations) vector ( $\delta e$ ), and nodal force vector ( $F_e$ ). Matrix 32 is the element equilibrium equations for a two-plane bending element with axial stiffness in matrix form. The axial  $[K_{axial}]$ , bending  $[K_{bending}]_{xy}$ , and bending  $[K_{bending}]_{xz}$  stiffness matrices are detailed in appendix 1. The calculation steps of the assembled stiffness matrix ( $K_{NgNg}$ ), and the assembled deflection vector ( $\delta_{NgNg}$ ) is nearly as reference [6] with difference in the size of the global stiffness matrix.

$$[K_{ij}] \cdot [\delta e] = [F_e] \quad (31)$$

$$\begin{bmatrix} [K_{axial}] & [0] & [0] \\ [0] & [K_{bending}]_{xy} & [0] \\ [0] & [0] & [K_{bending}]_{xz} \end{bmatrix} \begin{bmatrix} u_1 \\ u_2 \\ v_1 \\ \theta_{z1} \\ v_2 \\ \theta_{z2} \\ l_1 \\ \theta_{y1} \\ l_2 \\ \theta_{y2} \end{bmatrix} = \begin{bmatrix} f_{x1} \\ f_{x2} \\ f_{y1} \\ M_{z1} \\ f_{y2} \\ M_{z2} \\ f_{z1} \\ M_{y1} \\ f_{z2} \\ M_{y2} \end{bmatrix} \quad (32)$$

### 3.2 Stresses and Strains for the Truck Chassis in Three Axes.

In this article, Galerkin's method is used in stress analysis of the truck chassis in three dimensions. The truck chassis elements have been loaded tensional-compression in the  $x$  direction. From elementary strength of materials theory, the  $\epsilon_x$  represents the strain resulting from applied load while the induced strain components are given by  $\epsilon_y = \epsilon_z = -\nu \epsilon_x$ . Equations 33, 34 resulted from strength of materials' laws for tension load and the substitution in the general stress-strain relations. This study has been assumed two planes of stress, that  $xy$  and  $xz$  planes. When  $xy$  is the plane stress,  $\sigma_b(xy)$ ,  $\epsilon_y$ , and  $T_{xy}$  can be calculated from equations (35-38). Again, by assuming that the  $xz$  plane is the plane stress,  $\sigma_b(xz)$ ,  $\epsilon_z$ , and  $T_{xz}$  can be calculated from equations (39-42).

$$\sigma_{t,c} = F(x)/A \quad (33)$$

$$\epsilon_x = \sigma_{t,c} / E \quad (34)$$

$$\sigma_b(xy) = M(xy) * D / 2I_z \quad (35)$$

$$\epsilon_y = ((1+\nu) (1-2\nu) \sigma_b(xy) - \nu \sigma_{t,c}) / E(1-\nu) \quad (36)$$

$$T_{xy} = (F(y)BD^2) / (8I_z b) \quad (37)$$

$$\gamma_{xy} = T_{xy} / (E / (2(1+\nu))) = T_{xy} / G \quad (38)$$

$$\sigma_b(xz) = 6M(xz) / (D(B^2 + (b/B) - 1) - 2b((b/B) - 1)) \quad (39)$$

$$\epsilon_z = ((1-2\nu) / E(1-\nu)) ((1+\nu) \sigma_b(xz) - (\nu / (1-\nu)) ((1+\nu) \sigma_b(xy) + \sigma_{t,c})) \quad (40)$$

$$T_{xz} = (FzB^2D) / (16I_z b) \quad (41)$$

$$\gamma_{xz} = T_{xz} / G \quad (42)$$

#### 4. Results and Discussions of Truck Chassis's stresses and strains.

The vertical loads ( $w_l$ .....etc) and reaction forces on the wheels ( $R_A$ .....) for one side of the chassis in static case have been written in Table 1. The wheel angles for the two front truck axles' wheels have been taken equally while the two rear axles' wheels haven't adjustable angles. The values of the front wheels angles summarized in Appendix 2 Table 2. Appendix 2 also contains Tables 3, Table 4. Table 3 includes the variables' values for the variables of paragraph (2.2). Table 4 has the longitudinal and lateral forces' names and their values on one side of the truck chassis. All the Table in Appendix 2 has been used in drawing the stresses and strains graphs. Fig. 10, 11 represent the tension-compression stress and strain respectively. Fig. 12, 13 shows the vertical bending stress and strain respectively. Fig. 14, 15 have the vertical shear stress and strain respectively. The drawing in Fig. 16, 17 have the lateral bending stress and strain respectively. The lateral shear stress and strain have been represented through Fig. 18, 19 respectively. Each couple of the above figures has the same trend but with difference in their values. As example the maximum value of the lateral shear stress is about 36 N/mm<sup>2</sup> while the maximum of the lateral shear strain is about 44x10<sup>-5</sup> and so on for the others couples.

**Summary.** The noticed from this study is the wheel angles generate lateral force. Although the generated lateral force causes lateral stress on the frame chassis, it will help for smooth turning of the truck. Also, the noticed from the graphs 16, 17 that they have completely different trend in the shapes oppositely the others stresses and strains coupled graphs.

In this search, the description of the truck's accelerating motion on flat, asphalted, and smooth road generate valuable longitudinal stress whenever the maximum value its maximum value is 24 N/mm<sup>2</sup>.

This article considered a compromise of using the Finite Element Techniques (FET), MATLAB package; studying the effect of the steerable wheels' angles on truck frame's forces values and direction, analyze the forces, which result from the truck dynamic motion.

Finally, the article includes many drawings for the stresses and strains in  $x$ -axis,  $xy$  plane stress and  $xz$  plane stress.

#### Nomenclature

$F_x$ – Wheel longitudinal force	% $R_{YZA}$ – Percentage vertical reaction force at point A
$F_y$ – Wheel vertical load or $R_A$ or $R_B$ or $R_C$ or $R_D$	$R_{inA}$ , $R_{airA}$ – Inertia and air resistances at point A
$F_z$ – Lateral force due to wheel cambered	$R_r$ – Rolling resistance
$F_{zc}$ – Reaction force of the lateral force	$F_{in1} \dots \dots \dots F_{in8}$ – Inertia forces for the truck components
$F_{zt}$ – Summation of the lateral forces	$w_w$ – Tire width
$F_{xt}$ – Summation of the longitudinal forces	$r_n$ – Distance between the steering axis to the vertical wheel load at the wheel center
$F_{TC}$ – Tractive effort of one wheel of the first rear axle	$r_s$ – Kingpin offset
$F_{TD}$ – Tractive effort of one wheel of the second rear axle	$\beta$ – Kingpin inclination angle
$R_A$ , $R_B$ , $R_C$ , $R_D$ – Vertical truck wheels reaction forces before adding the effect of wheel angles	$\Phi$ – Wheel camber angle
$R_{YZA}$ , $R_{YZB}$ , $R_{YZC}$ , $R_{YZD}$ – Vertical truck wheels reaction forces after adding the effect of wheel angles	$r_a$ – Longitudinal force lever depends on the kingpin offset
$R_{air}$ – Air resistance	$r_t$ – Camber offset
$R_{in}$ – Inertia resistance	$\alpha$ – Toe-in angle
$d^2x/dt^2$ or ( $a=5.5$ m/s <sup>2</sup> ) – Linear acceleration of the truck	$\tau$ – Caster angle
$g$ – Acceleration due to gravity	$r_{t,k}$ – Caster trail
$\mu$ – Constant ( $(a/g)=0.56$ )	$r_{t,T}$ – Lateral force trail
$M_{emax}$ – Engine maximum torque (1770 N m at 1100 rpm)	$r_{dyn}$ – Dynamic radius
$i_{gn}$ – The gearbox reduction ratio	$m$ – Truck mass (kg)
$i_{f1}$ – The first differential reduction ratio (2.15)	$M(xy)$ – Moment in $xy$ plane
$i_{f2}$ – The second differential reduction ratio (2.15)	$M(xz)$ – Moment in $xz$ plane
$\eta_t$ – The drive line efficiency (0.9)	$\mathcal{O}_b(xy)$ – Bending moment in $xy$ plane
$n_{wl}$ – Number of wheels on the first rear axle (4)	$\mathcal{E}_y$ – Strain in $xy$ plane
$r_s$ – Wheel static radius	$T_{xy}$ – Shearing stress is acting in the direction of the $x$ axis on a surface perpendicular to the $y$ axis (N/mm <sup>2</sup> )
$r_d$ – Wheel dynamic radius	$\gamma_{xy}$ – Shear strain is in $xy$ plane (N/mm <sup>2</sup> )
$D_r$ – Diameter of wheel rim, m	

$B_t$  – Height of tire profile in a free state, m  
 $\lambda_t$  – Radial deformation coefficient of the tire  
 $K_a$  – Air resistance coefficient N.S<sup>2</sup>/m<sup>4</sup>  
 $B_a$  – Track in m  
 $H_a$  – Maximum height of the automobile in m  
 $V$  – Maximum truck speed (80 km/hr)  
 $f_0$  – Longitudinal rolling resistance coefficient at a low speed (0.018)  
 $f$  – Longitudinal rolling resistance coefficient at a maximum speed  
 $f_t$  – Transverse rolling resistance coefficient at a maximum speed  $\approx f$   
 $\nu$  – Poisson's ratio

$\sigma_b(xz)$  – Bending moment in xz plane (N/mm<sup>2</sup>)  
 $\epsilon_z$  – Strain in xz plane  
 $\tau_{xz}$  – Shearing stress in xz plane (N/mm<sup>2</sup>)  
 $\gamma_{xz}$  – Shear strain in xz plane (N/mm<sup>2</sup>)  
 $G$  – Shear modulus  
 $L$  – Finite element length (mm)  
 $\sigma_{t,c}$  – Tension-compression stress  
 $A$  – Chassis cross section area (mm<sup>2</sup>)  
 $E$  – Modulus of elasticity N/mm<sup>2</sup>  
 $I_z$  – Modulus of section related to z axis  
 $I_y$  – Modulus of section related to y axis  
 $D$  – Cross section height (mm)  
 $B$  – Cross section web (mm)  
 $b$  – Cross section thickness (mm)

## Appendix 1

The axial  $[K_{axial}]$ , bending  $[K_{bending}]_y$ , and bending  $[K_{bending}]_z$  stiffness matrices are:

$$[K_{axial}] = (AE/L) \begin{bmatrix} 1 & -1 \\ -1 & 1 \end{bmatrix}$$

$$[K_{bending}]_y = (EI_z/L^3) \begin{bmatrix} 12 & 6L & -12 & 6L \\ 6L & 4L^2 & -6L & 2L^2 \\ -12 & -6L & 12 & -6L \\ 6L & 2L^2 & -6L & 4L^2 \end{bmatrix}$$

$$[K_{bending}]_z = (EI_y/L^3) \begin{bmatrix} 12 & -6L & -12 & -6L \\ -6L & 4L^2 & 6L & 2L^2 \\ -12 & 6L & 12 & 6L \\ -6L & 2L^2 & 6L & 4L^2 \end{bmatrix}$$

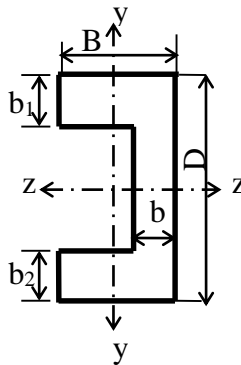


Fig. (A-1). Channel Cross Section Area ( $b=b_1=b_2$ )

## Appendix 2

Chassis components Loads, reactions, and resistances forces in static and dynamic cases for one side of the truck chassis:

Table 1. One Side Vertical Loads of Chassis's Truck and wheels Angles

Without Wheel Angles	Without Wheel Angles
Loads Name Values (N)	Loads Name Values (N)
$w_1$ 39208.3	$w_8$ 245.5
$w_2$ 2526.1	$R_A = F_y$ at wheel (A) 35177
$w_{c1}$ 6453.8	$R_B = F_y$ at wheel (B) 27599
$w_3$ 981	$R_C = F_y$ at wheel (C) 7777
$w_{cc2}$ 22758	$R_D = F_y$ at wheel (D) 29661
$w_4$ 1471.5	<b>With Wheel Angles</b>
$w_5$ 1895.5	<b>Loads Name Values (N)</b>
$w_6$ 245.5	$R_{yzA}$ 34840.3
$w_{cc3}$ 8967.3	$R_{yzB}$ 27323
$w_7$ 245.5	$R_{yzC} = R_C$
$w_{c4}$ 15217.3	$R_{yzD} = R_D$

Table 2. Wheel Angles Symbols and Values

$\beta$	$9^\circ$	$\Phi$	$1^\circ$	$\alpha$	$0.1^\circ$	$\tau$	$1^\circ$
---------	-----------	--------	-----------	----------	-------------	--------	-----------

Table 3. Values for the Variables of Paragraph (2.2)

Sy.	Value	Sy.	Value	Sy.	Value	Name	Value
$\lambda_t$	0.2	$B_t$	0.236 m	$Ka$	$0.7Ns^2/m^4$	$R_{inC}+R_{airC}$	4539 N
$f_0$	0.018	$r_d$	0.47 m	$\Sigma R_{in}$	56121 N	$R_{inD}+R_{airD}$	17341 N
$f$	0.024	$H_a$	3.24 m	$\Sigma R_{yz}$	99601 N	Without angles	
%R <sub>yzA</sub>	35	$B_a$	1.85 m	$\Sigma R_{air}$	2072 N	$F_A$	21212 N
%R <sub>yzB</sub>	27.4	$r_s$	0.522 m	$\Sigma(R_{in}+R_{air})$	58193 N	$F_B$	16607 N
%R <sub>yzC</sub>	7.8	$D_r$	0.572 m	$R_{inA}+R_{airA}$	20367 N	$F_C$	4725.6 N
%R <sub>yzD</sub>	29.8	$D_r$	0.572 m	$R_{inB}+R_{airB}$	15945 N	$F_D$	18053 N
Values for the Variables of stresses and Strains Equations							
$\gamma$	0.3	$B$	90 mm	$A$	3262 mm <sup>2</sup>	$I_z$	$40.69*10^6$ mm <sup>4</sup>
$D$	300 mm	$b$	7 mm	$E$	$2.1*10^5$ N/mm <sup>2</sup>	$I_Y$	$45.97*10^5$ mm <sup>4</sup>

Table 4. Longitudinal and Lateral Forces on One Side of Chassis's Truck

Longitudinal Force Value(N)	Longitudinal Force Value(N)
$F_A = F_{xwA}$ 20953	$F_C = F_{xwC}$ 4726
$F1 = w_1\mu$ 21957	$F_{TC}$ 26236
$F2 = w_2\mu$ 1415	$F_6 = w_6\mu$ 137
$F_{c1} = w_{c1}\mu$ 3614	$F_{cc3} = w_{cc3}\mu$ 5022
$F_B = F_{xwB}$ 16404	$F_D = F_{xwD}$ 18053
$F_3 = w_3\mu$ 549	$F_{TD}$ 56407
$F_{cc2} = w_{cc2}\mu$ 12744	$F_7 = w_7\mu$ 137
$F_4 = w_4\mu$ 824	$F_{c4} = w_{c4}\mu$ 8522
$F_5 = w_5\mu$ 1061	$F_8 = w_8\mu$ 137
Lateral Force Value(N)	Lateral Force Value(N)
$F_{zwA}$ 610	$F_{zwC}$ 187
$F_{zwB}$ 478	$F_{zwD}$ 712

### Appendix 3

The longitudinal, vertical, lateral stresses and strains.

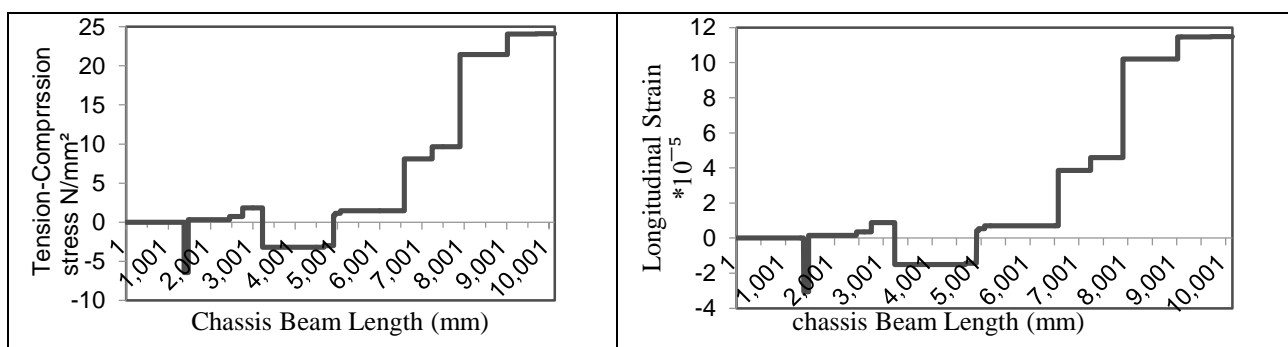


Fig. 10. Tension-Compression Stress versus Chassis Beam Length

Fig. 11 Longitudinal Strain versus Chassis Beam Length

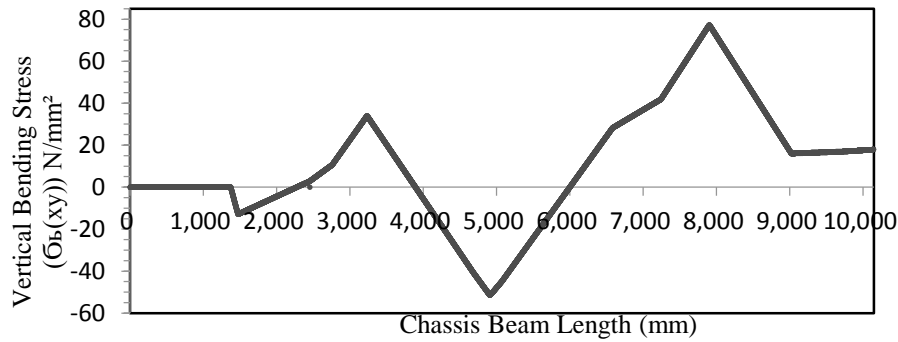


Fig. 12. Vertical Bending Strain versus Chassis Beam Length

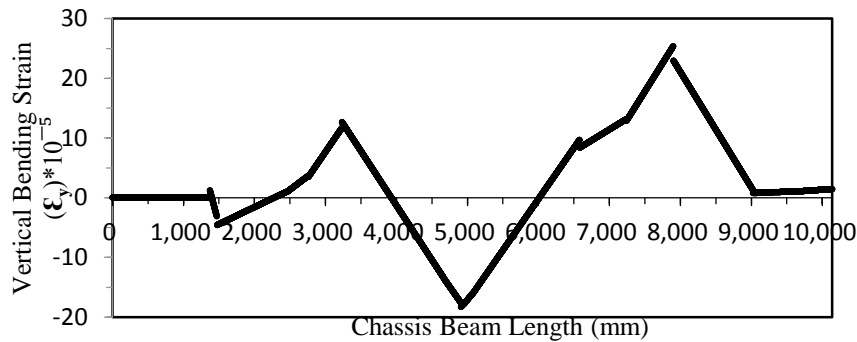


Fig. 13. Vertical Strain versus Chassis Beam Length

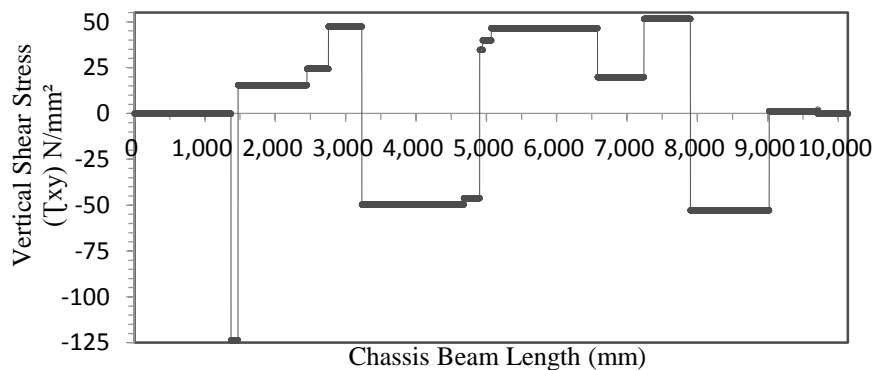


Fig. 14. Vertical Shear Stress versus Chassis Beam Length

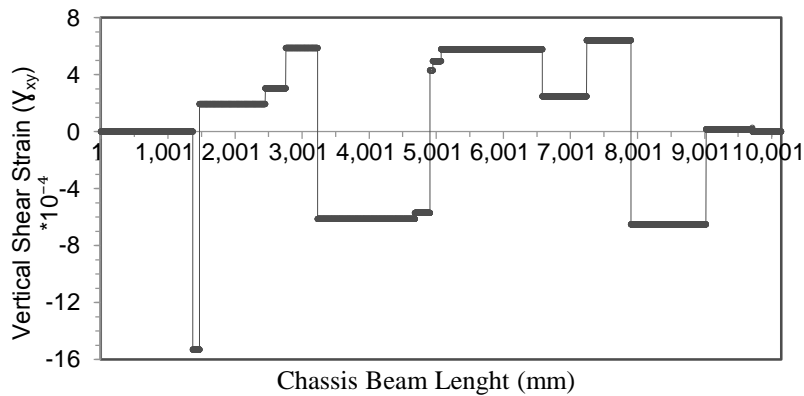


Fig. 15. Vertical Shear Strain versus Chassis Beam Length

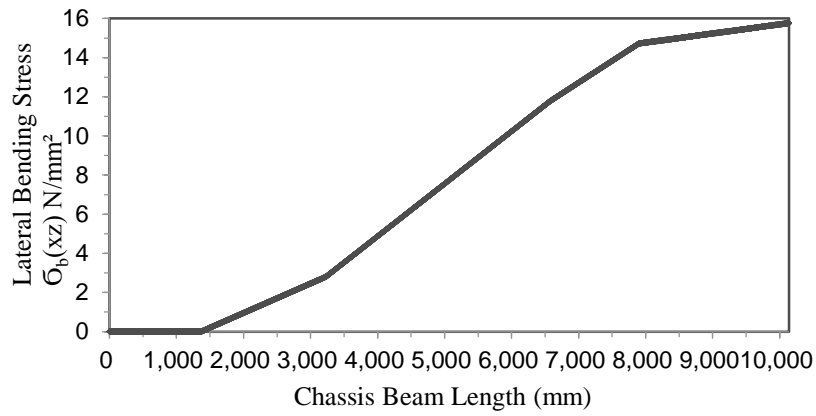


Fig. 16. Lateral Bending Stress versus Chassis Beam Length

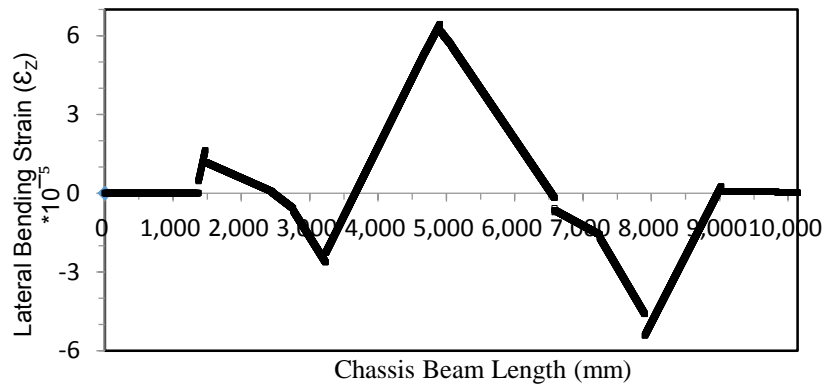


Fig. 17. Lateral Bending Strain versus Chassis Beam Length

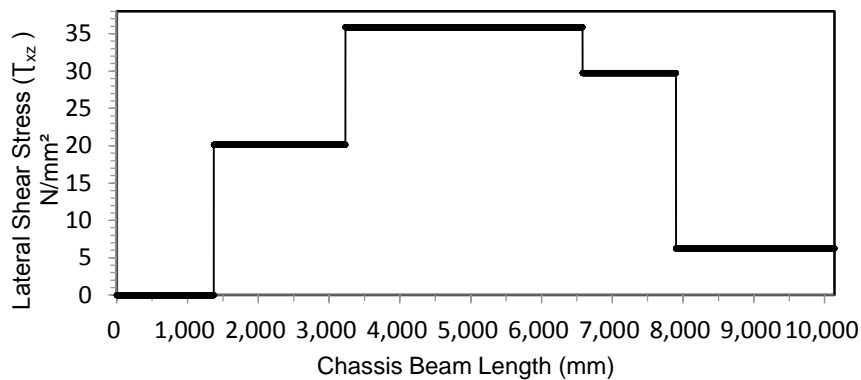


Fig. 18. Lateral Shear Stress versus Chassis Beam Length

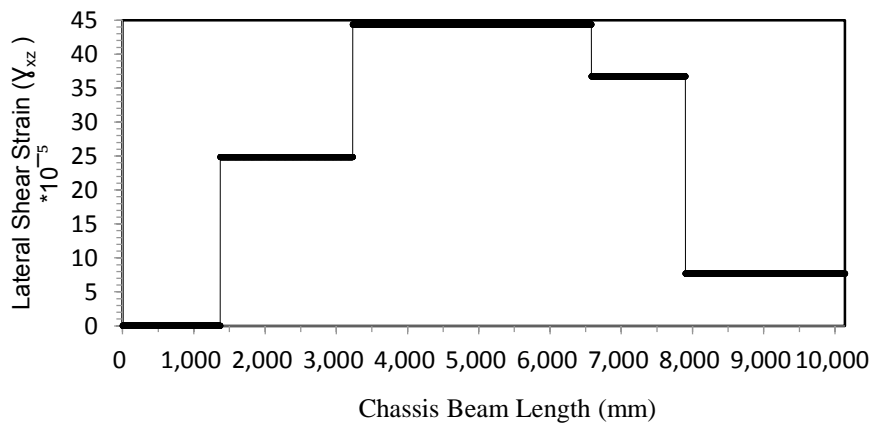


Fig. 19. Lateral Shear Strain versus Chassis Beam Length

## References

- [1] Teo Han Fui, Roslan Abd. Rahman (2007) ‘Statics and Dynamics Structural Analysis of A 4.5 Ton Truck Chassis’, Jurnal Mekanikal, No. 24, PP. 56-67.
- [2] Ashutosh Dubey and Vivek Dwivedi (2003) ‘Vehicle Chassis Analysis: Load Cases & Boundary Conditions for Stress Analysis’.
- [3] Dheeraj S. and Sabarish R. (2014) ‘Analysis of Truck Chassis Frame Using FEM’, Middle-East Journal of Scientific Research 20(5), ISSN 1990-9233, PP. 656-661.
- [4] Sani M. S. M., Arbain M. T. and et al (2009) ‘Stress Analysis and Modal Transient Response of Car Chassis’, International Conference on Advance Mechanical Engineering (ICAME09), 22-25 June 2009. Shah Alam, Selangor.
- [5] Abdel-halim Nagwa A. (2015) ‘Reflection of Truck Loads Distribution Methods on the Truck Wheels Reaction Forces’, American Journal of Engineering, Technology and Society, Issue 4, Vol. 2, Pages 67-76.
- [6] Abdel-halim Nagwa A., Abdel-hafiz Mohamed M. M. (2015) ‘Stress and Strain Analysis for a Ladder Truck Chassis’, American Journal of Engineering, Technology and Society, Issue 6, Vol. 2, Pages 131-139.
- [7] Dana Spicer, (2007) ‘Steer Axles Application Guidelines’, AXAG0400, PP. 1-46.
- [8] Prof. Dipl.-Ing. Jornsens Reimpell and Dipl.-Ing. Helmut Stoll (1996) ‘The Automotive Chassis: Engineering Principles, Types of drive and suspension, Tyres and wheels, Axle kinematics, steering, Springing, Chassis and vehicle overall’, English edition, Arnold London.
- [9] van Berkum A. (2006) Chassis and suspension design FSRTE02, Unpublished Master’s Thesis, Technische Universiteit Eindhoven, Department of Mechanical Engineering, Section Dynamics and Control Technology.
- [10] Artamonov M. D., Ilarionov V. A., and Morin M. M. (1976) ‘Motor Vehicles: Fundamentals and Design’, Mir publishers Moscow.
- [11] Wong J. Y. (1978) ‘Theory of Ground Vehicles’, A Wiley New York.
- [12] Mehdi Mahmoodi-k, Iraj Davoodabadi, and et al (2014) ‘Stress and Dynamic Analysis of Optimized Trailer Chassis’, Technical Gazette 21, 3, PP. 599-608.
- [13] Mitsubishi Fuso Truck & Bus Corporation (2009) Heavy Duty Fuso FS52JS4RFAB, Part No. TSH58A [www.fuso.com.au](http://www.fuso.com.au)
- [14] Hutton David V. (2004) ‘Fundamentals of Finite Element Analysis’, McGraw New York.
- [15] Mahvi Malik Shahzad, Shaikh Rizwan, Tarique khan (2015) ‘Finite Element Static Structural Analysis of 4X2 Truck Chassis Frame’, International Journal of Modern Trends in Engineering and Research, e-ISSN No.:2349-9745, Issue 7, Vol. 2, PP. 1909-19014. [www.ijmter.com](http://www.ijmter.com)

## Identification of Standing Pressure Waves Sources in Primary Loops of NPP with WWER and PWR

K.N. Proskuriakov <sup>1</sup>, A.I. Fedorov <sup>2</sup>, M.V. Zaporozhets <sup>1</sup> and G.Y. Volkov <sup>1</sup>

1 – Moscow Power Engineering Institute National Research University, Moscow, Russia

2 – Novovoronezh Nuclear Power Plant, a Branch of Rosenergoatom Concern, Novovoronezh, Russia



DOI 10.13140/RG.2.1.4562.0082

**Keywords:** vibration, vibro-acoustic resonance, Helmholtz resonator, Noise Analysis, electro-acoustic analogies.

**ABSTRACT.** Results of measurement and calculation of Eigen frequencies of coolant pressure oscillations in primary loops of NPP are presented. The simple calculation model based on equivalence of electric circuit with elastic wave propagation in liquids and gases, which gives a sensible interpretation of standing pressure waves sources is developed. It is shown, that pressurizer manifest itself as managed Helmholtz resonator generating a number of SPW (with Eigen frequencies of steam volume, water volume and their combination with coolant volume of respiratory line).

**Introduction.** Field experience gained from operation of nuclear power plants (NPPs) shows that the flows of working medium give rise to mechanical fluctuations and vibration of equipment and its elements. These processes are among the main factors determining the dynamic loads exerted on the equipment and the equipment service life and reliability. The most hazardous phenomena occur during interaction of equipment with a flow of fluid medium in the resonance fluctuation region of mechanical elements and flow, which gives rise to emergencies [1], [2]. For predicting the operation conditions under which resonance amplification of vibrations occurs and for determining the control measures to prevent their occurrence, it is necessary to develop vibro-acoustic certificates of the NPP reactor plant (RP). To this end, it is necessary to know the vibro-acoustic characteristics and, in particular, the natural vibration frequencies of equipment, of its elements and of their connections, as well as the natural oscillation frequencies of coolant in these systems in different modes of RP operation, when abnormalities occur, and in emergencies.

With the NPP RP's vibro-acoustic certificate available, it becomes possible to develop methods and means to prevent the conditions causing the occurrence of resonance interaction between equipment vibrations and pulsations of coolant or working fluid in operational and emergency modes. To this end, it is necessary to ensure mismatch (discrepancy) between the peaks of spectral characteristics of signals from the sensors measuring working medium pressure pulsations and signals from the sensors measuring vibrations, displacements, and dynamic stresses.

Unsteady hydrodynamic processes in the coolant (elastic waves, turbulence, vortex generation, cavitation, etc.) and the main circulating pumps (MCPs) are the main sources exciting oscillations in the primary coolant circuit of an NPP equipped with a water-cooled water moderated power generating reactor (commonly known in Russia and abroad as WWER). The oscillatory properties of the primary coolant circuit's hydro mechanical system are not merely a superposition of the properties of its constituent parts (the reactor, steam generator, pressurizer, pipelines, etc.), but acquire new systematic properties. The new qualitative effects [2] resulting from the system properties of oscillatory processes in the reactor coolant circuit are determined by the nonlinear dependence of pressure difference across the circuit elements on the coolant mass flow rate.

**Formulation of the problem.** The calculated and experimental substantiation of the methods for predicting and preventing the onset of conditions under which vibro-acoustic resonances arise in the primary coolant circuits of WWER based NPPs is carried out for the following purposes:

- extending the service life, modernizing, and improving the design and engineering developments, technical diagnostic tools, and systems for controlling the technological processes at NPPs;
- reducing the probability of sudden equipment failures;
- optimizing the design and engineering solutions for ensuring seismic stability of an NPP as a whole taking into account the mutual influence of the dynamic processes that take place in NPP building structures and process systems and resonance amplification of dynamic stresses under the effect of external periodic loads.

**Results of noise analysis in the WWER-440.** Mechanical vibrations of the reactor pressure vessel (RPV) and reactor internals (RI) as well as standing pressure waves (SPW) could be detected and identified by analysis of the signals of the standard reactor instrumentation of pressurized water reactor (PWR) and WWER (Russian PWR-type reactors). The results of these measurements and identification demonstrate that noise analysis is of high usefulness for monitoring the mechanical and thermohydraulic operating condition [3]. The isometric view of Fig. 1 illustrates the primary circuit with RPV, upper block (UB) with control rod drives, main circulation pumps (MCP), valves (V) and steam generators (SG). Sensor Position at NPP Dukovany with WWER-440 is showed in Fig. 2.

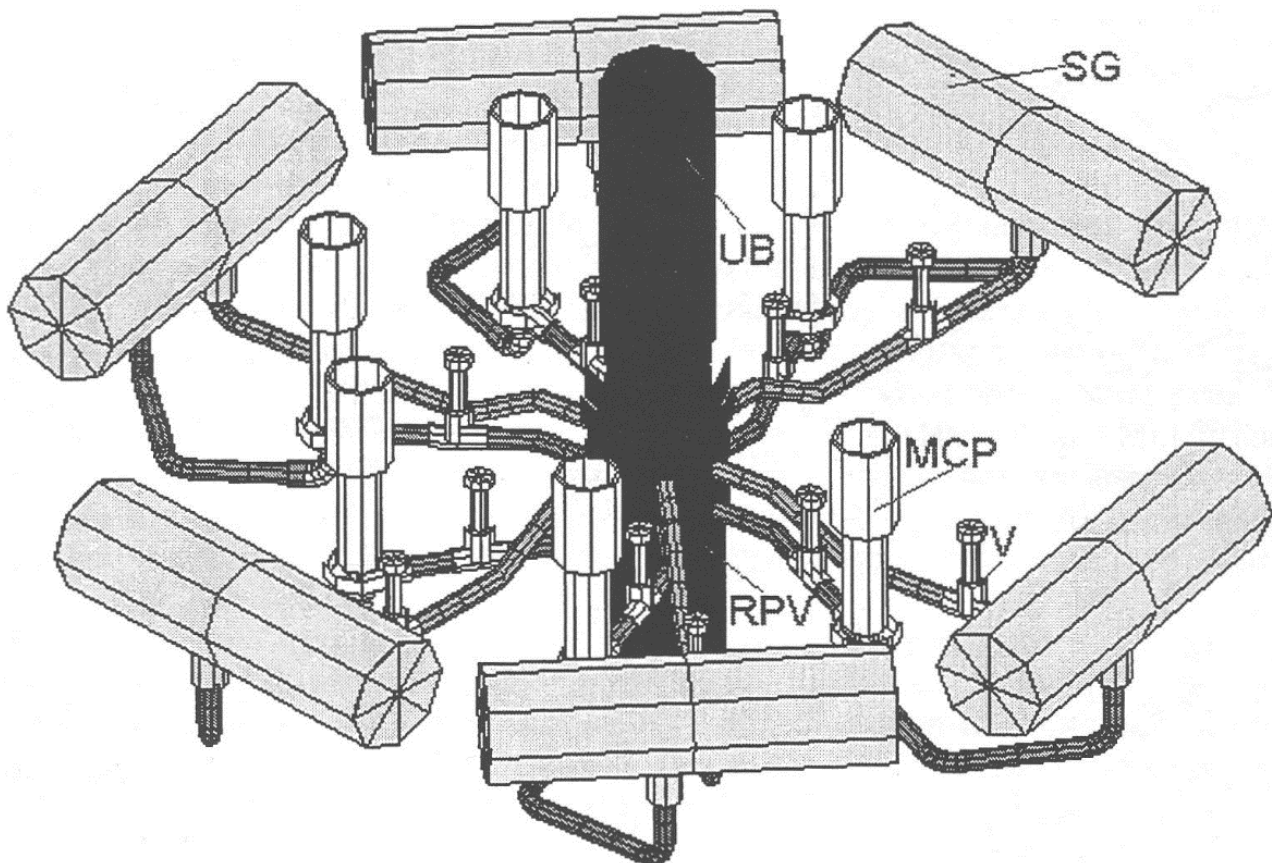


*Fig. 1. The isometric view of the primary circuit WWER-440*

The fluctuations of excore neutron flux signals can be caused by nuclear-thermohydraulic effects, by pressure-reactivity effects and/or by the vibrations of reactor components, mainly by the large

components like reactor pressure vessel, core barrel etc. The first modes of fuel assembly (FA) vibrations can also affect the signals of excore neutron chambers. In Fig. 3 typical normalized auto power spectral densities (NAPSD) of some signals of excore chambers of NPP unit 1, 2 and 4 are shown in Fig. 2.

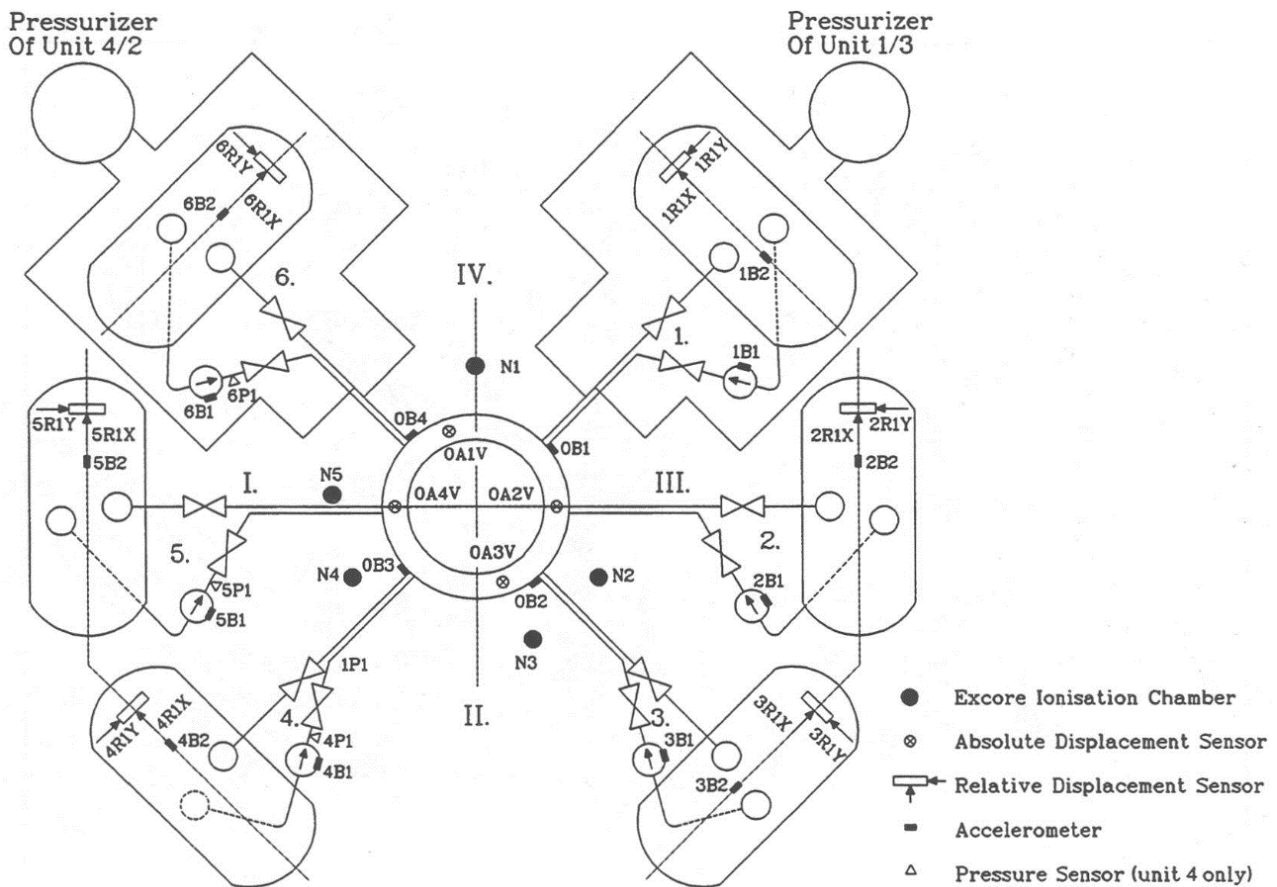


*Fig. 2. Sensor Position at NPP Dukovany*

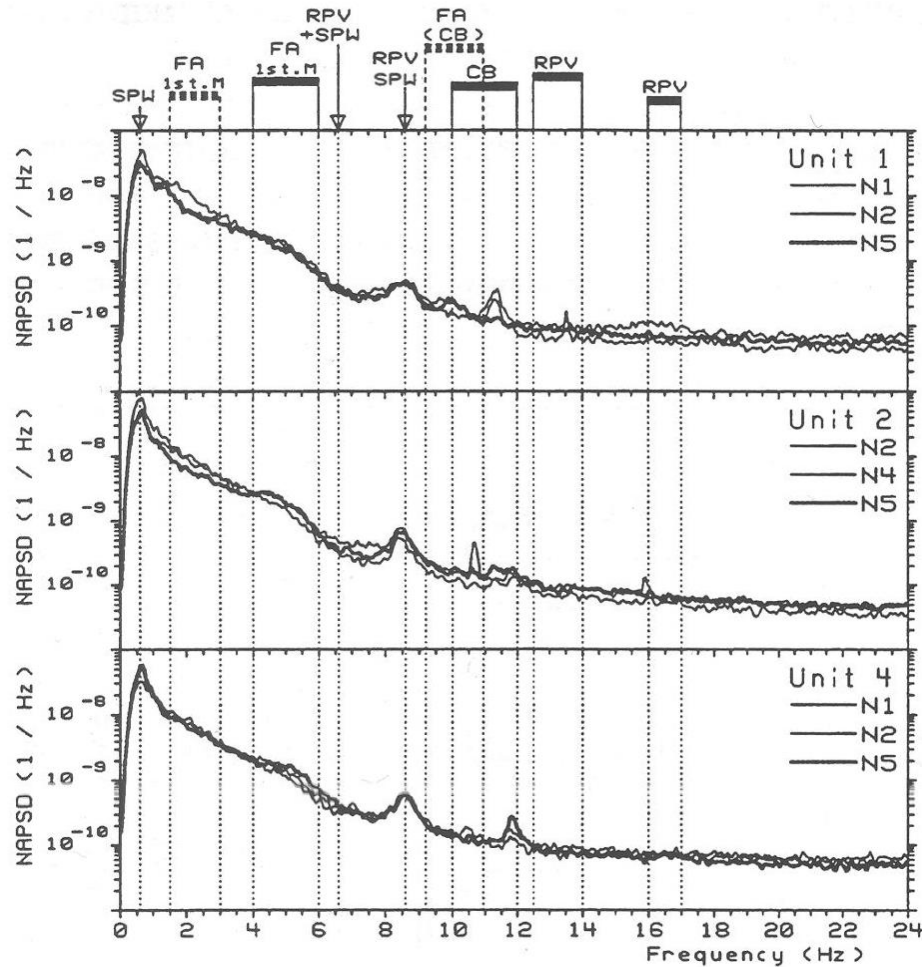


Fig. 3. NAPSD of Excore Neutron Flux

In the units 1, 2 and 4 of NPP Dukovany several movements of the RPV, CB and core basket can be identified in the auto power spectral densities of the signals of the absolute displacement sensors mounted at the top of the RPV (Fig. 2) as shown in Fig. 4. Vibrations of RPV, core barrel and core basket have been observed in WWER-type reactors and in other PWRs and BWRs [4]. In the neutron and displacement spectra (Fig. 3 and Fig. 4) and in the coherence among the signals of neutron chambers, of displacement sensors as well as among any neutron flux and displacement a distinct peak is around 8.6 Hz. As it can clearly be seen, all the signals are in phase in that frequency area. This can be interpreted [3] as a vertical movement of the RPV with its internals. In addition, a coherence exists to the signals of displacement sensors at the SG and of the accelerometers at the MCPs. From the fact, that all the signals are correlated at 8.6 Hz it was concluded, that the vertical movement of the reactor pressure vessel is transduced to the pumps and steam generators via the connecting pipes.

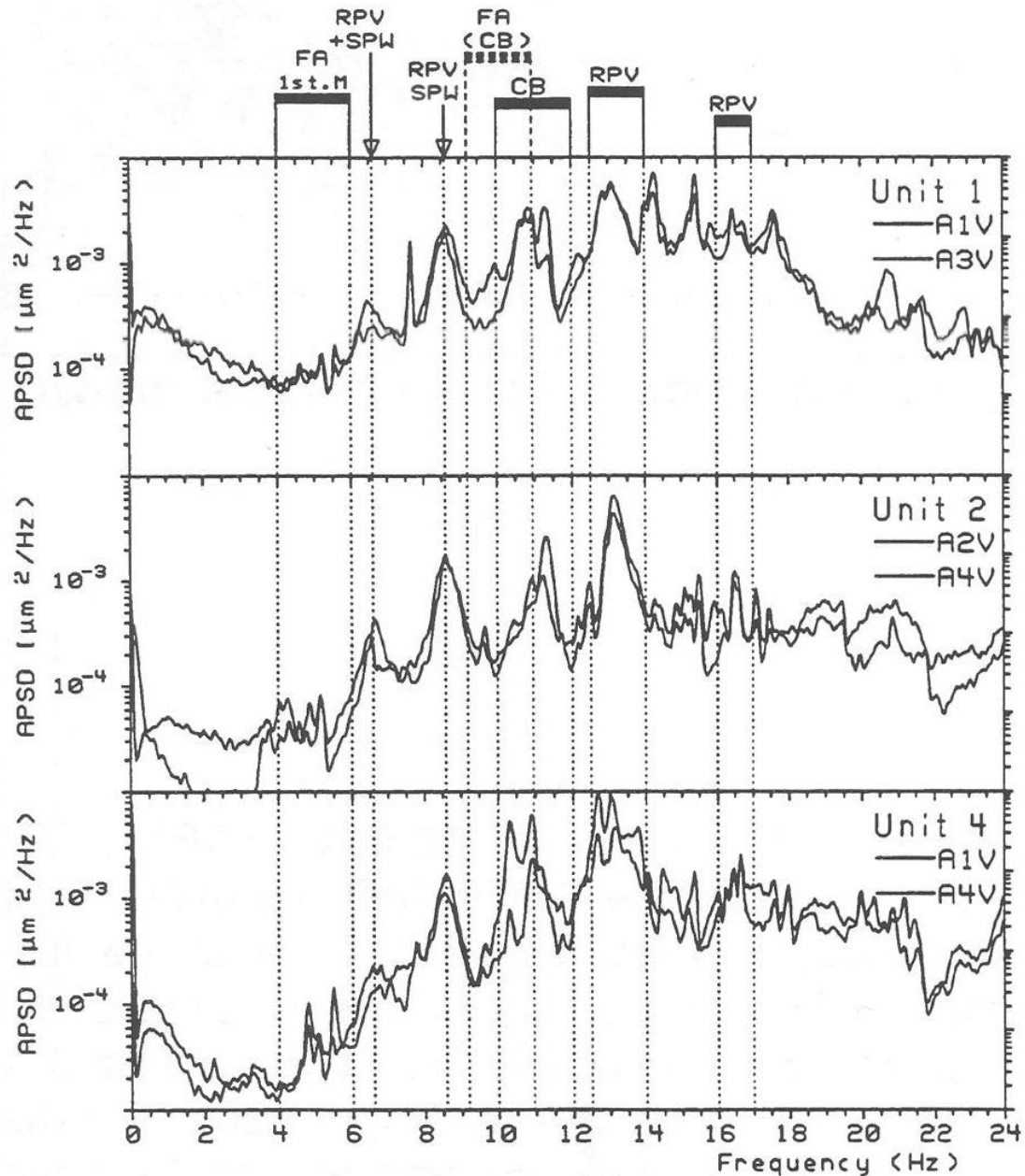


Fig. 4. APSD of Displacement Signals

Pendular movements of the RPV and CB can be identified from the phase relation among the signals of the displacement sensors around the frequencies 11.5 Hz and 13.5 Hz. At 6.6 Hz another pendular movement of the RPV combined and forced by a standing pressure wave (SPW) is visible. The peak around 13.5 Hz has been interpreted as pressure vessel pendular movement of unit 4 in NPP Dukovany previously.

In the case of the SPW at 0.6 Hz, clearly seen in Fig. 5, it was proved in other WWER- type reactors [5], [6] that this is a hydraulic oscillation between pressurizer and reactor pressure vessel. The influence of this low frequency SPW to the reactivity is the same as in case of the 8.6 Hz resonance (see coherence between pressure and neutron flux at 0.6 Hz and at 8.6 Hz in Fig. 5).

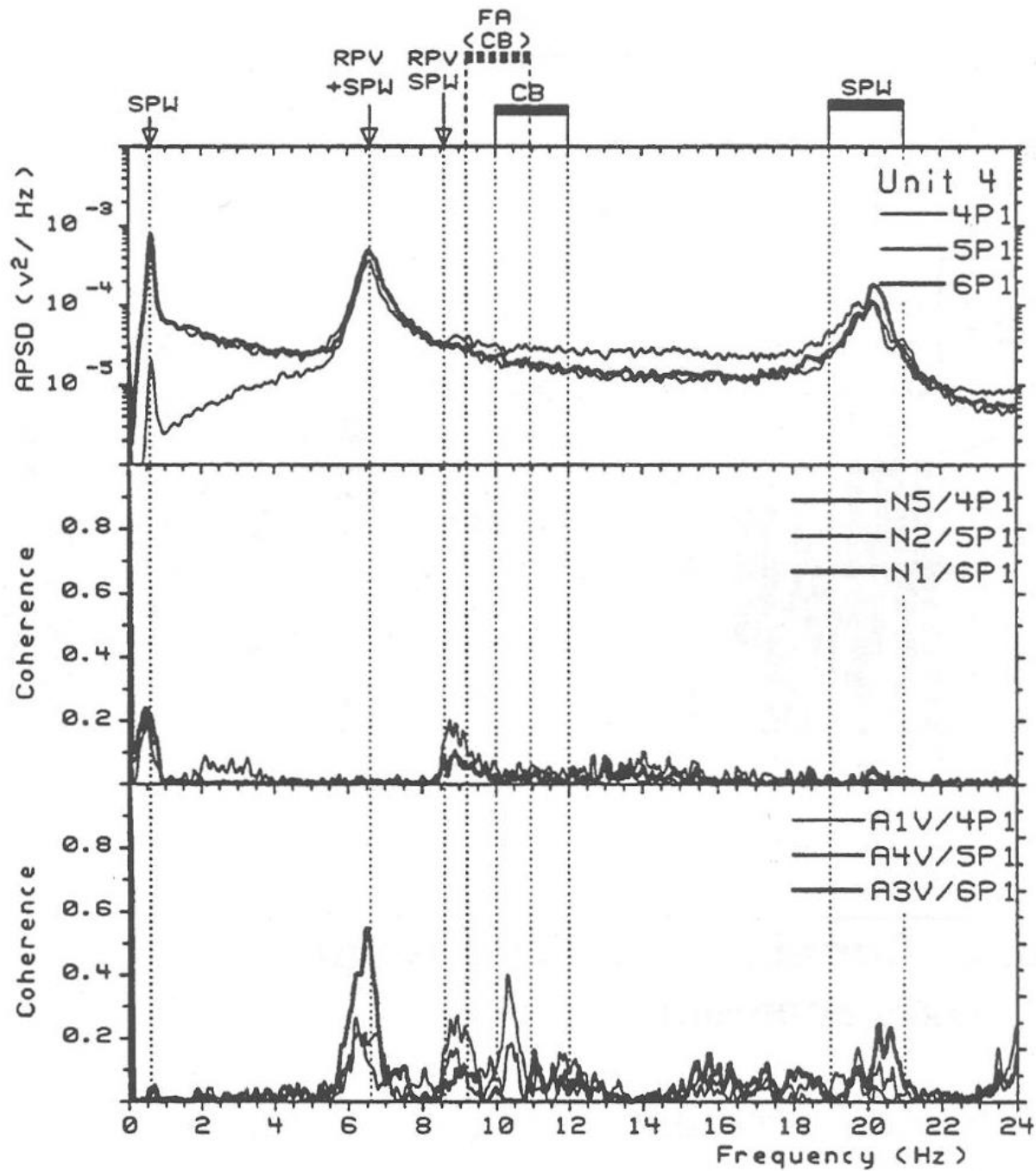


Fig. 5. APSD of Pressure Signals and Correlation to Neutron Flux and Displacement [3]

Single-loop design of Reactor WWER-440 of Novovoronezh NPP shown in Fig. 6.

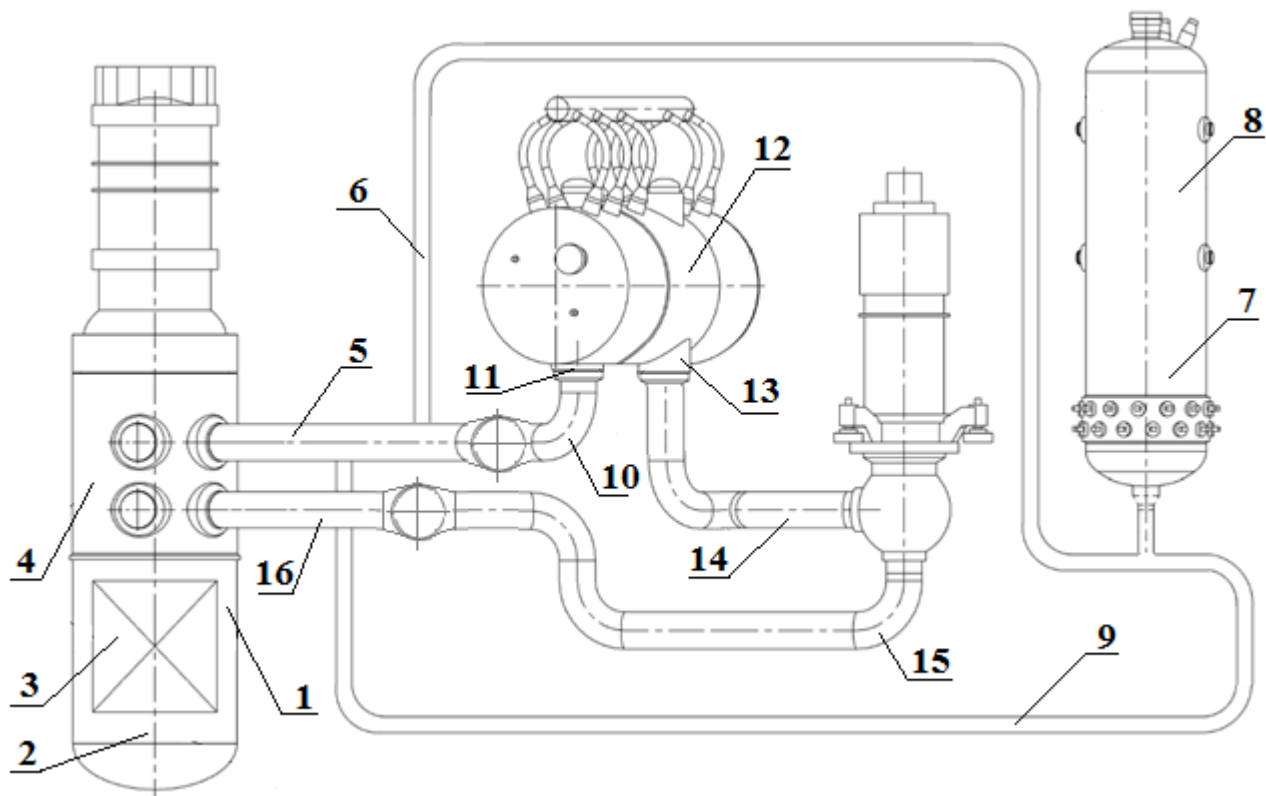


Fig. 6. Single-loop design of Reactor WWER-440 of Novovoronezh NPP

Acoustic elements: 1 – down camera , 2 – bottom plenum, 3 – reactor core, 4 – top plenum, 5 – «a hot loop» from a reactor up to an input in hot collector steam generator (SG) , 6, 9 – the respiratory pipelines, 7– volume of water in pressurizer (PR), 8 – volume of steam in pressurizer, 10- a «hot loop» from valve to hot collector, 11 – hot collector of SG, 12 – tubes, 13 – cold collector SG, 14 – «a cold loop» from an output from cold collector of SG up to MCP, 15 – «cold loop» from MCP to the valve, 16 – «cold loop» from MCP to reactor pressure vessel.

Standing pressure waves at 6.6 Hz and 20 Hz can be clearly identified in the auto power spectral densities of the pressure signals (Fig. 5). The one at 6.6 Hz is correlated to the pendulum movement of the RPV). Knowing the length of the pipes and the sound velocity in the cooling water the standing pressure wave at 6.6 Hz can be localized between the main valve installed on the pump outlet, and down camera 1 in Fig. 6.

The knowledge and monitoring of SPW can be very important for early failure detection, because even small changes in the thermohydraulic conditions (changes of water level in pressurizer, temperature changes of cooling water, blockages, boiling etc.) will change the frequency of SPW in a forecasting way. These changes can be detected by noise analysis in a beginning stage.

Well known the effect of the forced vibrations of all primary loop components due to residual imbalances of the MCP due to the pressure fluctuations caused by it. As it showed in [1], the rotation frequency of MCP will be multiplied due to nonlinear properties of hydraulic elements of primary loops. The nonlinear hydraulic elements possess the property of transformation of the external periodic loads frequency. This means that the spectral function of the response to a harmonic impact contains new frequencies, which have not founded in the acting sources of oscillations.

The most hazardous phenomena occur during interaction of equipment with a flow of fluid medium in the resonance fluctuation region of mechanical elements and SPW, which gives rise to emergencies [1], [2]. For predicting the operation conditions under which resonance amplification of vibrations occurs and to prevent their occurrence, it is necessary to develop vibro-acoustic certificates of the

NPP. To this end, it is necessary to know the vibro-acoustic characteristics and, in particular, the natural vibration frequencies of equipment, of its elements and of their connections, as well as the natural oscillation frequencies of coolant in these systems in different modes of operation, when abnormalities occur, and in emergencies.

With the NPP RP's vibro-acoustic certificate available, it becomes possible to develop methods and means to prevent the conditions causing the occurrence of resonance interaction between equipment vibrations and pulsations of coolant or working fluid in operational and emergency modes. To this end, it is necessary to ensure mismatch (discrepancy) between the peaks of spectral characteristics of signals from the sensors measuring working medium pressure pulsations and signals from the sensors measuring vibrations, displacements, and dynamic stresses.

Accident at Fukushima NPP demonstrated need for stricter regulations to ensure seismic resistance of NPP and the need to develop and implement additional anti-seismic measures in the course of their operation. This is particularly relevant issue for NPP are in operation 20 years or more, designed on obsolete regulatory requirements and the original seismic data. To solve the problem of seismic resistance of NPP must use a differentiated approach to the analysis and provide seismic stability: a) for existing NPP and b) for a newly built NPP. For existing plant, analysis with the actual residual life of refusal and damage to equipment and pipelines, including taking into account the activities carried out to extend the life of plants. For newly, built NPP to ensure their seismic resistance should be in accordance with current regulatory requirements of normative documents. Since the earthquake resistance of pipeline systems justify not only experimental but also computational methods, on the construction of dynamic models is of great importance. Question the validity of seismic nuclear piping systems are constantly evolving and improving. It focuses on the reliability of calculation methods and computer software, computer models, the values taken into account damping. As a seismic accelerogram used synthesized, and in determining the stability of sinusoidal vibration - harmonic load or broadband random vibration. Experimental and analytical evaluation method coolant nuclear power installation includes experimental and calculated determination of the amplitude-frequency response and phase response of the control points of the circuit under pulsed acoustic (shock) excitation of damped oscillations or a resonant excitation of forced oscillations in the frequency range. PNAE-G-7-002-86 and other regulations adopted standard value of the logarithmic coefficient of oscillation (decrement)  $d$  for the process equipment and piping plant, equal to 0.02, in the absence of reliable experimental data. However, not identified numerous instances in which  $d < 0.02$ . Because of this, the adoption of normative values of 0.05, as proposed in the methodology of seismic re-evaluation of existing NPP in the United States, often lead to unreasonably low levels of seismic effects. In this regard, the development of methods that increase the reliability of estimates of the logarithmic decrement of coolant is an extremely important task and its solution is necessary to ensure the seismic resistance of existing and planned NPP.

The structure of nuclear power construction is the basic equipment and connecting lines. Arising from the use of vibration significantly reduce the life of equipment, narrowing the range of acceptable modes of nuclear power, can cause serious accidents. In this connection, it is expedient development of mathematical models of acoustic vibrations of curved space and coolant pipes. Of particular importance is the use of one-dimensional models. They adequately describe the long-wavelength fluctuations of pipelines as well as acoustic oscillations of coolant, to determine the appropriate eigenfrequency and bandwidth of the acoustic circuit. Due to the urgency of the problem of improving the reliability of estimates of seismic effects on structures necessary to solve the nuclear power more of the following interrelated objectives:

- Develop methods for calculating  $Q$ -factor, the logarithmic decrement of coolant and bandwidth acoustic coolant;
- Carry out calculations of these parameters in the operating conditions for a modern NPP;
- Make recommendations for additions and improvement of anti-seismic action in the course of their operation and in the design phase.

**Method of calculation of acoustic performance coolant.** As noted in [2], important for reliable operation of equipment is the lack of coincidence between the natural frequencies of the interacting components of the system. It is important to understand that for thermal-hydraulic systems is a resonance phenomenon is observed both between the elements of equipment and external exciting force, and between equipment and working flow.

Determination of natural frequency, the rate of decay and other acoustic parameters for the working environment in the pipe, and more complex hydraulic systems, in general, is not certain.

**Calculation of eigenfrequency of coolant pressure oscillation (EFCPO) using method of electro-acoustic analogies.** In general, the system of equations describing the fluid dynamics of little use for the analysis of acoustic characteristics. One of the approximations used is to cast the equations of dynamics to the so-called telegraph equations.

The table 1 presents the list of the equivalent parameters.

Table 1. Equivalent parameters analogies

Acoustic system			Electrical System		
Parameter	Designation	Unit	Parameter	Designation	Unit
pressure drop	$\Delta P$	$N/m^2$	voltage	$u$	volt
volume flow	$W$	$m^3/s$	current	$i$	Amper
acoustic compliance	$C$	$m^3 \cdot s^2/kg$	capacity	$C$	Farad
acoustic weight	$m$	$kg/m^4$	inductance	$L$	Henry
active resistance	$R$	$kg/(s \cdot m^4)$	active resistance	$R$	Ohm
reactance	$X$	$kg/(s \cdot m^4)$	reactance	$X$	Ohm
active power	$NR$	Watt	active power	$P$	Watt
reactive power	$NX$	Watt	reactive power	$Q$	Var
wave resistance	$Z_w$	$kg/(s \cdot m^4)$	wave resistance	$Z_w$	Ohm
Own circular frequency	$\omega_0$	rad/s	Own circular frequency	$\omega_0$	rad/s
eigenfrequency	$f_0$	Hz	eigenfrequency	$f_0$	Hz
The bandwidth	$\Delta f$	Hz	The bandwidth	$\Delta f$	Hz

Like any constructive element, which has elasticity, heat transfer fluid has its own frequency, which may resonate with the sources of disturbances at the frequencies or less distinct lines in the spectrum (on site), the frequency of the working body is different frequency sources of hydrodynamic perturbations. To calculate the natural frequency of the coolant used method of electro-acoustic analogies.

The mass of the acoustic environment in a cell density  $\rho$  of channel length  $l$  and cross section  $S$  is given by:

$$m = \frac{\rho l}{S} \quad (1)$$

Acoustic compliance  $C$  of environment in the channel with volume  $V$  is:

$$C = \frac{V}{nP} \quad (2)$$

where  $n$  – the polytrophic index,

$P$  – the pressure in the channel.

It is known that the cumulative rate of propagation of vibrations in the environment is:

$$a = \sqrt{\frac{nP}{\rho}} \quad (3)$$

Using Eq. (3) we get:

$$C = \frac{V}{\rho a^2} \quad (4)$$

Own circular frequency of the medium in the channel:

$$\omega_0 = \frac{1}{\sqrt{Cm}} \quad (5)$$

The natural frequency of the medium:

$$f_0 = \omega_0 / 2\pi \quad (6)$$

Where  $R$  – hydraulic resistance of channel is determined by viscous forces.  $X$ -reactance is determined by the elastic forces. The wave resistance is calculated as:

$$Z_w = \sqrt{\frac{m}{C}} \quad (7)$$

The  $Q$ -factor – numerical characteristic of the resonance properties of the oscillating system, indicating how many times the amplitude of the steady-state forced vibrations at resonance exceeds the amplitude of forced vibrations far from resonance, that is in such low frequencies, where the

amplitude of forced vibrations can be considered independent of frequency  $Q$ -factor of an element or circuit, which determines the rate of decay of perturbations, given by:

$$Q = \frac{\Delta P_{C_0}}{\Delta P} = \frac{\Delta P_{m_0}}{\Delta P} = \frac{W_0 \omega_0 m}{W_0 R} = \frac{W_0 \frac{1}{\omega_0 m}}{W_0 R} = \frac{\sqrt{m/C}}{R} = \frac{Z_B}{R} \quad (8)$$

where  $W_0$  – the volume flow rate at resonance.

Quality factor and bandwidth are related by the following expression:

$$Q = \frac{f_0}{\Delta f} \quad (9)$$

Active power oscillation with the current flow  $W$  is defined as:

$$N_R = W^2 R \quad (10)$$

Reactive power fluctuations with the current flow  $W$  is defined as:

$$N_Z = W^2 X \quad (11)$$

As for the electrical circuits and circuits for electro-hydraulic circuit, the following rules. When the elements are connected in series, the total acoustic mass and compliance are:

$$\begin{aligned} m_\Sigma &= \sum_i m_i \\ C_\Sigma &= \sum_i C_i \end{aligned} \quad (12)$$

In the parallel connection of elements:

$$\begin{aligned} \frac{1}{m_\Sigma} &= \sum_i \frac{1}{m_i} \\ \frac{1}{C_\Sigma} &= \sum_i \frac{1}{C_i} \end{aligned} \quad (13)$$

Logarithmic decrement of oscillations ( $d$ ) determined from the relation:

$$d = \pi/Q \quad (14)$$

**Acoustic characteristics of the UNIT 3 of Novovoronezh NPP with WWER-440.** Worked out methods of calculating the eigenfrequency of the coolant pressure oscillation (ECPO) in the first loop equipment is based on the using of the value hydraulic shock velocity (HSW) instead of using the value propagation of sound velocity in the working environment. Such an approach is correct also when considering the water-steam circuit, or boiling water reactors (BWR).

Single-loop Acoustic Scheme of Reactor WWER-440 of Novovoronezh NPP shown in Fig. 7.

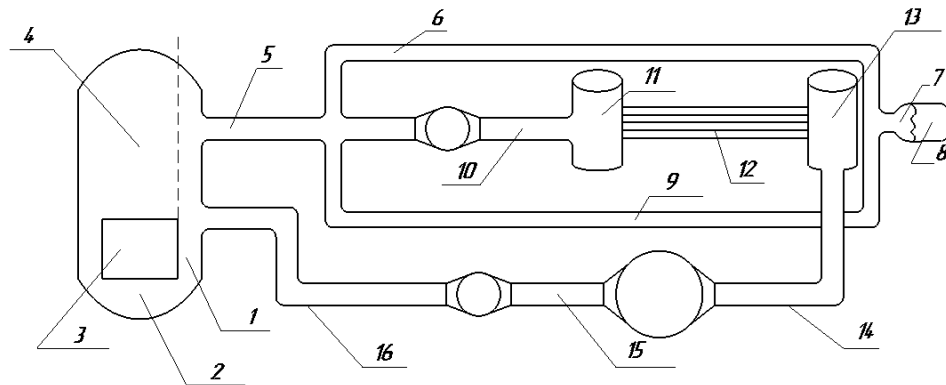


Fig. 7. Single-loop Acoustic Scheme of Reactor WWER-440 of Novovoronezh NPP

Acoustic elements: 1 - down camera , 2 – bottom plenum, 3 - reactor core, 4 – top plenum, 5 – «a hot loop» from a reactor up to an input in hot collector steam generator (SG) , 6,9 - the respiratory pipelines, 7– volume of water in pressurizer (PR), 8 – volume of steam in pressurizer, 10- a «hot loop» from valve to hot collector, 11 - hot collector of SG, 12 - tubes, 13 - cold collector SG, 14 – «a cold loop» from an output from cold collector of SG up to MCP, 15- «cold loop» from MCP to the valve, 16 – «cold loop» from MCP to reactor pressure vessel.

Table 2 shows the measuring values of the dominant peak frequencies in the spectrum obtained by pressure pulsations sensor in nominal mode; calculated values of eigenfrequencies of coolant pressure oscillation (EFCPO) for each acoustic element and their compositions and the value of difference.

Table 2. Comparing the calculation results with measurement data table

$N_{\text{sect}}$	$f_{\text{calc}}$	$f_{\text{meas}}$	$\Delta f$
1	17.5	17.7	-0.2
2	42.8	42.7	0.1
3	64.9	-	-
4	24.5	24.7	-0.2
5	17.3	17.7	-0.4
6	6.3	6.6	-0.3
7	23.9	23.6	0.3
8	11.5	11.4	0.1
9	5.9	6.6	-0.7

10	37.0	36.6	0.4
11	35.7	35.1	0.6
12	17.4	17.7	-0.3
13	40.9	41.4	-0.5
14	20.0	19.5	0.5
15	54.8	-	-
16	35.0	35.1	-0.1
16+1	6.9	6.6	0.3
1+2	10.9	11.0	-0.1
1+2+3	9.3	9.5	-0.2
1+2+3+4	6.1	6.6	-0.5
10+11	16.3	16.3	0.0
13+14	12.2	12.7	-0.5
11+12+13	8.9	8.8	0.1
10+11+12+13+14	4.5	4.5	0.0
7+8	3.8	3.8	0.0
6+7	0.8	0.8	0.0
9+7	0.8	0.8	0.0
6+7+8	0.1	-	-
9+7+8	0.1	-	-
16+1+2	4.5	4.5	0.0
16+1+2+3	4.1	3.8	0.3
16+1+2+3+4	2.8	3.4	0.6
16+1+2+3+4+5	1.9	2.1	0.2

The following abbreviations are used in Table 1:

$f_{meas}$  – dominant frequency peak in the spectrum obtained from the pressure sensor ripple, Hz;

$f_{calc}$  – calculated ECPO at the sector  $N_{yq}$ , Hz;

$\Delta f$  – difference between the calculation  $f_{calc}$  and measurement  $f_{calc}$  at the sector  $N_{yq}$ , Hz;

$N_{sec}$  – Number of acoustic circuit section.

APSD WWER-440 (unit 3 of Novovoronezh NPP) is presented in Fig. 8.

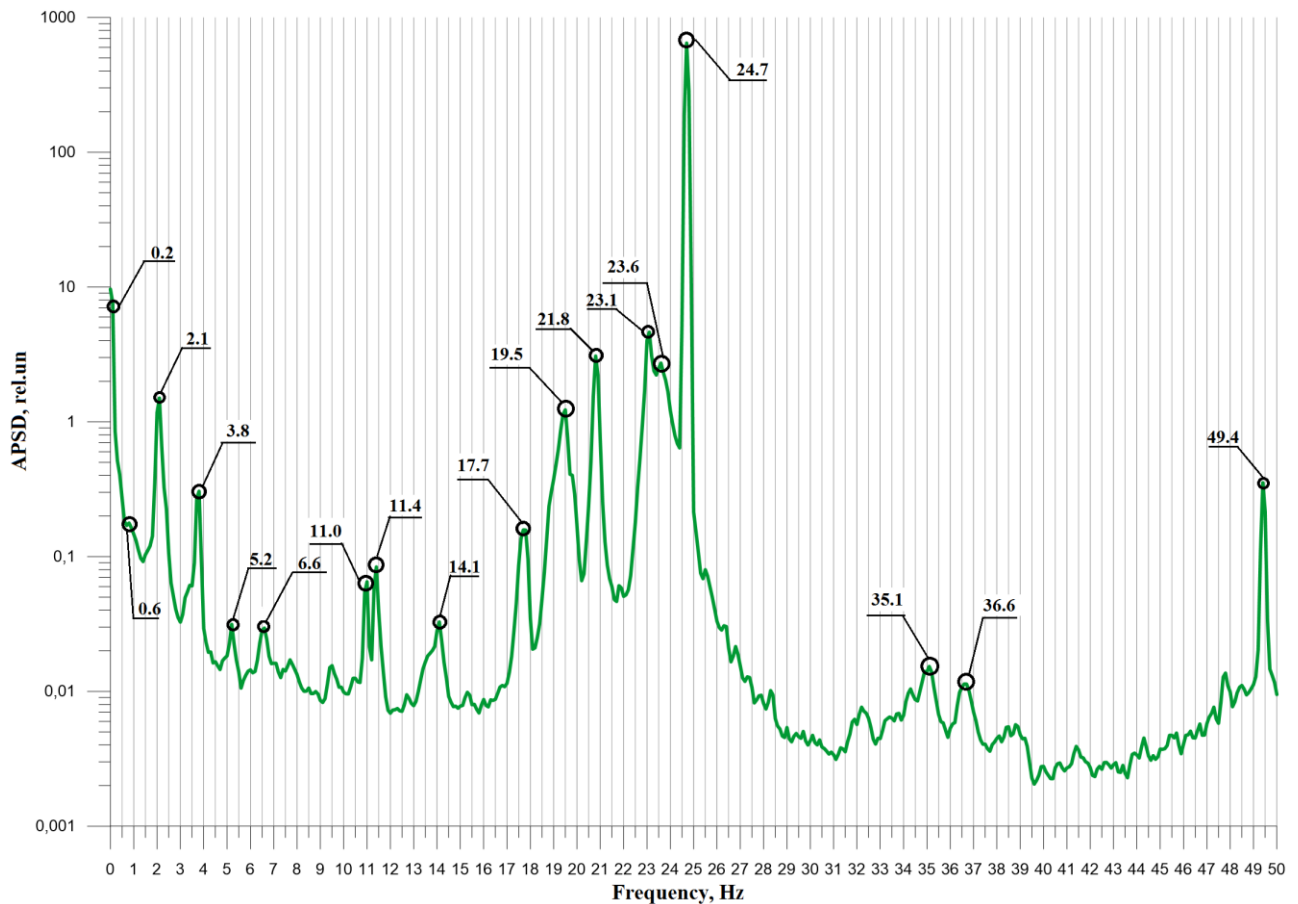


Fig. 8. APSD WWER-440

It should be pointed out that the natural coolant pressure pulsations caused by elastic waves do not have a strictly fixed frequency and usually manifest themselves in the definite range Hz depending on many factors (the equipment acoustic parameters, which are individual for each power unit; the temperature and pressure parameters; the level in the pressurizer; etc.).

It should be pointed also that pressurizer manifest itself as managed Helmholtz resonator generating a number of SPW (with eigenfrequencies of steam volume, water volume and their combination with coolant volume of respiratory line).

Comparing the calculation results with measurement are shown in table 3.

Table 3. Comparing the calculation results with measurement (Dukovany) data [3]

Source	Frequency, Hz	$N_{sect}$	$f_{calc}, Hz$
<i>Figure 3 - NAPSD of Excore Neutron Flux</i>			
SPW	0.6	6+7	0.8
		9+7	0.8
FA	1.5-3.0	6	6.3
		9	5.9
	4.0-6.0	7+8	3.8
		1+2+3+4	6.1

Source	Frequency, Hz	$N_{sect}$	$f_{calc}$ , Hz
		10+11+12+13+14	4.5
RPW + SPW	6.6	6	6.3
	8.6	16+1	6.9
		11+12+13	8.9
FA(CB)	9.1-11.0	1+2	10.9
		1+2+3	9.3
		11+12+13	8.9
RPV	12.5-14.0 16.0-17.0	1	17.5
		5	17.3
		8	11.5
		12	17.4
		13+14	12.2
		10+11	16.3
CB	10.0-12.0	1+2	10.9
		13+14	12.2

Figure 4 – APSD of Displacement Signals

FA	4.0-6.0	6	6.3
		9	5.9
		7+8	3.8
		1+2+3+4	6.1
		10+11+12+13+14	4.5
RPW + SPW	6.6	6	6.3
	8.6	16+1	6.9
		11+12+13	8.9
FA(CB)	9.1-11.0	1+2	10.9
		1+2+3	9.3
		11+12+13	8.9
RPV	12.5-14.0 16.0-17.0	1	17.5
		5	17.3
		8	11.5
		12	17.4
		13+14	12.2
		10+11	16.3
CB	10.0-12.0	1+2	10.9
		13+14	12.2

Source	Frequency, Hz	$N_{sect}$	$f_{calc}$ , Hz
Source	Frequency, Hz	$N_{sect}$	$f_{calc}$ , Hz
<i>Figure 5 – APSD of Pressure Signals and Correlation to Neutron Flux and Displacement</i>			
SPW	0.6	14	20.0
	19.0-21.0	6+7	0.8
		9+7	0.8
RPW + SPW	6.6	6	6.3
	8.6	16+1	6.9
		11+12+13	8.9
FA(CB)	9.1-11.0	1+2	10.9
		1+2+3	9.3
		11+12+13	8.9
RPV	12.5-14.0	1	17.5
		5	17.3
	16.0-17.0	8	11.5
		12	17.4
		13+14	12.2
		10+11	16.3
CB	10.0-12.0	1+2	10.9
		13+14	12.2

**Exceeding the design level of equipment vibrations under external periodic loads caused by an earthquake.** At present, after the events occurred at the Fukushima Daiichi NPP, stress tests for external impacts exceeding the design level are to be mandatorily carried at all Russian NPPs. In view of this requirement, calculated analyses for external impacts exceeding the design level must be carried out for the NPP reactor plant equipment and pipelines apart from calculations for the design level of impacts. In carrying out calculations for estimating the intensity of vibrations in equipment and acoustic pulsations in the coolant, the external impact during an earthquake is specified in the form of response spectra graphs of a no conservative system with one degree of freedom as a function of natural vibration frequency and energy dissipation factor [7]. In so doing, the response spectra for displacements, velocities, and accelerations of the system with one degree of freedom are used. Acceleration spectra are used in most frequent cases. Fig. 9 shows the calculated response spectra  $g$  corresponding to the relative damping equal to 2%.

It follows from a comparison of the structure foundations response spectrum shown in Fig. 9 with the APSD of displacement signals showed in Fig. 5, that the vibration frequencies of the NPP with WWER-440 main equipment fall in the frequency band in the response spectrum corresponding to the maximal envelope response spectra. It is well known that the experimental methods of investigations carried out under laboratory conditions and under the conditions of real NPPs do not always fully simulate the specific features pertinent to interaction of an NPP with seismic loads, due to which the predicted results may differ essentially from the real ones. Lack of the results from experimental investigations on a full-scale facility is one of the main factors behind such inconsistency. Such investigations would make it possible to substantiate the seismic stability of

NPPs taking into account their specific features, the main of them being the neutron physical and thermal hydraulic processes under the conditions when they are superposed with external dynamic forces simultaneously acting on all building and process systems. Long-term experience gained in Russia with combined calculated and experimental substantiation of NPP seismic stability [7] is of much importance for ensuring seismic stability of nuclear power facilities. The conceptual and procedural levels include the relevant IAEA standards. One specific feature of the Russian system of regulatory documents [8] is that they put forward the mandatory requirement of studying the dynamic characteristics of systems and components important to safety using the dynamic test method under the real conditions of their fastening and associated pipe work at the NPPs.

Natural frequency oscillation can be determined by calculation methods, but it requires the most accurate simulation of the equipment, including a consideration of all possible factors affecting the natural frequencies such as breakout conditions, the availability of connected equipment, records and elastic ties etc. For «rough» (preliminary) dynamic strength evaluation is acceptable settlement definition of natural frequencies, but to get the real forces and stresses arising in the pieces of equipment against external mechanical impacts, we must know the real resonant frequency equipment, adequately define who can only experimental way.

Decrement, in contrast to the natural frequencies can be determined only by experiment, due to the rather complex nature of damping in the physical sense, which is not amenable to rigorous mathematical analysis. Surveys have shown at numerous nuclear power plants that are very common cases where the value decrements are much lower than the standard required in the RF values (2%). Thus, the use of 5% decrement values may lead to an underestimation of seismic impact values in the resonance region in two or more times (Fig. 9).

Transferring the stability analysis of the results of equipment at external influences on one NPP to another similar equipment is unacceptable for the different forms of impact spectra, depending on the specific placement site. An example of the differences perceived stress for various NPP sites presented in Fig. 10. An example of a floor response spectrum, which determines the load on the equipment in earthquake conditions presented in Fig. 11.

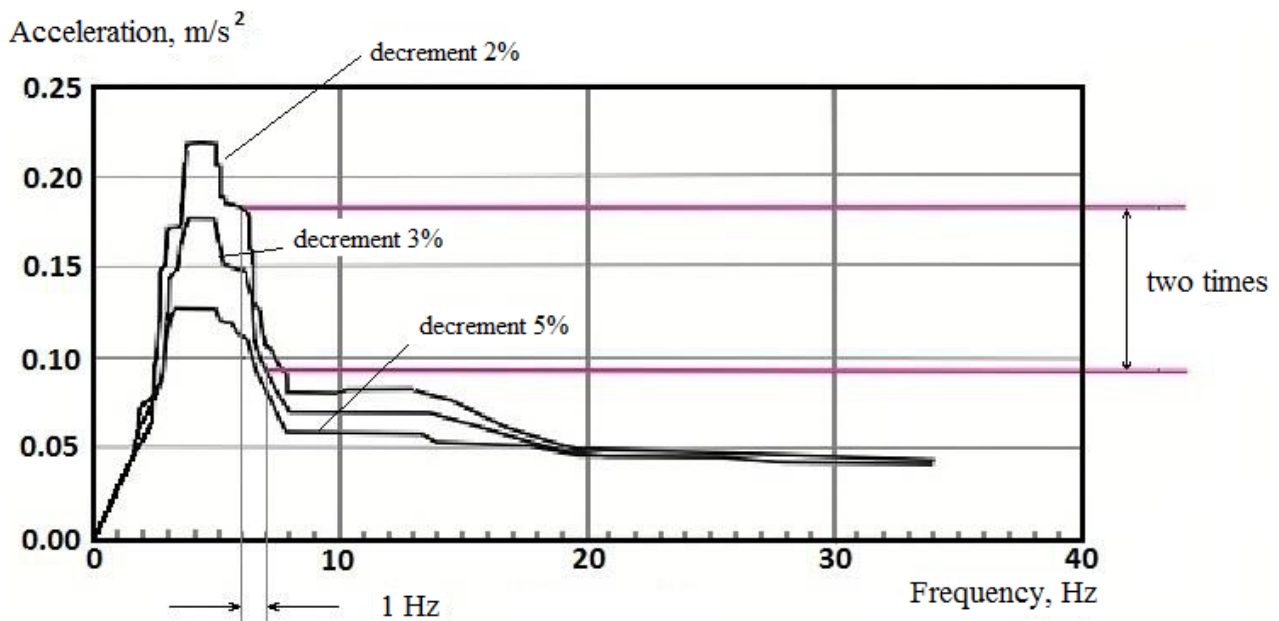


*Fig. 9. An example of the spectrum of responses to the seismic action for the various decrements*

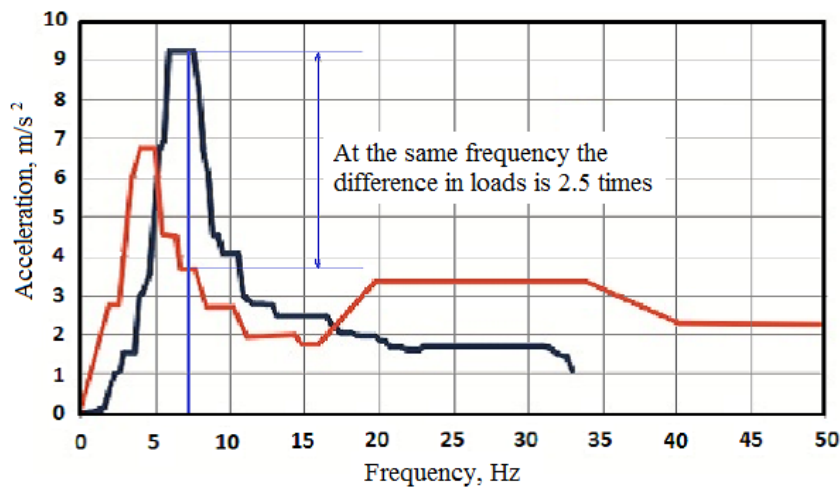


Fig. 10. An example of the differences perceived stress for various NPP sites

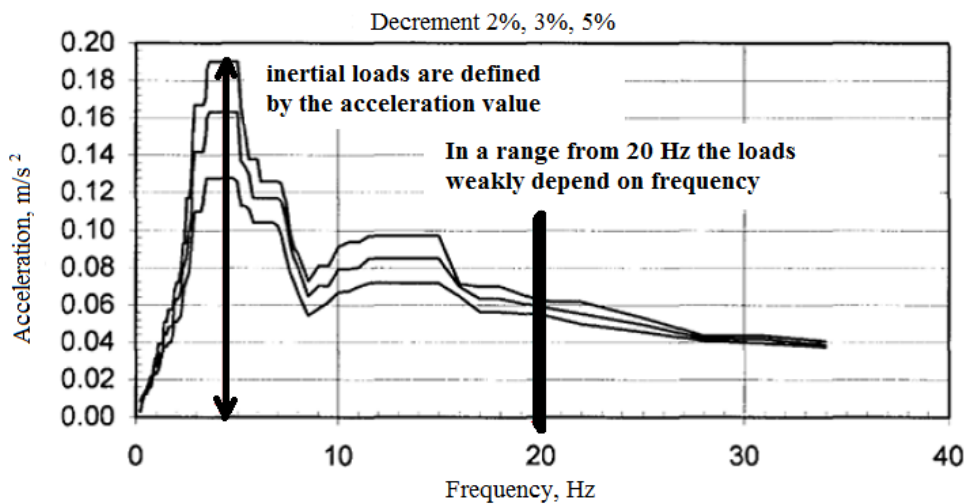


Fig. 11. An example of a floor response spectrum, which determines the load on the equipment in earthquake conditions

Analysis of many spectra response for various NPP has shown that on-load from the seismic effects at the lower of their own equipment frequencies above 20 Hz depends weakly on its own dynamic characteristics. Consequently, lower oscillation frequency equipment was not more than 20 Hz.

Application of the developed methods and algorithms for the identification of the sources of acoustic standing waves 6.6 Hz in the primary circuit of NPP with WVER shows that the source of this ASV is an acoustic circuit is formed by sections 16 and 1, shown in Fig 6.

The developed model can be used both in normal operation and in emergency modes for the following tasks:

- Development of vibro-acoustic certification of reactor facilities;
- Diagnosis and prognosis of equipment condition;
- Improvement of process control;
- Study design and design decisions in the selection of equipment and layout of the reactor heat removal systems;
- Improvement of computer code.

Solution of these tasks will allow giving a scientific substantiation of directions of modernization and improvement of the design development, technical diagnostics and process control systems, NPP. These new systems will be an important additional means of improving the safety, efficiency and operating life, both existing and planned NPP. The developed methods and algorithms for the identification of the sources of the SPW in the primary circuit of NPP with WWER and PWR are designed for use in the following thematic areas of current research and design work, which should be reflected in the work of the industry:

- Justification for the integrity of the main equipment of new switchgear on the life of 60-80 years, including the provision of materials science;
- Study the possibility of extending the operation of existing units over the design life;
- Study the possibility of prediction and prevention of vibro-acoustic resonances in the nuclear power plant equipment in manoeuvring and emergency modes, as well as under the influence of shock and seismic loads.

## References

- [1] K.N. Proskuryakov, Mathematical Models of Sources of Thermohydraulic Disturbances in Circuits of Nuclear Power Stations, *Teploenergetika*, No. 6, 6–11 (1999) *Therm. Eng.*46(6), 439–445 (1999)]
- [2] K.N. Proskuriakov, A.I. Fedorov, M.V. Zaporozhets, Predicting the Conditions under Which Vibro-acoustic Resonances with External Periodic Loads Occur in the Primary Coolant Circuits of WWER-Based NPPs ISSN 0040 6015, *Thermal Engineering*, 2015, Vol. 62, No. 8, pp. 553–559. © Pleiades Publishing, Inc., 2015
- [3] J. Runkel, D. Stegemann, J. Fiedler, P. Hrosso, S. Fignedy, J. Sadilek, J. Huh'n Results of Noise Analysis in the WWER 440 – Type Nuclear Power Plant Dukovany. // SMORN VII, Avignon, France, 19-23 June 1995. NEA OECD Vol. 1, pp.81-85
- [4] Husemann E., Laggiard H.P. Mies, R. Oed, J. Runkel, D. Stegemann BWR Vibration Measurement by Incore Neutron Noise Analysis SMORN VI, Gatlinburg, 199155
- [5] K.N. Proskuryakov, S.P. Stoyanov, G. Nidtsballa, A Theoretical Method for Determining the Natural Oscillation Frequencies of Coolant in the Primary Coolant Circuit of a Nuclear Power Station, *Trudy Mosk. Energ. Inst.*, No. 407, 87-93 (1979)
- [6] G. Por, E. Izsak and J. Valko Some results of noise measurements in a PWR NPP. *Progress in Nuclear Energy*. 1985. Vol. 15, pp. 387-393 Printed in Great Britain. Pergamon Press Ltd.
- [7] P.S. Kaznovskii, K.G. Kas'yanov, A.D. Emel'yanova, A.P. Kaznovskii, S.I. Rysnyi, An analysis of modern Russian and foreign approaches to estimating the seismic stability of NPP equipment under the conditions of its operation, in *Proceedings of the 8th International Scientific\_Technical Conference «Safety Assurance of WWER-Based NPPs»*, Podolsk, May 28–31, 2013. [in Russian].
- [8] M.T. (Methodical Document) 1.2.2.04.0069\_2012: A Procedure for Confirming the Dynamic Characteristics of NPP Power Unit Systems and Components Important to Safety (Rosenergoatom Concern, Moscow, 2012) [in Russian]

## Methods for Solving a Stress Behaviour of Welded Joints under Repeated Loads

Semrád K.<sup>1, a</sup>, Čerňan J.<sup>1, b</sup>

1 – Department of Aviation Technical Studies, Technical University of Kosice, Faculty of Aeronautics, Slovakia

a – karol.semrad@tuke.sk

b – jozef.cernan@tuke.sk



DOI 10.13140/RG.2.1.5113.9440

**Keywords:** finite element analysis (*FEA*), factor of Safety for fatigue stresses (*FSF*), factor of safety for static stresses (*FS*), the stress ratio (*R*), the experimental maximum stress at *R*=0 (*S*<sub>0</sub>), slope of experimental curve (*m*), allowable maximum stress (*f*), equivalent stress (*f<sub>eq</sub>*), bending stress (*f<sub>b</sub>*), shear stress (*f<sub>s</sub>*), yield strength (*f<sub>y</sub>*).

**ABSTRACT.** The article processes issue of strength of cyclically loaded welded joints with a focus on fillet welds. The data for used steels and basic informations were obtained at U.S. Steel's Research Laboratory and from articles by Lehigh University and the University of Illinois in USA. The practical application of the solution is presented for crane car body to crawler connection.

**Introduction.** The paper deals with the design of structural members subjected to repeated loads. The design of fillet welded connections is included and emphasized. The practical application is presented for crane car body to crawler connection.

**Fatigue strength of fillet welded connections.** The fatigue strength of fillet welds depends on the type of connection in which the weld is used; for example, the fatigue strength of a fillet welded lap joint is much lower than the fatigue strength of fillet welded flange to web connections in fabricated beams. Hence, data must be obtained for specific types of fillet welded connections rather than for fillet welds in general.

The fatigue strength of fillet welded flange to web connections in a fabricated member is less than the fatigue strength of the base metal from which the member is fabricated, and cannot be increased significantly by using larger fillet welds. Fatigue data presently available from continuously fillet welded tee specimens loaded axially at the centroid of the tee cross section so that axial stresses but no shear stresses are developed, indicate that such longitudinal flange to web fillet welded connections have fatigue strength equal to, or greater than, transversely groove welded joints with the weld reinforcement in place. This comparison is for welds made in the same steel subjected to equal fatigue lives. Therefore, it is conservative to design longitudinal fillet welded joints subjected to repeated normal stresses only (axial or bending stresses without shear stresses) by the same formulas used to design transversely groove welded joints with the weld reinforcement in place [1].

The available fatigue data on flange to web fillet welds under combined stresses indicate that it is reasonable to design such welds subjected to combined bending and shear stress for the following equivalent stress, *f<sub>eq</sub>*:

$$f_{eq} = \sqrt{f_b^2 + 3f_s^2} \quad (1)$$

where *f<sub>b</sub>* and *f<sub>s</sub>* - are the bending and shear stress present, respectively (*f<sub>eq</sub>* - should be given the same algebraic sign as *f<sub>b</sub>*). The maximum and minimum values of *f<sub>b</sub>* and *f<sub>s</sub>* caused by given loading may be

used to compute the maximum and minimum values of  $f_{eq}$ , respectively. The maximum and minimum values of  $f_{eq}$ , in turn, may then be used to obtain the fatigue life from the appropriate fatigue chart for groove-welded plates. Conversely, Equation (1) can be used in conjunction with allowable stress formulas to determine allowable weld sizes. In many practical applications the effect of shear on the fatigue strength of fabricated beams is small enough to be neglected [2].

**Application of fatigue data to design.** To efficiently design a structure to resist fatigue, each individual detail should be checked for the stress conditions that exist at that detail. For example, in designing a rolled beam with a splice in the region of low stress, the fatigue life of the splice under the low stress would be checked, and the fatigue life of the beam itself would be checked at the location of maximum stress.

To utilize the experimental fatigue charts in the design of structures, however, it is usually necessary to apply a factor of safety to compensate for:

1. Scatter among the fatigue data;
2. And uncertainties in the loading.

The choice of the magnitude and method of application of the factor of safety for a specific application can best be made by the designer. However, a smaller factor of safety is usually justified for fatigue stresses than for non-repetitive stresses because of the minor effect of a few overloads on fatigue life, and the decreased likelihood of the number of stress cycles occurring at the design stress magnitude [3].

One convenient method of applying the factor of safety is to multiply either the maximum design stress or both the maximum and minimum design stresses by the factor and to use the resulting stresses in the mean value fatigue charts to determine expected life. Another method is to derive allowable stress formulas by dividing the stresses in the fatigue charts by the factor of safety. Again, this latter method can be done in several different ways. Both the maximum and minimum stresses corresponding to any point on a life line of an experimental fatigue chart can be divided by the factor of safety to obtain a point on a life line of an allowable stress chart as shown in Fig. 1. Alternatively, the experimental maximum stress and not the minimum stress can be divided by the factor of safety to obtain the allowable stress chart that might be appropriate for some applications in which the minimum stress results from a known dead load. For another alternative, the experimental stress range the difference between the maximum and minimum stresses can be divided by a factor of safety to obtain an allowable stress range [4].

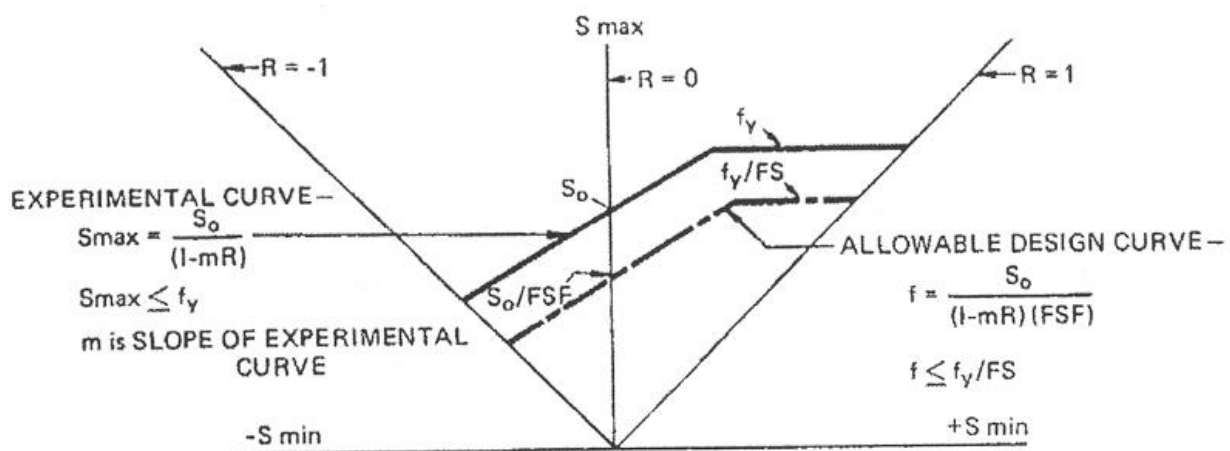


Fig.1. Fatigue chart for design

The allowable design stresses shown in the illustrative fatigue chart (Fig. 1), may be expressed as the smaller of the following equations:

$$f = \frac{S_0}{(1 - mR)(FSF)}, \quad f = \frac{f_y}{FS} \quad (2)$$

In the equations,  $f$  – is the allowable maximum stress;

$S_0$  – is the experimental maximum stress at  $R=0$ ;

$m$  – is the slope of the experimental fatigue curve;

$R$  – is the stress ratio (algebraic ratio of minimum to maximum stress);

$FSF$  – is the factor of safety for fatigue stresses;

$FS$  – is the factor of safety for static stresses.

Equations (2) give allowable stresses in as-received material and transversely groove-welded joints for the high-strength and high-strength low-alloy steels, and the structural carbon steels. The fatigue strength of groove-welds with the reinforcement properly removed is about the same as that of as-received material. Allowable stresses for fillet welded joints of various types can be computed from the formulas for allowable stresses for transverse groove welds by applying the suggested reduction factors to the suggested allowable stress values given for transverse groove-welded connections. For allowable stresses in longitudinally fillet-welded flange-to-web connections subjected to fluctuating combined normal and shear stresses, Equation (1) can be used with the allowable formulas for transverse groove welds [4].

Design example of the crane carbody to crawler connection. The practical application of the solution is presented for crane car body to crawler connection (Fig. 2). We made 18 stress analyses by finite element method for 18 load cases for 2 series of the cranes with and without load on the hook and directly in line with center of car body, directly over front corner and directly over side of the crane. From these analyses we found maximum and minimum equivalent stress in the interesting area [5, 6, 7].

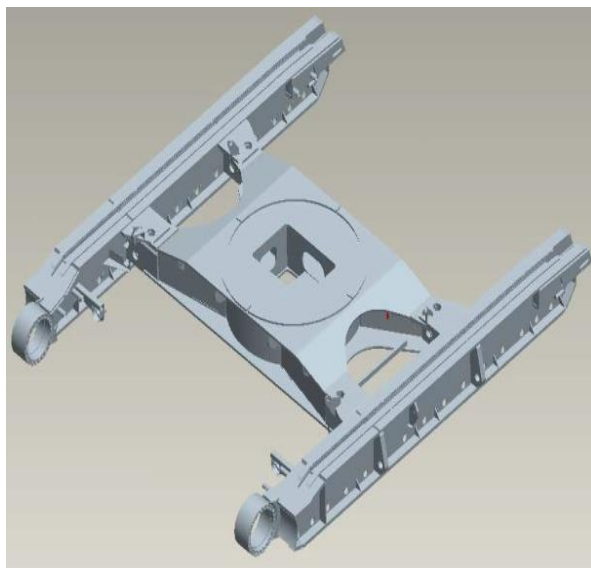


*Fig. 2. Pro/Engineer CAD model*

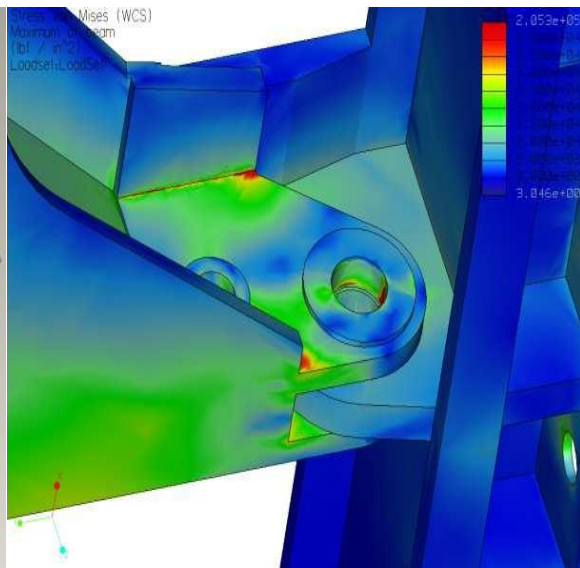


*Fig. 3. Pro/Mechanica FEA results*

The fillet welds in a lugs-to-plates crane car body to crawler connection of A36 steel are subjected to 2000000 cycles of fluctuating loads which cause equivalent stresses in the weld metal at a section to

vary from min. to max. stress. The next we used equations (2) for specification the allowable maximum stress compared to equivalent stress from FEA and made design changes. From FEA (Fig. 3), The Stress von Misses (equivalent stress) in the interesting area is about:

- 23000 psi - if the crane is directly in line with center of car body with load,
- 2000 psi - without load on hook.
- 15000 psi - if the crane is directly over side with load,
- 800 psi (min.) - without load on hook.
- 25000 psi (max.) - if the crane is directly over front corner with load,
- 4000 psi - without load on hook.

The fillet welds in a lugs-to-plates crane car body to crawler connection of A36 steel are subjected to 2000000 cycles of fluctuating loads which cause equivalent stresses in the weld metal at a section to vary from 800 to 25000psi. The required factor of safety is 1,35 for both yielding and fatigue ( $FSF$  – is the factor of safety for fatigue stresses,  $FS$  – for static stresses). The maximum allowable stress in a weld for 2000000 load cycles, when:  $FSF = FS = 1,35$  and  $R = 800 / 25000 = 0,032$  ( $R$  – is the stress ratio) is:

$$f = \frac{S_0}{(1 - mR)(FSF)} = \frac{19000}{(1 - 0,73 \cdot 0,032) \cdot (1,35)} = 14411 \text{ psi} = 99,36 \text{ MPa}$$

$$f = \frac{f_y}{FS} = \frac{36000}{1,35} = 26666 \text{ psi} = 183,86 \text{ MPa}$$

The maximum allowable stress in the weld is limited by fatigue to 14411psi. Let us assume that 10000psi. ( $S_0$  – is the experimental maximum stress at  $R=0$ ).

**Summary.** The Stress von Mises (equivalent stress) in the interesting area from FEA is about 2,5 times higher than the maximum allowable stress. The value is about 25000psi. We need the value about 10000psi. From 25000psi to 10000psi is 2,5 times less.

By results we will increase the section high from previous 25 to 35 inch (Fig. 4). Results of the Inertia tensors from Pro/Engineer calculation:

1. INERTIA at CENTRE OF GRAVITY of the previous section (high 25 inch):

INERTIA TENSOR (INCH<sup>4</sup>)

Ixx Ixy 1.3493198e+04 2.1863934e+03

Iyx Iyy 2.1863934e+03 5.2185535e+03

POLAR MOMENT OF INERTIA

1.8711751e+04 INCH<sup>4</sup>

2. INERTIA at CENTRE OF GRAVITY of the new section (high 25+10 inch):

INERTIA TENSOR (INCH<sup>4</sup>)

Ixx Ixy 3.2780793e+04 3.3240231e+03 is 2,5 times higher.

Iyx Iyy 3.3240231e+03 6.2154487e+03 is 1,2 times higher.

POLAR MOMENT OF INERTIA

3.8996242e+04 INCH<sup>4</sup>

is 2,1 times higher.

Increasing the cross-section we achieved increase the inertia tensors and reduce stress in the interesting area to the level of allowable stress.

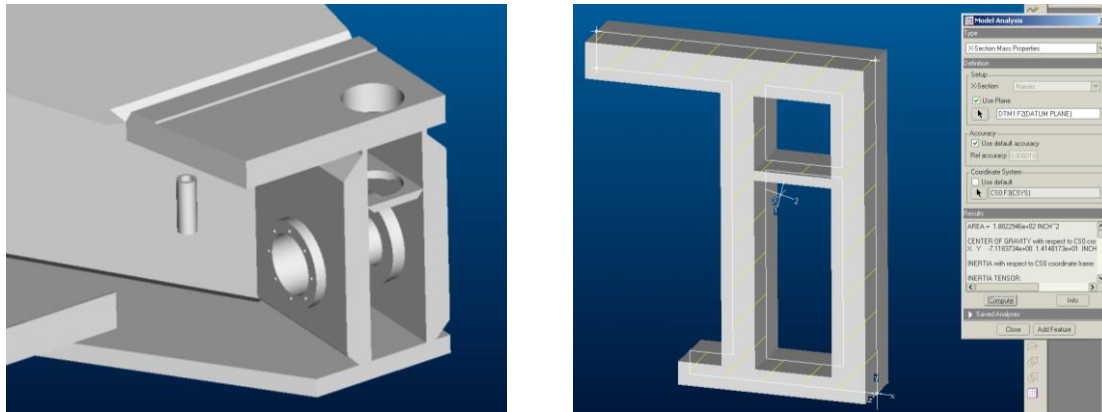


*Fig. 4. Design of the crane carbody connection lugs and shape of the section*

## References

- [1] J. Burák, K. Semrád, *Základy navrhovania konštrukcií technických, technologických a energetických zariadení*. Košice : elfa, s.r.o., 2013. 350 p. ISBN 978-80-8086-223-7.
- [2] J. Burák, O. Ostertag, *Základy projektovania konštrukčných prvkov pomocou metódy konečných prvkov*. Košice : elfa, s.r.o., 2010. 324 p. ISBN 978-80-8086-137-7.
- [3] J. E. Shingley, Ch. R. Mischke, R. G. Budynas, *Konstruování strojních součástí*. Brno: VUTUM, 2010, 1160 p. ISBN 978-80-214-2629-0.
- [4] Design for Repeated Load. Articles by Lehigh University and the University of Illinois, USA.
- [5] Pro/ENGINEER & Pro/MECHANICA. User guide, Parametric Technology Corporation, Waltham, 1997.
- [6] CADTRAIN-COACH for Pro/ENGINEER. COACH e-Learning Solutions, Irvine, USA, Available from: <<http://www.cadtrain.com/>>
- [7] Pro/ENGINEER Wildfire 3 Help Page. Cambridge University Engineering Department, Cambridge UK, Available from: <http://www.eng.cam.ac.uk/DesignOffice/cad/>

## Numerical Modelling of Basin Type Solar Stills

Nguyen The Bao <sup>1,a</sup>

1 – Director, Institute of Sustainable Energy Development (ISED), Ho Chi Minh, Vietnam

a – [drthebao@gmail.com](mailto:drthebao@gmail.com)



DOI 10.13140/RG.2.1.4601.9449

**Keywords:** numerical modelling, basin type solar still, standard free convection solar still, forced convection solar still, enhanced heat recovery, active solar still.

**ABSTRACT.** A numerical modelling for estimating the performance of basin type solar stills is described. Models for both the standard free convection solar still and a forced convection solar still with enhanced heat recovery are included. For the conventional free convection systems, the numerical modelling enables simulation of more complex systems with many more parameters compared to the existing models found in the literature. A new model incorporating heat and mass transfer in forced convection solar stills with enhanced heat recovery is described in this paper. The comparison of experimental and simulation results indicates that this modelling can predict distillate production at an acceptable level of accuracy.

**1. Introduction.** Nowadays, people around the World are facing many problems associated with the lack of clean and fresh water. Every year, millions of people die from the diseases related to unclean water. Many methods and processes are used globally to purify water, but most of them are costly and energy expensive. Therefore, methods of water purification at low cost, less energy consumption and environmentally friendly are always needed. Solar distillation seems to satisfy all these categories. It is not only capable to remove wide variety of contaminants in just one step, but is also simple, cost effective, and environmentally friendly.

Solar stills are the devices used to make potable water from impure water with the help of solar energy. It uses evaporation and condensation processes by which many impurities ranging from salts to micro-organisms can be effectively removed from saline or brackish water to obtain potable water. Basin type solar stills are widely used because of their simple in design and operation as well as their stable and durable property.

Conventional solar stills are passive solar stills, which directly use solar radiation in the distillation process [1]. They are simple in construction, operation, usually small in size, and less costly. Passive solar stills only utilize exorbitant available solar energy to remove the impurities in contaminated water, thus it is safe, clean, eco-friendly, and energy saving process. Therefore, it is still worth to investigate in this type of stills to further improve its designs and performance. This is one of the purposes of this paper.

One of the main disadvantages of conventional solar still is its low efficiency and distillation output. Therefore, a forced circulation solar still with enhanced water recovery was developed and modelled, both theoretically and experimentally. This paper will present the results of this research as well.

### 2. The numerical modelling of a conventional basin type solar still.

Dunkle [2] was the first to investigate the heat and mass transfer relationships in a solar still under steady state conditions. Based on the widely used relations from Dunkle, this study has analysed the transient performance of the solar still in which all coefficients and still parameters are calculated

using equations within the model. The weather data used for simulation will be either from actual measured data or data generated from the computer program developed by the author [3].

The heat and mass transfer processes in the still are shown in Figure 1. The following assumptions are made in order to develop the equations for the energy balances in the still:

1. The amount of water lost through evaporation is small compared to the amount of saline water in the basin;
2. The heat required to heat the water from the ambient (before adding to the basin) temperature to the temperature of water in the basin is negligible as compared to that required to evaporate the same quantity of water, that means  $C_{pw}(T_w - T_a) \ll h_w$ ;
3. There is no vapour leakage in the still, assuming a well designed still;
4. The areas of the cover, the water surface and the basin are considered to be equal;
5. The temperature gradients along the cover thickness and the water depth are absent.

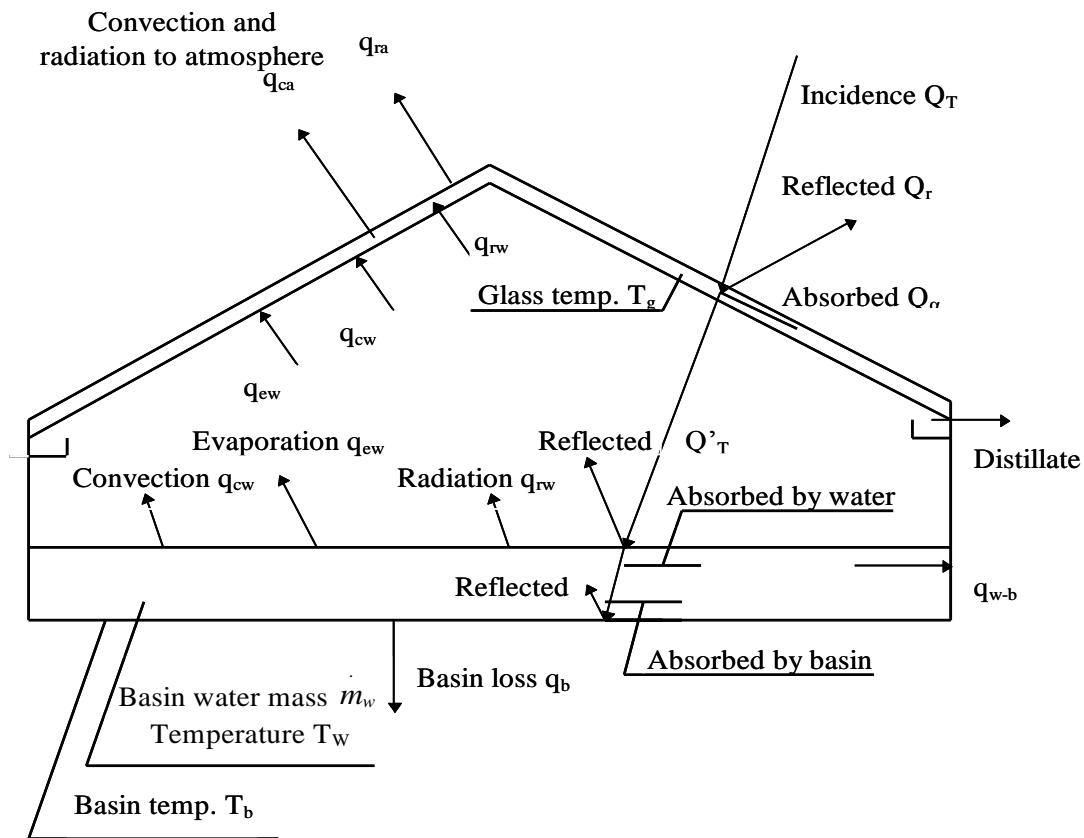


Fig. 1. The heat and mass transfer processes in a conventional solar still

Based on these assumptions and from Figure1, the energy balances for the glass, for the basin water and for the basin are:

$$q_{cw} + q_{ew} + q_{rw} + \alpha_g Q_T = (q_{ra} + q_{ca}) + M_g \frac{dT_g}{dt}, \quad (1a)$$

$$\alpha_w Q_T' = q_{cw} + q_{ew} + q_{rw} + q_{w-b} + M_w \frac{dT_w}{dt}, \quad (2a)$$

$$\alpha_b Q_T'' + q_{w-b} = q_b + M_b \frac{dT_b}{dt}, \quad (3a)$$

where  $q_{cw}$  – is the convective heat transfer rate between the basin water and the cover (in W/m<sup>2</sup>), and can be calculated by using Dunkle's equation:

$$q_{cw} = 0.884 \left[ (T_w - T_g) + \frac{(p_w - p_g)(T_w + 273.15)}{(268.9 \times 10^3 - p_w)} \right]^{1/3} (T_w - T_g) \quad (4)$$

with  $p_w$  and  $p_g$  are partial pressure of water vapour at the temperatures of the basin water and the cover, respectively (in Pa).

$q_{ew}$  is the evaporative heat transfer rate between the basin water and the cover (in W/m<sup>2</sup>):

$$q_{ew} = 16.276 \times 10^{-3} q_{cw} \frac{(p_w - p_g)}{(T_w - T_g)} \quad (5)$$

$q_{rw}$  is the radiative heat transfer rate between the basin water and the cover (in W/m<sup>2</sup>), expressed as:

$$q_{rw} = \varepsilon_w \sigma [(T_w + 273.15)^4 - (T_g + 273.15)^4] \quad (6)$$

with  $\varepsilon_w$  is the emissivity of water surface and  $\sigma$  is the Stefan-Boltzmann constant,  $5.67 \times 10^{-8}$  W/m<sup>2</sup>. K<sup>4</sup>

$q_{ca}$  – is the convective heat transfer rate between the cover and the ambient surroundings (in W/m<sup>2</sup>), computed from [4]:

$$q_{ca} = (5.7w + 3.8)(T_g - T_a) \quad (7)$$

where  $w$  is the wind speed (m/sec.) and  $T_a$  is the ambient temperature (°C).

$q_{ra}$  is the radiative heat transfer rate between the cover and the ambient surroundings (in W/m<sup>2</sup>):

$$q_{ra} = \varepsilon_g \sigma [(T_g + 273.15)^4 - (T_a + 261.15)^4] \quad (8)$$

where  $\varepsilon_g$  – is the emissivity of the cover;

$q_{w-b}$  is the heat transfer rate between the water and the basin (in  $\text{W/m}^2$ ):

$$q_{w-b} = h_{w-b}(T_w - T_b) \quad (9)$$

where  $h_{w-b}$  is the heat transfer coefficient between the water and the basin absorbing surface (in  $\text{W/m}^2 \cdot ^\circ\text{C}$ ).

$q_b$  is the heat transfer rate between the basin and the ambient surroundings (in  $\text{W/m}^2$ ):

$$q_b = h_b(T_b - T_a) \quad (10a)$$

where  $h_b$  – is the heat transfer coefficient between the basin and the ambient surroundings (in  $\text{W/m}^2 \cdot ^\circ\text{C}$ ):

$$\frac{1}{h_b} = \frac{\delta_{insul}}{k_{insul}} + \frac{1}{h_i} \quad (10b)$$

where  $\delta_{insul}$  (m) and  $k_{insul}$  ( $\text{W/m} \cdot ^\circ\text{C}$ ) – are the thickness and thermal conductivity of the basin insulation, respectively;

$h_i$  – is the combined convective and radiative heat transfer coefficient between the insulation and ambient, and can be computed by the derivation of equations (6) and (7);

$Q_T$  – is the total solar radiation incidence on the cover, in  $\text{W/m}^2$ ;

$Q_T'$  – is the total solar radiation incidence on the water surface, after transmittance through the cover, in  $\text{W/m}^2$ ;

$Q_T''$  – is the total solar radiation incidence on the basin, after transmittance through the basin water, in  $\text{W/m}^2$ ;

$\alpha_g, \alpha_w$  and  $\alpha_b$  – are the absorptance of the cover, of the water and of the basin for solar radiation, respectively;

$M_g, M_w$  and  $M_b$  – are the heat capacities per unit area of the cover, of the water and of the basin for solar radiation, in  $\text{J/m}^2 \cdot ^\circ\text{C}$ ;

$T_g, T_w$  and  $T_b$  – are respectively the transient temperatures of the cover, of the water and of the basin for solar radiation, in  $^\circ\text{C}$ .

Equations (1a), (2a) and (3a) can be rewritten as:

$$M_g \frac{dT_g}{dt} = \alpha_g Q_T + q_{cw} + q_{ew} + q_{rw} - (q_{ra} + q_{ca}) \quad (1b)$$

$$M_w \frac{dT_w}{dt} = \alpha_w Q_T' - (q_{cw} + q_{ew} + q_{rw} + q_{w-b}) \quad (2b)$$

$$M_b \frac{dT_b}{dt} = \alpha_b Q_T'' + q_{w-b} - q_b \quad (3b)$$

It is convenient to present all solar components  $Q_T$ ,  $Q_T'$  and  $Q_T''$  in the above equations by the common total solar incidence of the sloped cover,  $Q_T$ , which is readily calculated [3]. If  $\tau_g$ ,  $\tau_w$  and  $\tau_b$  are defined as the fractions of solar insolation incident absorbed by the cover, basin water and basin liner respectively, equations (1b), (2b) and (3b) may be written as :

$$M_g \frac{dT_g}{dt} = \tau_g Q_T + q_{cw} + q_{ew} + q_{rw} - (q_{ra} + q_{ca}) \quad (1c)$$

$$M_w \frac{dT_w}{dt} = \tau_w Q_T - (q_{cw} + q_{ew} + q_{rw} + q_{w-b}) \quad (2c)$$

$$M_b \frac{dT_b}{dt} = \tau_b Q_T + q_{w-b} - q_b \quad (3c)$$

### 3. The numerical modelling of a basin type forced circulation solar still with enhanced water recovery.

In this study, the heat and mass transfer relationships in the forced circulation solar still with enhanced water recovery will be developed. Then, this numerical modelling will be validated by comparing its results with those from the experimental model.

The forced circulation solar still has been chosen in this study for several reasons. Compared with other types of solar powered distillation systems such as the solar multistage flash distillation, solar vapor compression, solar powered reverse osmosis, solar powered electrodialysis, and solar membrane distillation systems, solar stills represent simple, yet mature technology. This is suitable for developing countries like Vietnam.

The low efficiencies of a conventional solar still may be overcome by changing the principle of operation as follows:

- Using air as an intermediate medium and substituting forced convection for natural convection to increase the heat coefficients in the still, resulting in increased evaporation of water.
- Replacing saturated air in the standard still by “drier” air to increase the potential for mass transfer in the still, leading to higher outputs.
- Circulating the air-vapour mixture from the standard still to external water cooled condensers to gain efficiency from a lower condensing temperature. The cooler the cooling water available, the more effective this condensing process will be.

- Recovering some of the heat extracted in the condensing process and using it to preheat the air-vapour mixture entering the still.
- Substituting the condensing area of the flat sheet covers in the standard still by the external condenser with much larger heat exchange areas to increase condensation efficiencies.

### 3.1 The development of the heat and mass transfer relationships in a forced circulation solar still.

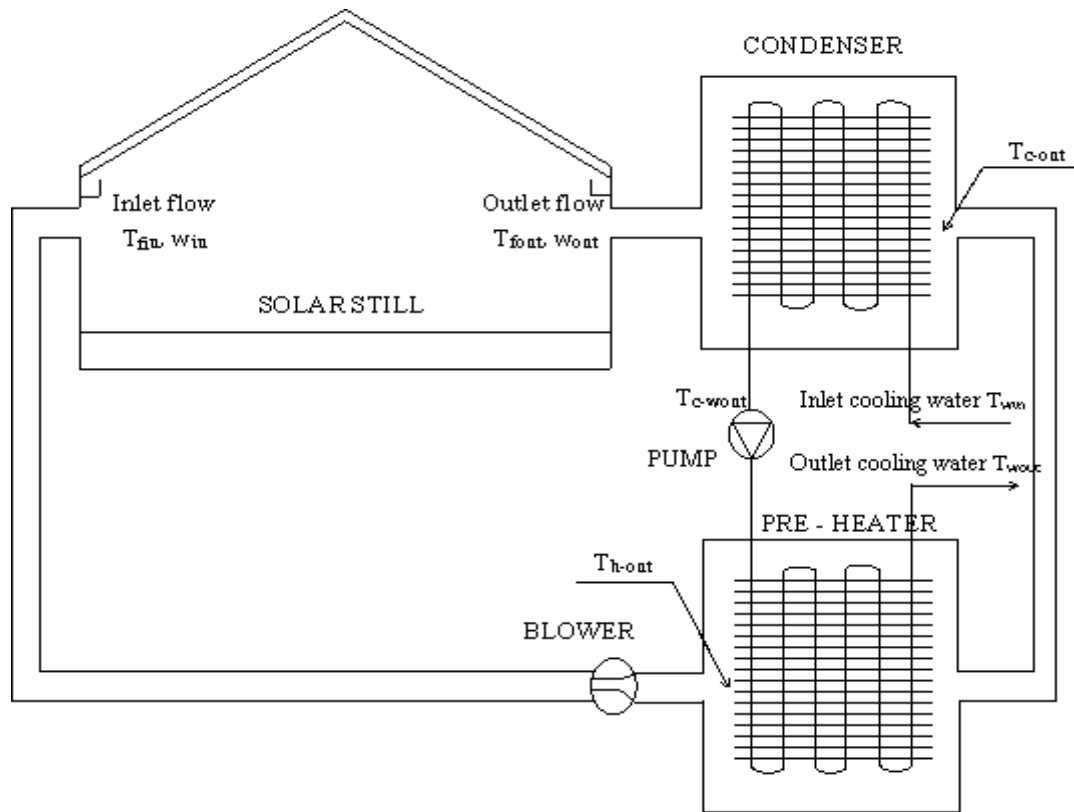
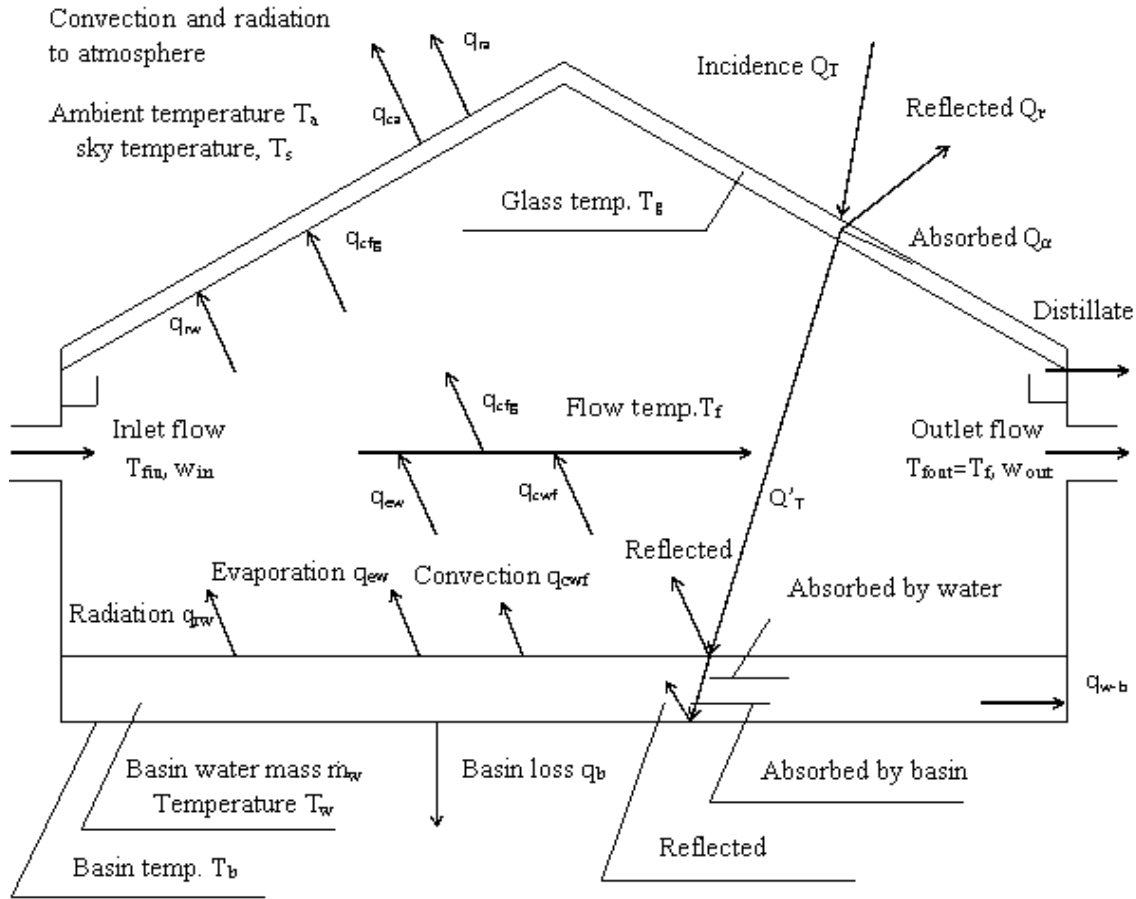


Fig. 2. Schematic diagram of a forced circulation solar still with enhanced water recovery

Figure 2 shows a schematic diagram of the forced circulation solar still with enhanced water recovery. The air flow having a temperature of  $T_{fin}$  and moisture content  $w_{in}$  enters the still and is heated up. It absorbs the vapour from the basin water and exits the still at a temperature of  $T_{fout}$  and moisture content  $w_{out}$ . This air flow goes through the dehumidifying coil, which acts a condenser. The hot air-vapour mixture from the still is passed over the coil and attached fins while the cooling water runs inside the coil.

The hot air-vapour mixture losses heat to the cooling water and subsequently cools down. When the temperature of the mixture falls below its dew point temperature, the condensation process starts. The air exits the condenser at a temperature of  $T_{c-out}$  and a moisture content of  $w_{c-out}$ . Some of the heat extracted from the air flow will be recovered in the pre-heater, since the air flow goes through it before going back to the still.



*Fig. 3. The heat and mass transfer process in a forced circulation solar still*

The heat and mass transfer relationships in this still can be seen from Figure 3. From this figure, the energy and mass balances for the glass, for the flow in the still, for the basin water and for the basin are:

$$q_{cfg} + q_{rw} + \alpha_g Q_T = (q_{ra} + q_{ca}) + M_g \frac{dT_g}{dt} \quad (11)$$

$$q_{ew} + q_{cwf} = q_{cfg} + m_f(h_{out} - h_{in}) + M_f \frac{dT_f}{dt} \quad (12)$$

$$m_{ew} = \frac{q_{ew}}{h_{fg}} = m_f(w_{out} - w_{in}) + m_{ew-g} \quad (13)$$

$$\alpha_w Q'_T = q_{cwf} + q_{ew} + q_{rw} + q_{w-b} + M_w \frac{dT_w}{dt} \quad (14)$$

$$\alpha_b Q_T'' + q_{w-b} = q_b + M_b \frac{dT_b}{dt} \quad (15)$$

$q_{cwf}$  is the convective heat transfer rate between the basin water and the flow (in  $\text{W/m}^2$ ). In principle, the blower used to transport the air should have the lowest possible energy consumption. The heat transfer process in the still may be natural convection or combined natural and forced convection. In this model, the heat coefficient in the still is calculated by using the forced and natural convection relations separately; and the larger one is chosen. The Grashof and the Reynolds number are first calculated [4]:

$$Gr = \frac{g\beta' \Delta T L^3}{\nu^2}, \quad (16)$$

$$Re = \frac{VD_h}{\nu}, \quad (17)$$

where  $L$  – average spacing between the water surface and the cover, in m

$g$  – gravitational constant,  $9.81 \text{ m/s}^2$ ;

$\beta'$  – volumetric coefficient of expansion, in  $\text{K}^{-1}$ ; for air  $\beta' = 1/T$ ;

$\Delta T$  – temperature difference between the water and the cover, in  $^\circ\text{K}$ ;

$\nu$  – kinematic viscosity, in  $\text{m}^2/\text{s}$ ;

$V$  – air flow velocity, in  $\text{m/s}$ ;

$D_h$  – the hydraulic diameter of the still, defined as  $D_h = \frac{4 \times (\text{flow area})}{\text{wetted perimeter}}$ .

Then, if the natural convection dominates, the convective heat transfer rate between the basin water and the flow can be derived from:

$$Nu = \frac{h_{cwf} L}{k} = 0.075 (Gr \cdot Pr)^{1/3} \quad (18)$$

where  $Pr = \frac{\nu}{\alpha}$  – is the Prandtl number.

To achieve a similar equation to Dunkle's expression [2] with  $T_g$  replaced by  $T_f$ :

$$q_{cwf} = 0.884 \left[ (T_w - T_f) + \frac{(T_w - T_f)(T_w + 273.15)}{(268 \times 10^3 - p_w)} \right]^{1/3} (T_w - T_f) \quad (19)$$

where  $p_w$  and  $p_f$  – are partial pressures (in Pa) of water vapour at the temperatures of the basin water and the flow respectively.

If the forced convection dominates, the relation between  $Nu$  and  $Re$  is given by [4]:

$$Nu = \frac{h_{cwf} D_h}{k} = 0.664 \times Re^{1/2} \times Pr^{1/3} \quad (20a)$$

Considering  $T_w = 50^\circ\text{C}$  and  $T_f = 40^\circ\text{C}$  and introducing the corresponding air properties into equation (20a), the convective heat transfer rate between the basin water and the flow can be computed by:

$$q_{cwf} = 3.908 \left( \frac{V}{D_h} \right)^{1/2} (T_w - T_f) \quad (20b)$$

$q_{ew}$  is the evaporative heat transfer and the radiative heat transfer rates (in  $\text{W/m}^2$ ) between the basin water and the air flow, and can be approximately by equation (5) with  $T_g$  and  $p_g$  replaced by  $T_f$  and  $p_r$ .

$q_{rw}$  is the radiative heat transfer rates (in  $\text{W/m}^2$ ) between the basin water and the cover, and can be calculated by equation (6).

$q_{cfg}$  is the convective heat transfer rate ( $\text{W/m}^2$ ) between the flow and the cover given by:

$$q_{cfg} = 2.785 \left( \frac{V^{0.8}}{L_s^{0.2}} \right) (T_f - T_g) \quad (21)$$

Where  $V$  – is the air flow velocity (m/sec) and  $L_s$  is the still length (m);

$q_{ca}$  and  $q_{ra}$  – are the convective and radiative heat transfer rates (in  $\text{W/m}^2$ ) between the cover and the ambient surroundings, computed from by using equations (7) and (8) respectively;

$q_{w-b}$  and  $q_b$  – are the heat transfer rates (in  $\text{W/m}^2$ ) between the water and the basin and between the basin and the ambient surroundings, and can be calculated from equation (9) and (10) respectively;

$Q_T$  – is the total horizontal solar radiation incident on the still, in  $\text{W/m}^2$ ;

$Q'_T$  – is the total solar radiation incident on the water surface, after transmittance through the cover, in  $\text{W/m}^2$ ;

$Q''_T$  – is the total solar radiation incident on the basin, after transmittance through the basin water, in  $\text{W/m}^2$ ;

$m_f$  – is the mass rate of the air flow, in kg/s;

$m_{ew}$  – is the mass rate pf the evaporation from the basin water to the air flow, in kg/s;

$\alpha_g$ ,  $\alpha_w$ , and  $\alpha_b$  – are the solar absorptance values of the cover, of the water and of the basin respectively;

$M_g$ ,  $M_w$ ,  $M_f$  and  $M_b$  – are the heat capacities are unit area of the cover, of the water, of the air in the still and of the basin, in  $\text{J/m}^2\text{ }^\circ\text{C}$ ;

$T_g$ ,  $T_w$ ,  $T_f$  and  $T_b$  – are respectively the temperatures of the cover, water, air in the still and the basin, in  $^\circ\text{C}$ ;

$H_{fg}$  – is the latent heat of vaporisation of water at the temperature  $T_f$ , in J/kg.

$w_{in}$  and  $w_{out}$  – are the moisture contents of the air-vapour mixture at the inlet and outlet of the still, in kg/kg.

$h_{in}$  and  $h_{out}$  – are the enthalpies of the still inlet and outlet air, in J/kg. Assuming that the air in the still is reasonably well mixed, the enthalpy of the still outlet  $h_{out}$  can be calculated as a function of the temperature  $T_f$  as follows:

$$h_{out} = (T_f + w_{out} \times (2501 + 1.805T_f)) \times 10^3 \text{ (J/kg)} \quad (22)$$

The amount of the distillate water collected inside the still will depend on the temperatures of the air and the cover. Water will condense on the cover surface only when the dew point temperature of the air flow,  $T_{fd}$ , is higher than the cover temperature,  $T_g$ . In this case, the amount of the distillate water collected from the cover,  $m_{ew-g}$  (in  $\text{kg/s.m}^2$ ) can be calculated from:

$$\dot{m}_{ew-g} = \frac{q_{con-g}}{h_{fg}} \text{ (kg/s.m}^2\text{)}, \quad (23)$$

where  $h_{fg}$  – is the latent heat of vaporisation of water at the temperature,  $T_f$ , in J/kg.

$q_{con-g} = h_{con-g}(T_f - T_g)$  is the condensate heat transfer rate between the flow and the cover (in W/m<sup>2</sup>). Using the Nusselt number in condensing:

$$Nu = \frac{h_{con-g}L_c}{k} = 0.943 \left( \frac{g\rho^2 \sin \beta h_{fg}L_c^3}{\mu k \Delta T} \right)^{1/4} \quad (24)$$

where  $L_c$  – the length of the cover, in m;  $L_c = L_s$

$k$  – thermal conductivity, in W/m K

$g$  – gravitational constant, 9.81 m/s<sup>2</sup>

$\beta$  – the slope of the cover, in degree

$\rho$  – the air density, in kg/m<sup>3</sup>

$\Delta T$  – the difference between the dew point temperature of the flow and the cover temperature, in °K

$\mu$  – absolute viscosity, in Pa·s

Using the properties of the air at  $T_f = 40^\circ\text{C}$ , one can achieve:

$$q_{con-g} = 70.93 \left( \frac{\sin \beta}{\Delta T L_c} \right)^{0.25} \quad (25)$$

Therefore, using the five equations from (11) to (12) the five unknown parameters,  $T_g$ ,  $T_w$ ,  $T_f$ ,  $w_{out}$  and  $T_b$ , can be solved.

### 3.2. The performance of the condenser and pre-heater.

The theory of the performance of dehumidifying and of heating coils has been developed and is presented in [5] and [6]. However, an explicit procedure for calculating the performance of dehumidifying coils was not available in these references. Therefore, the modelling of the performance of the condenser and the pre-heater in this simulation program was derived from the handbook and the standard. The calculation procedures for the psychometric properties of humid air were given in [5]. A detail description of the procedures for modelling the performance of the pre-heater and dehumidifying coils in solar still is described in [3].

The procedure for modelling the performance of the pre-heating coil involves: (i) calculating the overall coefficient of heat transfer for the coil; (ii) calculating the effectiveness of the coil, and then (iii) computing the temperatures of the air and cooling water leaving the coil.

The procedure for modelling the performance of the dehumidifying coil involves using an iterative process to find a consistent set of temperature and humidity values, subject to the constraints imposed by the performance characteristics of the dehumidifying coil.

#### 4. The comparison of results from numerical modelling and experimental results.

##### 4.1. The conventional solar still.

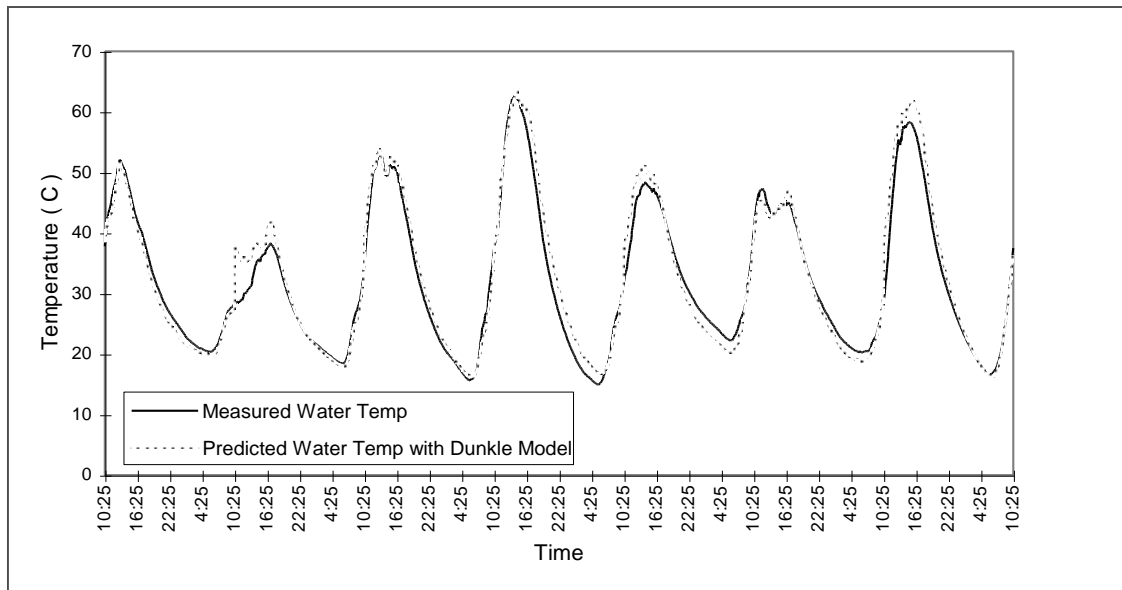


*Fig. 4. The measured and predicted temperature of water in a conventional solar still*

The predicted water temperatures in the basin and the calculated distillate outputs from the numerical modelling compared to those from the experiments are shown in Figures 4 and 5 respectively. It shows that the developed numerical model gave very high accurate results. Therefore, this model can be reliably used to simulate the performance of solar passive stills.

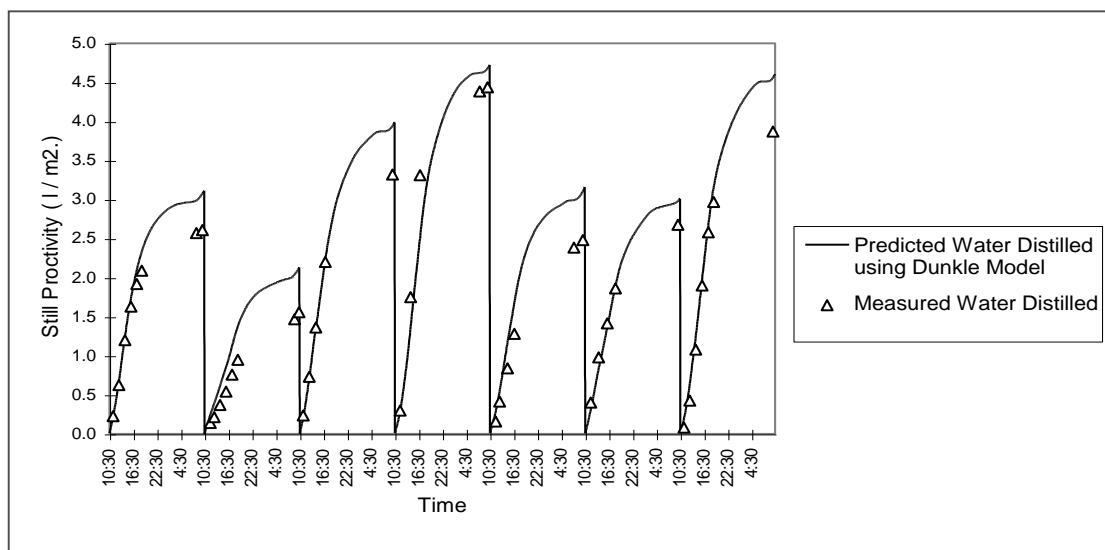


*Fig. 5. The measured and predicted distillate outputs of a conventional solar still*

##### 4.2. The forced circulation basin solar with enhanced water recovery.

The input data for the numerical model includes measured weather parameters and the measured temperature and relative humidity values of the air entering the still. The outputs of the simulation consist of the temperature of the water in the still, the cover temperature, the basin temperature, the temperature and relative humidity of the air leaving the still, the temperature of the air leaving the condenser, the temperature and relative humidity of the air leaving the heat recovery (or the pre-heater), as well as the distillate production from the glass and from the condenser. Figures 6 and 7 show the measured and predicted values of the temperature and relative humidity of the air leaving the still and the pre-heater, respectively. Figure 8 shows the predicted and measured moisture content of the air leaving the still and Figure 9 shows the predicted and measured temperatures of the water in the still. Figures 10 and 11 show the predicted and measured distillate production from the glass and the condenser, respectively.

As shown in figure 6, the simulation is able to predict both the trends in, and the actual values, for the temperature of the air leaving the still quite well. The maximum error is of the order of 5 °C and occurs in the early afternoon. The errors in the relative humidity calculation are more significant with errors ranging up to 20% RH with an average error of 10%. For most of the time, the calculated values are less than the measured values. The results in Figure 8 confirm that the simulation program under-predicts the amount of water in the air leaving the still during the middle of the day. At other times, the measured and calculated values of the absolute humidity of the outlet air are very similar, which indicates that the differences observed in RH at these times are due to variations between the calculated and measured air temperature.

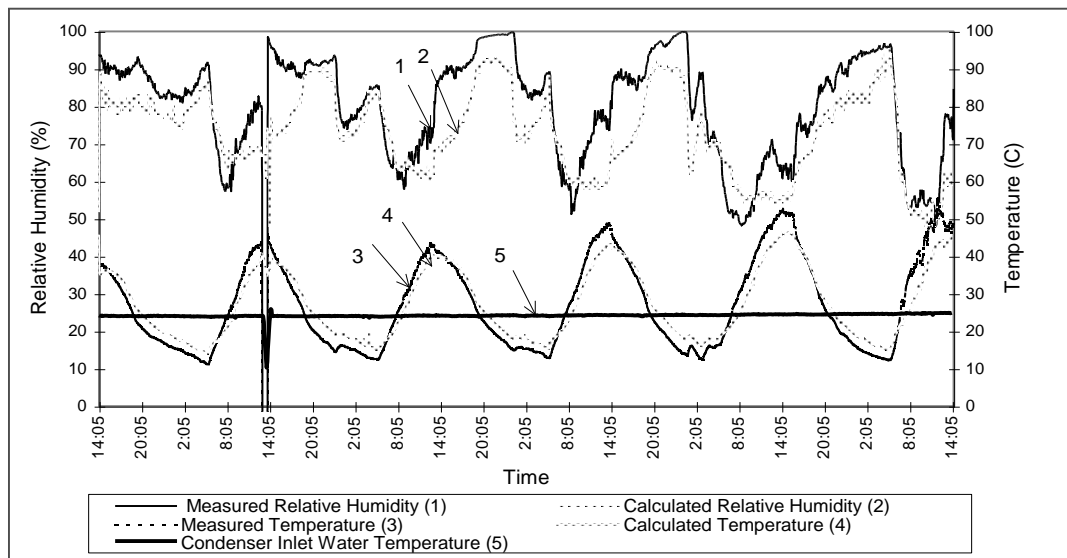


*Fig. 6. The predicted and measured temperature and relative humidity of the air leaving the forced convection still.*

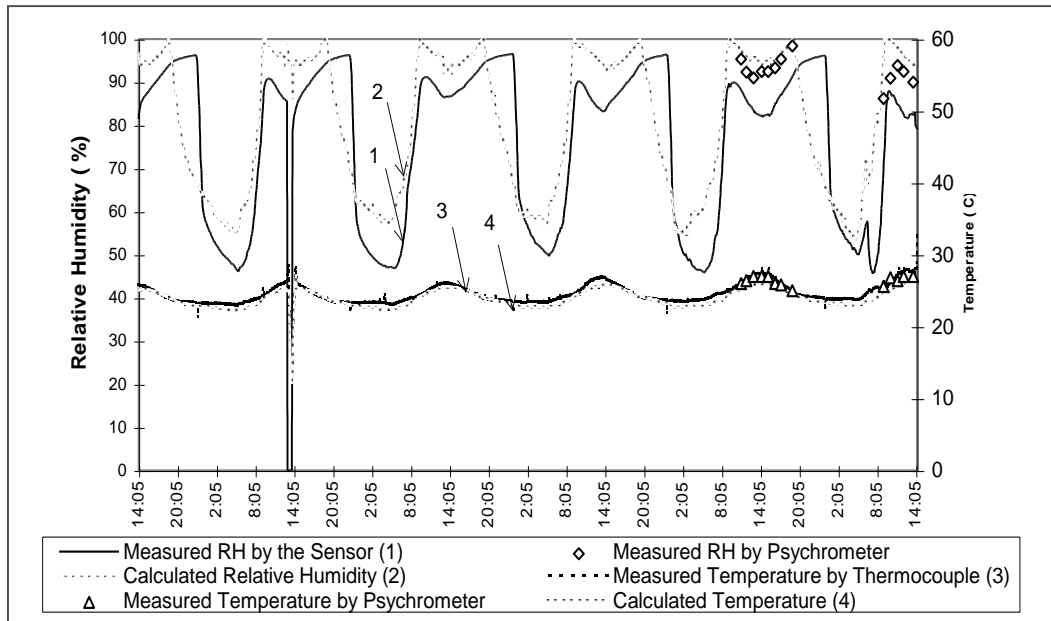


Fig. 7. The predicted and measured temperature and relative humidity of the air leaving the pre-heater.

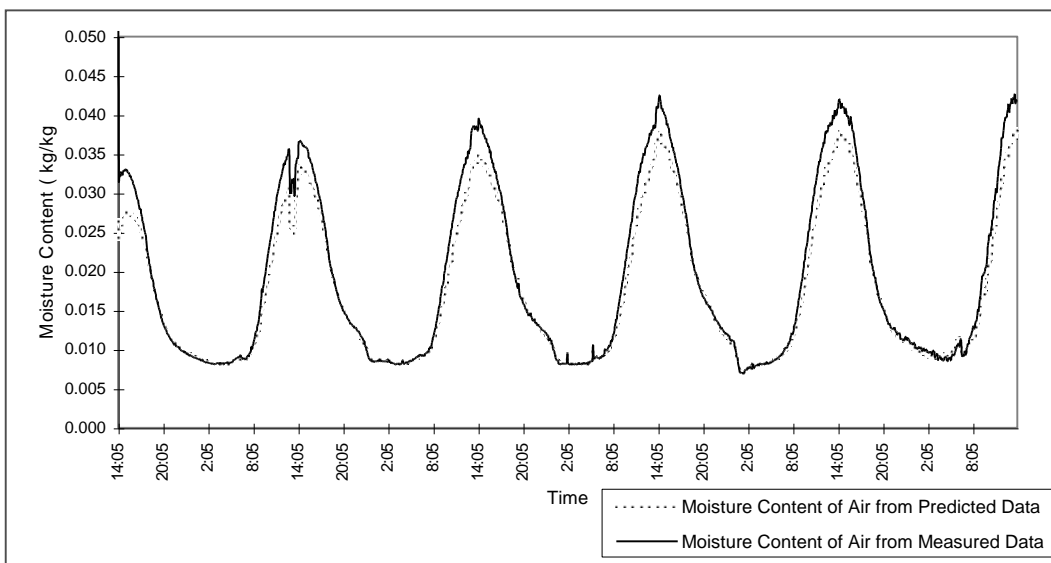


Fig. 8. The predicted and measured moisture content of the air leaving the still.

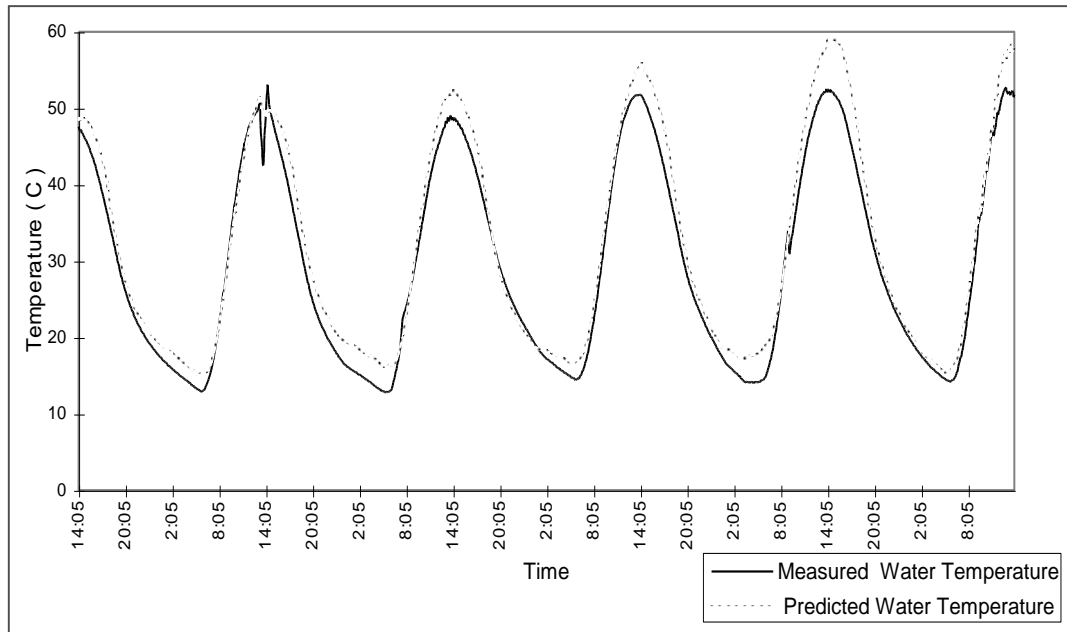


Fig. 9. The predicted and measured temperature of the water in the still.

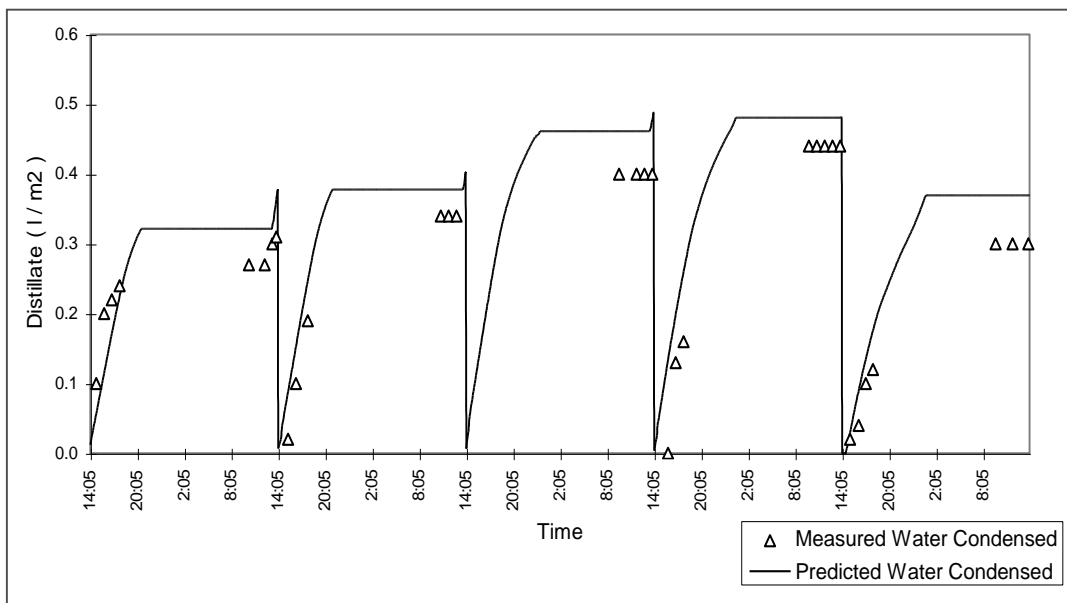


Fig. 10. The predicted and measured distillate condensed on the glass of the still.

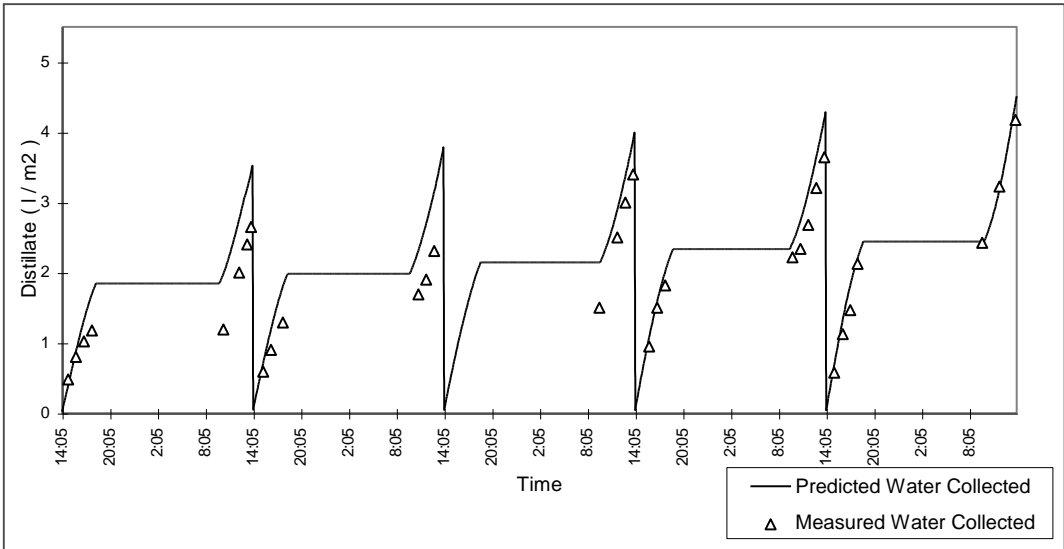


Figure 11. The predicted and measured distillate collected from the condenser of the still.

**Summary.** The development of the numerical models for estimating the performance of basin type solar stills was described. Models for both the free convection solar still and a forced convection solar still with enhanced heat recovery were included in the program. For the conventional free convection systems, the numerical model also enables simulation of more complex systems with many more parameters compared to the existing models found in the literature. A new model incorporating heat and mass transfer in forced convection solar stills with enhanced heat recovery was described in this paper. The comparison of experimental and numerical results indicated that the models can predict distillate production at an acceptable level of accuracy.

## References

- [1] H. Manchanda & M. Kumar (2015). *A comprehensive decade review and analysis on designs and performance parameters of passive solar still*. Renewables: Wind, Water and Solar, Springer Open Journal.
- [2] Dunkle, R.V. (1961). Solar water distillation: the roof type still and a multiple effect diffusion still. *International Developments in Heat Transfer, American Society of Mechanical Engineers, Proceedings of International Heat Transfer*, pp. 895-902.
- [3] Nguyen The Bao (2004), *SOLSTILL - A Simulation Program For Solar Distillation Systems*, Proceedings of EUROSUN 2004, Freiburg, Germany, pp.96-105.
- [4] Duffie J.A. and Beckman W.A. (2013). *Solar Engineering of Thermal Processes* (4<sup>th</sup> Edn.). John Wiley and Sons Inc., New York.
- [5] ASHRAE Systems and Equipment Handbook (2012). American Society of Heating, Refrigerating and Air-Conditioning Engineers, New York.
- [6] AHRI (2014). Forced-circulation air-cooling and heating coils. *Standard 410*. Air-Conditioning, Heating and Refrigeration Institute. Arlington, VA.

**VII. Environmental Safety**  
**MMSE Journal Vol. 4**



# HAVS and HAV-nots: Investigating Resonance in the Human Arm Caused by Contact with Machinery

Irina Viktorova<sup>1</sup>, Matthew Fleck<sup>1</sup> and Muhammed Kose<sup>1</sup>

1 – Department of Mathematical Sciences, Clemson University, Clemson, South Carolina



DOI 10.13140/RG.2.1.4580.2648

**Keywords:** resonance, vibrations, hand-arm vibration syndrome, frequency, amplitude, viscoelastic

**ABSTRACT.** Mechanical vibration is a vast field composed of thousands of studies and experiments regarding individual systems and structures' vibrations and oscillations. In this paper a special and complex case regarding hand-arm vibration will be studied and analyzed mathematically. The human hand-arm system is affected by vibrations caused by contact with vibrating objects. In order to understand the effect on the hand-arm system, a mathematical model of the system as two viscoelastic rods connected by a hinge was derived. Using this model, it was possible to derive the propagation of both the longitudinal and bending vibrations of the arm, and find the resonance frequencies of the system from the elbow to the shoulder. The harmful effect of these frequencies is discussed with regards to Hand-Arm Vibration Syndrome, a disease stemming from repeated contact with vibrating objects. Hand-Arm Vibration Syndrome is found to be a pervasive issue among physical laborers who use vibrating machinery. A sample set of construction tools is analyzed and compared with the modeled resonance frequencies of the arm. Considering the resonance frequencies of the arm is significant for tools manufacturers. Research on the frequencies at which tools function may be overly dangerous to workers who are required to handle such tools frequently.

**Introduction.** Vibration is a common byproduct of mechanical technology. Construction and contract workers typically are in contact with such technology on a daily basis. This interaction has been found to lead to a disease known as Hand-Arm Vibration Syndrome (HAVS). The disease causes intensive damage to the hand and arm and can be debilitating. Individual machines emit vibration at a specific frequency, and if it is at the natural frequency of the material in the human arm or hand, can cause devastating damage and more quickly lead to the development of HAVS. Therefore it is important to know accurately the resonance frequencies in the arm and compare them to the individual frequencies emitted by construction technology. Due to the extreme difficulty of gathering data on the human arm from a living subject, models of the arm are a practical solution to the resonance problem. An investigation of the arm modeled and analyzed as two viscoelastic rods is conducted below.

**Resonance.** Resonance is the phenomenon at which an externally forced frequency coincides with the natural frequency, defined by a ratio close to one between the two frequencies. When damping is present, pseudo resonance will occur with the maximum amplitude of the vibrating object. In general, amplitude is not linearly dependent on frequency. An important case of resonance, including the hand-arm system, relates amplitude  $A$  to the square of the frequency  $\omega$  [1]. The case of resonance in the hand-arm system will be examined later.

**The Hand-Arm System and Vibration.** It is difficult to envision the human body, or any living organism, as a structure that can be mathematically modeled. The vast complexity of the body makes it incredibly difficult to predict, record, or analyze information about bones or organs, despite the large variety of stresses they undergo. Vibration is one such stress; it enters the body when an organ makes contact with a vibrating object, such as a jackhammer. An instance of whole body vibration would be sitting in a car when driving on a gravel road. A very common tremor experienced by humans is hand-arm vibration. When exposed repeatedly over long periods of time, there is risk to the nerves in the fingers, hand, and arm. This condition is known as hand-arm vibration syndrome

(HAVS). HAVS symptoms include, but are not limited to, loss of feeling in the hand or arm, recurrent pain, and blanching [2]. The National Institute of Occupational Safety and Health estimates over 1.2 million workers are subject to hand-arm vibration and are at risk for HAVS. This is seen below in Fig. 1. Clearly, HAVS is a pervasive issue for many physical laborers. Prolonged exposure to vibrating machinery increases the severity of the syndrome. This means that by decreasing the number of machines and tools that operate at a resonant frequency of the hand or arm, long term damage to the hand-arm system can be drastically lessened.

No. of Workers	Industry	Type of Tool
500,000	Construction	Handtools
200,000	Farming	Gasoline chain saws
14,000	Metal working	Handtools
54,000	Steel	Furnace cleaning using powered handtools
30,000	Lumber and wood	Gasoline chain saws
34,000	Furniture manufacturing	Handtools
100,000	Mining	Pneumatic drills
250,000	Truck and auto manufacturing	Handtools
64,000	Foundries	Handtools
<b>Total</b>	<b>1,246,000</b>	

*Fig. 1. Hand-arm vibration exposure statistics by occupation [2]*

**Viscoelastic Modeling of the Hand-Arm System:** The problems of vibrosafety are connected with considering the human reaction to various mechanical inputs and traditionally is sorted as a mechanical system with concentrated, undistributed parameters.

This is a simple and effective approach, but with an obvious drawback; setting up a system similar to the actual human arm is possible only if an experimental subject is available. However, analyzing the human body and its parts as a solid mechanical body presents of a lot of challenges. Human organs have a complicated shape and the biomaterial of human tissue is not fully researched. There is plenty of data on the experimental study of bone structures, but it is difficult to compare due to the different conditions of testing, the different animal species they belong to, et cetera. Similarly, the available data on mechanical properties of human muscle tissue is contradictive and unreliable. Thus the methods of mechanics of solids has not been applied to analysis of the hand-arm vibration. The same reasoning is applied to the problem of the vibrations propagation in the human tissue. The objective of this model is to show how to generalize the analysis of the harmonic wave propagation along the human arm.

The human arm is modeled as the system of two homogeneous viscoelastic rods of  $\lambda_1$  and  $\lambda_2$  lengths each, joined by a hinge [3]. The modality of the muscle and bone tissue as a homogeneous and viscoelastic solid is based on the experimental mechanical testing data on the bone structure which shows that the bone tissue does behave as the linear viscoelastic material. The material surrounding the bone muscle tissue causes the increase in viscoelasticity and accounts for the parameters of the model equation. The rods are considered homogeneous since the wavelengths, at lengths of tens of meters, at the frequencies considered are overwhelmingly greater than the maximum cross-sectional measurements for the human arm, which the results in the propagation solely in a two dimensional front plane. This allows nonhomogeneity to be neglected [3].

**Mathematical Analysis:** The problem of vibrations propagating along the human arm is divided into two parts. The first is related to longitudinal oscillations propagating from the hand to the elbow. The second is related to propagation of the superposition of longitudinal and bending vibrations from the elbow to the shoulder, with the action ratio being defined by the angle of bending for the elbow joint. Thus, if the arm is straight and the bending angle is 0, there is no bending mode involved. On the contrary, if the angle is 90 degrees, then only the bending component is important to account for [3]. In the following equations,  $W$  is the amplitude;  $\omega$  is the vibrational frequency;  $\lambda$  is the length of the rod; and  $x$  is the position of the cross section of the rod in relation to  $\lambda=0$ .  $k$  is a constant equal to  $\frac{r}{2}$  where  $r$  is the radius of the cylinder. The amplitude of the bending vibrations is then given by the formula:

$$W = \frac{\omega}{2} \left[ \frac{S_1 \sin(kx) - S_2 \sinh(kx)}{\sin(k\lambda) \cosh(k\lambda) - \cos(k\lambda) \sinh(k\lambda)} \right] + \cos(kx) + \cosh(kx) \quad (1)$$

where

$$S_1 = 1 - \cos(k\lambda) \cosh(k\lambda) - \sin(k\lambda) \sinh(k\lambda) \quad (2)$$

$$S_2 = 1 - \cos(k\lambda) \cosh(k\lambda) + \sin(k\lambda) \sinh(k\lambda) \quad (3)$$

The propagation of longitudinal and bending vibrations along a viscoelastic rod of finite length can be modeled by the combined theory of wave propagation in viscoelastic solids. [4][5]. It should be stressed that the combination of longitudinal and bending vibrations along the second rod between the elbow and the shoulder are characterized by the amplitude value, which depends on the angle of the bent elbow. The amplitude of longitudinal vibrations that have reached the shoulder joint decreases due to the viscosity of the body tissue and the distribution into the bending and longitudinal modes. The simplified amplitude of the bending vibrations at  $x = \lambda_2$ , where  $\lambda_2$  is the length of the rod between the elbow and the shoulder, is defined by the expression:

$$W(x = \lambda) = \omega * \left[ \frac{\sin(k\lambda) - \sinh(k\lambda)}{\sin(k\lambda) \cosh(k\lambda) - \cos(k\lambda) \sinh(k\lambda)} \right] \quad (4)$$

Equation (4) models the amplitude  $W$  as a function of  $\omega$  and  $\lambda$ , where  $k$  is a constant. In addition, there is an amplification factor  $\rho$  that relates the amplitude of displacement and the frequency  $\omega$  of bending vibrations [3]. The relationship is represented by the equation:

$$\rho = \frac{(\cosh(\omega) - \cos(\omega) - \sin(\omega) \sinh(\omega))^{\frac{1}{2}}}{\sqrt{2}(\sinh(\omega) - \sin(\omega))} \quad (5)$$

It is important to note that equations (1) and (4) only characterize the bending vibrations in the arm, while (5) encompasses the complex vibrations in the hand-arm system. Differentiating equation 5 with respect to  $\omega$  and setting it equal to zero obtains the values of  $\omega$  that produce the minimum and maximum amplitudes of vibration. Setting the derivative equal to zero and solving gives the first extremum at  $\omega=3\pi$  [3]. Simplifying the first derivative of (5) with  $\omega = 3\pi$  gives:

$$\frac{d\rho}{d\omega} = \sinh(\omega)^2 * [\sin(\omega) - \cos(\omega) - 1] = 0 \quad (6)$$

This solution shows that maximum and minimum amplitudes occur at frequency intervals  $\omega = \frac{\pi}{2} + n\pi$  and  $\omega = \pi + n\pi$  for all  $n$ . By differentiating  $\rho$  again, it is possible to find whether the extremum frequency is a maximum or a minimum value. Plugging in  $3\pi$  to the second derivative of (5) produces a negative value. This means that the frequencies at  $\omega = 3\pi, 5\pi, 7\pi \dots$  are where the maximum values of amplitude occur. These values are the resonance frequencies.

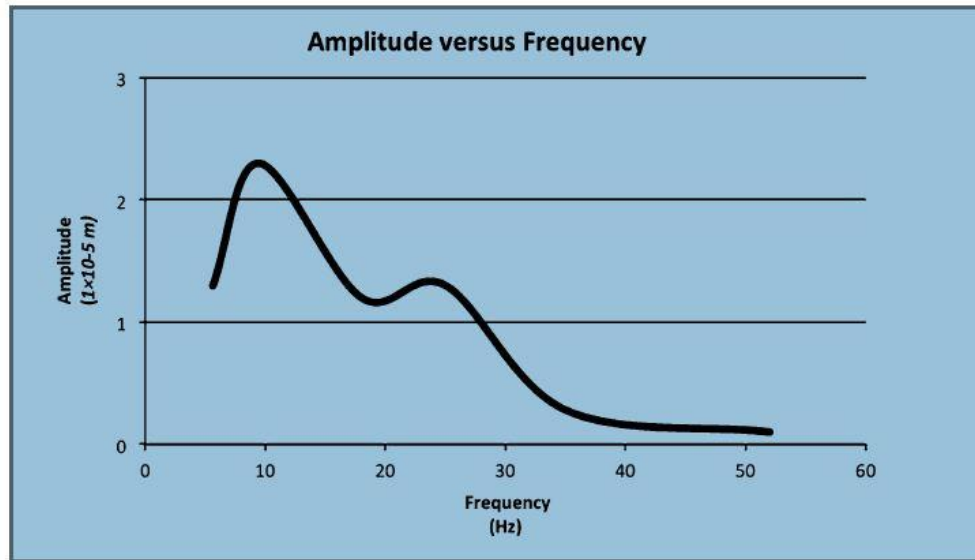


Fig. 2. Relationship between Frequency and Bending Amplitude for human arm vibration [3]

Fig. 2 shows that the amplitude of a propagating wave along the human arm is a function of the frequency. Equation (5) also demonstrated that the ratio of the amplitudes is proportional to the squares of the frequency ratios [3]. By plugging in the frequencies at which the first maximum amplitudes occur,  $3\pi$  and  $5\pi$ , and using the relationship between the amplitude and frequency ratios, it can be determined that the first ratio of maximum amplitudes is  $\frac{(3\pi)^2}{(5\pi)^2} = \frac{9}{25}$ . This ratio,  $\frac{9}{25}$ , matches the data shown in Fig. 2, which contains experimental data collected from an external study [3]. This confirms the theoretical results of the resonance frequencies in the human arm. The amplitude increases significantly when a piece of equipment vibrates at a resonant frequency. For example, the amplitude at the frequency  $3\pi$  Hz is approximately  $2.4 \times 10^{-5}$  meters, compared to about  $1.3 \times 10^{-5}$  meters at 6 Hz and 15 Hz. Fig. 2 illustrates this spike in amplitude. The increased amplitude means that a larger amount of energy is being transferred into the hand-arm system because the energy is proportional to the square of the vibrational amplitude.

**Constructional Tool Data:** Clearly, the vibration of a handheld tool vibrating at a resonance frequency will lead to a great amount of energy propagating through the arm. This higher amplitude resulting from resonance also means the hand-arm system undergoes larger displacements. The vibrations from work equipment displace the arm repeatedly, damaging the tissue and bone. When a piece of equipment vibrates at one of the arm's resonance frequencies, the amplitude is increased along with the amount of energy surging through the arm. This displacement of the arm is one of the central causes of HAVS.

**TABLE II**  
Summary of Dominant Frequency and Corresponding Individual Axis Acceleration Magnitude for Tools Tested

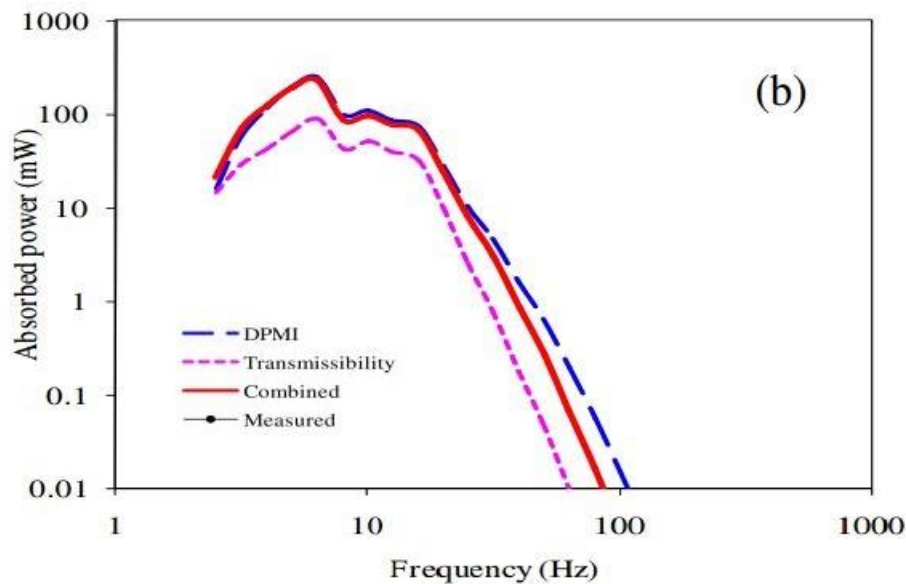
Tool Description	Handle	No. of Hands	Abrasive	Frequency (Hz)	Magnitude (m/s <sup>2</sup> ) Axis		
					X	Y	Z
Hand grip orbital sander	main	1	100 grit	90	50	60	190
		2	100 grit	90	30	70	220
		1	80 grit	90	70	50	120
		2	80 grit	90	40	90	110
	body	2	100 grit	90	90	110	140
		2	80 grit	90	60	80	90
Palm grip orbital sander	body	1	320 grit	150	120	70	40
	body	1	100 grit	150	120	70	170
	body	1	80 grit	150	115	60	120
Impact wrench	body	2	locked spindle	50	10	10	10
Heavy duty right angle sander	main	2	80 grit	45	5	2	2
	dead	2	80 grit	45	5	6	6
	main	2	grinding disc	80	90	70	40
	dead	2	grinding disc	80	40	50	80
Trimming shear	main	1	blade	35	6	15	10
Light duty right angle sander	main	2	fine disc	70	3	2	1
	dead	2	fine disc	70	2	6	7
Jitterbug sander	body	1	230 grit	100	290	110	130
Vertical polisher	right	2	polishing pad	100	20	20	20
	left	2	pad	100	30	20	150

Fig. 3: Frequencies and Directional Accelerations of Various Tools used in an Automotive Assembly [6]

It is crucial then to know the frequencies at which tools typically operate. A list of frequencies specific to certain tools in an automotive assembly plant is shown in Fig. 3.

In the example set of tools above, the dominant frequencies of all tools measured were greater than the theoretically calculated resonance frequencies of  $3\pi$  and  $5\pi$  hertz. These resonance frequencies apply to the region of the arm beyond the elbow and extending to the shoulder. According to research done by the Center for Disease Control, most mathematical models find that vibration energy propagating at frequencies lower than 80 hertz affects the arm, while tools with vibrating frequencies greater than 100 hertz typically are limited to transferring energy just into the hand [2]. This agrees with what was found in the mathematical analysis for the viscoelastic rod model.

Fig. 4 demonstrates a model done by an external study that agrees with this above trend. Vibrations at lower frequencies transfer more energy per unit time to the shoulder, while higher frequencies transfer much less. There is also a spike in absorbed power at approximately  $3\pi$  Hz, which concurs with the resonance frequency found using the viscoelastic rod model [3]. The tools included in the study shown in Fig. 3 would not cause resonance in the shoulder region of the arm. However, this sample set is clearly not enough data to conclude that a majority of power and construction tools do not vibrate at a frequency to cause resonance and therefore increase the amplitude of stress waves propagating across the human arm. It is recommended that all tools manufacturers list the dominant frequencies at which their products operate and attempt to minimize the production of tools that operate near the resonance frequencies of the arm.



*Fig. 4. Vibrational power absorbed at the shoulder of an extender arm as a function of frequency [7]*

**HAVS Prevention Methods:** It may be recommended that the workers invest in anti-vibration gloves. Manufacturers produce the protective characteristics of the gloves in several ways. They may increase the thickness of the contact patch on the glove in order to absorb vibration with the extra padding. This is the most commonly used technique. They may also use an anti-vibrational polymer such as Vibrastop Nylon. Adding such a polymer to the fabric increases glove's vibrational absorption. This method maintains a slimmer sized glove. Another method, patented by the worker safety firm Impacto©, is to insert small air bubbles into the glove. The glove acts similarly to bubble wrap and protects the hand [8][9]. These types of gloves can be purchased at a price close to non-protection construction gloves and are an inexpensive and effective way to lower the risk of damage to the hand-arm system due to contact with vibrating machinery.

It may also be recommended that the construction companies invest in anti-vibrational machinery for the long-term health and safety of their workers. Unfortunately anti-vibrational mechanisms in machinery are only built into the high cost brands. In some instances, like the Bosch jackhammer, manufacturers claim a reduction of the vibrational transmission to the hand-arm system by up to 40% [10].

**Summary** It is clear that the hand-arm system has been greatly simplified for analysis. However, the model system of two linear viscoelastic rods and a hinge allows the study of resonance using the relationship between amplitude and frequency. The model also determines the viscoelastic parameters of the hand-arm system. This model ultimately allows for a fair representation of the hand-arm system and at what frequencies external vibration will cause resonance and do the most damage to a living human arm. Since it is dangerous and difficult to obtain data regarding the response of bones to vibration from human subjects, the viscoelastic rod model is a valuable alternative. Information obtained from the analysis of this model should be used by manufacturers of vibrating equipment, specifically construction machinery, to limit the risk to those operating the equipment. Based on all the information provided and the side effects that HAVS produce in the long-term, it is highly recommended that companies invest in anti-vibrational gloves and machinery with anti-vibrational mechanisms built in. These precautions are likely to decrease the probability of the onset of HAVS in a worker and continued progress in the field of anti-vibration may further eliminate the risk. Effective application of this information may be able to prevent damage to the hand-arm system and HAVS.

## References

- [1] Pieter, Den Hartog Jacob. *Mechanical Vibrations*. New York: Dover Publications, 1985. Print.
- [2] "Vibration Syndrome." Centers for Disease Control and Prevention. Centers for Disease Control and Prevention, 06 June 2014. Web. 15 Jan. 2016.
- [3] Viktorova, Irina, Lauren Holden, and Sara Bailey Stocks. "Analysis of Resonance Frequencies for the Problem of Induced Vibrations Along the Human Arm." *Collaborative Mathematics and Statistics Research Springer Proceedings in Mathematics and Statistics* (2014): 67-73. Web.
- [4] Christensen, R. M. *Theory of Viscoelasticity: An Introduction*. New York: Academic, 1971. Print.
- [5] Coleman, Bernard D. *Wave Propagation in Dissipative Materials*. Berlin: Springer, 1965. Print.
- [6] Radwin, Robert G., Thomas J. Armstrong, and Ernst Vanbergeijk. "Vibration Exposure for Selected Power Hand Tools Used in Automobile Assembly." *American Industrial Hygiene Association Journal* 51.9 (1990): 510-18. Web.
- [7] Adewusi, S., S. Rakheja, P. Marcotte, and M. Thomas. "Distributed Vibration Power Absorption of the Human Hand-arm System in Different Postures Coupled with Vibrating Handle and Power Tools." *International Journal of Industrial Ergonomics* 43.4 (2013): 363-74. Web.
- [8] "Anti-Vibration Gloves Are Worth Every Penny." *Chainsaw Journal*. N.p., 27 Feb. 2015. Web. 29 Feb. 2016.
- [9] "Impacto BG40840 Anti-Vibration Mechanic's Air Glove, Black." *Anti Vibration Safety Gloves*. N.p., n.d. Web. 29 Feb. 2016.
- [10] "Robot Check." *Robot Check*. N.p., n.d. Web. 29 Feb. 2016.

# Monitoring the Natural Factors Influence on Vegetation Development by Using Moderate-Resolution Imaging Spectroradiometer (Modis) Images with OBIA Method in Uzbekistan

Sh. B. Akmalov<sup>1</sup>, J. V. Gerts<sup>2</sup>, D. B. Omonov<sup>3</sup>

1 – Lille 1 University of Science and Technology Villeneuve d'ASCQ, Paris, France

2 – Tashkent Institute of Irrigation and Melioration, Tashkent, Uzbekistan

3 – Tashkent State Agrarian University, Tashkent, Uzbekistan



DOI 10.13140/RG.2.1.1185.1920

**Keywords:** Syrdarya, remote sensing, object based image analysis (OBIA), eCognition, moderate-resolution imaging spectroradiometer (MODIS), NDVI.

**ABSTRACT.** In the study, natural and anthropogenic effects on vegetation are discussed and degree of their influence are shown in Syrdarya province (Uzbekistan). A statistical model of integrated meteo- and hydro- remote sensing data was developed. By the use of this model the correlation of various natural factors in vegetation period was analyzed and scale-dependency of spatial relationships between NDVI and three climatic factors were investigated. MODIS NDVI images have been used for the study area and OBIA method was applied via eCognition software.

**Introduction.** Agriculture is a vital industry in Syrdarya province (Uzbekistan) and it plays a key role in supporting the greatest part of population. However, hot summer winds drain the soil and harm the plants. Intense evaporation in summer cause salinization and other negative processes on the surface of the field [1].

Nowadays, remote sensing techniques are widely used in updating land cover information, environmental protection and ecological monitoring. The use of RS data prove to be useful for observation anthropogenic effects, natural and ecological processes on a large scale [2]. RS allows observation of processes over long timescales and at the same time helps us to solve many difficulties and necessities, existing in traditional ecological analyzing method [3].

The high temporal resolution of the MODIS datasets can provide an efficient and consistent way for monitoring of biomass, vegetation and above-mentioned factors. [4] Consequently, such high temporal and medium spatial resolution sensor like MODIS could be a very useful tool for such investigations on the regional scale.

**Methods and materials. Study area.** Syrdarya is one of twelve provinces of Uzbekistan, which borders on Kazakhstan Republic in the north, on Tashkent province in the east, on Tajikistan Republic on the south and on Jizzakh province in the west. Gulistan city is the center of the province. The province is located on the left riverside of Syrdarya, the main source of irrigation water in the province. (Figure 1).

The climate of the region is continental with hot and long summers, and short winters with little snow. The long-term annual average temperature in the region is + 14.75°C. Ground in daylight time warms up to 38-40 °C, in winter temperature decreases up to -10°C (UzGidroMet data 2000-2012). Precipitations mainly occur during the winter-spring months showing and averages at 340 mm per year. Relative moisture of the air at wintertime forms 74-78%, but in a year, it is about 29-31%, at average annual rate of 56%. Annual evaporability is 1500 mms [5] (Figure 2).

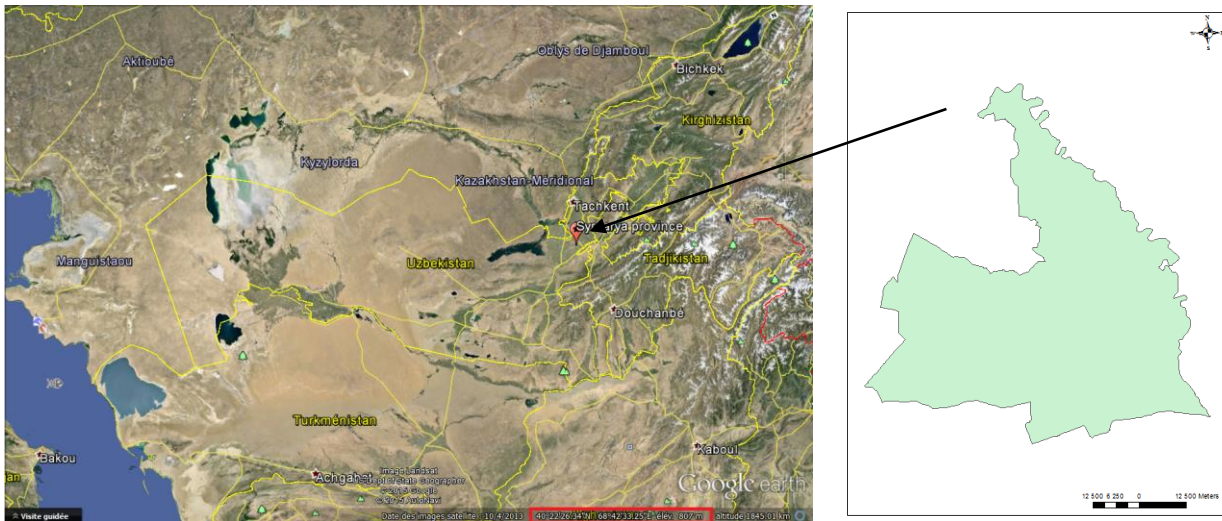


Fig. 1. Study area. (Source: Google earth image and GIS shape file of Syrdarya province)

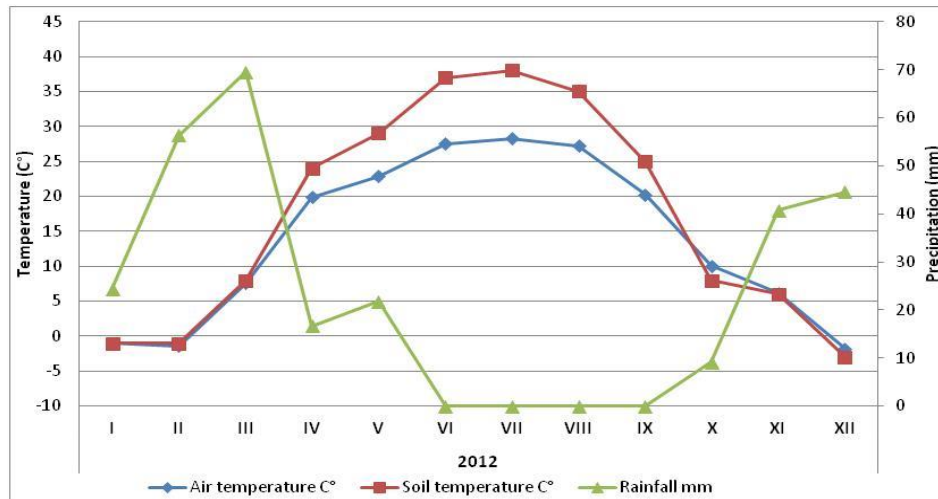


Fig. 2. Average annual meteorological data of Syrdarya province. (Source: UzGidroMet data)

**Data.** Some meteo data was selected for correlation analysis of MODIS NDVI value to natural factors. This data (2000-2012) has been provided by UZGIDROMET center and includes the following: air temperature, runoff value of Syrdarya River, participations.

**MODIS NDVI data.** Analysis required Terra (MOD13Q1) MODIS vegetation index products which are provided every 16 days at a spatial resolution of 250 meters as gridded level-3 products in the Sinusoidal projection. The Terra 16-day period starts from the day 001. In the study 154 images from the period between 2000 and 2012 were taken in sequence of one image per month. Georeferenced MODIS NDVI images were provided free of charge by [glovis.usgs.gov](http://glovis.usgs.gov).

**Tools and software.** OBIA method was used during the analysis, which was performed by eCognition program. With this software, MODIS NDVI images have been segmented up to the homogenous object of the surface for the whole Syrdarya province. Segmentation parameters were chosen as follows in Table 1.

After the segmentation, monthly average values of NDVI have been copied from the window of "image object information" and pasted to Excel file. Then, the water volume of river, average values of temperature and monthly total sum of precipitation were added to the data base in accordance with months in a year.

**Results and discussion.** By statistical analysis, the correlation coefficients (R) of monthly NDVI changes have been found. Table 2 shows the correlation of vegetation with natural factors within the last 12 years.

Table 1. Segmentation parameter of MODIS NDVI images

Name	Number of images	Image layer weight	Scale Parameter	Shape	Compactness	Number of object
MODIS NDVI	154	1	80	0,1	0,9	1 Province

Table 2. Correlation results

	Amount of water (entrance to Syrdarya reg.) m3/s	Rainfall mm	Air temperature C°
Mean NDVI of province	-0.73	-0.47	0.87

In accordance to the results, the precipitation almost do not have an impact on vegetation period, since the correlation coefficient between them is equal to  $R=-0.47$ , which means the absence of any relation. It could be explained by the fact that precipitation in province mostly falls in the non-vegetation period and the greatest part of agriculture is based on irrigation.

At the same time, NDVI has strong negative correlation with the change of water volume of the Syrdarya river. In spite of the fact that this river is among ice-fed rivers R is equal to -0.73.

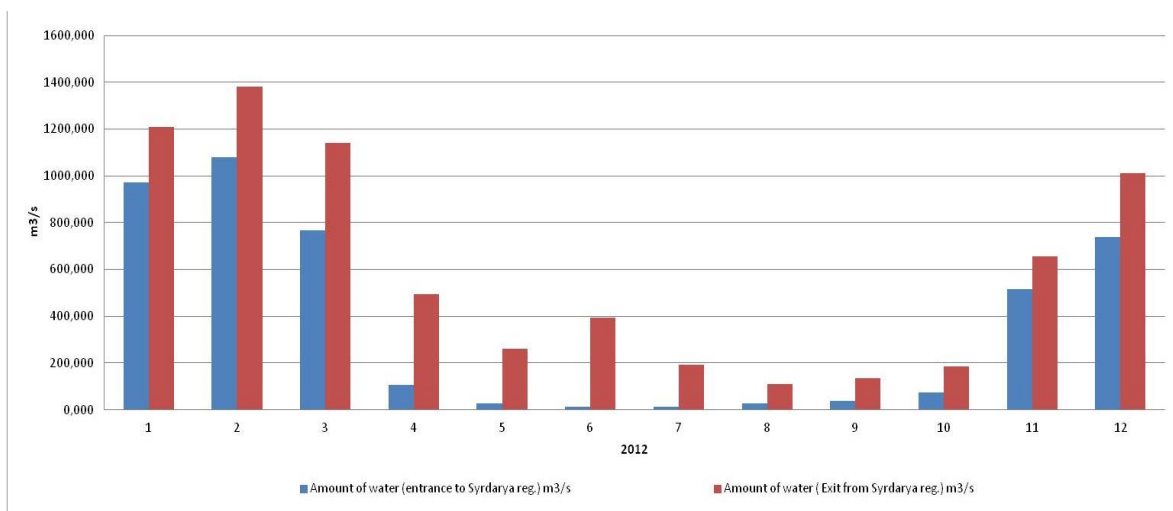


Fig. 3. Annual average volume of water of Syrdarya river. (Source: UzGidroMet data)

We imply that this fact appears because two water reservoirs in the up-flow part of the river (Tohtagul reservoir in Kyrgyzstan and Kayrakkum reservoir in Tajikistan) collect water intensively during

vegetation period and in non-vegetation period a huge amount of water is dropped to Syrdarya in order to produce electrical energy (Figure 3). Water do not almost influence the vegetation period in province, because it is dropped in down-stream and drain water reaches the river which flows straight away to the neighboring Kazakhstan.

However, correlation index of vegetation period with temperature is very high (0.87), which means that the vegetation period occurs in hot seasons of the year.

**Conclusion and recommendations.** Satellite information (in particular MODIS data) is very important if we are going to solve the influence of natural and anthropogenic factors on vegetation development. For such issues remote sensing provides a wealth of time-consuming information at a global scale.

Nowdays, MODIS images are in open access, and the analysis program of eCognition Developer is not very expensive, which means their accessibility for the researches. Besides, MODIS images have NDVI band, which saves us from the difficulties of calculation.

In accrodance with analysis result, vegetation development has high levels of concordance with temperature, but at the same time negative relations with water volume and precepitations revialed. Influences of hot summer, artificial irrigation and water shortage in agricultural areas were chosen as a main factors for that.

Trans boundary water problems are international issues requiring global interferences. It could be recommended to continue current investigations by gathering field experiments with results and conducting future analysis of factors influencing the natural changes.

## References

- [1] Tukhliev N., Kremensova A. Republic of Uzbekistan: encyclopedic reference. [country and the administrative division of the people, history, government structure, economy, education, science, health, life, cultural life]. "National encyclopedia of Uzbekistan" State Scientific Publishing, Tashkent. 2007.
- [2] Gyuris, Mr Peter. 2015. "WP4-Satellite RS deliverable D4. 1 report on the limitations and potentials of Satellite eo data." Accessed June 9.
- [3] Giniyatullina, O. L., V. P. Potapov, and E. L. Schactlivtcev. 2015. "Integral Methods of Environmental Assessment at Mining Provinces Based on Remote Sensing Data." Accessed June 8.
- [4] Brigante, Raffaella, and Fabio Radicionis. 2014. "Use of Multispectral Sensors with High Spatial Resolution for Territorial and Environmental Analysis." *Geographia Technica* 9 (2).
- [5] World Bank Project 2010. «Water supply of Syrdarya province». Agency «Uzkommunservice». Uzbekistan, Tashkent.
- [6] Law, Beverly E., Tim Arkebauer, John L. Campbell, Jing Chen, Osbert Sun, Mark Schwartz, Catharine van Ingen, and Shashi Verma. 2008. "Terrestrial Carbon Observations: Protocols for Vegetation Sampling and Data Submission." FAO, Rome.

# An Empirically Derived Arc Flash Discharge Energy Model and Comparison to Established Safety Codes

Irina Viktorova<sup>1, a</sup> & Michael Bates<sup>2, b</sup>

1 – Department of mathematical sciences, Clemson University, Clemson, USA, SC

2 – Department of mechanical engineering, Clemson University, USA, SC

a – [iviktor@clemson.edu](mailto:iviktor@clemson.edu)

b – [mabates@clemson.edu](mailto:mabates@clemson.edu)



DOI 10.13140/RG.2.1.4793.6404

**Keywords:** electric arc, arc flash, Lambert W function, Paschen's law.

**ABSTRACT.** Arc flash is a constant hazard when discussing industrial safety, however, little is known about the arc flash. Current safety standards require the use of the NFPA 70E equation to establish safety limits for arc flash hazards. However, when compared to an empirically derived model, these safety limits are much too low to account for all working conditions. A comparison of these two methods will lead to the conclusion that arc flash safety distances must be increased.

**1. Introduction.** In industrial electrical safety, arc flash hazards can be some of the most disastrous and deadly accidents in the work place. An arc flash can reach temperatures of over 35000 degC and cause an explosion with a blast force of 2000 psi and an audible report of over 140 decibels. At a current of just 0.5 Amps, an electrical shock, such as the shock generated from an arc flash, will stop the heart of an adult. [1]. Current arc flash safety codes require that the worker be at a distance that, if an arc flash were to occur, would only result in 2nd degree burns. The current accepted standard for arc flash energy calculations is given by the NFPA 70E equation, which was derived experimentally. However, an empirical approach to determining arc energy will be derived in this paper and the results compared and examined.

**2. Methods.** In analyzing the safety limits for arc flashes, two methods will be used. The first is the well-known NFPA 70E equation for calculating arc flash energy. The second method is an expression derived from Paschen's law.

**2.1. The NFPA 70E Equation.** Current safety limits require that a worker be at a distance that is at least far enough away from the arc flash hazard to produce only 2nd degree burns if an arc flash is initiated. To calculate this the NFPA 70E equation for a cubic box must be considered. This equation gives the arc energy,  $E_{MB}$  as

$$E_{MB} = 1038.7 D_B^{-1.4738} t_A [0.0093 F^2 + 0.3453 F + 5.9673], \quad (1)$$

where  $E_{MB}$  – is the arc flash energy in  $cal/cm^2$ ;

$D_B$  – is the working distance in inches and  $F$  is the short circuit, in amps.

Fig. (1) below shows the arc energy as a function of distance from the hazard [2].

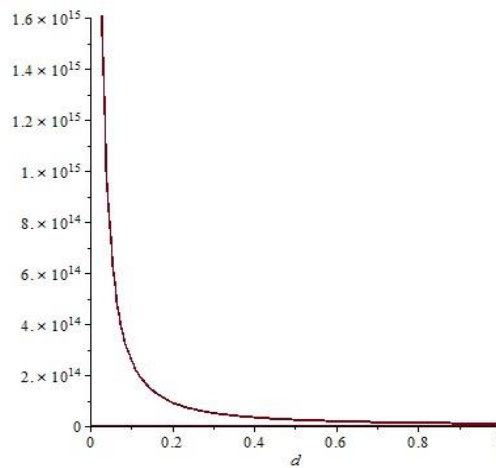


Fig. 1. Arc Energy with respect to distance

In accordance with Eq. (1) a worker would have to be 0.52 meters away from the potential hazard to only receive a 2nd degree burn.

**2.2. Paschen's Law.** While NFPA 70E provides a convenient experimentally derived equation for calculating arc energy, a more empirical approach by applying the well-known Paschen's law can be developed. The breakdown voltage,  $V_B$  or the minimum voltage required to discharge an electric arc between two electrodes, is described by Paschen's Law, named after the Friedrich Paschen in the 19-th Century. This relationship is a function only of the pressure,  $p$  and the gap distance,  $d$ . and the gap distance. In this system, a human and an electrical breaker box are modeled as two cathodes. Paschen's law is given as [3]

$$V_B = \frac{BpD_B}{\ln(APD_B) - \ln[\ln(1 + \frac{1}{\gamma_{se}})]}, \quad (2)$$

where the experimental constants  $A$  and  $B$  are determined experimentally.

For air at atmospheric pressure, the breakdown voltage as a function of gap distance is shown below in Fig. (2).

It can be shown that the electrical power  $P$  could be written as follows:

$$P = VI, \quad (3)$$

where  $V$  – is voltage;

$i$  – is the electrical current.

Combining Eqs. (2 - 3) yields the following expression for the electrical power generated in an electric arc at the breakdown voltage,  $P_{EA}$ , such that

$$P_{EA} = \frac{BpD_B}{\ln(APD_B) - \ln[\ln(1 + \frac{1}{\gamma_{se}})]} I \quad (4)$$

Finally, to calculate the total energy from the electric arc over a sustained time period,  $E_{EA}$  the product of the electric power and the total time that the arc is sustained,  $t_A$  must be taken such that

$$E_{EA} = \frac{BpD_B}{\ln(APD_B) - \ln[\ln(1 + \frac{1}{\gamma_{se}})]} It_A \quad (5)$$

This expression, when the theoretical constants for  $A$ ,  $B$  and  $\gamma_{se}$  are substituted in depends solely on the distance from the arc flash hazard. Because in the segment of the Paschen curve, the breakdown voltage increases with distance, at the same current and same discharge time – the arc will require a greater potential difference to initiate. Thus increasing the total output energy as distance increases as shown below in Fig. 2. Solving Eq. (5) for the distance from the arc hazard,  $d$ , yields the following expression

$$D_B = -0.2300e^{-5} E_{EA} W(-\frac{0.3813e^{-1}}{E_{EA}}), \quad (6)$$

where  $W$  – is the Lambert  $W$  function described as the function, which satisfies:

$$W(z)e^{W(z)} = z \quad (7)$$

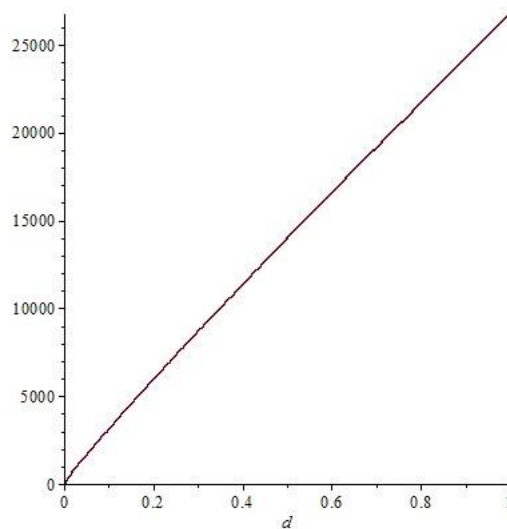


Fig. 2. Output energy based on distance from arc flash hazard

**3. Results.** In both cases, the current used in the system was 20 Amps. In the case of a short circuit, this would deliver 20 Amps of current to the worker. It is also important to note that the specified "safe distance" from an arc flash hazard is the distance where a worker would only receive second degree burns as a direct of being hit with an arc. This is calculated to be 2 cal/cm<sup>2</sup> of discharge energy. For the NFPA 70 E equation, it was calculated that the "safe distance" from the hazard for a worker was 0.52 meters. This is a very reasonable distance. However, when that same distance of 0.52 meters was used to calculate the arc energy in the Paschen's law derivation, a resulting discharge of 3.46 cal/cm<sup>2</sup> was obtained using the following parameters:

*Table 1. Arc Discharge Parameters*

Parameter	Value
<i>A</i>	112.5
<i>B</i>	2737.5
<i>p</i>	101325 Pa
$\gamma_{SE}$	1.5
<i>i</i>	20 A

**Summary.** It is obvious, that this value is much higher and capable of inflicting more than a second-degree burn. There are several reasons for this discrepancy. First, the NFPA 70E standard requires the use of certain protective equipment to reduce the Creative Inquiry risk of the arc flash. Secondly the 70E equation also assumes that the hazard is placed within and electrical box, while this is not always the case. To improve worker health and safety, it is necessary to increase the distance of the worker from the hazard to account for a more general case. Such considerations indicate that the 70E equation indicates and inadequate safe distance for the worker and this distance must be increased to conform the limits set in Eq. (5).

## References

- [1] Bowman, Bruce, P.E. *NFPA 70E Electrical Safety Presentation*. Rep. N.p.: Alliance, n.d. Print.
- [2] Elgazzar, Mohamed G., P.E. *The Secret to Understanding Arc Flash Calculations*. The Secret to Understanding Arc Flash Calculations. ECM, n.d. Web. 22 Mar. 2016.
- [3] Lieberman, Michael A.; Lichtenberg, Allan J. (2005). *Principles of plasma discharges and materials processing (2nd ed.)*. Hoboken, N.J.: WileyInterscience. 546. ISBN 978-0471005773. OCLC 59760348.

## On Development of a New Filtering Half-Mask

S.I. Cheberyachko<sup>1</sup>, D.I. Radchuk<sup>2</sup>, Y.I. Cheberyachko<sup>2</sup>, M.O. Ziborova<sup>3</sup>

1 – Professor, National Mining University, Ukraine

2 – Associated professor, Dnepropetrovsk National University, Ukraine

3 – M.Sc., National Mining University, Ukraine



DOI 10.13140/RG.2.1.3389.4802

**Keywords:** penetration ratio, heat exposure, fiber, polypropylene filter, Leaf-type respirators.

**ABSTRACT.** The paper describes adapting problems for respirators, produced in Ukraine to European standards. It was found that the Leaf type respirator of FPP material doesn't meet the parameters of DSTU EN 149: 2003 at a rate of dust penetration through the respirator filter after thermal and mechanical influences and flameproof. Study has shown, that increasing duration of heat exposure the structure of the filter material undergoes irreversible changes. This leads to a decrease in the protective efficiency. Using polypropylene filter materials allow replacing FPP materials, which indicators meets European standards, and do not contradict the traditional view of potential consumers.

**Introduction.** Dust bronchitis and pneumoconiosis today dominate among all occupational diseases. Their level is formed by the coal and mining industry and is 60 – 70% [1]. This is due to lack of efficacy and collective means of protection and violation of the process, that leads to a deterioration of working conditions, and non-compliance with safety regulations, and the lack of effective control of the dust load. In addition, the chemical composition of the mine dust is very diverse and may contain lead and mercury, fluoride and arsenic materials, compounding effect on the body of silica present in the rock dust [2]. Influence of the dust dispersion generally predominate with fraction particle size less, than 5 microns [3].

A significant role in the prevention of occupational diseases caused by dust factor is personal protective respirators (RPE). The most widely used in the mining industry respirator type " Leaf". Its technical characteristics allow providing sufficiently high protection (enough lifetime during dust concentration 200 mg/m<sup>3</sup>) as opposed to a combination of other samples has a minimal effect on the functional state of the person. Note, that for the manufacture of the respirator previously used filter material *FPP*, which is characterized by its fiber electrostatic charges, which significantly increase the capture of fine dust particles [4].

The reason for this discrepancy is that the material *FPP* can resist mechanical deformation and do not collapse, as it consists of dry fibers bonded at points of contact only by adhesion forces, and pressed to each other by electrical forces [6]. Irreversible damaging influence of mechanical action can cause significant penetration of the test aerosol paraffin and oil (determined at a rate of 95 l / min) from a relatively stretching of rolled into a tube samples FPP 15-1,5 tensile material axially coagulation (Fig. 1). For comparison was also tested a polypropylene filter material Eleflen, which specifications denoted in [7]. It can be seen, that the permeability of the material FPP grows faster, than Eleflen, that confirms our assumption.

Moreover, the temperature influence on the operational factors FPP lead to a change in the mechanical properties of the fiber layer and disruption of its structural parameters and hence to its destruction.

This is evident from the experimental dependence of the relative ratio of penetration  $\frac{K(t)}{K}$  duration of isothermal heating of samples of filter materials in a furnace at a temperature  $t = 300$  °C (fig. 2).

Table 1. Key indicators FFP2 respirators Leaf DSTU EN 149: 2003

Defined indicators	The value of indicators	
	Factual	According to EN 149 for FFP2
Penetration ratio for the test aerosol paraffin oil at a rate of 95 l / min, K,% - after delivery; - After the temperature exposure - After a mechanical action	2,5 8,1 4,6	No more 6
Permanent resistance to airflow at a flow rate of 95 l / min, R, Pa, - After delivery; - After the temperature exposure; - After a mechanical action;	90 77 86	No more 240
Test for flammability under $t = + 800^{\circ}\text{C}$	Ignites and continues to burn	Not flammable

As a result, during filter heat exposure increase the material suffers irreversible structure change. This decreases the protective efficacy of RPE as filtering properties of the material and has sustainable performance only up to  $60^{\circ}\text{C}$ . According to the State Standard DSTU EN 149: 2003, before the start of the test there is need some time to withstand the test samples in a chamber with a temperature of  $70^{\circ}\text{C}$ .

Therefore, harmonization of Ukrainian and European standards requires to develop a new type of respiratory protective equipment, whose technical specifications meet European standard. The problem is also caused by the fact, that workers, who have used to respirator " Leaf" in recent decades, are wary about new types of products, refusing to recognize their quality.

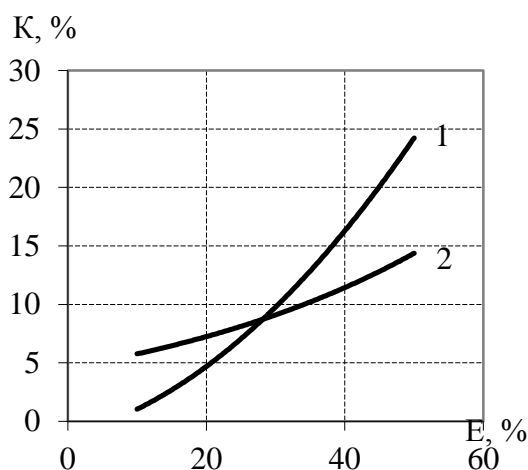


Fig. 1. Dependence of the coefficient of penetration by the oil mist from the relative stretching filter material folded into a tube during tension along the axis: 1 - 15 FFP - 1.5; 2 - Eleflen

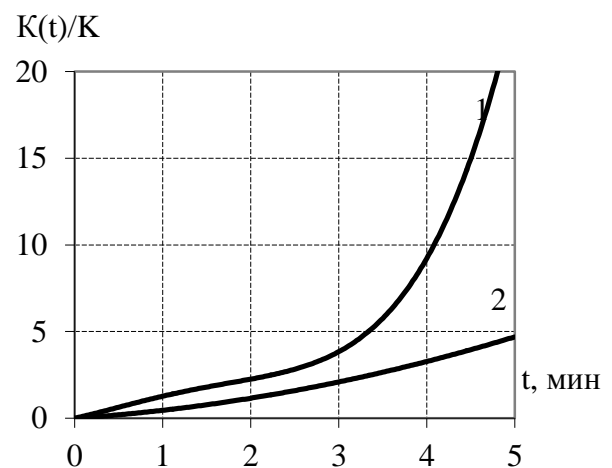


Fig. 2. Dependence permeation coefficient for the duration of oil mist filter materials isothermal heating the samples in an oven at  $t = 150^{\circ}\text{C}$ : 1 - 15 FFP - 1.5; 2 - Eleflen

To solve the problem it is necessary to follow the path of existing respirator " Leaf" modernization, which is going to substitute filtering material FFP.

Polypropylene filter materials have been used for a long time. However, safety features of them are enough low. This is due to the relatively large fiber diameter 3-8 microns and their large spread, significant unevenness of surface density, the surface electrostatic charge in contrast to bulk materials in *FPP*. Therefore, proposals for the improvement of technologies have been developed to improve the quality of the filter material.

The process for producing a fiber from melt consists the following steps: melting the polymer forming fibers from the melt, and cooling the fixing device on the receiving fiber (figure 3.). The fiber produced by extrusion. Extrusion - is to obtain products from polymeric materials by extruding the molten polymer through a forming head (nozzles) of the desired profile. The simplest and most common is a single screw extruder without degassing zone (Fig. 4).

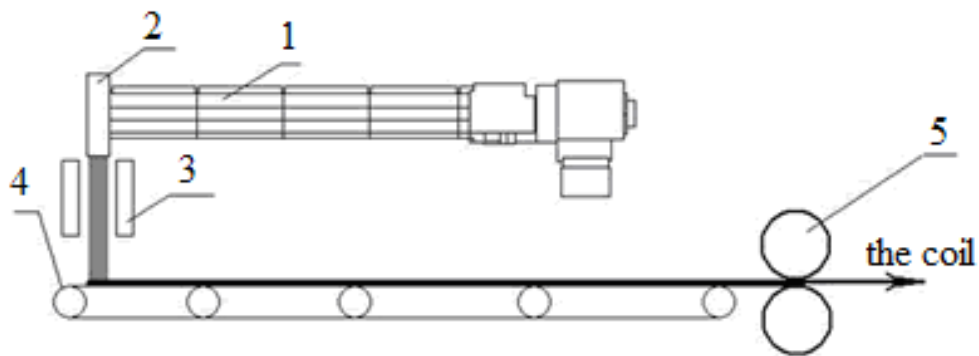


Fig. 3. Block diagram of the installation for the production of polypropylene filter material: 1 - extruder; 2 - forming head; 3 - die; 4 - the pipeline; 5 – drums

After loading the resin into the hopper, it transports to the hotter zones of the cylinder. With decreasing cutting depth and volume of the coil is reduced, which leads to the compression of granules which are melted. This improves the mixing of the polymer and makes better heat distribution in the melt. The final zone of the screw is a final melt homogenization. However, the process of material extrusion occurs outside the forming head [8].

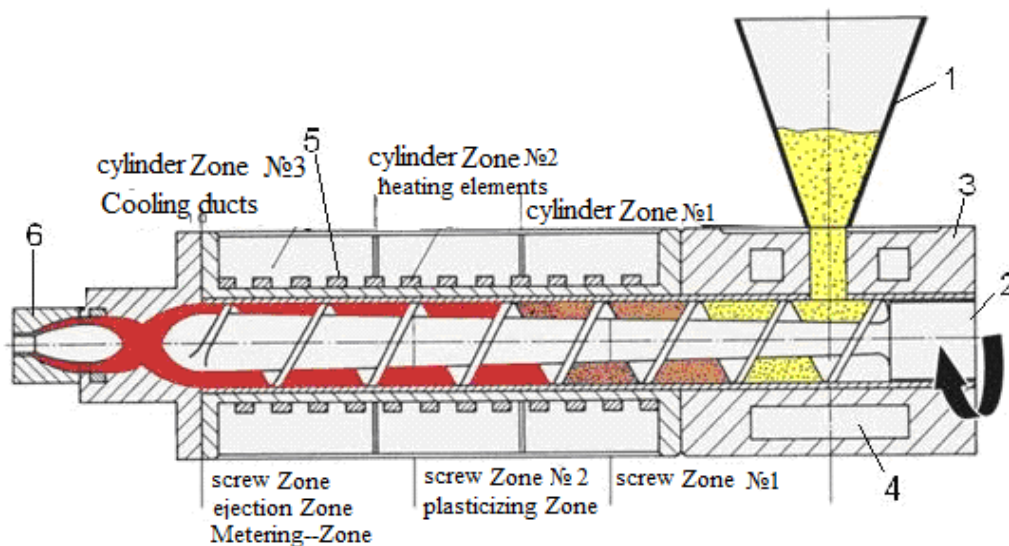
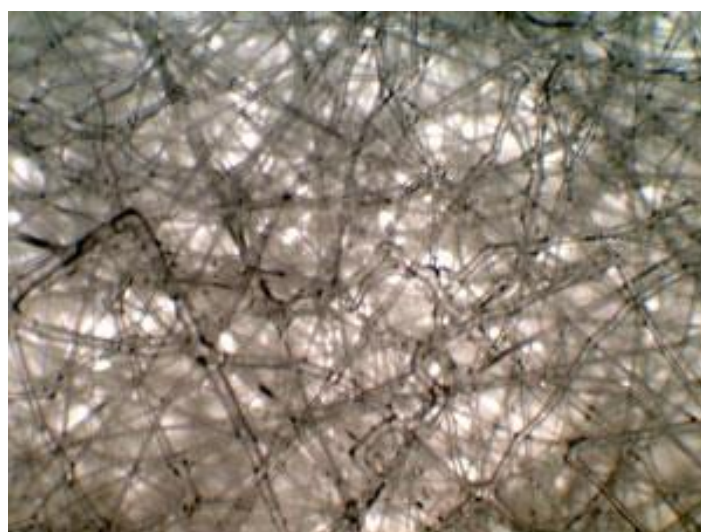


Fig. 4. Extruding tool: 1 – hopper; 2 – the screw; 3 – cylinder; 4 – cavity for water; 5 – heater; 6 – forming head

Molten polymer flows to and through the spinnerets holes a different diameter is applied to the zone where the fibers are drawn by hot air. Polymeric fibers entering the drum or conveyor, stretch out and intertwine crystallize, forming a filter layer. The main influence on its quality has a working temperature of the melt. Increasing melt temperature, viscosity decreases polypropylene facilitating thinning the fiber diameter, more uniform distribution of the fibers on the drum, but adversely affect the plant operation parameters. Thus, the long term effects high temperatures leads to slagging setup that interferes with normal feeding of the melt to spinnerets. Therefore results in a larger fibers, deterioration of their distribution on the drum width, the appearance of significant voids in the filter layer, for adhering fibers to the drum, or conveyor. Hence, to obtain high-quality filter material must adhere to a specific, sensitive to changes, temperature [9].

As a result, a long experimentation with temperature parameters a filter material has ben developed, which is a nonwoven grid of thermally ultrathin polypropylene fiber diameter of 2...5 mkm, weighing 38 - 42 g/m<sup>2</sup>, supported on a layer of gauze (fig. 5.). Which in its performance is not inferior materials FPP. Laboratory studies proved its high protective characteristics (table 2).



*Fig. 5. The structure of the propylene polymer material*

*Table 2. Technical characteristics of polypropylene material*

Materials	Surface density, g / m <sup>2</sup>	Resistance to air flow in the filtration velocity of 1 cm / s, Pa	Breaking strength, N	The rigidity of the material, sm	Relative extension, %	The fiber diameter, microns	permeation coefficient for a test aerosol, paraffin oil, K%
Eleflen - 40	38-42	4,2	6,0	6,0	50	2-4	0,6
Eleflen 40M	38-42	3,2	6,0	6,3	50	2-5	1,1

A pilot batch of 100 pieces dust mask "Standard" (fig. 6) was manufactured in NPP "Standard" and after laboratory tests showed a positive result, these products have been submitted to the test center (Lodz, Poland). As a result, it was found that the protective properties of the indicators developed by the half-mask defined after preliminary thermal exposure and modeling socks mode, comply with the requirements of EN 149 (Table. 3).

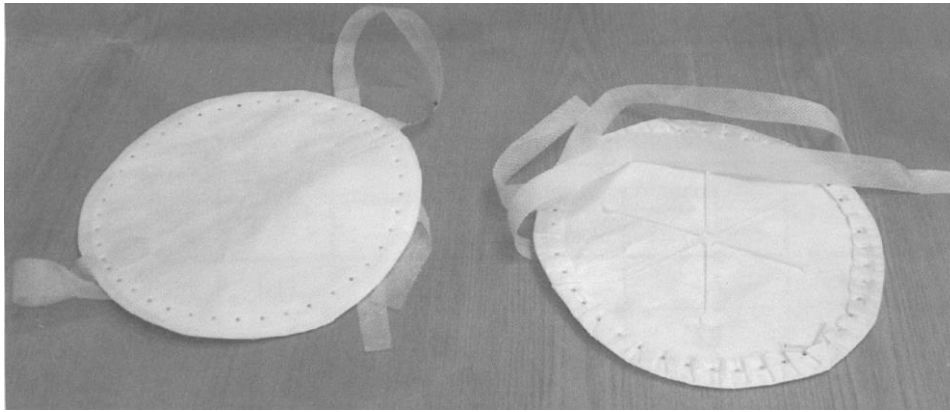


Fig. 6. Experimental samples of respirators

Table 3. Key indicators respirator FFP2 standard in accordance with EN 149: 2003

Defined indicators	Value indicators respirators prototypes
permeation coefficient for a test - aerosol, paraffin oil at a rate of 95 l/min, K, % - after delivery; - After the temperature exposure - After a mechanical action	0,6±0,1 2,9±0,2 0,67±0,1
Resistance to constant air flow at a rate of 30 l / min, R, Pa - After delivery; - After the temperature exposure - After a mechanical action	18±0,4 17±0,4 18±0,3
Test for flammability under $t = 800^{\circ}\text{C}$	not flammable
The content of carbon dioxide in the air breathed, %	no more 1 %

**Summary.** It was found that FPP material of Leaf type respirator does not meet the parameters of DSTU EN 149: 2003 at a rate of dust penetration through the respirator filter after thermal and mechanical influences (for FFP2 class products - the average efficiency) and product flammability. Study showed, that increasing duration of exposure to heat the structure of the filter material undergoes irreversible changes. This leads to a decrease in the protective efficacy of RPE as filtering properties of the material FPP are characterized by stable performance only up to  $60^{\circ}\text{C}$  temperature. Using polypropylene filter materials can replace FPP materials, which are indicators both meet European standards and does not contradict the traditional view of potential consumers.

## References

- [1] Cohen, H. J. Determining and validating the adequacy of airpurifying respirators used in industry Part I – Evaluating the Performance of a Disposable Respirator for Protection Against Mercury Vapor [Text], International Society for Respiratory Protection Journal of the International Society for Respiratory Protection. – 1984. – Vol. 2, Issue 3. – P. 296–304
- [2] Basmanov P.I., Kaminsky S.L., Korobeinikova A.V., Trubitsyna M.E., Personal Protective Respiratory Protection. Reference Guide, 2002. - 399 p.
- [3] Cheberyachko S.I., Analysis of filter materials used for the manufacture of personal respiratory protection. Development of ore deposits, 2001. - № 76. - p. 98-102.

- [4] H.E. Mullins, S.G. Danisch & A.R. Johnston, Development of a New Qualitative Test for Fit Testing Respirators, American Industrial Hygiene Association Journal, Volume 56, Issue 11, 1995, DOI: 10.1080/15428119591016278
- [5]. A.S. Ishchenko, Cheberyachko S.I., On transition to the European standards in the area of the particle of personal respiratory protection, Coll. Scien. tr. NSU, RIK NSU. - 2003. - P. 384-386.
- [6] C.C. Chen, J. Ruuskanen, W. Pilacinski & K., Willeke Filter and Leak Penetration Characteristics Of a Dust And Mist Filtering Facepiece, American Industrial Hygiene Association Journal, Volume 51, Issue 12, 1990, DOI: 10.1080/15298669091370275
- [7]. K.V. Polyakov, Yuri Brown, S.P. Tkachuk, Patant 22314 Ukraine, MKI3 A62 B23 / 02 Filtruyuchy element respiratora. Number 97031310.
- [9]. Radchuk D.I. Influence of temperature on filtering properties of materials, Scientific Bulletin of NMU, 2009, № 10, p. 44-48.

## Fluid Injection Induced Seismicity in the Oil and Gas Field Areas: Monitoring and Modelling

A. Zabolotin <sup>1</sup>, A.V. Konovalov <sup>1</sup>, A.A. Stepnov <sup>1</sup>, A.S. Sychov <sup>1</sup>, D.E. Tomilev <sup>1</sup>

<sup>1</sup> – Federal State Budgetary Establishment of a Science Institute of Marine Geology & Geophysics of Far Eastern Branch of Russian Academy of Sciences, 693022 Yuzhno-Sakhalinsk, Russian Federation



DOI 10.13140/RG.2.1.5102.4249

**Keywords:** injection-triggered seismicity, 2D simulation, poroelastic media, oil & gas fields, faults.

**ABSTRACT.** Past experience has shown that injection-triggered seismicity is an extremely important phenomenon that must be considered when operation oil and gas fields. It is widely accepted that transmission of reservoir pore pressure through the faults, cracks and fractures is the main cause of stress transfer in the rock surrounding the fault zone. As a result, it provides an excessive stress accumulation within the fault zone that may lead to a failure. In order to estimate the excessive shear stress accumulation rate that may trigger the seismic activity according to the rate and state friction model we simulated a stress-strain process in a narrow fault zone between two units during the fluid injection into the one of the units in a simplified 2D model. The simulation is based on the theory of fluid-saturated poroelastic media. We considered the fault zone simulated by relatively higher permeability. The numerical calculations were performed using software libraries with the Freefem++ open code. Injection-triggered seismicity field study was made by the induced seismicity monitoring system in the Northern Sakhalin, Russia. The unusual swarm activity was registered in 2013-2016 in the vicinity of the fluid injection well and is discussed in this study.

**Introduction.** Over last decade, there was an intensive development of oil and gas industry in the Sakhalin Island, Russia. Main number of the offshore oil and gas fields in the northeastern part of the island are located in the vicinity of active tectonic faults. Many types of seismic events associated with oil and gas production, referred to in general as induced or triggered earthquakes, have been recognized over the past decades [1].

Induced/triggered seismicity monitoring by permanent seismic local network was started in September 2006 in the northeastern part of Sakhalin Island (Fig 1a). The authors developed the real-time seismic monitoring system based on open source software and Russian-made hardware components [2].

The unusual swarm activity was registered in 2013-2016 in the vicinity of the fluid injection well (Fig. 1b). Past experience (e.g., [3, 4]) has shown that injection-triggered seismicity is an extremely important phenomenon that must be considered when operation oil and gas fields. In terms of the physical mechanisms associated with fluid injection that trigger earthquakes, it is widely accepted that transmission of reservoir pore pressure through the faults, cracks and fractures is the main cause of stress transfer in the rock surrounding the fault zone. As a result, it provides an excessive stress accumulation within the fault zone that may lead to a failure.

We have analysed in this study the seismicity patterns of swarm activity and made the numerical simulation of stress-strain process in a fault zone during the fluid injection based on the theory of fluid-saturated poroelastic media in order to estimate the excessive shear stress accumulation rate that may trigger the seismic activity according to the rate and state friction model [5].

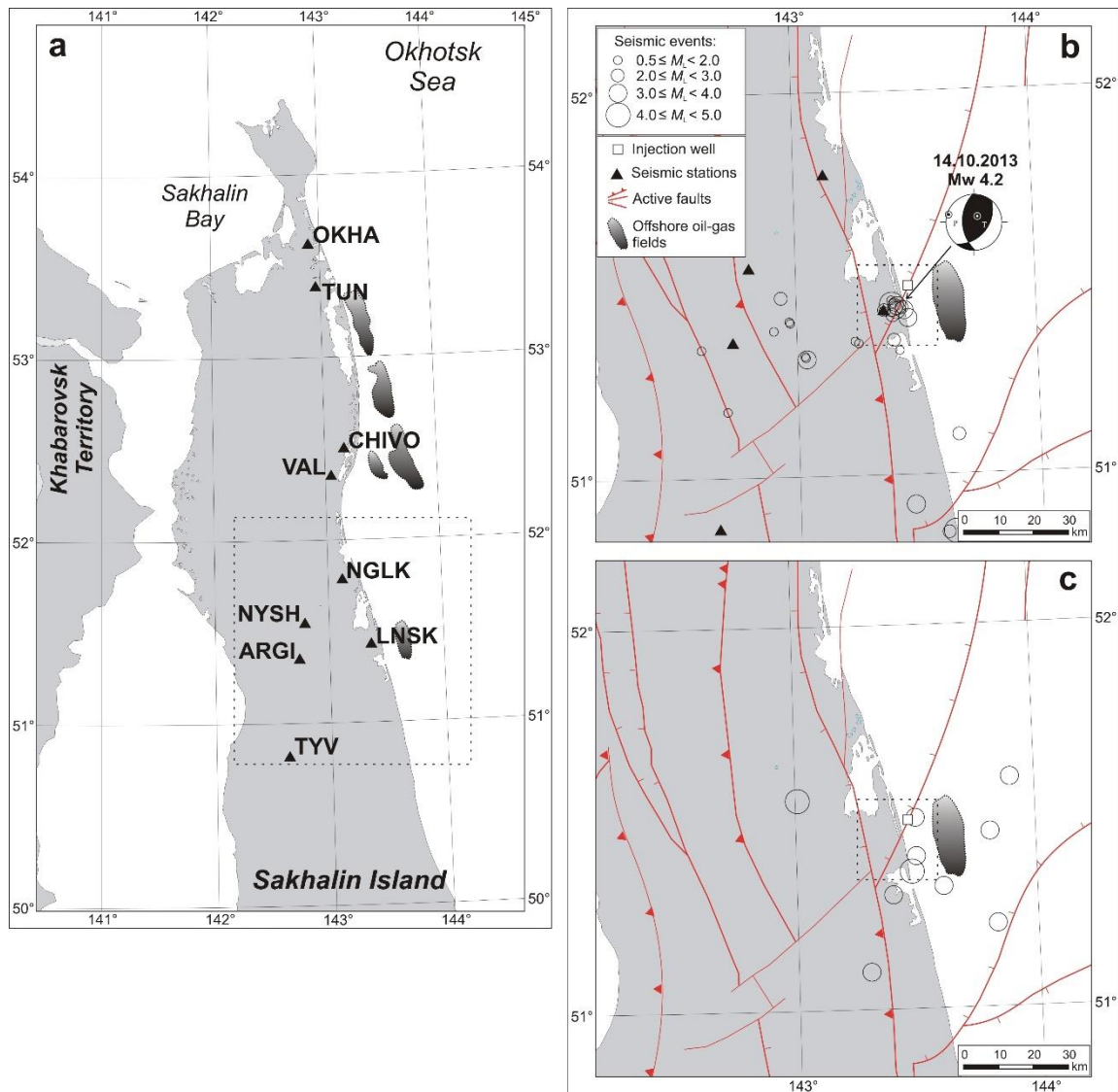


Fig. 1. The location of the seismic monitoring stations in the north of the Sakhalin island (a), the map of the epicentres of the earthquakes swarm ( $M_L \geq 0.5$ ) in 2013 in the fluid injection well area (b), and the map of historical earthquakes ( $M_L \geq 3.5$ ), localized in the same area from 1964 to 1997 years (c). The location of the landfill of disposal of industrial sewage through injection well is indicated with white squares, the stations of the seismic monitoring network are indicated with black triangles, the scheme of active tectonic faults of the Northern Sakhalin in the considered region is shown.

**Injection-Triggered Seismicity Case Study.** According to the recent studies (e.g., [6]) the high seismicity rate in Sakhalin Island is caused by tectonic activity. A boundary between the Eurasian (or the Amurian) and the North American (or the Okhotsk) plate is supposed to run from north to south of the island. Seismicity is the primary basis for identifying the plate boundary and tectonic settings of the region. Sakhalin Island is dominated structurally by compressive features.

On May 27, 1995, the catastrophic earthquake ( $M_w$  7.2) occurred near small town Neftegorsk, Sakhalin Island, Russia [6]. The town was completely destroyed, more than 2 000 people died. Although the weak seismicity was relatively high before this earthquake, the historical earthquakes larger than  $M_w$  7 were not known in the northern part of the island. Some of seismologists recognized the Neftegorsk earthquake as triggered by oil field production, although the region of Northern Sakhalin (where the town is located) is the region of high seismic rate.

In 2006 the local seismic network was deployed along the eastern coast of the Northern Sakhalin (Fig. 1a) in the area of offshore hydrocarbon fields, which were just started to be developed at that time. The main aim of the seismic network installation was to detect any possible changes in the controlled area seismic activity, which could be caused by the fields development.

The major number of the earthquake sources localized in the north of the Sakhalin Island has natural origin, including moderate events which have been earlier registered in the offshore zone of the island. [7].

The only possible exception is the seismic activation in the coastal area of the island, to the south of the Nogliki town, in the direct vicinity from the LNSK station. The source zone of earthquakes swarm is located in a few kilometers to South-West from the landfill of disposal of industrial sewage of one of the companies, performing works on the industrial development of offshore oil and gas fields. The authors have no precise well and operational data. However, it is known that its operation was scheduled for 2006.

As we can see from Fig. 1b localized seismic events are mainly grouped in the area of axial line of Aukan-Lunskoe active fault. The first microearthquakes with negative magnitudes were registered in the examined area in June 2012. The LNSK station was installed in December 2011 and operated without omissions and failures till the February 2013, further continuous functioning of the station has been renewed since the end of July 2013 (Fig. 2f). At the same time during the down-time of the LNSK station, no seismic events with  $M_L \geq 2.5$  that could be registered and localized by the closest stations were observed. As can be seen from Fig. 2a-2d the major part of seismic events (both the total energy and the seismic rate) falls on October-November 2013, i.e. after about 500 days after the registration of the first microearthquakes in the specified area. The magnitude of the strongest event in this sequence was  $M_L$  4.1 and the source depth was 10.2 km.

For the specified earthquake the seismic moment tensor inversion was applied (Fig. 1b). The resulted source mechanism is a reverse fault. The orientation of compressive stresses lies in the sub latitudinal direction in accordance with recent study of plate motion features of the specified region [8].

The graph of the Benioff strain accumulation (Fig. 2d) demonstrates the release of the greater part of seismic energy in the considering fault zone on the 14-th of October 2013, herewith the seismic process was accompanied by the increase of the earthquake magnitude from  $M_L$  3.2 to  $M_L$  4.1. Despite the subsequent decrease of the magnitudes the level of seismic activity remained substantially higher than the background seismic rate till October 2013. The observed seismic series has swarm origin: it has no prominent by mainshock magnitude, as well as foreshock and aftershock sequences. The total number of registered small and microearthquakes, starting with the magnitude of completeness  $M_L$  0.5, reached 40 events. The average source depth was about 10-12 km, which is substantially greater than the depth of the layers (about 2 km), on the horizons of which the fluid injection is produced. At the moment (April 2016) microearthquakes with magnitude that doesn't exceed  $M_L$  1.5 are irregularly recorded in the specified area.

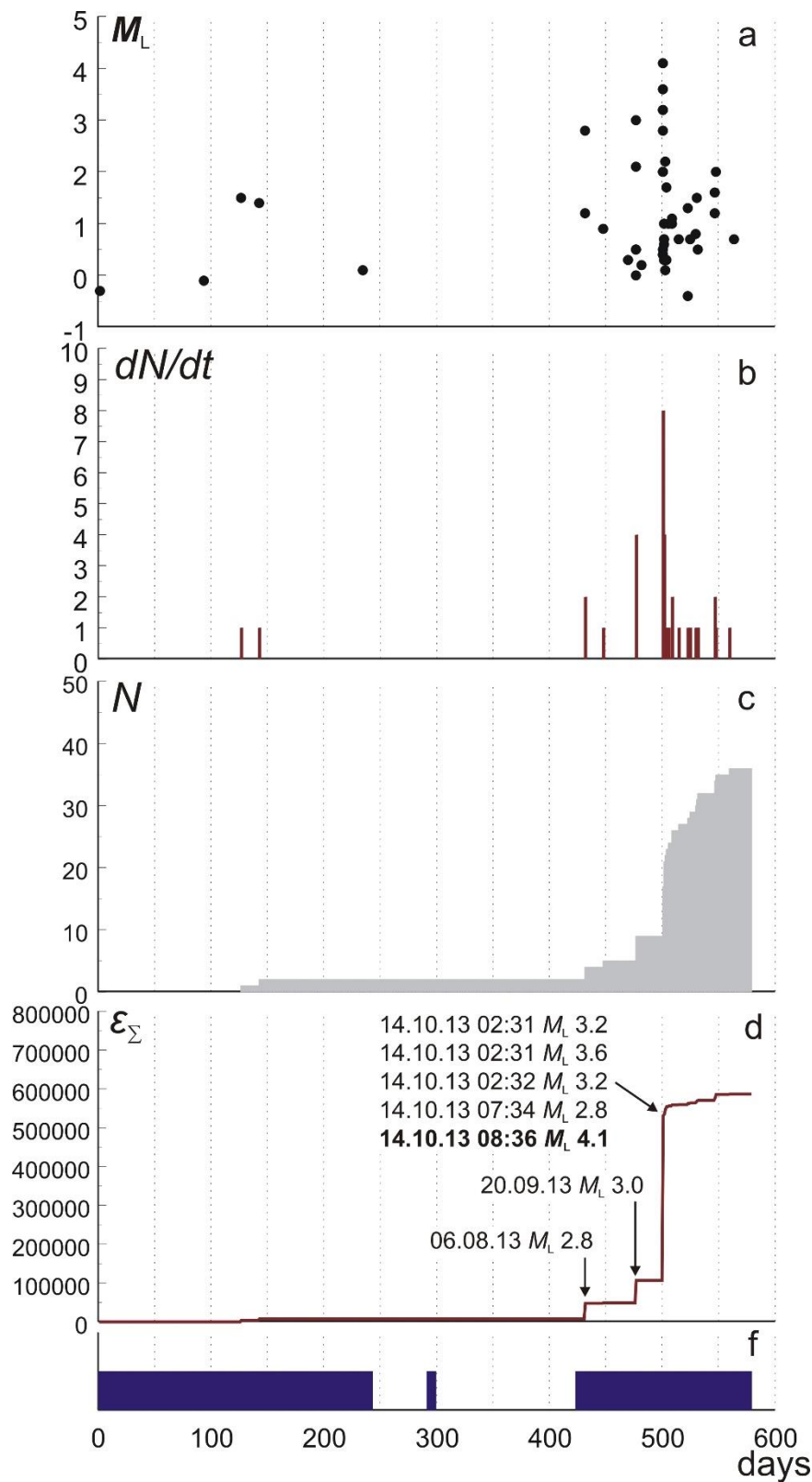


Fig. 2. The graph of time dependent seismic process in the fluid injection well area: (a) – by magnitude  $M_L \geq -1.0$ ; (b) – by the number of recorded earthquakes per day ( $M_L \geq 0.5$ ); c – by the cumulative number of recorded earthquakes ( $M_L \geq 0.5$ ); d – by accumulated Benioff strain ( $M_L \geq 0.5$ ); e – by the duration of the LNSK seismic station operation. LNSK seismic station is located in a few kilometres from the injection well. The countdown begins from the 1-st of July 2012.

Throughout the whole period of instrumental observations at the north of the Sakhalin Island seismicity was occasionally recorded close to the considered area. The Fig. 1c shows localized in the coastal area earthquakes according to the regional seismological observations since 1964 to 2005. On the August 24-th 1988 the moderate earthquake with magnitude ML 4.5 and the source depth of 9.0 km occurred in this area. Small seismic events with magnitude from 3.0 to 3.9 (Fig. 1c) and the depth of about 10 km were also registered. However, all these events are separated in time and any signs of swarming or aftershock activity that accompanies them have been revealed, due to low sensitivity of regional seismic network, which was operating at that time. Besides, the low density of stations network complicated the precise earthquake source location.

However, such seismic activity in relatively aseismic area, close to the landfill of the fluid injection, looks unusual. Apparently, hydraulic transmission of pore pressure through the faults and fractures to the sites, where the combination of effective stresses in the solid is close to the critical values, is the main cause of the triggered seismicity. This could explain the stress transfer to the depth of the seismogenic layer 5-10 km. For this purpose, the numerical simulation of the stress-strain state was performed.

**Numerical Simulation.** In this study we consider the deformation process in the narrow fault zone, between the two units, during the fluid injection into the reservoir (Fig. 3), located at some distance from the fault. The simulated region is represented as a continuous medium consisting of two units – zones, in one of which (unit 1) the injection well is located and a second one (unit 2) is the homogeneous by physical properties block that is attached to it along the fault.

To solve this problem the model based on the theory of poroelastic fluid-saturated medium, developed by M.Bio [9], is taken, the full wording of which is presented in work [10]. In this case the environment for isotropic blocks is described by two equations:

$$\sigma_{ij} = (\lambda I_1) \delta_{ij} + 2\mu \varepsilon_{ij} - \frac{BK_u}{\rho_0} \Delta m \delta_{ij}, \quad (1)$$

$$\frac{\partial \Delta m}{\partial t} - c \nabla^2 (\Delta m) = y, \quad (2)$$

where  $\sigma_{ij}$  – the stress tensor;

$\varepsilon_{ij}$  – the strain tensor;

$I_1 = \varepsilon_{kk} = \varepsilon_x + \varepsilon_y + \varepsilon_z$  – the first invariant of the strain tensor;

$\mu$  – the shear modulus;

$\lambda$  – Lamé's modulus;

$B$  – Skempton's coefficient;

$K_u$  – the bulk modulus;

$\Delta m$  – the change in mass per bulk unit;

$y$  – the density of bulk sources;

$c$  – the coefficient of piezo conductivity.

$$c = \frac{K_s}{\eta} \left[ \frac{2\mu(1-\nu)}{(1-2\nu)} \right] \left[ \frac{B^2(1+\nu_n)^2}{9(1-\nu_n)(\nu_n-\nu)} \right], \quad (3)$$

where  $K_s, \eta$  – the permeability and the viscosity of the compressible fluid,

$\nu_n, \nu$  the “non – drainage” and “drainage” Poisson’s coefficients, respectively.

The distance between two main units is simulated by 1 m wide narrow zone with a damage parameter  $a_d$ , that depends on time. In this case, according to V.Lyakhovsky (e.g., [11-13]), permeability is exponentially dependent on the damage parameter.

$$K_s(a_d) = K_0 e^{(ba_d)}, \quad (4)$$

where  $K_0$  – the initial value of the permeability;

$b$  – the constant;

$a_d$  – the damage parameter.

In case of slow changes of the shear stresses the seismicity rate  $R$ , according to the work [5], can be presented as following:

$$R = \frac{r\dot{\tau}}{\dot{\tau}_l}, \quad (5)$$

where  $r$  – the background seismicity rate corresponding to the tectonic load  $\dot{\tau}_l$ ,  $\dot{\tau}$  is the overall accumulation rate of shear stresses.

In our case the value of  $\dot{\tau}$  is determined by the sum of the accumulation rate of tectonic shear stresses  $\dot{\tau}_l$  caused by the slow motion of the fault boundaries and the accumulation rate of excessive shear stresses  $\dot{\tau}_{tr}$  in the simulated fault zone (averaged over its length within the seismogenic layer) caused by fluid injection.

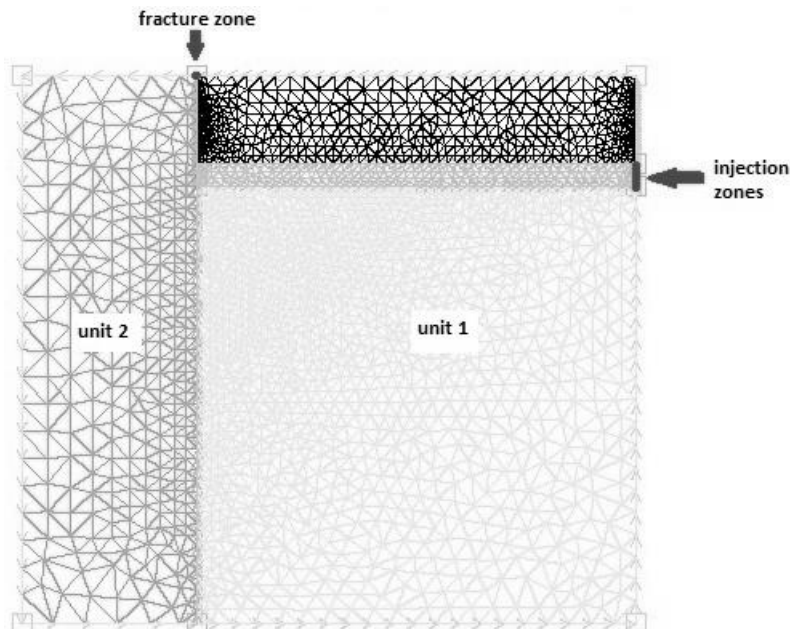


*Fig. 3. Schematic representation of the simulated region.*

To the numerical calculation of the stress-strain state of geological medium for the simulated 2 D region (Fig. 3) the following assumptions are adopted. At the depth the first unit is divided into three

layers and has dimensions  $5 \times 10 \text{ km}^2$ . The upper layer of the simulated region with a thickness of 1900 m is almost impermeable. The middle layer within which the fluid injection is produced is a highly permeable layer of 100 m. The lower, low permeable layer, extends to the lower boundary of the model. The second unit over the fault zone has correspondingly sizes  $1 \times 10 \text{ km}^2$  and is low permeable with coefficient of piezo conductivity equal to  $2 \times 10^{-4} \text{ m}^2/\text{sec}$ . The physical parameters for the considered area depending on the depth are presented in the Table 1.

The Skempton's coefficient and the Poisson's coefficients in non – drainage and drainage conditions are 0.6, 0.2 and 0.33, respectively, and are used throughout the simulated region. It is also assumed that the density of the medium is  $2300 \text{ kg/m}^3$ , and the value of the shear modulus over the fault zone is equal to  $5.5 \times 10^9 \text{ Pa}$ .

Table 1. The distribution of the piezo conductivity value and shear modulus based on the depth.

Depth, m	$c, \text{ m}^2/\text{sec}$	$\mu, \text{ Pa}$
0-1900	$10^{-4}$	$5.33 \times 10^9$
1900-2000	0.6	$5.43 \times 10^9$
2000-10000	$10^{-3}$	$5.62 \times 10^9$

For simplicity it is assumed that the fluid injection into the reservoir is produced on the right side of the unit 1 at the depth interval of 1900-2000 m (Fig. 3) with a constant rate of 20 kg/sec.

The distance between two basic units is modeled by a narrow area, 1m wide (Fig. 3), with a damage parameter that depends on time, according to the works of V.Lyakhovsky [11]. For such a zone higher permeability is peculiar. According to the study [11], when  $a_d$  (the damage parameter) reaches values of 0.58-0.7, permeability increases to 5-6 orders. Based on this fact the piezo conductivity coefficient for this region is taken equal to  $0.6 \times 10^5 \text{ m}^2/\text{sec}$ .

The numerical calculations were performed using software libraries with the open code Freefem++ [14].

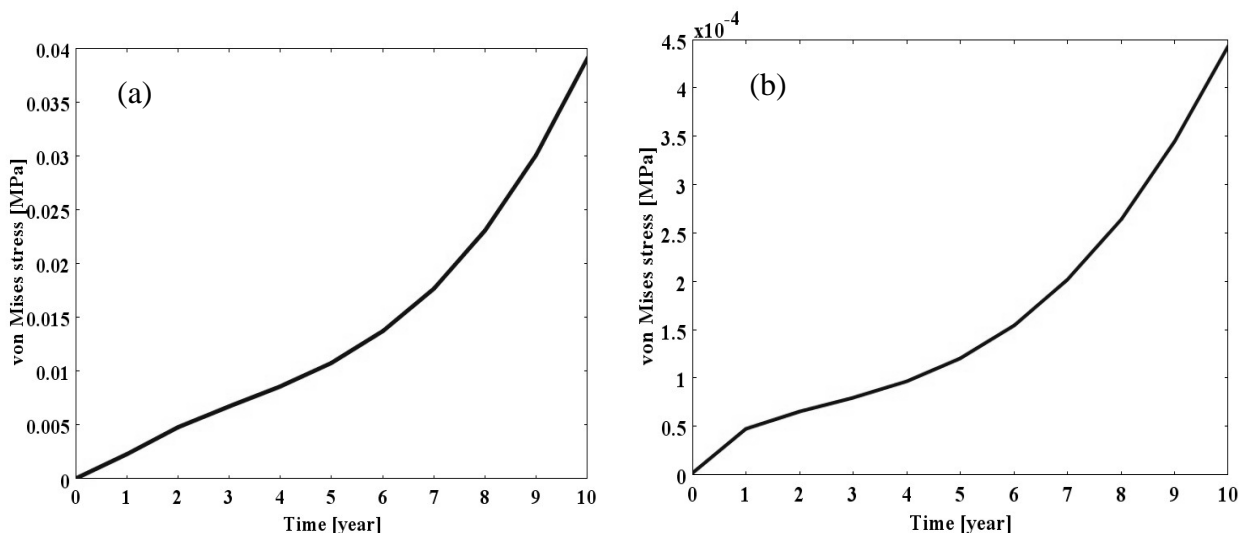


Fig. 4. The time dependence of the shear stresses intensity, resulting from fluid injection into the rock at the fault zone at the depth of 5 km: (a) the fault zone with high permeability, (b) the fault zone that is simulated only by border.

For the specified above area, schematically represented in the Fig. 3, depending on the planned fluid injection, numerical calculations of excessive shear stresses arising from the anthropogenic impact on the environment for 10 years were produced. Under the value of excess shear stress such scalar measure as the intensity of stress via Mises is accepted. The intensities of the shear stresses occurring at a depth of 5 km in the fault zone, depending on the time of the hydrocarbon filed developing, are presented in the Fig. 4a. The magnitudes of shear stress increase monotonically during the whole period of fluid injection and reach its maximal value  $4 \times 10^{-2}$  MPa on the 10-th year. It should be noted that the assumption of the sharp rise in permeability in the fault zone accepted in our model leads to quite a difference of intensity of shear stresses accumulation in comparison with the model where the fault is modeled only by the border between the units (Fig. 4b).

Our suggested approach assumes that with the available results of seismological observations or GPS measurements in the fault zone, it will provide an opportunity to estimate the rate of background tectonic loading. The latest statement allows to predict the rate of the stimulated seismicity, using the equation (5).

**Summary.** Earthquake triggering has been widely reported. There is a good correlation of the Coulomb stress change produced by large earthquakes with the spatial distribution of aftershocks. For example, aftershocks are triggered by the stress step greater than 0.01 MPa. Most of these studies rely on the assumption that aftershocks occur on planes optimally oriented for failure, which are mainly dominated by the regional tectonic stresses.

The tidal forces produce periodic stress variations of the order by 0.001 MPa in the Earth. This stress change is much smaller than the typical stress drop of earthquakes, but its rate is generally larger than the tectonic stress accumulation rate of order 0.001-0.01 MPa per year. Therefore the tidal stress could lead to a failure when the stress in the source zone is close to the critical value.

In our study we obtained that the characteristic value of the shear stress changes, reproduced for a decade of fluid injection, is about 0.04 MPa at the depth of the seismogenic layer, which is equivalent to the rate of excess stresses accumulation about 0.004 MPa per year. This value is several times higher (or at least is comparable to it) than the value of accumulation of natural (tectonic) stresses, which can lead to an increase of the seismicity rate in several times.

For more accurate estimates of the trigger effects it is necessary to conduct numerical calculations of the shear and normal stresses on the fault planar, which is characterized by its dipping angle. This will allow to estimate the change of Coulomb stresses in time. The obtained results can be used for prediction of seismicity rate, caused by fluid injection in terms of probability seismic hazard analysis.

**Acknowledgements.** The study is supported by the Federal Special-Purpose Program "Research and development in priority areas of scientific and technological complex of Russia for 2014-2020" (Project No. RFMEF160714X0105).

## References

- [1] V.V. Adushkin, S.B. Turuntaev, Technogenic seismicity – induced and triggered, Moscow Institute of Geosphere Dynamics RAS, 2015.
- [2] A.A. Stepnov, A.V. Gavrilov, A.V. Konovalov, [et al.], L. New Architecture of an Automated System for Acquisition, Storage and Processing of Seismic Data. Seismic Instruments, 2014.
- [3] D.F. Sumy [et al.], Observations of static Coulomb stress triggering of the November 2011 M5.7 Oklahoma earthquake sequence. Journal of Geophysical Research: Solid Earth, 2014.
- [4] T. H. W. Goebel, S. M. Hosseini, F. Cappa, [et al.], Wastewater disposal and earthquake swarm activity at the southern end of the Central Valley, California. Geophys. Res. Lett., 2016. DOI:10.1002/2015GL066948.
- [5] A. Helmstetter, B.E. Shaw, Afterslip and aftershocks in the rate-and-state friction law. J. Geophys. Res., 2009. DOI: 10.1029/2007JB005077.

- [6] K. Katsumata, M. Kasahara, M. Ichiyanagi, [et al.] The 27 May 1995  $M_S$  7.6 Northern Sakhalin earthquake: an earthquake on an uncertain plate boundary, *Bul. Seis. Soc. Am.*, 2004.
- [7] A.V. Konovalov, [et al.], Mw 5.6 Piltun Earthquake of June 12, 2005, and the Contemporary Seismicity in the Area of Oil-and-Gas Fields in the Northeastern Shelf of Sakhalin Island. *Russ. J. Pac. Geol.*, 2015.
- [8] N.F. Vasilenko, A.S. Prytkov, GPS-based modeling of the interaction between the lithospheric plates in Sakhalin, *Russ. J. Pac. Geol.*, 2012.
- [9] M.A. Biot, General theory of three-dimensional consolidation, *J. Appl. Phys.*, 1941.
- [10] J.R. Rice, M.P. Cleary, Some basic stress diffusion solutions for fluid-saturated elastic porous media with compressible constituents, *Review of Geophysics and Space Physics*, 1976.
- [11] E. Shalev, V. Lyakhovsky, The processes controlling damage zone propagation induced by wellbore fluid injection. *Geophys. J. Int.*, 2013.
- [12] V. Lyakhovsky, Y. Hamiel, Y. Ben-Zion, A non-local visco-elastic damage model and dynamic fracture. *Journal of the Mechanics and Physics of Solids*, 2011.
- [13] Y. Hamiel, V. Lyakhovsky, A. Agnon, Coupled evolution of damage and porosity in poroelastic media: theory and applications to deformation of porous rocks. *Geophys. J. Int.*, 2004.
- [14] Partial differential equation solver [<http://www.freefem.org>]

## The Effect of Microwave Radiation on the Properties of Canola Seeds

Roudane M. <sup>1</sup>, Hemis M. <sup>2</sup>

1 – Faculty of Technology, University of Blida, Blida, Algeria

2 – University Djillali Bouamama of Khemis Miliana, Road of Theniat Elhad Ain Defla 44225 Algeria



DOI 10.13140/RG.2.1.1679.4488

**Keywords:** canola seed, MW drying, mathematical modelling, moisture loss, drying rate.

**ABSTRACT.** The evolution of moisture content loss, which appears during drying of Canola seeds using microwaves radiation (MW) was studied in this work. A mathematical model was adopted to simulate the physical phenomenon of heat and mass transfer between the seeds and the surrounding air. Initial conditions of 20% (w.b.) of moisture content and 20°C of grains temperature were taken in the modelling; the relative humidity in the room before starting tests was 30%. The drying was down under different MW power from 100 W to 300W. Result show that the predicted moisture loss profiles obtained from the modelling compared well with those obtained experimentally on canola seeds. we were observed also that the drying rate was increased from low to high value of  $4.5 \times 10^{-4}$  to  $8.5 \times 10^{-4}$  kg water / (kg wb. S), whilst the MW power increased from 100 to 300W.

**1. Introduction.** Canadian plant breeders from the University of Manitoba produced in 1974 canola by genetically altering rapeseed. Rapeseed was developed by Canadian plant breeders specifically for its nutritional qualities and its low level of saturated fat. Demand on canola continues to grow as the world learns more about its advantages for human health and as a source of high-quality feed and biofuel feedstock [25].

New research discovery included a new Canola Council study showing a low glycemic-load diet with canola oil helps improve both cholesterol and blood glucose control in Type 2 diabetes patients [25]. The advantage of canola push the world of researchers working on it to develop new methods of drying and storage and of that grains which can use also as new biofuel and a good oil.

A value of 19 g canola oil, around 1 ½ tablespoons per day may reduce the risk of coronary heart disease due to its unsaturated fat content, according to supportive but not conclusive research. Canola oil should replace a similar amount of saturated fat in the diet without increasing calories [26].

Global canola production has risen quickly over the past 40 years, it is around 72 Thousand Metric Tons in 2014 [USDA, February 2016 report], increasing from the sixth largest oil crops to the second largest [USDA, 2014]. Spring canola varieties are primarily planted in parts of China, India, and the western prairies of Canada and in the United States.

The behaviour of canola seed and rapeseed is similar, because both products have the same morphological, physical and thermal characteristics. Extreme care is needed to safely store rapeseed because high moisture content limit of so-called dry seed which is currently 10%. Canola seeds are less storable under high: temperature, moisture content and oil contents [17].

Storage conditions play essential role in determining canola seed and oil quality. High moisture content or/and high temperature cause damage in the properties of the stored products, causing loss in seed viability and increase levels of free fatty acids (FFA) and products of oxidation in oil [17].

Cassells et al. [17] have presented the moisture isotherms of Australian canola varieties at 20 and 30°C. They determine that it is recommended to store cool and dry canola to minimize spoilage of oil

### Nomenclature

$a_p$	Compactness of canola ( $\text{m}^2/\text{m}^3$ )
$A$	Area ( $\text{m}^2$ )
$C$	Specific heat of dry air ( $\text{J/kg K}$ )
$C_p$	Specific heat of canola kernel ( $\text{J/kg K}$ )
$C_v$	Specific heat of vapour ( $\text{J/kg K}$ )
$C_w$	Specific heat of water ( $\text{J/kg K}$ )
$D$	Diffusion coefficient of moisture in grain ( $\text{m}^2/\text{s}$ )
$GI$	Geometric index
$h$	Heat transfer coefficient ( $\text{W/m}^2 \text{ }^\circ\text{C}$ )
$K$	Drying constant
$k$	Thermal conductivity of grain ( $\text{W/m K}$ )
$k_m$	Mass transfer coefficient ( $\text{m/s}$ )
$L$	Half-thickness or radius ( $\text{m}$ )
$m$	Moisture content of grain in microwave model ( $\text{kg water/kg w.b.}$ )
$m_e$	Equilibrium moisture content in microwave model ( $\text{kg water/kg w.b.}$ )
$M$	Grain moisture content in convective model ( $\text{kg water/kg w.b.}$ )
$M_e$	Equilibrium moisture content in convective model ( $\text{kg water/kg w.b.}$ )
$P$	Power ( $\text{W}$ )
$P_0$	Surface power ( $\text{W}$ )
$R_g$	Gas constant ( $\text{J/mol K}$ )
$RH$	Relative humidity (%)
$t$	Time ( $\text{s}$ )
$T$	Temperature ( $^\circ\text{C}$ )
$T_a$	Ambient temperature ( $^\circ\text{C}$ )
$T_p$	Grain temperature ( $^\circ\text{C}$ )
$u$	Inlet air velocity ( $\text{m/s}$ )
$V$	Volume ( $\text{m}^3$ )
$W$	Absolute humidity of air ( $\text{kg water/kg dry air}$ )
$x$	Spatial coordinate ( $\text{m}$ )

### Greek symbols

$\delta$	Attenuation factor ( $\text{m}$ )
$\epsilon'$	Dielectric constant (dimensionless)
$\epsilon''$	Dielectric loss (dimensionless)
$\epsilon$	Void fraction
$\lambda$	Wavelength ( $\text{m}$ )
$\rho$	Density ( $\text{kg/m}^3$ )
$\rho_p$	Density of the product (grain) ( $\text{kg/m}^3$ )
$\rho_a$	Density of dry air ( $\text{kg/m}^3$ )
Subscripts and Abbreviations	
a	Air
e	Equilibrium
IMC	Initial Moisture Content
EMC	Equilibrium Moisture Content
p	Product
w	Water
w.b.	Wet basis

because excessive moisture levels during storage of canola lead to rapid heating and loss of oil quality.

Canola seed contain both high oil and high protein content. It contains around 40% oil and 23% protein compared to 20 and 40%, respectively, for soybean. When the oil is crushed out from canola, it leaves a high quality; high protein (37%) feed concentrate which is highly palatable to livestock [12].

Oomah and Mazza [21] studied the moisture loss of the canola seed and others oilseed using conventional household microwave oven operated at 80 and 100% power level. They found that the drying time was influenced by the size of seed and the *IMC* of the dried sample.

The aim of this work is to study the effect of the microwaves radiation on the behaviour of canola seeds under different conditions of drying; the effect of the temperature of seed reached during drying on the drying rate evolution was also an objective of the present study.

## 2. Materials and methods.

**2.1. Moisture measurement.** The measurement of initial and final moisture content of canola seed before each test was conducted using an oven set at  $130^\circ\text{C}$  for 4 hours [1] and it was expressed on wet basis. Initial moisture content was raised to desired level by adding a quantity of distilled water which was calculated using the following equation [4]:

$$W_2 = W_1 \left[ \frac{M_2 - M_1}{100 - M_2} \right] \quad (1)$$

where  $W_2$  – is the mass of distilled water added in kg;

$W_1$  – initial sample mass in kg;

$M_1$  – initial moisture content of the canola seeds in % w.b.,

$M_2$  – the desired moisture content of the sample in wet basis.

## 2.2. Thermal Properties.

Knowledge thermal properties of canola seed are very important to study the problems encountered in drying and storage of an oilseed product. Thermal and dielectric properties of canola are shown in Table 1.

**2.3. Drying Equipment.** The apparatus used to conduct tests of drying canola seed is a domestic microwave oven

of frequency 2.45 GHz and 800 Watt of power. The inner volume of the microwave cavity is  $28.9 \text{ m}^3$ . A circular Teflon plate was suspended in the cavity of the microwave oven by means of wire that was attached through the top of the MW oven to an electronic balance for data acquisition. (Fig. 1)

Table 1. Physical and thermal properties of canola seed

Characteristics	Canola
Dimension of seeds (mm)	Width 1.0-2.1xlength 1.1-2.5
Shape	Spherical
Kernel density (kg/m <sup>3</sup> )	1090-1130 [22]
Porosity of bulk seeds (% air)	33-35 [22]
Specific heat of dry mass (J/kg.k)	1553-1569
Thermal conductivity (W/m °C)	0.02 [18]
Thermal diffusivity (m <sup>2</sup> /s)	0.106·10 <sup>-6</sup> at MC=10% [20]
Bulk density kg/m <sup>3</sup>	670 [22]
Effective diffusivity	$D_{effe}=D_0 \exp(Ea/RT)$ [23]
Activation energy (j/(g mol))	11030 [5]

**2.4. Drying Conditions.** The drying kinetics of Canola seed were studied for three MW power levels: 100, 180 and 300W. During tests, the following assumptions were taken: The initial moisture content of canola seed was 0.20 kg water/kg w.b, the relative humidity of air in the room before starting tests was 30%,

**3. Modelling.** The eat and mass transfer between seed and the surrounding air during drying by MW oven under various conditions was modelled using a mathematical model described by Campanone, et al. [24] and Hemis et al. [7], [9] adapted to simulate the drying process of canola seed.

A system of nonlinear partial differential equations obtained by coupling mass and energy equations was solved using Crank-Nicolson finite differential method by writing a program in MATLAB.

The mathematical model takes into account the following assumptions: uniform initial temperature and humidity diffusion in canola, the temperature dependent thermal and dielectric properties of the product, a constant kernel volume, convective boundary conditions, water migration by diffusion, and a spherical shape of canola.

The energy balance equation during the microwave drying process was expressed as [15]:

$$V\rho C_p \frac{\partial T}{\partial t} = V \frac{\partial k}{\partial x} \frac{\partial T}{\partial x} + V k \frac{\partial^2 T}{\partial x^2} + V G I \frac{k}{x} \frac{\partial T}{\partial x} + P \quad (2)$$

Initial condition:

$$T = T_0 \text{ at } t=0 \text{ and at } 0 \leq x \leq L \quad (3)$$

$$x = L - k \frac{\partial T}{\partial x} = h(T - T_a) \quad (4)$$

$$x=0, -k \frac{\partial T}{\partial x} = 0 \text{ } t>0 \quad (5)$$

The power generated by the microwave oven was calculated by Lambert's law, which is governed by the equation given by Swami [10]:

$$P = P_0 e^{-2\alpha(L-x)} \quad (6)$$

The attenuation factor was calculated using the dielectric properties of the dehydrated material (the dielectric constant  $\epsilon'$  and the loss factor  $\epsilon''$ ) in the equation given by Nelson et al. [11], [13]:

$$\alpha = \frac{2\pi}{\lambda} \sqrt{\frac{\epsilon'[(1+\tan^2 \delta)^{1/2}-1]}{2}} \quad (7)$$

$$\delta = \tan^{-1} \left( \frac{\epsilon''}{\epsilon'} \right) \quad (8)$$

where  $\lambda$  is the wavelength 0.122 m at a frequency of 2.45 GHz and at a temperature of 20°C.

To predict drying kinetics of the products studied through drying by the process of microwave and convective hot-air, a microscopic mass balance equation was used:

$$\frac{\partial m}{\partial t} = \nabla(D\nabla m) \quad (9)$$

Initial and boundary conditions using to solve the above equation are:

$$t=0, m=m_0, 0 \leq x \leq L \quad (10)$$

$$\frac{\partial m}{\partial x} = 0, x=0, \text{ and } t>0 \quad (11)$$

$$-D \frac{\partial m}{\partial x} = k'_m(m - m_e), x=L, t>0 \quad (12)$$

Equilibrium moisture content of oilseed for the microwave modelling was calculated by the equation of Salek and Villota [14]:

$$m_e = \frac{m_1+m_2-m_3^2}{m_1+m_2-2m_3} \quad (13)$$

Where,  $m_1$ ,  $m_2$  and  $m_3$  are the moisture content values at times  $t_1$ ,  $t_2$  and  $t_3$ , respectively. The time intervals are equally spaced such that  $t_3 = 0.5(t_1+t_2)$ .

The parameters which affect drying behaviour of grains in a deep bed during drying by convective hot-air are: moisture content of grain, relative humidity, grain temperature and air temperature.

**4. Results and Discussion.** Predicted results of moisture loss from canola for three MW powers (100, 180 and 300W) are shown in figure 2. Moisture content was observed to decrease fast at high applied power level. Canola seeds in this case lose more than 50% of its moisture content after 30 minutes of drying.

The evolution of the predicted temperature of canola seeds by the modelling at different MW power is shown in Figure 3. The relative humidity and the velocity of air applied in the tests were 25% and 0.7m/s, respectively. It is clear from the figure 3 that, the temperature reached by the seeds is appropriate to dry safe canola and it will not affect the characteristics of the grains. We observed also from these results that the drying was fast in the first minutes of drying, this is may be due to the presence of the free water in the grains. We observed in figure 4 that as we approach to the equilibrium moisture content as the drying becomes hard.

We concluded through this study that high microwave power applied increased drying rate of canola seeds during drying by microwave oven at three MW powers 100, 180 and 300W. A comparison between experimental and predicted results of canola seeds during drying by a domestic microwave oven at an *IMC* of 0.20 (kg water/kg w.b.) figure 5 show that the experimental tests are in good agreement with those predicted using the mathematical modelling adopted in this work. From these results we concluded that the drying of canola can be faster at high MW power because the drying rate is higher, without exceeding the temperature limit that can damage the product.

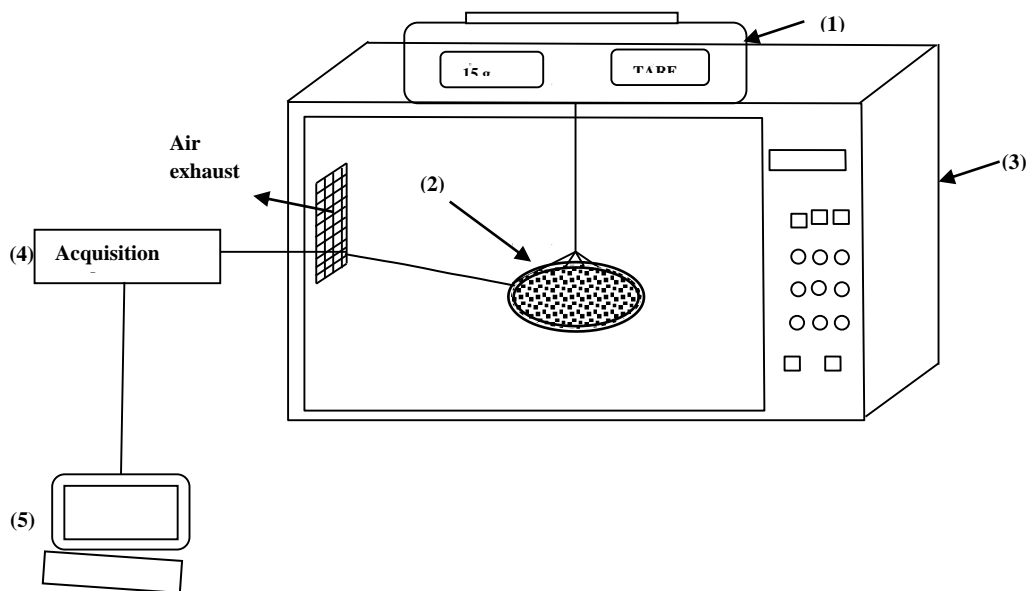


Fig. 1. Scheme of the microwave dryer used in this study; (1) electronic balance; (2) Plate of teflon; (3) domestic MW oven; (4) Acquisition card; (5) Computer

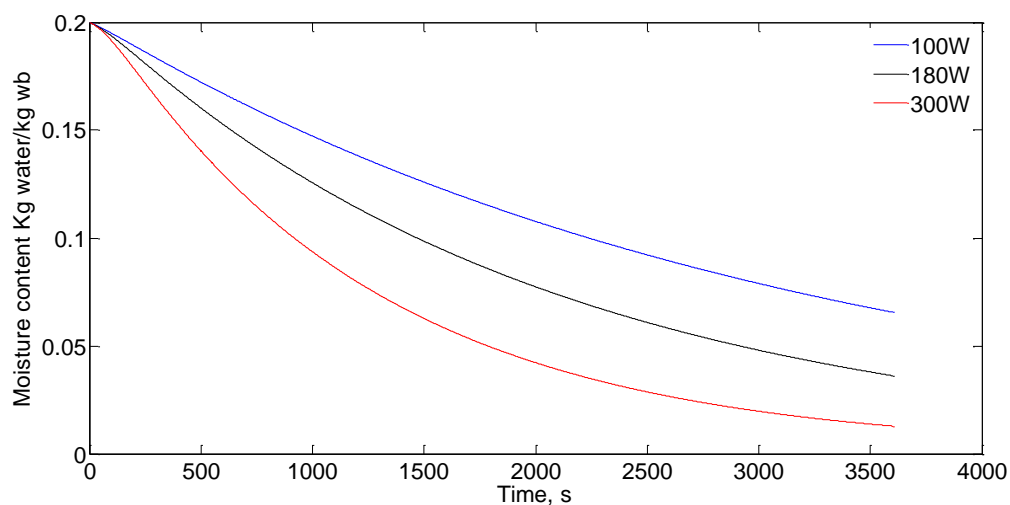


Fig. 2. Predicted result of canola seeds dried by MW oven under different power 100, 180 and 300W, relative humidity was 25%, the velocity of air 0.7m/s.

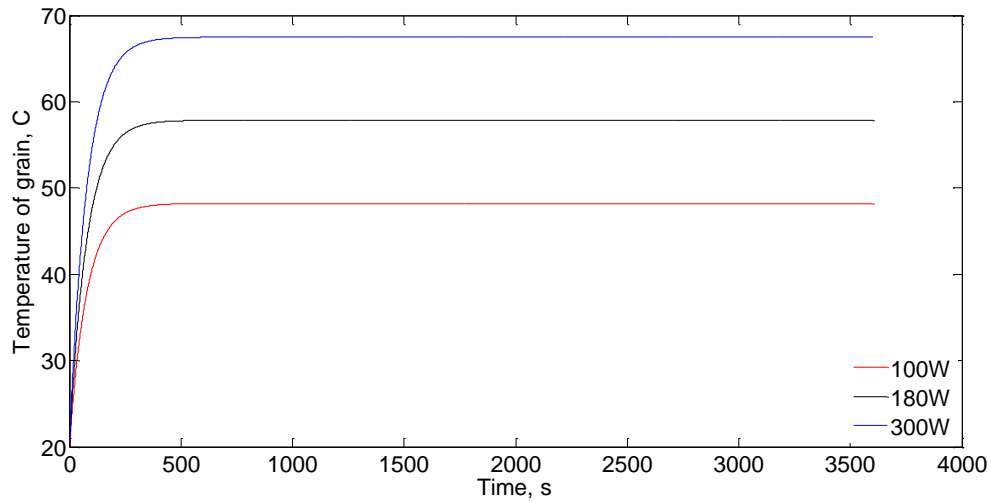


Fig. 3. Temperature evolution of the canola seeds during drying by microwave oven under three MW power of 100, 180 and 300W, the temperature of the inlet air was 20°C.

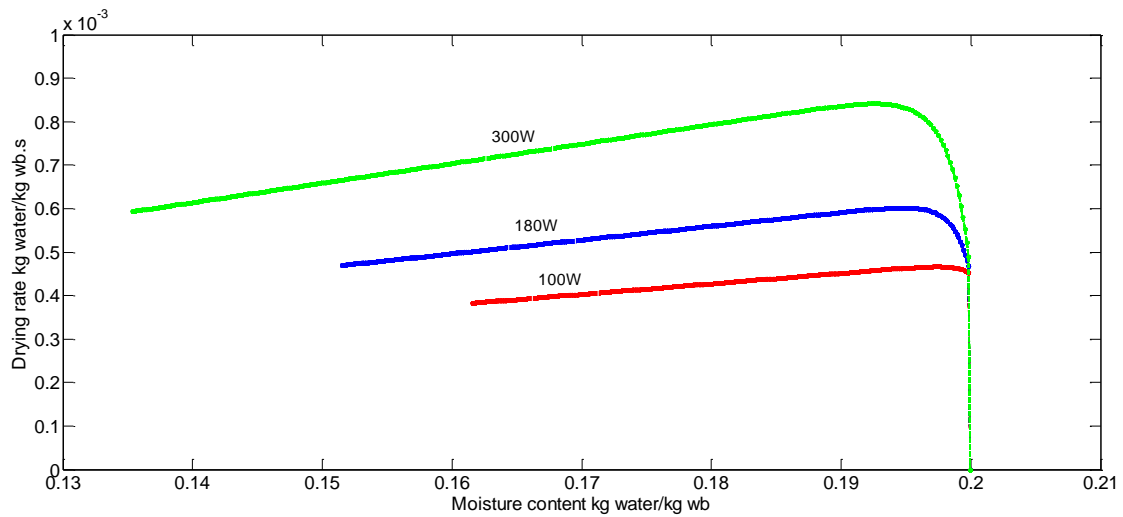


Fig. 4. Drying rate evolution of canola, drying under a MW power of 100, 180 and 300W at IMC of 0.20 kg water/kg w.b.

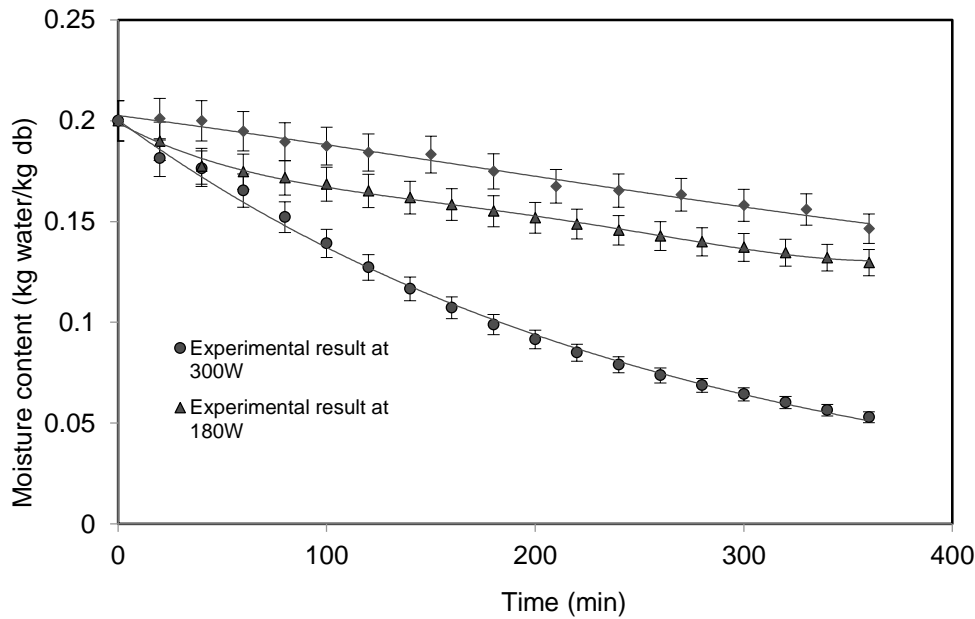


Fig. 5. Comparison between experimental and predicted results of canola seeds during drying by a domestic microwave oven at an IMC of 0.20 [kg water/kg w.b.]

**Summary.** The use of MW radiation in drying of canola seeds was studied in the present investigation. We concluded through the experimental tests and through the predicted results that the exposure time, the MW power and the temperature reached by the seeds during drying can cause high damage on the qualities of grains due to the presence of high amount of protein in canola seeds. We think that the use of a combined process of hot-air assisted to a MW dryer will be the best process to dry safe canola, because a good drying process will allow a safe storage of the product without affecting its characteristics.

## References

- [1] American Society of Agricultural Engineers (1985) ASAE Standards, Am. Soc. Agric. Eng., St. Joseph, MI.
- [2] USDA: United States Department of Agriculture (2011). <http://www.ers.usda.gov/>
- [3] FAQ : Organisation des Nations Unies pour l'alimentation et l'agriculture. <http://www.fao.org/>
- [4] Tabatabaeefar A (2003) Moisture Dependent Physical Properties of Wheat. Int. Agroph. 17: 207-211.
- [5] Gazor HR, Mohsenimanesh A (2010) Modelling the Drying Kinetics of Canola in Fluidised Bed Dryer. Czech J. Food. Sci. 28(6): 531–537
- [6] Jian F, Jayas DS, White NDG (2012) Thermal conductivity, bulk density and germination of a canola variety with high oil content under different temperatures, moisture contents and storage periods. Transactions of the ASABE 55(5): 1837-1843
- [7] Hemis M., Raghavan G.S.V. (2014) Effect of Convective Air Attributes with Microwave Drying of Soybean: Model Prediction and Experimental Validation. Drying Technology: An International Journal 32(5): 543-549
- [8] Thakor NJ, Sokhansanj S, Sosulski FW, Yannacopoulos S (1999) Mass and dimensional changes of single canola kernels during drying. Journal of food engineering 40: 159-160.

- [9] Hemis M, Choudhary R, Watson DG (2012) A coupled mathematical model for simultaneous microwave and convective drying of wheat seeds. *Journal of Biosystems Engineering* 112(3): 202-209.
- [10] Swami S (1982) Microwave heating characteristics of simulated high moisture foods. MSc Thesis, University of Massachusetts, Amherst, Massachusetts.
- [11] Nelson SO, Trabelsi S (2011) Sensing grain and seed moisture and density from dielectric properties. *International Journal of Agricultural & Biological Engineering* 4(1): 1-7.
- [12] Oplinger ES, Hardman LL, Gritton ET, Doll JD, Kelling KA (1989) Canola (Rapeseed). *Alternative Field crops manual*.
- [13] Nelson SO, Kraszewski AW, Trabelsi S, Lawrence KC (2000) Using cereal grain permittivity for sensing moisture content. *IEEE Transactions on Instrumentation and Measurement* 49(3): 470-475.
- [14] Salek J., Villota R., (1984). A comparative study of whirling and conventional fluidized beds in their application to dehydration. I. Heat and mass transfer analysis. *Journal of Food Processing and Preservation* 8(2): 73-98.
- [15] Chen AA, Singh RK, Haghighi K, Nelson PE (1993) Finite element analysis of temperature distribution in microwaved cylindrical potato tissue. *Journal of Food Engineering* 18: 351-368
- [16] Aregba AW, Nadeau J.P. (2007) Comparison of two non-equilibrium models for static grain deep bed drying by numerical simulation. *Journal of Food Engineering* 78(4): 1174–1187
- [17] Cassells JA, Caddick LP, Green JR., Reuss R (2003) Proceedings of the Australian Postharvest Technical Conference, Canberra. CSIRO Stored Grain Research Laboratory, Canberra.
- [18] Mosey EJ, Shaw T, Lampman WP (1977) The effect of temperature and moisture on the thermal properties of rapeseed. *Trans. ASAE* 20(4): 768-771
- [19] Mills JT (1989) Spoilage and heating of stored agricultural products. Prevention, detection and control. Research Branch, Agriculture and Agri-Food Canada Ottawa, Canada.
- [20] Timbers GE (1975) Properties of Rapeseed 1. Thermal Conductivity and Specific Heat. *Canadian Agricultural Engineering* 17(2)
- [21] Oomah BD, Mazza G (1992) Microwave oven drying for moisture determination in flax, canola and yellow mustard seeds. *Lebensmittel-Wissenschaft und Technologie* 25: 523–526.
- [22] Muir WE, Sinha RN (1988) Physical properties of cereal and oilseed cultivars grown in western Canada. *Canadian Agricultural Engineering* 30: 51-55.
- [23] Falade KO, Abbo E (2007) Air-drying and rehydration characteristics of date palm (*Phoenix dactylifera* L.) fruits. *Journal of food engineering* 79: 724-730.
- [24] Campanone LA, Zaritzky NE (2005) Mathematical analysis of microwave heating process. *Journal of Food Engineering* 69: 359–368.
- [25] CCC: Canola Council of Canada. (2015) <http://www.canolacouncil.org/>
- [26] FDA: U.S. Food and Drug Administration. <http://www.fda.gov/Food/IngredientsPackagingLabeling/LabelingNutrition/ucm072958.htm>
- [27] Ranjbaran M., Zare D. 2012. A New Approach For Modeling Of Hot Air-Microwave Thin Layer Drying Of Soybean, *Ejpa*, 15(3), #01.

# **IX. Economics & Management**

## **MMSE Journal Vol. 4**



## Human Capital and Growth of E-postal Services: A cross-country Analysis in Developing Countries

Dalibor Gottwald<sup>1,a</sup>, Libor Švadlenka<sup>2,b</sup>, Hana Pavlisová<sup>3,c</sup>

1 – Ph.D. Candidate, University of Pardubice, Jan Perner Transport Faculty, Department of Transport Management, Marketing and Logistics, Pardubice, Czech Republic

2 – Associate professor, University of Pardubice, Jan Perner Transport Faculty, Department of Transport Management, Marketing and Logistics, Pardubice, Czech Republic

3 – Researcher, Palacký University in Olomouc, Faculty of Arts, Department of English and American Studies, Olomouc, Czech Republic

a – [dalibor.gottwald@student.upce.cz](mailto:dalibor.gottwald@student.upce.cz)

b – [libor.svadlenka@upce.cz](mailto:libor.svadlenka@upce.cz)

c – [hana.pavlisova02@upol.cz](mailto:hana.pavlisova02@upol.cz)



DOI 10.13140/RG.2.1.3554.8561

**Keywords:** human capital, e-services, Asia, Africa, developing countries

**ABSTRACT.** Postal e-services and human capital as a part of intellectual capital are currently two much discussed concepts in the context of developing countries. This paper uses Human Capital Index (HCI) and Postal E-services index (PES index) in order to analyze the level of development of developing countries and to point to the inaccuracy of the developed/developing classification of the World Bank. The paper has two objectives: to discover whether there is a statistical dependence between human capital and postal e-services in developing countries as it is in developed countries, and to create a new sub-group of “more developed” developing countries where this dependence confirms. Results of this paper document that there is a great diversity among developing countries and that additional sub-groups may be defined within the rather broad classification of the World Bank, which is based on the GNI per capita indicator only. Human capital is being under scrutiny in numerous contexts but not yet in the context of postal e-services. Our paper presents a new method of analyzing the level of development and widens the range of aspects that must be taken into consideration when implementing measures to promote development.

**Introduction.** Human capital, or rather the collection of resources known as human capital, has gained increasing importance over the last few years [9], [8]. Currently, it can be described as one of the major social constructs, especially when taking into account the wide range of studies which consider human capital one of the keystones of development of a company and of a society as a whole [15], [18], [67]. The factors which define human capital in individual studies are viewed as worthy of respect in the application of specific measures in order to ensure sustainable development in a given field [31], 0. On the other hand, there are also studies, which show that there is no dependence of tracked indicators in an area. These studies are also important because they demonstrate that there is a need to investigate the problem further and in different contexts. Such areas where indicators may be uncorrelated are for example developing states: a closer examination may reveal some extreme values of selected parameters related to their development [21], [36], [59].

Issues of developing countries are among topics, which are of considerable interest to both world organizations and industrialized countries. World organizations make efforts to promote activities that would guarantee at least the basic level of living standards, such as basic material support, healthcare services, education, etc. [44], [61]. States with developed economy perceive developing countries as untapped economic potential, as prospective market outlets for their production and as

potential strategic partners. This “conflict of interest” is one of the forces, which drive globalization at the present time [46], [60].

Each sector of the world economy has undergone development in the last few decades. Among other things, its efficiency has increased and the quality of production and additional services has improved. These development trends are, among other things, the result of development of technical equipment and technological processes, or rather the result of gradual change of place where supply and demand collide [28], [29]. These innovations led to a new way of doing business – the use of e-communications, which include e-postal services, e-commerce, e-government, etc. [30], [33], [40].

Research on the above-mentioned trends is both current and relevant, especially because human capital, postal e-services and the issues of developing countries determine the current direction of development of a society. They are also essential in determining global economic development [27], [32].

The objectives of the article are to prove the effect of human capital development on the development of postal e-services in developing countries and to search for further explanation when defining possible differences between states.

**1. Background and related literature.** Human capital as a part of intellectual capital is a term well established in the scientific community. Edvinsson & Malone [23] defined the components of intellectual capital and stated that human capital, which consists of knowledge, skills and competences, is one of them. Its definition is interesting especially in the relation to property: according to the authors, human capital is always property of an individual and cannot be property of a company or society. At present many authors use human capital as a tool for evaluation of various integration or development trends. Barro [2] states that the GDP growth rate is a convenient indicator of the impact of human capital. Verbic, Majcev, & Cok [65] stress the importance of human capital as the main endogenous growth element. The method using human capital as a tool for prediction of development trends is applicable across scientific disciplines. It is relevant for evaluation or prediction of development of a company or of a national economy as a whole [10], [11], [34]. Human capital is fundamental for economic growth [17], [20], [52]. Various methods are used to examine human capital more closely [6], [35], [58]. These methods always reflect specific indicators based on which it is possible to prove their interdependence or predict development [64]. Research on the definition of human capital has resulted in the establishment of composite indices (in this case, the human capital index, HCI), which are relevant for evaluation of integration tendencies. In its study from 2010 focused on e-government development, the United Nations assigns a weight of 33 % to the HCI indicator within the calculation of the composite e-government development index (EGDI). The HCI has been defined as a composite of two indicators: adult literacy rate and the combined primary, secondary, and tertiary gross enrolment ratio.

The results of research on human capital can be regarded as relevant in the prediction if the analyzed data reflect current discussion topics in either nation or transnational level [48], [57]. The availability of postal services, their range and quality are among the basic prerequisites for development of a society in each state [1], [39], [56]. A trend towards computerization is evident in postal market, just like in other sectors of national economy, leading to the emergence of e-government, e-commerce, and e-postal services. Universal Postal Union [63] claims in its study that this is a consequence of digital economy development, because in the light of general computerization, postal operators feel the need to innovate and to develop electronic versions of their services. The pace, scope and degree of transition to digital postal services, however, differs among continents, countries, and individual markets. Among the reasons for this diversification is the lack of accurate and reliable information about the scope of services provided and particularly about their added value - the impact on development of a given area. Liu [42] in his work analyzes transactional communications (Postal and Telecommunications, and associations) in post-Mao mainland China on five levels: national, regional, provincial, community, and individual. Results of his research confirm that the development of transactional communications from 1980 onwards has resulted in gradual dissolution of the

artificial nationalism created by the Communist Party propaganda, thus leading to a considerable diversification of the society. On the other hand, the classic mass communications still nurture substantive nationalism in mainland China.

Together with states under totalitarian regimes and states with unstable political situation, developing countries can be classified as “extreme states” in comparison with industrialized countries [5]. Economic potential of developing countries is the subject of increasing number of studies, which also study human capital and confirm that human capital (potential) has major impact on further development of a given state [12], [25], [45]. Dunning [19], Lucas [43], Zhang & Markusen [43] classify human capital as one of the key determinants in development of foreign direct investment (FDI) in developing countries. Renström & Spataro [51] confirm the relationship between economic and population growth in an endogenous growth model driven by human capital accumulation and support their claim with evidence from selected developing countries based on the classification of the World Bank. Cooray, Mallick, & Dutta [14] in their study point to the differentiation of impact of human capital (among other things) on the development of market in South Asia. They examine the issue from gender perspective: primary education has a positive effect on secondary education among men, while among women, no such effect has been found, and i.e. primary education has no major impact on secondary education among women. Authors highlight the need to ensure stability of nationwide education system as a necessary prerequisite for stimulation of overall economic growth in a given group developing countries. Further studies confirm these findings. In the last few years, researches have increasingly focused on gender in the relation to the development of human potential, in particular in developing countries where this phenomenon belongs among the major challenges posed to overall growth of the society [7], [24], [49] and [54].

**1.1 Conflict of interest.** A certain conflict of interest may be perceived in the relation to human capital and postal e-services in the context of developing countries. It is mainly because of the different approaches to developing countries adopted by industrialized countries and world organizations.

The World Bank (2015) divides states into four basic categories according to the GNI per capita; the first two categories are Low-income economies and Lower-middle income economies, together labeled developing countries.

To ensure such a form of intervention that would guarantee stability and consequently jump-started the development of a sector of national economy in developing countries, it is necessary to provide a suitable classification of developing countries, i.e. of such states, which show dependence on certain variables, which are important in the relation to determination of relative economic stability. Thus it is necessary to respect not only the classification of developing countries according to the World Bank, but also results of partial studies, which examine stability of developing countries by the means of proving interdependence of chosen indicators that reflect current phenomena of globalized society [4], [13], [55], [37]. E-postal services is undoubtedly one of them [62].

**2. Methodology.** In order to define a group of developing countries, which show significant dependence in the relation to the current level of human capital development, it is necessary to define variables, which will be used to prove the dependence. This research is a global evaluation of current development tendencies in developing countries. All the input data are therefore supported by research of world leading institutions, which deal with these topics systematically.

**2.1 Measurement of human capital index.** To define human capital as a possible tool for prediction of development of e-postal services in developing countries, it is possible to employ the study of World Economic Forum [66], which provides a comprehensive look at the measurement of human potential. The basis for quantification of human capital are the following propositions:

- Human capital is understood as an economic value, which represents an employee’s set of knowledge, skills and competences.

- Human capital reflects not only the current state of a given country, but also its past as it includes indicators which result from policy decisions that will shape the future workforce.
- The Index aims to take into account the individual life course.
- The composite index also takes into account indicators defining productivity of older population.

These propositions are analyzed in four basic thematic pillars:

- The Education pillar presents indicators relating to quantitative and qualitative aspects of education across primary, secondary and tertiary levels. It also contains information on the present state of labor market and its future potential.
- The Health and Wellness pillar presents indicators relating to physical and mental well-being of a population from childhood to adulthood.
- The Workforce and Employment pillar presents indicators that quantify the experience, talent, knowledge and skills of the working-age population of a given country.
- The Enabling Environment pillar is designed to capture the impacts of legal framework, infrastructure and other factors, on the value of human potential.

The Human Capital Index (HCI) consists of several input indicators, which together express the composite index. Individual indicators are assigned such a weight that each group of indicators (i.e. Education, Health and Wellness, Workforce and Employment, Enabling Environment) has a weight of 25 %, and all together make 100 %. The following tables list the individual indicators defining the four basic pillars of human capital.

*Table 1. Education*

Sub-pillar	Indicator	Weight	Source
Access	Primary enrolment rate	2.08	UNESCO, Institute for Statistics, provided database extraction, 2013 (latest available data 2003-2012)
	Secondary enrolment rate	2.08	
	Tertiary enrolment rate	2.08	
	Education gender gap	2.08	World Economic Forum, <i>Global Gender Gap Report</i> , 2012
Quality	Internet access in schools	2.08	World Economic Forum, <i>Executive Opinion Survey</i> , 2013-2014
	Quality of the education system	2.08	
	Quality of primary schools	2.08	
	Quality of math and science education	2.08	
	Quality of management schools	2.08	
Attainment	Primary education attainment	2.08	UNESCO Institute for Statistics, <i>Education Statistics</i> , 2011 or latest year available
	Secondary education attainment	2.08	
	Tertiary education attainment	2.08	
<b>Total Pillar Weight:</b>		<b>25.00</b>	

Source: World Economic Forum (2013)

*Table 2. Health and Wellness*

Sub-pillar	Indicator	Weight	Source
<i>Survival</i>	Infant mortality	1.79	World Health Organization, Global Health Observatory, <i>World Health Statistics, Mortality and Burden of Disease, Child Mortality</i> , 2011
	Life expectancy	1.79	
	Survival gender gap	1.79	World Economic Forum, <i>Executive Opinion Survey</i> , 2012
<i>Health</i>	Stunting and wasting	1.79	World Health Organization, Global Health Observatory, <i>World Health Statistics, Nutrition, Child malnutrition</i> , latest available data 2003-2011
	Unhealthy life years	1.79	Healthy adjusted life expectancy, World Health Organization data, 2007, taken from the <i>Global Gender Gap Report 2012</i> ; life expectancy, as above
	Deaths under 60 from non-communicable diseases	1.79	World Health Organization, Global Health Observatory, <i>World Health Statistics, Non-communicable diseases</i> , 2008
	Obesity	1.79	World Health Organization, Global Health Observatory, <i>World Health Statistics, Adult risk factors</i> , 2008
	Business impact of non-communicable diseases	1.79	World Economic Forum, <i>Executive Opinion Survey</i> , 2013-2014
	Business impact of communicable diseases	1.79	
<i>Well-being</i>	Stress	1.79	Gallup, <i>Worldview database</i> , latest available data 2009-2013
	Depression	1.79	Gallup, <i>Worldview database</i> , latest available data 2006-2011
<i>Services</i>	Water, sanitation and hygiene	1.79	World Health Organization, Global Health Observatory, <i>World Health Statistics, Environmental Health</i> , latest available data 2005-2011
	Healthcare quality	1.79	World Economic Forum, <i>Executive Opinion Survey</i> , 2013-2014
	Healthcare accessibility	1.79	
<b>Total Pillar Weight:</b>		<b>25.00</b>	

Source: World Economic Forum (2013)

Table 3. Workforce and Employment

Sub-pillar	Indicator	Weight	Source
Participation	Labor force participation, age 15-64	1.56	ILO, <i>Key Indicators of the Labour Market (KILM)</i> , 2010
	Labor force participation, age 65+	1.56	
	Economic participation gender gap	1.56	World Economic Forum, <i>Global Gender Gap Report</i> , 2012
	Unemployment rate	1.56	ILO, <i>ILOstat</i> , latest available data 2003-2010
	Youth unemployment rate	1.56	ILO, <i>Laborstat</i> , latest available data 2003-2010
Talent	Country capacity to attract talent	1.56	World Economic Forum, <i>Executive Opinion Survey</i> , 2013-2014
	Country capacity to retain talent	1.56	
	Ease of finding skilled employees	1.56	
	Pay related to productivity	1.56	
	Capacity for innovation	1.56	
	Index of Economic Complexity	1.56	Hausmann, R., Hidalgo, C., et al. <i>The Atlas of Economic Complexity</i> . Cambridge: Puritan Press, 2011
	Firm level technology journal articles	1.56	World Economic Forum, <i>Executive Opinion Survey</i> , 2013-2014
	Scientific and technical journal articles	1.56	World Bank, <i>World Development Indicators online database</i> , 2009 and United Nations, Department of Economic and Social Affairs, <i>World Population Prospects</i> , 2009
	Median age of the working population	1.56	United Nations, Department of Economic and Social Affairs, Population Division, <i>World Population Prospects DEMOBASE 2010</i>
Training	Staff training	1.56	World Economic Forum, <i>Executive Opinion Survey</i> , 2013-2014
	Training services	1.56	
Total Pillar Weight:		25.00	

Source: World Economic Forum (2013)

Table 4. Enabling Environment

Sub-pillar	Indicator	Weight	Source
Infrastructure	Mobile users	2.78	World Bank, <i>World Development Indicators</i> online database, 2011
	Internet users	2.78	
	Quality of domestic transport	2.78	World Economic Forum, <i>Executive Opinion Survey</i> , 2013-2014
Collaboration	State of cluster development	2.78	World Economic Forum, <i>Executive Opinion Survey</i> , 2013-2014
	Business and university R&D collaboration	2.78	
Legal framework	Doing Business Index	2.78	World Bank and International Finance Corporation, 2012
	Social safety net protection	2.78	World Economic Forum, <i>Executive Opinion Survey</i> , 2013-2014
	Intellectual property protection and property rights	2.78	
Social mobility	Social mobility	2.78	World Economic Forum, <i>Executive Opinion Survey</i> , 2013-2014
<b>Total Pillar Weight:</b>		<b>25.00</b>	

Source: World Economic Forum (2013)

**2.1.1 Calculating the composite Index.** The composite Human Capital Index consists of several indicators that are measured on different scales, so the Standard Score method was used to standardize the data obtained. The Standard Score method is used in cases when it is desirable to clearly express position of individual figures within the entire dataset or to compare results from multiple measurements on various scales, which have various means and dispersions. The following mathematical formula is used to calculate the standardized score:

$$x' = \mu' + \sigma' \frac{x - \mu}{\sigma}, \quad (1)$$

where  $x'$  – is the standardized score;

$x$  – is the original raw data;

$\sigma$  – is the original standard deviation;

$\mu$  – is the original mean;

$\sigma'$  – is the desired standard deviation of the standardized score;

$\mu'$  – is the desired mean value of the standardized score.

One of the methods most commonly used in calculation of the standardized score is z-score. Z-score is a statistical method used to express a score's relationship to the mean in a given group of scores. Z-score is expressed as a standard deviation from the mean. The mean is zero and has a standard deviation of one. Thus, all data points above the mean are expressed as positive scores, while all data points below the mean are expressed as negative scores. The z-score method is based on the assumption of normal distribution. A standard deviation of plus (minus) 1 represents the area 34.13 % above (below) the mean and a standard deviation of plus (minus) 2 represents the area 47.72 % above (below) the mean. The z-score of a data point indicates the number of standard deviations

above or below the mean. This means that a z-score of -2 is exactly two standard deviations (or 47.72 %) below the mean.

In the case when z-score ( $z$ ) has the mean 0 and a standard deviation of 1, the formula can be simplified:

$$z = \frac{x - \mu}{\sigma}, \quad (2)$$

where  $\mu$  – is the mean of the population;

$\sigma$  – is the standard deviation of the population.

Once all the input data is converted to a z-score, the score of a given country on a given pillar is established by an unweighted average of all available scores in that pillar. Finally, a country's score on the composite Index is determined by an unweighted average of the four pillar scores.

It was discovered, that to be included in the Index, an indicator must have non-missing data for at least 50 percent of the countries. To be included in the Index, each country must have non-missing data for at least 70 percent of all the indicators defined in Tables 1 through 4. This means that a country must have data for at least:

- 8 out of the 12 indicators in the Education pillar,
- 10 out of 14 indicators in the Health and Wellness pillar,
- 11 out of 16 indicators in the Workforce and Employment pillar,
- 6 out of 9 indicators in the Enabling Environment pillar.

*Table 5. Composite Human Capital Index (Lower income economies)*

	<b>Composite Index</b>	Education	Health and Wellness	Workforce and employment	Enabling environment
Malawi	<b>-0.629</b>	-0.897	-0.723	-0.007	-0.890
Burkina Faso	<b>-1.077</b>	-1.817	-0.943	-0.374	-1.173
Mozambique	<b>-0.966</b>	-1.474	-0.916	-0.337	-1.135
Tanzania	<b>-0.680</b>	-0.870	-0.957	-0.087	-0.805
Cameroon	<b>-0.728</b>	-0.687	-0.850	-0.295	-1.082
Mali	<b>-1.034</b>	-1.747	-0.826	-0.614	-0.949
Lao PDR	<b>-0.297</b>	-0.320	-0.407	-0.097	-0.364
Ghana	<b>-0.363</b>	-0.505	-0.533	-0.099	-0.317
Guinea	<b>-1.272</b>	-1.482	-1.026	-0.911	-1.667
El Salvador	<b>-0.405</b>	-0.612	-0.409	-0.175	-0.425
Philippines	<b>-0.161</b>	0.011	-0.473	0.164	-0.344

Source: World Economic Forum (2013)

*Table 6. Composite Human Capital Index (Lower-middle income economies)*

	<b>Composite Index</b>	Education	Health and Wellness	Workforce and employment	Enabling environment
Egypt	<b>-0.790</b>	-1.206	-0.521	-0.878	-0.555
Sri Lanka	<b>0.020</b>	0.172	0.323	-0.127	-0.288
Nigeria	<b>-0.878</b>	-1.411	-1.034	-0.328	-0.740
Bhutan	<b>-0.370</b>	-0.498	-0.208	-0.231	-0.545
Guatemala	<b>-0.341</b>	-0.968	-0.196	0.035	-0.234
Pakistan	<b>-0.837</b>	-1.166	-0.920	-0.545	-0.718

Source: World Economic Forum (2013)

The World Bank divides states into several categories according to the GNI per capita. The first two groups of states are labeled developing:

- Low-income economies (\$1,045 or less);
- Lower-middle-income economies (\$1,046 to \$4,125).

Tables 5 and 6 present data expressed by the Composite Human Capital Index, calculated by the means of the above defined method of standardized score. It is evident that the Composite Index does not respect the classification of developing countries according to the World Bank based on GNI per capita: for example, The Philippines has scored -0.161, while Pakistan -0.837.

**2.2 Measurement of postal electronic services index (PES index).** Information and communication technologies have radically altered both social and business communication and have a major share in the significant decline of the traditional mail correspondence. Although the trend is global, it is possible to perceive a considerable diversity among postal operators and the degree of provision of e-services to their customers. Following the declared state of postal services development, the UPU (2012) has carried out a study, which investigates the importance of use of information and communication technologies as connecting channels in the communication between post offices and their customers.

Although the Internet is the main delivery channel for e-services, other telecommunication channels (such as mobile phones, call centres or televisions) are also involved in the development of e-services and thus considered in the study. The use of information and communication technologies in the internal processes of individual postal operators is not a part of the scope of this study. In this study, postal operators are those national postal operators who are members of the Universal Postal Union. In addition, e-postal services are those services, which are provided by given national postal operators in a given country.

Designing the survey:

Firstly, members of the Electronic Services Group (working group of the UPU) identified 55 postal e-services to be included in the survey. These e-services have been divided into four categories: e-post, e-commerce, e-finance, and e-government. The respondents (national postal operators) were asked to fill in information about availability of a given e-service, its name and the year of its introduction on the market, together with evaluation of its strategic importance on a scale from one to five (with five being the most important). The aim of the survey was to gather information about the number of e-services offered by individual national operators, including information about perceived value of a given service from the perspective of national postal operators themselves. The survey did not examine the perceived value of the service from the perspective of the customers.

Study participants:

The survey was sent by letter to national postal operators in 191 member countries of the Universal Postal Union and followed a prior notice about the planned survey issued by the regional project

coordinators. 49 percent of the questionnaires were returned to the UPU International Bureau by email, post or fax. Thus, the response rate was 49 %.

**2.2.1 Calculating the composite Index.** To express the composite Index, i.e. the Postal E-services Index, which consists of results from a questionnaire survey evaluating 55 e-services, the Principal Component Analysis (PCA) has been used. It has been used to express one composite indicator based on three individual indices: e-post, e-commerce, and e-finance.

Using the PCA, it is possible to convert a set of observations of possibly correlated variables into a set of values of uncorrelated variables, which are called principal components. This transformation is defined in the following way: the first component has a high variance, thus it aggregates most of the information contained in the original dataset. This first component is used in this study as the resulting index for the establishment of level of e-services development in the countries, which participated in the UPU survey.

Mathematically, the transformation to the principal component of the PCA is defined by a set of p-dimensional vectors of weights or loadings:

$$w_{(k)} = (w_1, \dots, w_p)_{(k)}, \quad (3)$$

that map each row vector to a new vector of principal component scores

$$t_{(i)} = (t_1, \dots, t_p)_{(i)}, \quad (4)$$

given by

$$t_{k(i)} = x_i \cdot w_{(k)} \quad (5)$$

in such a way that the individual variables of  $t$  considered over the data set successively inherit the maximum possible variance from  $x$ , with each loading vector  $w$  constrained to be a unit vector.

First component:

The first loading vector  $w_{(1)}$  thus has to satisfy

$$w_{(1)} = \arg \max_{\|w\|=1} \left\{ \sum_i (t_1)_{(i)}^2 \right\} = \arg \max_{\|w\|=1} \left\{ \sum_i (x_{(i)} \cdot w)^2 \right\} \quad (6)$$

Equivalently, writing this in matrix form gives

$$w_{(1)} = \arg \max_{\|w\|=1} \left\{ \|Xw\|^2 \right\} = \arg \max_{\|w\|=1} \left\{ w^T X^T X w \right\} \quad (7)$$

since  $w_{(1)}$  has been defined to be a unit vector, it equivalently also satisfies

$$w_{(1)} = \arg \max \left\{ \frac{w^T X^T X w}{w^T w} \right\} \quad (8)$$

A standard result for a symmetric matrix such as  $X^T X$  is that the quotient's maximum possible value is the largest characteristic vector of the matrix, which occurs when  $w$  is the corresponding characteristic vector.

With  $w_{(1)}$  found, the first component of a data vector  $x_{(i)}$  can then be given as a score  $t_{1(i)} = x_{(i)} \cdot w_{(1)}$  in the transformed co-ordinates, or as the corresponding vector in the original variables,  $\{x_{(i)} \cdot w_{(1)}\} w_{(1)}$ .

The full principal components decomposition of  $X$  can therefore be given as

$$T = XW, \quad (9)$$

where  $W$  – is a p-by-p matrix whose columns are the characteristic vector of  $X^T X$ .

Table 7. Composite Index of postal e-services (Lower income economies)

	<b>PES index</b>
Malawi	<b>-0.47</b>
Burkina Faso	<b>-0.59</b>
Mozambique	<b>-0.60</b>
Tanzania	<b>-0.79</b>
Cameroon	<b>-1.06</b>
Mali	<b>-1.18</b>
Lao PDR	<b>-1.29</b>
Ghana	<b>-1.29</b>
Guinea	<b>-1.37</b>
El Salvador	<b>-1.44</b>
Philippines	<b>-1.54</b>

Source: United Postal Union (2012)

Table 8. Composite Index of postal e-services (Lower-middle income economies)

	<b>PES index</b>
Egypt	<b>0.23</b>
Sri Lanka	<b>-0.45</b>
Nigeria	<b>-0.70</b>
Bhutan	<b>-0.72</b>
Guatemala	<b>-0.81</b>
Pakistan	<b>-1.22</b>

Source: United Postal Union (2012)

Tables 7 and 8 show results of the above defined Principal Component Analysis for the same group of developing countries that is presented in Tables 5 and 6 (which report their scores on the Composite Human Capital Index). Once again, it is clearly visible that the results are inconsistent with the classification of developing countries according to the World Bank (GNI per capita indicator): Malawi has scored -0.47, while Egypt 0.23.

**2.3 Validity of predicted relationship between human capital index and PES index in developing countries.** Pearson's correlation coefficient was used to verify the predicted relation, i.e. to confirm the dependence of PES index on the human capital index in Lower-income economies and Lower-middle income economies groups.

$$r = \frac{\sum \left[ \left( x_i - \bar{x} \right) \cdot \left( y_i - \bar{y} \right) \right]}{\sqrt{\sum \left( x_i - \bar{x} \right)^2 \cdot \sum \left( y_i - \bar{y} \right)^2}} \quad (10)$$

Probability value (*P* value) with significance level at 5 % was used to establish the final determination of significance of correlation.

It has been rather a challenge to determine the procedure of the testing and a particular methodology, especially because this approach has not been used in this field before. Authors generally assume significance of relationship of PES index and the HCI in countries labeled *developed*, i.e. in countries whose GNI per capita is higher than in states which are under consideration in this study. This trend has been verified by the authors at the beginning of this study (Fig. 1).

The following procedure was derived from the first step of the testing - monitoring the significance of relation between two variables in the group of countries classified as developing by the World Bank. Nevertheless, this classification did not show as suitable, especially when taking into account a number of studies [38], [41], [22], which state that developing countries are very specific in comparison with industrialized countries.

UPU (2012) in its study shows the relationship between PES index and HCI by the means of quadratic regression. They claim that there is a possible explanation for the quadratic functional dependence between the development of postal e-service and human capital development: once human capital reaches a certain level, the speed of e-service adoption is higher, which leads to greater provision of postal e-services. This finding raises the question of the possible role of postal e-services development and its relationship to education in countries where the HCI is low.

The research of relationship between PES index and the HCI follows the attempts to define new sub-groups of developing countries, which could be described as being developed on the basis of defined variables enough to be able to adopt measures to kick-start further development of e-service market in order to sustain continuous development in relation to HCI. If any extreme values are found, a sub-group of states showing these extreme values will be defined, unless it already exists in the classification by the World Bank.

This research focused on analysis of the trend of quadratic function. In the testing of statistical dependence of tracked variables (PES index and the HCI), the study focused on explanation of the trend of relationship between the two variables in two groups of developing countries according to the World Bank (i.e. Lower income economies and Lower-middle income economies). In the first step, dependencies of defined variables (PES and HCI) were tested in all states of a respective group of developing countries. In the second step, countries under the curve of quadratic function were

excluded, and a new testing of dependence was carried out among the remaining countries (see Fig. 2 and 3). Fig. Results of the testing are presented in the following chapter.

**3. Results.** In the first round of testing, countries labeled developed by the World Bank (i.e. High-income economies with GNI per capita of \$12,736 or more) were chosen to verify the assumption of dependence between the development of human capital and postal e-services. These countries were: Switzerland, Germany, Australia, Austria, Republic of Korea, Canada, France, Russian Federation, Israel, United States of America, Spain, Portugal, Italy, and Hungary.

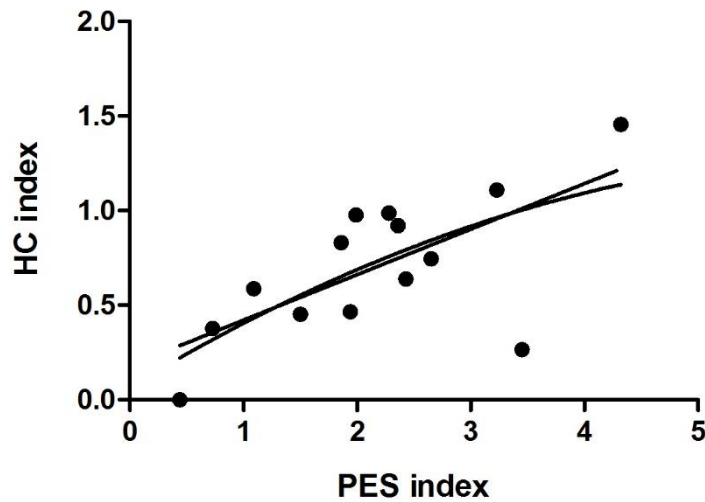


*Fig. 1. Dependence of development of HC and e-postal services in developed countries (authors)*

In this group of countries, linear function practically copies the quadratic function and the statistical dependence of the indices shows immediately.

*Table 9. Outputs from statistical linear regression analysis (High income economies)*

$r^2$	0.4488
$F$ test	9.772
$P$ value	0.0088
Deviation from zero?	Significant

Source: Authors

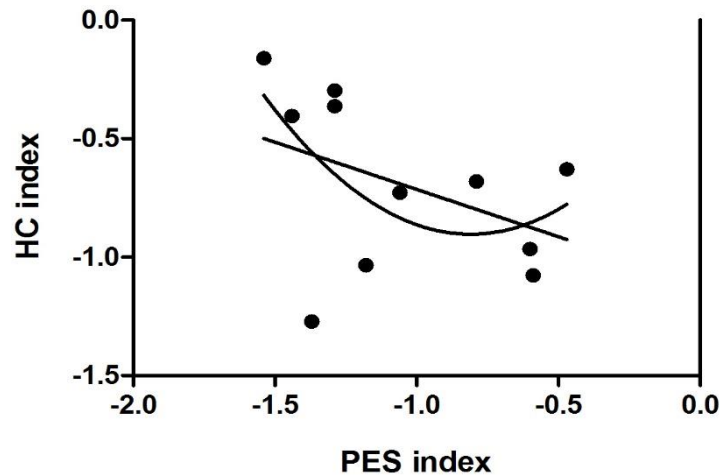


Fig. 2. Dependence of development of HC and e-postal services in Lower-income countries (authors)

It is evident from Fig. 2 that in this group, there are significant differences between the indices: the linear function does not correspond with the trend of the quadratic function (compare with Fig. 1). When considering all the countries in the Lower-income economies group, the dependence has not been confirmed.

Table 10. Outputs from statistical linear regression analysis (Lower-income economies) – first step

$r^2$	0.1754
$F$ test	1.914
$P$ value	0.1999
Deviation from zero?	Not Significant

Source: Authors

Countries, which were under the curve of the quadratic function (Fig. 2) were excluded from the second step of testing (namely Burkina Faso, Mozambique, Mali, and Guinea). In the remaining states, the dependence has shown to be statistically significant (see Table 11). However, another extreme has been discovered in the remaining states: countries with a higher HCI value show lower values of PES index, which should be vice versa (when compared with the trend in Fig. 1). This result confirms that the development of human capital in relation to the development of postal market as one of the basic parts of national economy, is uneven. Generally, it can be said that in this group of developing countries, the sectors of Education system, Health and Wellness, Workforce and employment and Enabling environment are not directed effectively. Therefore the development of human capital of the population of individual states does not go hand in hand with development of other sectors of the national economy. Nevertheless, the assumption of inequality of relationship between the tracked indicators in all countries in this category has been confirmed. Thus it is possible to define a sub-group of states which show this extreme trend in order to apply measures which would stabilize the current situation and deal with the issues comprehensively.

Table 11. Outputs from statistical linear regression analysis (Lower-income economies) – second step

$r^2$	0.6180
$F$ test	8.088
$P$ value	0.0361
Deviation from zero?	Significant

Source: Authors

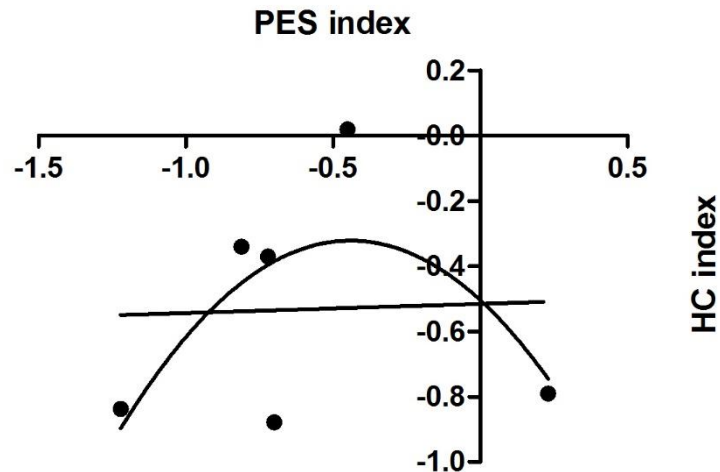


Fig. 3. Dependence of development of HC and postal e-services in Lower-middle income economies (authors)

In the Lower-middle income economies group, it is possible to see a significant difference between the trend of the linear function and that of the quadratic function, and the same applies to the Lower income economies group. In the first testing, when all states from this group were considered, no dependence has been established as statistically significant.

Table 12. Outputs from statistical linear regression analysis (Lower-middle income economies) – first step

$r^2$	0.001427
$F$ test	0.005714
$P$ value	0.9434
Deviation from zero?	Not Significant

Source: Authors

This group has also been tested two times, the second time with exclusion of the countries which were under the curve of the quadratic function (namely Egypt and Nigeria). The dependence has proven to be statistically significant in the group of remaining states (see Table 13). In this case, no extreme values have been found, in contrast with the Lower-income economies group. The trend of the linear function shows similar direction as in results presented in Fig. 1; in other words, PES index is directly proportional to HCI.

*Table 13. Outputs from statistical linear regression analysis (Lower-middle income economies) – second step*

$r^2$	0.9763
$F$ test	82.43
$P$ value	0.0119
Deviation from zero?	Significant

Source: Authors

**4. Discussion.** Based on the statistical results of this article, it can be confirmed that it is not suitable to classify states according to the GNI per capita indicator only. Generally, it can be stated that classification according to this indicator is even less up-to-date when it comes to decision-making and provision of basic services to inhabitants of developing countries, or when establishing strategic relations with industrialized states, which would mean cooperation on development of a sector of national economy.

Outputs from Fig. 1 confirm that in industrialized countries, there is a clear dependence of PES index on the HCI. Following this finding, these indicators may be identified as possible tools for modeling economic potential of individual states. In the two groups of developing countries, it has been found that the classification of developing countries according to the GNI per capita indicator (issued annually by the World Bank) does not correspond with the trend which has been found in industrialized countries. This is because the countries labeled developing must be examined from various points of view; it is not satisfactory to restrict the examination to the commonly used indicator only. The use of PES index indicator in examination of its relation to the development of human capital is relevant because it is a composite indicator analyzing current development trends in this important field of national economy.

This paper had two objectives:

- To define a sub-group of developing countries which are developed “enough” (because the dependence has shown to be significant), and thus can be labeled as states “more developed”, more economically stable and thus ready to establish new strategic relations with industrialized countries.
- If any extreme values are found, to define a sub-group of states which show these extreme values, unless it already exists in the classification by the World Bank.

Even though there are studies, which deal with human capital in developing countries and with its important role in insurance of maximum stability and finding the right direction for future development of these countries. Dutta & Osei-Yeboah [21], Suliman & Mollick [59] – these papers are the first one to examine human capital in the context of postal e-services.

Guren et al., [27] deal with the relationship of human capital and labor market from the perspective of current challenges of the world trade in developing countries. Goldberg & Pavcnik [26] focus on issues of developing countries and on the impact of globalization on income inequality. Blanton & Blanton [3] deal with the concept of gender as a current phenomenon vital for promotion of stable development of society in both developed and developing countries. They focus specifically on the role of women’s rights in attracting foreign direct investment (FDI) and prove that developing countries show different trends than developed countries, which must be respected when implementing measures.

**4.1 Limitations of the study.** This research used data from primary research of two institutions: the Universal Postal Union and the World Economic Forum. Some limitations of the study may be perceived because of the possible inconsistency of the data. Tables 1 through 4 list the individual indicators which were used to establish the human capital index. It is visible in Tables 1 through 4

that the data used do not always proceed from the same time period. With regards to this, it is important to note that especially in developing countries, it is particularly difficult to gather data about Secondary enrolment rate, Stunting and wasting, etc. on annual basis so that there would be data from all the countries considered and from the same time period. In cases when there was not enough input data available for a given indicator, these indicators were excluded from the quantification of the final composite index.

For quantification of the HCI, the study of the World Economic Forum from 2013 (containing data from 2012) was used. This independent international organization issued further studies on quantification of HCI development in 2015. Authors of the paper have nevertheless decided to use the data from the 2012 study, mainly because the primary research of United Postal Union on calculation of PES index was carried out in January 2012 (containing data from 2011).

Another limitation of the study might be also the range of countries considered. In developing countries (here in this particular context, developing countries are those countries that are generally less industrialized than countries which were subject to the testing in Fig. 1), political stability is a great obstacle in the way of continuous development, as indicated in studies dealing with the issues of human capital. In many cases these are states where the executive branch itself is not transparent and does not gather or share data with third countries. This is a key issue in the attempt to explain long-term development plans of developing countries, because some measures are implemented only partially, or not at all [16], [47], [53].

**4.2 Benefits of the study and recommendations for further research.** It can be concluded that the important effect of relationship between e-postal services and human capital in developing countries has been confirmed. This relationship has proven to be statistically significant in the defined sub-group of developing countries. Therefore it can be confirmed that the field of postal services, in particular its computerization, can be regarded as relevant in the process of classification of countries as developing. Thus it is necessary to respect this aspect when implementing measures which are directed at developing countries in the attempt to ensure maximum stability and further development of these countries.

Based on the defined methodology for calculation of the PES index and on its results, it has been stated that a possible explanation for the quadratic functional dependence between the development of postal e-services and the level of human capital can be the following: once a country's human capital reaches a certain level, the speed of adoption of postal e-services is higher, which leads to general growth of these services. This trend raises a question of the impact of postal e-services development on education in countries with low level of human capital (UPU, 2012). More research is needed. In relation to the results of this study, two basic areas have been identified where further research would be recommended:

- The explanation of the functional dependence of the trend of quadratic function, which has divided states into sub-groups, where the statistical dependence of human capital and postal e-services has been confirmed.

- An in-depth analysis of education or other indicators of the composite HCI in relation to development of postal market, which, especially in countries from the Lower-income economies group, shows reverse (extreme) trend.

Further studies striving to determine the borderline value of human capital at which the speed of adoption of postal e-services would correspond with development in other countries could use the following input information: the value will definitely not be negative.

There are other facts that justify the need of classification of developing countries based on other parameters than the indicator GNI per capita only. From resulting values of HCI in states which have been excluded from the second round of testing (because they were below the axis of the quadratic function in Fig. 2 and 3), it is evident that the classification on the basis of GNI per capita is not respected: Philippines has scored -0.161 but according to the classification of the World Bank belongs

among Lower income economies, while Pakistan has scored -0.837 and belongs among Lower-middle economies.

The classification of states based on GNI per capita does not correspond with the found extreme trend either: extreme values have been found in the Lower income economies group. Statistically significant dependence of relation of PES index and the HCI has then been found in states which show the following trend: with increasing HCI, the PES index decreases, which should be vice versa.

These findings are relevant and topical, in particular with reference to the works of other authors, who define human capital as a key concept vital for a country's development. The field of postal services is one of the main components of national economy and recommendations for further research stem from the need to broaden knowledge about this sector.

**Summary.** The issues of developing countries, as documented in this article, surely are among topics of current discussions of both world organizations ensuring basic services in developing countries and of industrialized countries which perceive developing countries as potential outlets for their production. This can be described as the general paradigm for most of research inquiring into the issues of developing countries. In this study, which presents a new way of analyzing developing countries, this paradigm has been defined by means of two indices which reflect the current debates in the globalized world. Firstly, it is human capital used as a tool which has the informative capability about the economic potential of a country. Secondly it is the field of postal services, which is one of the main sectors of national economy of every state (especially the area of postal e-services as one of the current trends of development in postal market). Both human capital and postal e-services are currently being discussed internationally and define the general development trend of the society.

The whole study is based on up-to-date data. Tests of statistical significance of relationship between postal e-services development and HCI have proven this relationship significant, and therefore it must be respected in decision-making especially in developing countries. The study has proven that defined classification of states according to the World Bank does not respect values of the defined indicators. This article brings a new method of analyzing issues of developing states and widens the range of aspects that must be taken into consideration in implementing measures to promote development.

To conclude, it should be noted that there are some limitations of the study. Transparency and effective application of measures to enforce development are not always the main objective of legislative and executive powers in developing countries. However, this fact should not belittle the relevance of results of this study, especially because the data in partial indicators, which have been used to calculate the composite indices, proceed from independent organizations and describe the current status as it is. Nevertheless, to ensure political stability should be the primary aim of all interested parts who have any interest in cooperation with developing countries. The results of this study (and other studies analyzing the human capital in different contexts) can be further taken into account when applying specific measures in the process of targeted economic development in developing countries.

### **Acknowledgements**

The article was supported by student grant – SGSDFJP\_2015001.

### **References**

- [1] Ankrah, E. (2015). The Impact of Technology on Postal Services in Ghana. *International Journal of Scientific and Technological Research (New Delhi)*, 4(1), 125-129.
- [2] Barro, R. J. (2001). Human capital and growth. *American Economic Review*, 91(2), 12-17. doi:10.1257/aer.91.2.12
- [3] Blanton, R. G., & Blanton, S. L. (2015). Is Foreign Direct Investment "Gender Blind"? Women's Rights as a Determinant of US FDI. *Feminist Economics*, 21(4), 61-88. doi:10.1080/13545701.2015.1006651

- [4] Boccanfuso, D., Larouche, A., & Trandafir, M. (2015). Quality of Higher Education and the Labor Market in Developing Countries: Evidence from an Education Reform in Senegal. *World Development*, 74, 412-424. doi:10.1016/j.worlddev.2015.05.007
- [5] Bourguignon, F., & Morrisson, C. (2002). Inequality among World Citizens: 1820-1992. *American Economic Review*, 92(4), 727-744. doi: 10.1257/00028280260344443
- [6] Brooking, A. (1997). Managing engineering and technology means managing intellectual capital. In Kocaoglu D. A., (Ed.), *Innovation in Technology Management - The Key to Global Leadership. PICMET '97: Portland International Conference on Management and Technology*. Portland. doi:10.1109/PICMET.1997.653388
- [7] Çağatay, N., & Özler, Ş. (1995). Feminization of the Labor Force: The Effects of Long-term Development and Structural Adjustment. *World Development*, 23(11), 1883-1894. doi: 10.1016/0305-750X(95)00086-R
- [8] Castanias, R. P., & Helfat, C. E. (1991). Managerial Resources and Rents. *Journal of Management*, 17(1), 155-171. doi:10.1177/014920639101700110
- [9] Castanias, R. P., & Helfat, C. E. (2001). The Managerial Rents Model: Theory and Empirical Analysis. *Journal of Management*, 27(6), 661-678. doi:10.1177/014920630102700604
- [10] Chatzoudes, D., Chatzoglou, P., & Vraimaki, E. (2015). The Central Role of Knowledge Management in Business Operations Developing a New Conceptual Framework. *Business Process Management Journal*, 21(5), 1117-1139. doi:10.1108/BPMJ-10-2014-0099
- [11] Ciutiene, R., Meiliene, E., Savaneviciene, A., & Vaitkevicius, S. (2015). Interdependence between Human Capital and the Power of a Shadow Economy: Lithuanian Case Study. *Technological and Economic Development of Economy*, 21(3), 460-482. doi:10.3846/20294913.2015.1017864
- [12] Cleeve, E. A., Debrah, Y., & Yiheyis, Z. (2015). Human Capital and FDI Inflow: An Assessment of the African Case. *World Development*, 74, 1-14. doi:10.1016/j.worlddev.2015.04.003
- [13] Cook, N. P. S., & Jones, J. C. (2015). The African Growth and Opportunity Act (AGOA) and Export Diversification. *Journal of International Trade & Economic Development*, 24(7), 947-967. doi:10.1080/09638199.2014.986663
- [14] Cooray, A., Mallick, S., & Dutta, N. (2014). Gender-Specific Human Capital, Openness and Growth: Exploring the Linkages for South Asia. *Review of Development Economics*, 18(1), 107-122. doi:10.1111/rode.12072
- [15] Davenport, T. (2005). The Coming Commoditization of Processes. *Harvard Business Review*, 83(6), 100-108. doi: 10.1225/R0506F
- [16] Dornan, M. (2014). Reform Despite Politics? The Political Economy of Power Sector Reform in Fiji, 1996-2013. *Energy Policy*, 67, 703-712. doi:10.1016/j.enpol.2013.11.070
- [17] Driskill, R., Horowitz, A. W., & Mendez, F. (2009). Hierarchical Human Capital and Economic Growth: Theory and Evidence. *Journal of Institutional and Theoretical Economics-Zeitschrift Fur Die Gesamte Staatswissenschaft*, 165(4), 723-743. doi: 10.1628/093245609789919612
- [18] Drucker, P. F. (1999). Knowledge-Worker Productivity: The Biggest Challenge. *California Management Review*, 41(2), 79-+. doi: 10.1109/EMR.2006.1679053
- [19] Dunning, J. H. (1981). Explaining the International Direct-Investment Position of Countries - Towards a Dynamic or Developmental-Approach. *Weltwirtschaftliches Archiv-Review of World Economics*, 117(1), 30-64. doi:10.1007/BF02696577
- [20] Durlauf, S. N., & Johnson, P. A. (1995). Multiple Regimes and Cross-Country Growth-Behavior. *Journal of Applied Econometrics*, 10(4), 365-384. doi:10.1002/jae.3950100404

- [21] Dutta, N., & Osei-Yeboah, K. (2013). A New Dimension to the Relationship between Foreign Direct Investment and Human Capital: The Role of Political and Civil Rights. *Journal of International Development*, 25(2), 160-179. doi:10.1002/jid.1739
- [22] Easterly, W., & Rebelo, S. (1993). Fiscal-Policy and Economic-Growth - an Empirical-Investigation. *Journal of Monetary Economics*, 32(3), 417-458. doi:10.1016/0304-3932(93)90025-B
- [23] Edvinsson, L., & Malone, M. S. (1997). *Intellectual capital: Realizing your company's true value by finding its hidden brainpower*. 240 p. New York: Harper Business. ISBN 0887308414.
- [24] Fontana, M., & Wood, A. (2000). Modeling the Effects of Trade on Women, at Work and at Home. *World Development*, 28(7), 1173-1190. doi:10.1016/S0305-750X(00)00033-4
- [25] Gille, V. (2015). Distribution of Human Capital and Income: An Empirical Study on Indian States. *Journal of Macroeconomics*, 43, 239-256. doi:10.1016/j.jmacro.2014.11.003
- [26] Goldberg, P. K., & Pavcnik, N. (2007). Distributional Effects of Globalization in Developing Countries. *Journal of Economic Literature*, 45(1), 39-82. doi:10.1257/jel.45.1.39
- [27] Guren, A., Hemous, D., & Olsen, M. (2015). Trade Dynamics with Sector-Specific Human Capital. *Journal of International Economics*, 97(1), 126-147. doi:10.1016/j.jinteco.2015.04.003
- [28] Haque, A., & Khatibi, A. (2005). E-shopping: Current Practices and Future Opportunities Towards Malaysian Customer Perspective. *Journal of Social Science*, 1(1), 41-46. doi: 10.3844/jssp.2005.41.46
- [29] Haque, A., Sadeghzadeh, J., & Khatibi, A. (2006). Identifying Potentiality Online Sales in Malaysia : A Study on Customer Relationships Online Shopping. *The Journal of Applied Business Research*, 22(4), 119-130. doi: <http://dx.doi.org/10.19030/jabr.v22i4.1420>
- [30] Haucap, J. (2015). Editorial: Consumer Behavior and Telecommunications Policy. *Telecommunications Policy*, 39(8), 625-626. doi:10.1016/j.telpol.2015.07.013
- [31] Hinostroza, J. E., Isaacs, S., & Bougroum, M. (2014). Learning and Education in Developing Countries: Research and Policy for the Post-2015 UN Development Goals. In D. A. Wagner (Ed.), *Information and communications technologies for improving learning opportunities and outcomes in developing countries* (pp. 42-57) Palgrave Macmillan US. doi:10.1057/9781137455970\_3
- [32] Hollenbeck, J. R., & Jamieson, B. B. (2015). Human Capital, Social Capital, and Social Network Analysis: Implications for Strategic Human Resource Management. *The Academy of Management Perspectives*, 29(3), 370-385. doi:10.5465/amp.2014.0140
- [33] Huang, Z., & Benyoucef, M. (2013). From E-commerce to Social Commerce: A close Look at Design Features. *Electronic Commerce Research and Applications*, 12(4), 246-259. doi:10.1016/j.elerap.2012.12.003
- [34] Kalfa, S., & Taksa, L. (2015). Cultural Capital in Business Higher Education: Reconsidering the Graduate Attributes Movement and the Focus on Employability. *Studies in Higher Education*, 40(4), 580-595. doi:10.1080/03075079.2013.842210
- [35] Kaplan, R. S., & Norton, D. P. (1996). Linking the Balanced Scorecard to Strategy. *California Management Review*, 39(1), 53-+. doi:10.2307/41165876
- [36] Kinda, T. (2013). Beyond Natural Resources: Horizontal and Vertical FDI Diversification in sub-saharan Africa. *Applied Economics*, 45(25), 3587-3598. doi:10.1080/00036846.2012.678982
- [37] Klomp, J., & de Haan, J. (2015). Bank Regulation, the Quality of Institutions, and Banking Risk in Emerging and Developing Countries: An Empirical Analysis. *Emerging Markets Finance and Trade*, 50(6), 19-40. doi:10.1080/1540496X.2014.1013874

- [38] Kormendi, R. C., & Meguire, P. G. (1985). Macroeconomic Determinants of Growth - Cross-Country Evidence. *Journal of Monetary Economics*, 16(2), 141-163. doi:10.1016/0304-3932(85)90027-3
- [39] Kujacic, M., Blagojevic, M., Sarac, D., & Vesovic, V. (2015). The modified activity-based costing method in universal postal service area: Case study of the montenegro post. *Inzinerine Ekonomika-Engineering Economics*, 26(2), 142-151. doi:10.5755/j01.ee.26.2.2818
- [40] La Paz, A. I., Ramaprasad, A., Syn, T., & Vasquez, J. (2015). An ontology of E-commerce - mapping a relevant corpus of knowledge. *Journal of Theoretical and Applied Electronic Commerce Research*, 10(2), 1-9. doi: 10.4067/S0718-18762015000200001
- [41] Levine, R., & Renelt, D. (1992). A sensitivity analysis of cross-country growth regressions. *The American Economic Review*, 82(4), 942-963.
- [42] Liu, A. P. L. (1991). Communications and development in post-mao mainland china. *Issues & Studies*, 27(12), 73-99.
- [43] Lucas, R. E. (1990). Why doesn't capital flow from rich to poor countries? *The American Economic Review*, 80(2), 92-96.
- [44] Marc, A., Verjee, N., & Mogaka, S. (2015). *The challenge of stability and security in west Africa*, 215p. World Bank: International Bank for Reconstruction and Development
- [45] Morita, T., & Sugawara, K. (2015). Human capital and FDI: Development process of the developing country in an overlapping generation model. *Journal of International Trade & Economic Development*, 24(7), 922-946. doi:10.1080/09638199.2014.986748
- [46] Morris, M. D. (1979). Measuring the condition of the world's poor: The physical quality of life index. *Economic Development and Culture Change*, 30 (4), 887-889. doi: 10.2307/2619179
- [47] Newell, P., Bulkeley, H., Turner, K., Shaw, C., Caney, S., Shove, E., & Pidgeon, N. (2015). Governance traps in climate change politics: Re-framing the debate in terms of responsibilities and rights. *Wiley Interdisciplinary Reviews-Climate Change*, 6(6), 535-540. doi:10.1002/wcc.356
- [48] Ngcwangu, S. (2015). The ideological underpinnings of world bank tvet policy: Implications of the influence of human capital theory on south african tvet policy. *Education as Change*, 19(3), 24-45. doi:10.1080/16823206.2015.1085620
- [49] Ozler, S. (2000). Export orientation and female share of employment: Evidence from turkey. *World Development*, 28(7), 1239-1248. doi:10.1016/S0305-750X(00)00034-6
- [50] Prajogo, D. I. (2006). The relationship between innovation and business performance? A comparative study between manufacturing and service firms. *Knowledge and Process Management*, 13(3), 218-225. doi:10.1002/kpm.259
- [51] Renström, T. I., & Spataro, L. (2015). Population growth and human capital: A welfarist approach. *The Manchester School*, 83, 110-141. doi:10.1111/manc.12110
- [52] Rosenzweig, M. R. (1990). Population-growth and human-capital investments - theory and evidence. *Journal of Political Economy*, 98(5), 38-70. doi:10.1086/261724
- [53] Rudra, N. (2015). Social protection in the developing world: Challenges, continuity, and change. *Politics & Society*, 43(4), 463-470. doi:10.1177/0032329215602884
- [54] Seguino, S. (2000). Gender inequality and economic growth: A cross-country analysis. *World Development*, 28(7), 1211-1230. doi 10.1016/S0305-750X(00)00018-8
- [55] Siah, A. K. L., & Lee, G. H. Y. (2015). Female labour force participation, infant mortality and fertility in malaysia. *Journal of the Asia Pacific Economy*, 20(4), 613-629. doi:10.1080/13547860.2015.1045326

- [56] Sidak, J. G. (2015). Maximizing the us postal service's profits from competitive products. *Journal of Competition Law & Economics*, 11(3), 617-669. doi:10.1093/joclec/nhv026
- [57] Squicciarini, M. P., & Voigtlaender, N. (2015). Human capital and industrialization: Evidence from the age of enlightenment. *Quarterly Journal of Economics*, 130(4), 1825-1883. doi:10.1093/qje/qjv025
- [58] Stewart, T. A. (1998). *Intellectual capital: The new wealth of organization*, 320p. Crown Business. ISBN 0385483813
- [59] Suliman, A. H., & Mollick, A. V. (2009). Human capital development, war and foreign direct investment in sub-saharan africa. *Oxford Development Studies*, 37(1), 47-61. doi:10.1080/13600810802660828
- [60] Todaro, M. P. (1992). *Population and Development Review*, 18(2), 359-363. doi:10.2307/1973685
- [61] Unicef. (2015). *Annual report 2014*, 64p. Unicef. ISBN: 978-92-806-4809-6.
- [62] United Nations. (2015). *Information economy report 2015*, 136p. United nations. ISBN 978-92-1-112887-1.
- [63] Universal Postal Union. (2012). *Measuring postal e-services development*, 63p. Electronic Postal Services Group.
- [64] Vaz, C. R., Inomata, D. O., Viegas, C. V., Selig, P. M., & Varvakis, G. (2015). Intellectual capital: Rating, measurement of forms and questioning about future uses. *Navus-Revista De Gestao E Tecnologia*, 5(2), 73-92.
- [65] Verbic, M., Majcev, B., & Cok, M. (2014). Education and economic growth in Slovenia: A dynamic general equilibrium approach with endogenous growth. *Ekonomický časopis*, 62(1), 19-45.
- [66] World Economic Forum. (2013). *The Human Capital Report*, 547p. World Economic Forum. ISBN 92-95044-52-5.
- [67] Zenger, T. R. (1994). Explaining organizational diseconomies of scale in R&D: Agency problems and the allocation of engineering talent, ideas, and effort by firm size. *Management Science*, 40(6), 708-729. doi:10.1287/mnsc.40.6.708
- Zhang, K. H., & Markusen, J. R. (1999). Vertical multinationals and host-country characteristics. *Journal of Development Economics*, 59(2), 233-252. doi:10.1016/S0304-3878(99)00011-5

# **X. Philosophy of Research and Education**

**M M S E J o u r n a l V o l . 4**



## **Systematic Analysis and Synthesis of Integral Estimations of Bachelors' Training in the Field of Financial Monitoring**

Alena Gaibatova <sup>1</sup>, Grigory Krylov <sup>1,2,a</sup>, Ilya Seryy <sup>1</sup>, Anastasiia Vorobeva <sup>1</sup>,  
Konstantin Vorobev <sup>1</sup>

1 – National Research Nuclear University MEPhI, Moscow, Russia

2 – Doctor of Technical Sciences, Professor, Distinguished Fellow of Higher school, Financial University, Moscow, Russia

a – [op50@mail.ru](mailto:op50@mail.ru)



DOI 10.13140/RG.2.1.4889.4329

**Keywords:** IFES, principal component analysis (PCA), professional selection, financial monitoring, professional orientation, systematic analysis.

**ABSTRACT.** The following article describes methods and algorithms of improving the quality of students' training in NRNU MEPhI on the profile activities in the sphere of financial monitoring. In this work, we have investigated a new subject field: application of the principal component analysis method to examine students' performance in different profiles of their training.

**Introduction.** Over the last years, innovative technologies are applied to assess human resources. The use of up to date high-tech methods of analysis of specialists training quality, in particular the method of principal components of factor analysis is one of such technologies.

Currently, preparation of qualified and competitive in the global labour market specialists by training students in multidisciplinary areas of education – is the main purpose of the higher education institutions of the Russian Federation.

O.Y.Golodets, Deputy Chairman of the Government of the Russian Federation, during her speech in the international conference “Intellectual basis of the modern education” in November 2014 noted, highlighting the range of tasks for the near future: “The man, who has an unusual combination of knowledge, has perspectives of creative breakthrough in the labour market [1].”

O.Y.Gorodets stressed that, based on the analytical indicators of the higher education institutions ratings, “Russia needs to develop multidisciplinary education as multi-discipline specialist are more valuable state labour reserve [1].”

Researches of the career guidance of students of economic security were conducted earlier to their further recruitment to the Federal Financial Monitoring Service. These researches are discussed in detail in the article “Profile-based students assignment to core financial intelligence unit departments”, authors D.I.Chukova, A.P. Pakhomov [3]. Also in the dissertation “Statistical methods of integrated assessments of institute human resources” for the degree of PhD in Economics D.N.Krymzin conducted a study to assess human resources of the higher education institutions on the example of N.P.Ogarev Mordovia State University [4]. Abstract of dissertation for the degree of Candidate of Juridical Sciences written by G.O.Krylov “The international experience of legal regulation of information security and the possibilities for its versatile application in the Russian Federation” [5]. The problem of improving the adequacy and authenticity of assessments of military-medical entities in the interests of procedures of medical decisions making using the PCA method, which is our primary concern, is solved in the dissertation “Automated synthesis of integral assessments of military-medical entities by the PCA method”, author V.M.Seleznev [6].

In this work, methods of system analysis, of mathematical statistics and of factor analysis are applied to solve the mentioned problem, as well as statistics of students' performance over the last 4 semesters in two different directions of training: "Informatics and computer science" and "Information-analytical security systems" are collected. The PCA method was used as tool for the analysis of statistical data. Performance of each student can be effectively evaluate based on the mentioned data.

In multivariate analysis object is described by different sets of data indicators. The direct perception and analysis of big amount of data is difficult. Thus, you have to use data with not high dimension, i.e. change multivariate sample to data with low dimension, when exploring an object. The main purpose of the PCA method is reducing dimension and "compression" of system of random variables without significant loss of information contained in the system. Method consists of decomposition of k-dimensional random vector by Formula 1 (using orthogonal transformation) for the system of linearly independent vectors, which is selected as orthonormal set of eigenvectors (eectors), corresponding to the eigenvalues (evalues) of covariance matrix of vector X [7]:

$$X = (X_1, X_2, \dots, X_k)^T \quad (1)$$

In other words, after the transformation of multidimensional observations, only attributes that have the most importance in transition from one object to another are selected.

Correlational symmetrical matrices are built on the basis of student's performance in two different directions, which characterize students' performance.

Dispersions of principal components and correlation coefficients are received on the basis of correlation matrices and are shown in Fig. 1 and 2.

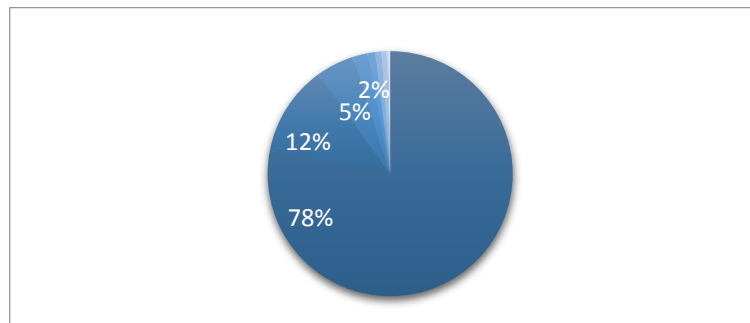


*Fig. 1. Characteristics of components' cumulative contribution into total variance by profile activities in the region of informatics and computer engineering.*

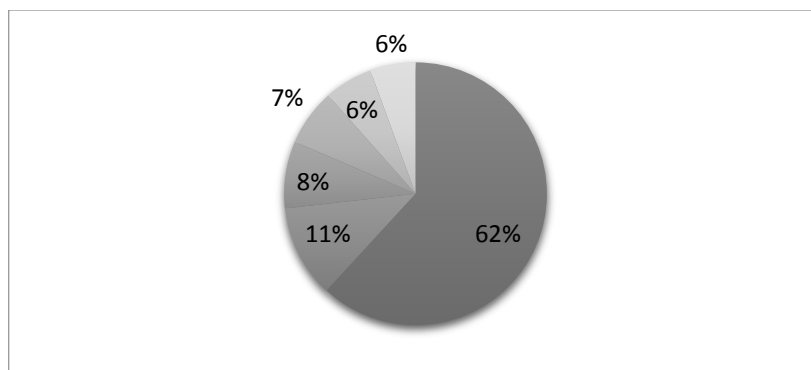


*Fig. 2. Characteristics of components' cumulative contribution into total variance by profile activities in the region of AML / CFT / FPWMD.*

The most important moment in implementing the PCA method is interpretation of received results and founded principal components.

Weight of contribution made by components of each discipline were determined by using Analytic Hierarchy Process. The analysis of hierarchy based on the survey of experts in relevant spheres (areas) about importance of knowledge and skills.

The following directions for specialization “Information-analytical security systems” are determined:

1. Analytical sphere of activity;
2. IT-sphere;
3. Activity in the sphere of information security;
4. International sphere of activity.

The following directions of training in “Informatics and computer science” discipline are determined:

1. System engineer;
2. Software engineer;
3. System analyst.

For the purpose of results verification it was carried out comparative analysis of values, revealed by the principal components method, with 24 expert assessments of knowledge contributions, the generation of which is foreseen by educational teaching process per said academic disciplines in profile activities in the field of financial monitoring (see. Fig. 3-6) and in the region of informatics and computer engineering (see. Fig. 7-9).

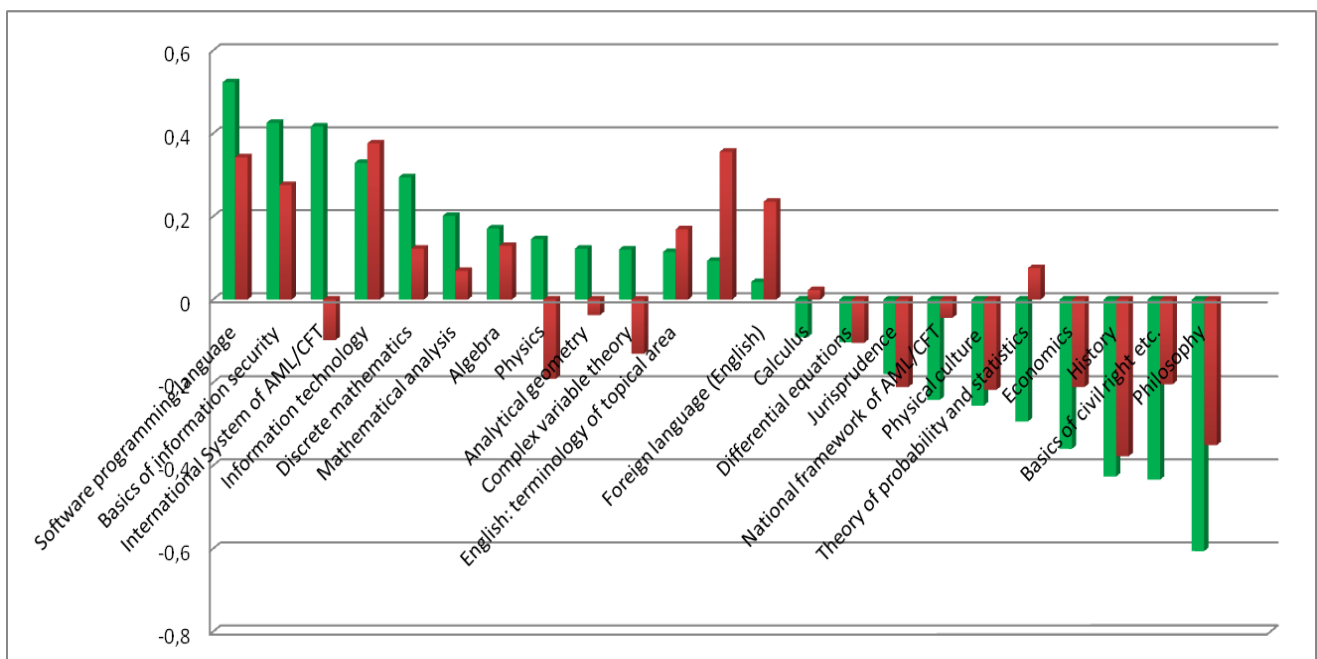


*Fig. 3. Comparative analysis of integral and expert estimations of tendency of bachelors' training in the field of IT - technologies and programming*

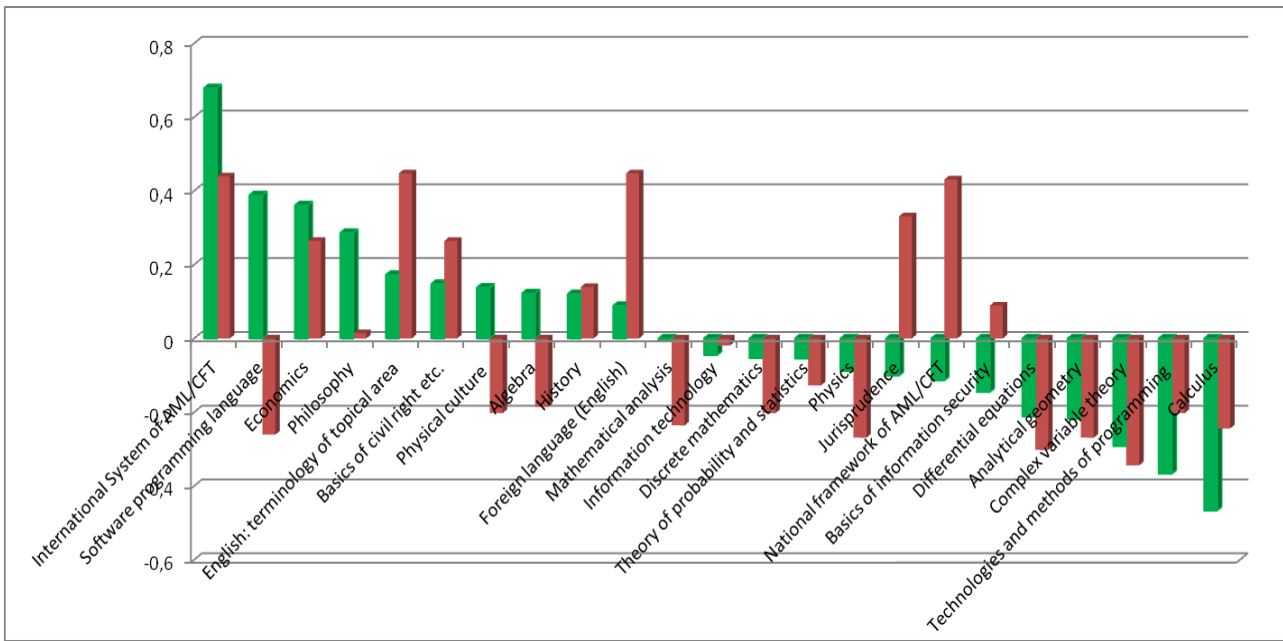


Fig. 4. Comparative analysis of integral and expert estimations of tendency of bachelors' in the field of information security

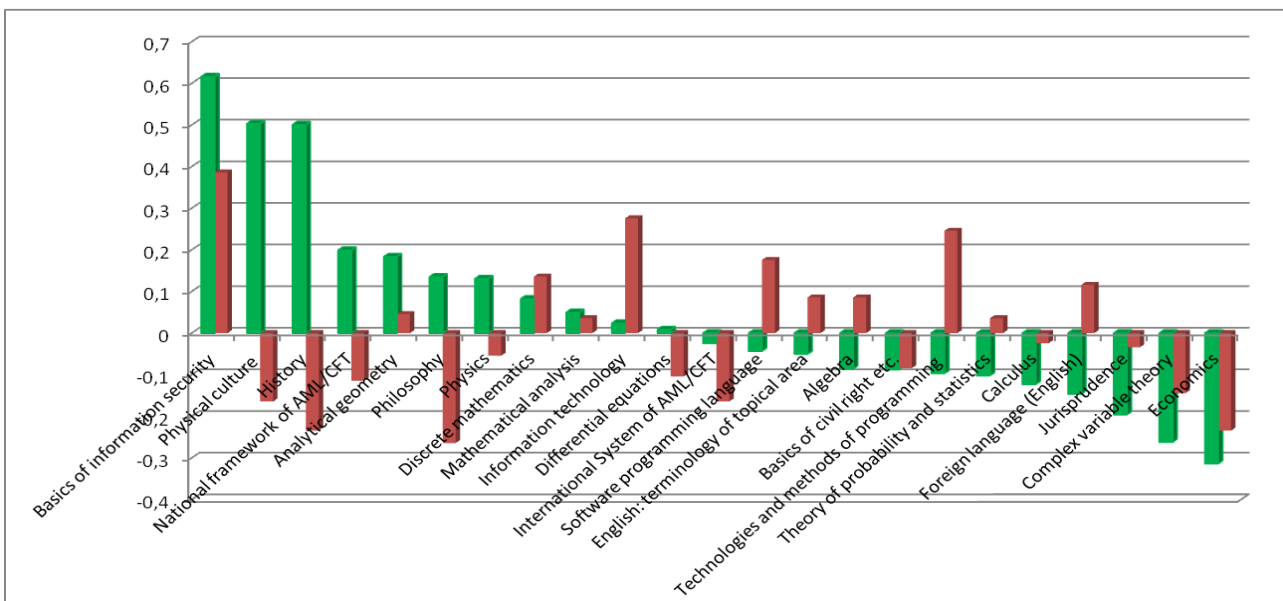


Fig. 5. Comparative analysis of integral and expert estimations of tendency of bachelors' in international sphere of AML / CFT / FPWMD

A comparative analysis showed that the second principal component is an integral assesstment of direction of training of specialists in IT spehere – technologies and programming; indicators obtained for the third principal component is an integral assesstment of specialists' training in international sphere; indicators of the forth principal component is an integral assesstment of specialists' trainig in sphere of information security.

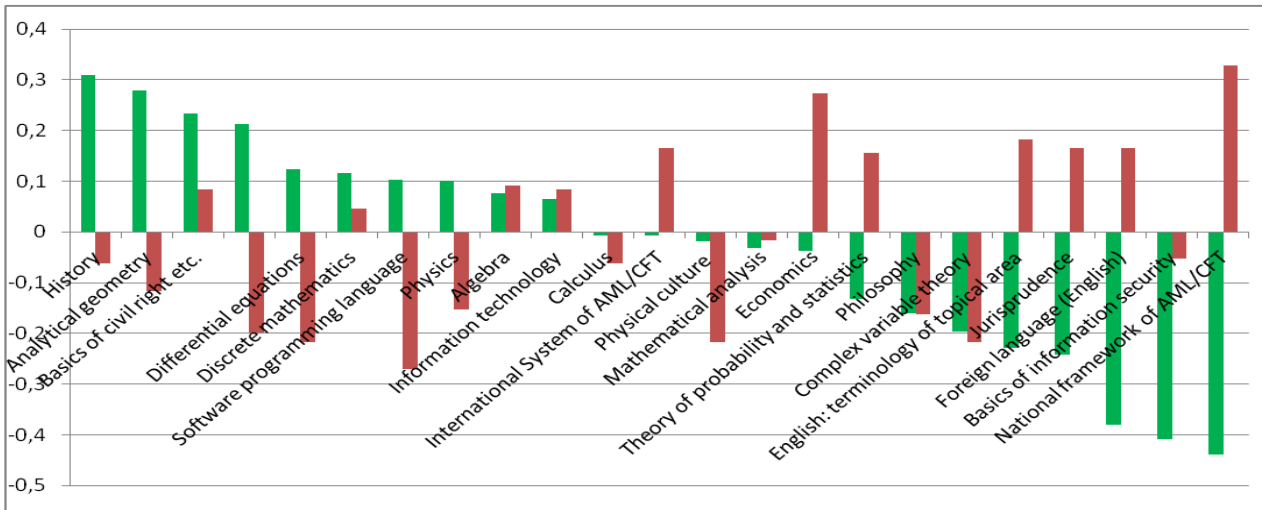


Fig. 6. Comparative analysis of integral and expert estimations of tendency of bachelors' training in the field of analytical activities for financial monitoring

As can be seen from the above, per the sixth principal component, the integral characteristic of factors, negatively affecting analytical specialists' training in the field of AML / CFT / FPWMD (see. Fig. 6) is specified.

Based on experts' judgments, it found that all disciplines, positively correlating with the sixth principal component, promote minimization of specialists' training of analytical orientation in the field of financial monitoring.

Fig. 7-9 show that for the direction of training in "Informatics and computer science" discipline the main component 4 is corresponding to the direction of systems engineer training. Principal component 8 fully characterizes the trend of programmer engineer training. Principal component 8 corresponds to the following trend - system analyst.

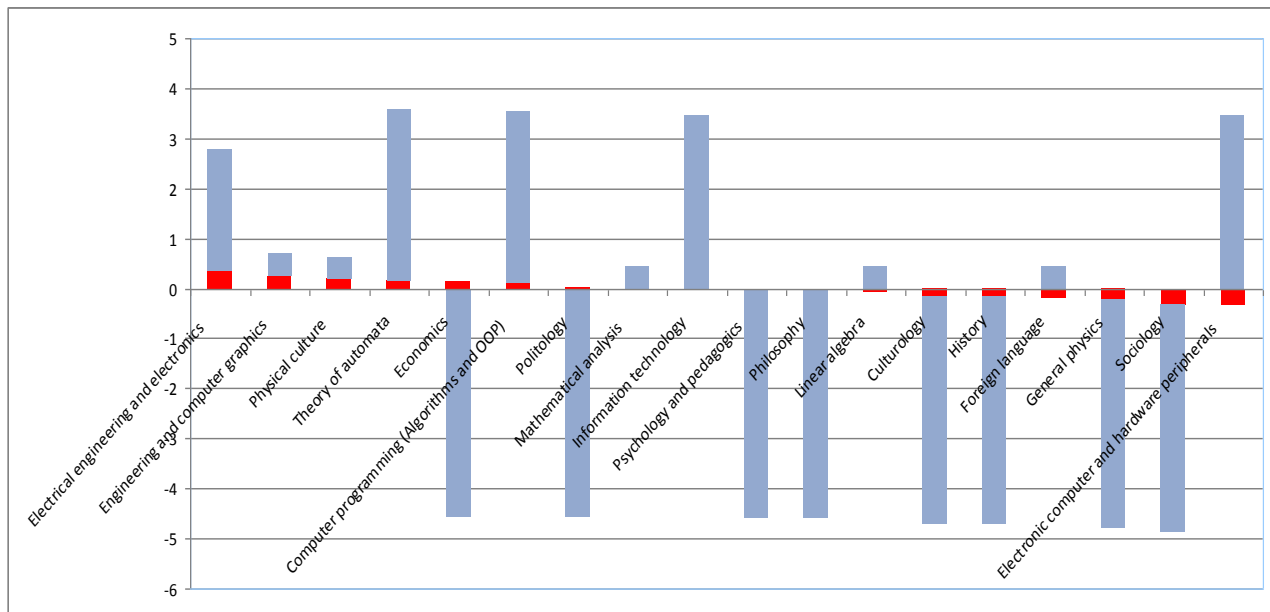


Fig. 7. Comparison of the fourth principal component with the indexes of system engineer training

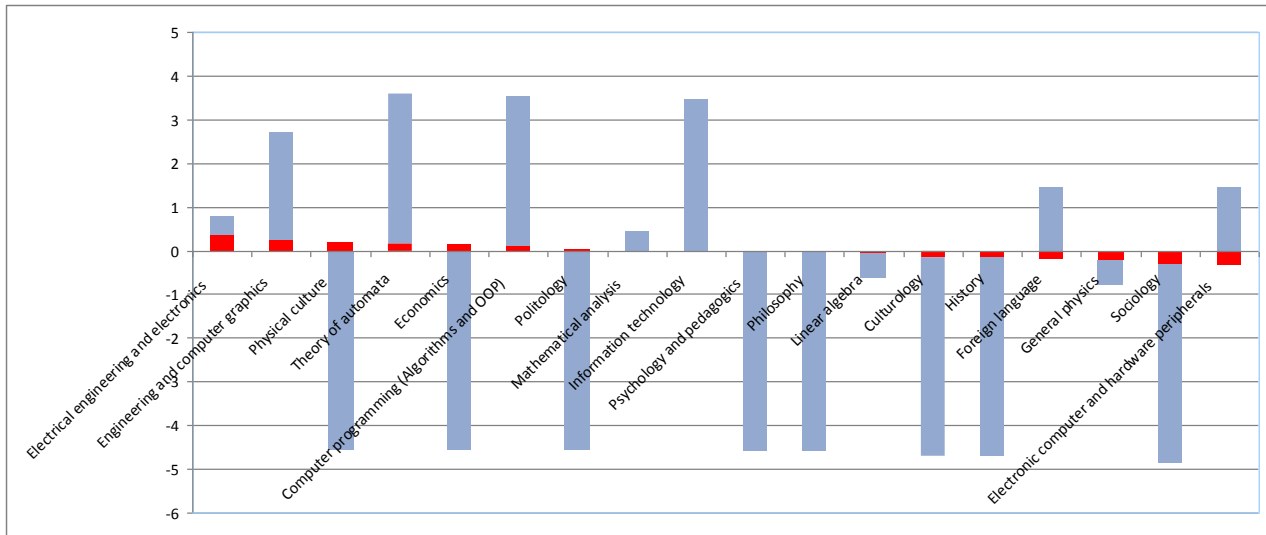


Fig. 8. Comparison of the eighth principal component with the indexes of programmer engineer training

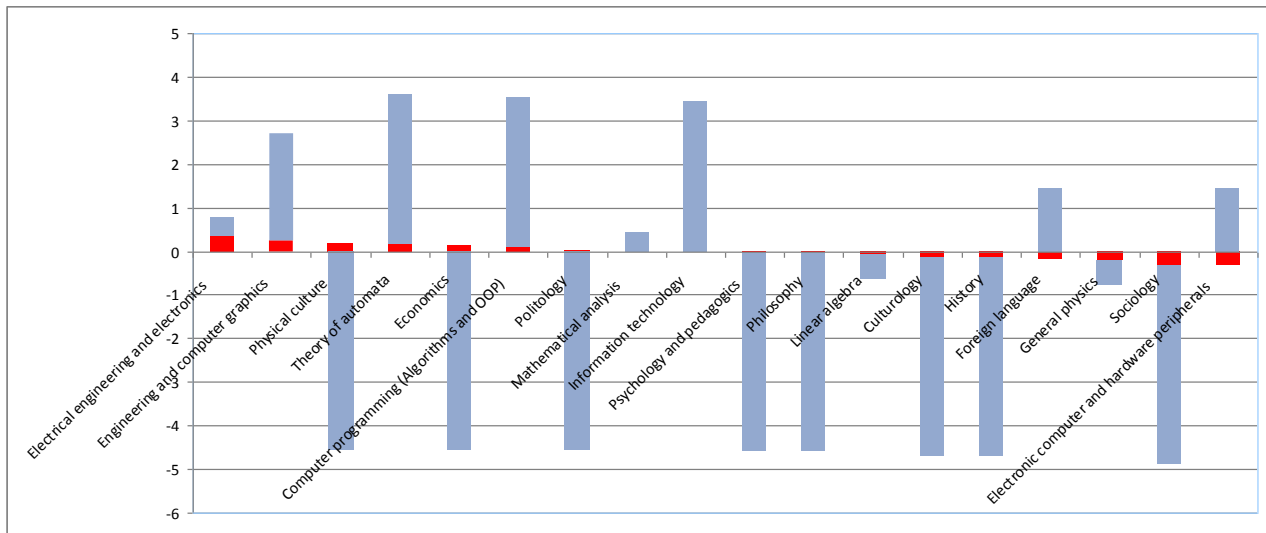


Fig. 9. Comparison of the eighth principal component with the indexes of system analyst training

During the work, analysis of data on students' performance was conducted to determine their predisposition to the one of direction of training provided by the curriculum.

The results were reported at a weekly seminars of the department No.75 "Financial monitoring", faculty of "Cybernetics and Information security" in NRNU MEPHI. Also they were used in students' distribution by specialized groups according to their propensity to the specific priority direction of activity. In addition, it is planned to use this method in determining of place of students' place of practice.

## References

- [1] O.Y.Golodets: modern universities should provide students a multidisciplinary education. [Online]. Available: <http://tass.ru/obschestvo/1574291>.
- [2] Daria Chukova, Pakhomov Alexey. "Profile-based students assignment to core financial intelligence unit departments ", SIN '15 Proceedings of the 8th International Conference on Security of Information and Networks, ACM New York, NY, USA, 2015, p. 107-108.

- [3] D.N. Krymzin. “Application of the log-linear analysis for researches of dependence of the assessment of the personnel capacity of higher education institution from characteristics of teachers“. Vestnik NSUEM, 2014, p. 134-141.
- [4] G.O. Krylov, V.M. Lazarev, A.E. Lyubimov. “The international experience of legal regulation of information security and the possibilities for its versatile application in the Russian Federation“, Legal Information, 2013, p. 15.
- [5] V.M.Seleznev. “Automated synthesis of integral assessments of military-medical entities by the PCA method“. PhD dissertation, Moscow, 2000.
- [6] S. A. Aivazyán, Applied statistics: Fundamentals of Modeling and Primary Data Processing [in Russian], Finansy i Statistika, Moscow, 1983, p. 472.



*Partnership advertisement Recruitment Advertisement*

**BEIJING INNOVATION CENTER FOR INTELLIGENT ROBOTS AND SYSTEMS**

**Professors, Engineers for Advanced Robotics**

**Research & Development**

at Innovation Center for Intelligent Robots and Systems, Beijing Institute  
of Technology, Beijing, China

(Apr. 2016 - Sep. 2020)



The center has an immediate need for robotics experts and mechanical engineers targeting robotics research/development (R&D) and commercialization of home service robots, medical rehabilitative robots, industrial robots, specialized robots, and unmanned systems.

Advanced Innovation Center for Intelligent Robots and Systems in Beijing Institute of Technology is a specialized research institution for robots among 13 Beijing government-supported advanced innovation centers.

**Research fields:**

- Mechanism design for robots
- Legged locomotion
- Pneumatic artificial muscle
- Electric drive
- Robotic software/hardware design for embedded system
- Software architectures for robotics
- Ethercat communication
- Computer vision and sensors
- Micro and Nano mechatronics
- Bio-robotic system
- Neurophysiology of perceptual cognition and motion control
- Artificial intelligence
- New material for robots
- Robotic appearance design

**Positions & Qualifications:**

**1. World's leading Senior Scientists in robotic fields**

- Served as distinguished professors or equivalent positions at elite international universities/institutes
- Engaged in the industry management and development of robots
- Salary: US\$ 90,000-150,000/year

**2. Professors, Scientists, Experienced Engineers**

- Served as distinguished professors, associate professors or equivalent positions at reputable international universities/institutes

- Ability to lead the scientific research team to tackle problems in key technologies
- Salary: US\$ 60,000-100,000/year

3. Associate Professors, Assistant Professors, Engineers, Perfect Lecturers, PhDs

- Outstanding academic ability and good development potentials
- Ability to assist and cooperate with the leader of the scientific research team to finish academic research and product development
- Salary: US\$ 30,000-60,000/year

Salary will be commensurate with qualifications and experience. To apply, please send your resume, including personal particulars, employment history, current and expected salary and your working assumption by both following emails.

**Deadline for application: May, 31, 2016**

**Requirements:**

Employment period: Apr. 2016-Sep.2020, Extendable

(Start from Apr. 2016 is very welcome!)

Annual working time: More than 9 months in China

**Contact Information:**

Email: [ninger1979@bit.edu.cn](mailto:ninger1979@bit.edu.cn), [renshichu@bit.edu.cn](mailto:renshichu@bit.edu.cn)

Tel: +86 10 68918231, +86 15301165837 Rouer Dai

+86 13426112302 Lin Li

Post: 217 Room, 6<sup>th</sup> School Building in Beijing Institute of Technology, 5 South Zhongguancun Street, Haidian District, Beijing, 100081, P.R. China.

*Mechanics, Materials Science & Engineering Journal*®

ISSN 2412-5954

*Published by Magnolithe GmbH*

*Printed by Magnolithe GmbH*



9 772412 595450